



VYSOKÉ UČENÍ TECHNICKÉ V BRNĚ

FAKULTA ELEKTROTECHNIKY
A KOMUNIKAČNÍCH TECHNOLOGIÍ

ÚSTAV MIKROELEKTRONIKY

**BIOROZHRAŇÍ MIKRO- A NANOSTRUKTUROVANÝCH
POVRCHŮ**

HABILITAČNÍ PRÁCE

AUTOR PRÁCE

Mgr. ZDENKA FOHLEROVÁ, Ph.D.

BRNO 2021

Biorozhraní mikro- a nanostrukturovaných povrchů

Fohlerová, 2021

Habilitační práce

Biorozhraní mikro- a nanostrukturovaných povrchů

Zdenka Fohlerová

2021

fohlerova@vutbr.cz

<https://www.vutbr.cz/lide/zdenka-fohlerova-25180>

Research ID: A-6893-2013

ORCID ID: 0000-0002-1232-2301

Vysoké učení technické v Brně

Fakulta elektrotechniky a komunikačních technologií

Ústav mikroelektroniky

Technická 10

616 00 Brno

www.vutbr.cz

Klíčová slova: strukturované povrchy; oxidy kovů; biorozhraní; parylen; oxid křemičitý; mechanotransdukce

Předmluva

Tato práce prezentuje oblasti zájmu a vybrané výsledky autorky týkající se jeho pedagogické a vědecké činnosti. Autorka v předložené práci propojuje oblasti technických věd s přírodními vědami (biologie, chemie, a biofyziky), což vedlo k vytváření a uskutečňování řady zajímavých projektů. V této práci bude především diskutováno studium (i) biorozhraní nanostrukturovaných materiálů z oxidů kovů, a (ii) výroba polymerních flexibilních sloupků pro měření síly generované buňkami. Autorkou popsána vědecká činnost se uskutečňovala především na Fakultě elektrotechniky a komunikačních technologií Vysokého učení technického v Brně, výrobní náležitosti byly řešeny v čistých prostorách Středoevropského technologického institutu VUT. Práce je rozdělena na dvě hlavní kapitoly (1 a 2) popisující specifickou vědecko-pedagogickou činnost autorky, přičemž publikační výstupy související s habilitační prací jsou shrnuty v kapitole 4. Tato kapitola je doplněna šesti články publikovanými v impaktovaných časopisech. Kapitola 3 pak stručně shrnuje vědecko-pedagogickou činnost uchazeče do budoucnosti. Všechny publikované práce se zaměřují na specifické aspekty výzkumné činnosti autorky. Část zde uvedených výsledků je také podpořena grantovou agenturou ČR v rámci juniorských projektů (GAČR č. 19-04270Y). Dále byly činnosti podporovány MŠMT v rámci výzkumného centra SIX na FEKT VUT.

Ráda bych zde poděkovala doc. Jiřímu Háze z Ústavu mikroelektroniky na FEKT za poskytnutí podpory v habilitačním řízení a možnosti vést habilitační řízení pod jeho ústavem. Poděkování patří i dalším kolegům ze skupiny Chytrých nástrojů na CEITEC VUT a LabSensNano na FEKT VUT. Jmenovitě bych uvedla především Dr. Mozaleva ve spolupráci s výrobou nanostrukturovaných povrchů z oxidů kovů, svým nadřízeným, doc. Hubálkovi a prof. Neužilovi za poskytnutí technického a finančního zázemí a Dr. Alexandru Otáhalovi za celkovou podporu a motivaci.

Zdenka Fohlerová

Obsah

Předmluva	4
Obsah	5
Úvod Biozhraní mikro- a nanostrukturovaných povrchů	6
1 Nanostrukturované povrchy z oxidu kovů	8
1.1 Nanotrubičky z oxidu titaničitého	9
1.1.1 Elektrochemická anodizace TiO ₂ nanotrubiček	10
1.1.2 Vliv anodizačních podmínek na přípravu TiO ₂ nanotrubiček	12
1.1.3 Modifikace vlastností TiO ₂ nanotrubiček	14
1.1.4 Vědecké práce v oblasti TiO ₂ nanotrubiček	14
1.2 Templátová metoda přípravy „nanotyčinek“ z oxidů kovů	16
1.2.1 Elektrochemická výroba PAA šablony	17
1.2.2 Příprava „nanotyčinek“ PAA asistovanou anodizací	18
1.2.3 Vědecká činnost v PAA asistované anodizaci	19
2 Mikrostrukturované povrchy z polymerů	22
2.1 Výroba PDMS sloupků	23
2.2 Vědecká činnost v oblasti výroby polymerních mikrosloupků	25
3 Perspektiva uchazeče	29
Závěr	30
Reference	32
4 Publikační činnost v rámci habilitační práce	36
Článek 1 Enhanced antibacterial and anticancer properties of Se-NPs decorated TiO ₂ nanotube film	
Článek 2 Antibacterial activity of AgNPs-TiO ₂ nanotubes: influence of different nanoparticle stabilizers	
Článek 3 Tuning the response of osteoblast-like cells to the porous-alumina-assisted mixed-oxide nanomound array	
Článek 4 Anodic formation and biomedical properties of hafnium-oxide nanofilms	
Článek 5 Nanostructured ZrO ₂ bioceramic coatings derived from the anodically oxidized Al/Zr metal layers	
Článek 6 SiO ₂ -decorated Parylene C micropillars designed to probe cellular force	

Mikro- a nanotechnologie a nanomateriály jako takové, tvoří v dnešní době velice široké spektrum možností a aplikací v řadě diverzních oborů. V současnosti nalézají uplatnění v oblastech běžného života jako je elektronika (paměťová média, bioelektronika), zdravotnictví (cílené doručování léčiv, tkáňové inženýrství, antibakteriální povrchy), textilní průmysl (nanovlákna, antibakteriální nanočástice, nesmáčivé povrchy), strojírenství (samočistící laky), chemický průmysl (nanotrubice, nanokompozity, selektivní katalýza, kosmetika), elektrotechnický průmysl (vysokokapacitní záznamová média, fotomateriály, palivové články), optický průmysl (optické filtry, fotonická vlákna, integrovaná optika), automobilový průmysl, kosmický průmysl (katalyzátory, odolné povrchy satelitů), vojenský průmysl (nanosenzory, konstrukční prvky raketoplánů), životní prostředí (biodegradace).

Pokrok v oblasti výzkumu a vývoje pokročilých funkčních materiálů na základě vzestupu a dostupnosti řady technik umožnil přesnou kontrolu a modifikaci povrchu materiálů, jak z hlediska chemického, tak především topografického. Výroba povrchů s definovanou topografií v mikro- a nanoměřítku na kovových oxidech a polymerních materiálech nabyla, mimo jiného, velkého významu jako slibná strategie pro kontrolu a modulaci interakce těchto povrchů s biologickým materiálem. Tím se může dosáhnout např. vylepšení povrchových vlastností pro implantáty a antibakteriální povrchy. Povrchová topografie a chemie materiálu ovlivňuje biologické procesy, včetně adsorpce a konformace bílkovin, adsorpce organických látek, má vliv na chování buněk, bakteriální adhezi nebo interakci s krevními elementy. Tyto důsledky se pak staly všeobecně významnými i pro další aplikace včetně materiálů používanými v mikrofluidních systémech a biosenzorech. Změna povrchové topografie, a s tím související i určité vlastnosti či následné interakce, se navíc může dít bez nutnosti měnit objemové vlastnosti materiálu nebo povrchovou chemii.

Různou topografií mikro- a nanopovrchů je možno vytvořit řadou fyzikálně-chemických metod s náhodnou i organizovanou strukturou v řadě kovových a polymerních materiálů.^[1] V současné době běžně dostupné kovové materiály v biomedicíně, používané jako zubní a ortopedické implantáty nebo jako chirurgické nástroje, tvoří titan a jeho slitiny, nerezová ocel nebo slitina chromu a kobaltu. Velkého významu také nabývají další kovové materiály jako je tantal, zirkon a hafnium. Nicméně řadu těchto materiálů spíše nacházíme ve formě slitin nebo tenkých povrchových vrstev, jelikož jsou poměrně drahé. Metod modifikace povrchových vlastností je celá řada, počínaje mechanickým zdrsňením, plazmatickým ošetřením, leptáním, anodizací atd., vedoucí k vytváření porézních povrchů, nanotrubiček, nanotyčinek, nanoteček či náhodných struktur, z nichž některé budou probrány v dalších kapitolách. Vedle těchto topografických úprav je možné modifikovat povrchy dalšími postupy, včetně proteinové adsorpce, UV zářením, silanizováním povrchu, adsorpcí nanočástic nebo adsorpcí bioaktivních látek. V současné době je obecně známo, že chemické vlastnosti a morfologie v mikro- a nanoměřítku jsou významnou vlastností materiálu podporující adsorpci bílkovin, buněčnou adhezi, proliferaci či diferenciaci; výzkum také přešel z kovů a kovových slitin na jejich oxidy či

kompozity, čímž bylo často dosaženo zvýšené biokompatibility, a strukturováním povrchů se mohly např. vytvářet povrchy s definovanými vlastnostmi pro konkrétní aplikaci.

V poslední době nabylo velkého významu také použití polymerů. Mimo jiné, využití polymerních povrchů v medicíně např. ve formě implantovatelných bioelektronických zařízení, slouží polymerní strukturované povrchy také jako senzor v oblasti mechanotransdukce, tj. detekce buněčné síly pomocí flexibilních polymerních sloupků. Stejně jako kovy či oxidy kovů mohou být polymerní povrchy upraveny tak, aby modulovaly biologické interakce. Tyto úpravy se opět můžou týkat vytvářením mikro- a nanostrukturovaných povrchů, změnou objemových vlastností či změnou povrchové chemie. Například ošetření polymeru kyslíkem v plazmě, jako je polymethylmetakrylát a polypropylen, může indukovat povrchové změny v rozsahu nano- a mikroskopických rozměrů, ale také zvyšuje množství polárních skupin na povrchu, čímž se zároveň mění i chemické vlastnosti na povrchu polymeru. Alternativně, pro zpracování fluorovaných polymerů se používá kyslíková plazma k vytváření povrchů s drsností v řádech nanometrů beze změny povrchové chemie. Proces vytváření vysoce uspořádaných pravidelných struktur v řádech od stovek mikrometrů po desítky nanometrů začal využívat litografické techniky spojené s technikami odlévání, nanotisku či leptáním. Definované struktury byly vytvářeny v polymerech jako polydimetylsiloxan (PDMS), SU-8 fotorezist, polykarbonát nebo parylen, jež bude dále zmíněn v souvislosti s výrobou mikrosloupeků v kapitole 2.

Cílem této práce je tedy čtenáři ukázat možnosti výroby nanostrukturovaných povrchů z oxidů kovů jako je oxid titanu, oxid tantalu, hafnia či zirkonia, jak citlivě můžou tkáňové buňky či bakterie reagovat na tyto nanostrukturované povrchy neboli jak jen velmi malá změna v topografii může mít zásadní vliv na chování buněk. Vše je namířeno s cílem modulovat povrchové vlastnosti materiálů mající potenciál v tkáňovém inženýrství nebo jako antibakteriální povrchy. V druhé kapitole bude probírána technologie výroby pole polymerních sloupeků jako vertikálních kantileverů a jejich aplikaci v mechanotransdukci.

1 Nanostrukturované povrchy z oxidu kovů

Historicky byla nanostrukturovaná pole nanotrubiček, nanosloupek či nanoteček z oxidů kovů vyráběna za účelem aplikace v oblastech počínaje od antikoročních povrchů, samočisticích povlaků, solárních článků, fotokatalýzy či elektrokatalýzy.^[2] Na druhé straně získaly své místo i v biomedicínských směrech jako biokompatibilní materiály se zvýšenou osteointegrací, jako systém pro doručování léčiv a v pokročilém tkáňovém inženýrství.^[3] Řada nanostrukturovaných oxidů prokázala dobrou biokompatibilitu, tj. vykazují určité antibakteriální vlastnosti, nízkou cytotoxicitu, dobrou stabilitu a cytocompatibilitu, včetně zlepšení adheze, proliferace a diferenciac buněk či naopak jako antiadhezni povrch^[4, 5], a to i právě v závislosti na geometrii příslušných nanostruktur a jejich následných modifikací. Obecně řečeno, materiály z čistých kovů jako např. hojně používaný titan nemají dostatečnou antibakteriální schopnost nebo bioaktivitu, proto začalo intenzivní studium oxidu titanu a jiných kovů či kompozitů včetně jejich nanostrukturování jako možnost vylepšení vlastností povrchu biomateriálů dle specifických požadavků.

Z hlediska interakce nanostrukturovaných povrchů s buňkami řada in vitro a in vivo studií prokázala, že buňky včetně kmenových buněk, osteoblastů aj. vykazují selektivní odpověď na délku, průměr, tvar a vzdálenost nanotrubiček, nanosloupek a jiných, topograficky se odlišujících struktur.^[6-8] Tyto studie dále pokračovaly v modulaci těchto parametrů s cílem optimalizovat výslednou topografii nanostruktur tak, aby splňovala požadovanou funkci. Tím je myšleno zlepšení např. antibakteriálních vlastností nebo zlepšená adheze, proliferace, metabolická aktivita či diferenciac buněk, modulace za účelem snížené nebo zvýšené adsorpce biomolekul atd. Zde existuje nespočet studií v tomto směru, nicméně jednoznačné konstatování, který povrch je neoptimálnější neexistuje, jelikož řada prací byla prováděna na různých, topograficky odlišných nanostrukturách, materiálech, lišily se v syntetických procesech či buněčných systémech, a je tedy obtížné srovnat a vyvodit konkrétní závěry. Chemické vlastnosti materiálů, včetně jejich nanostrukturování v podstatě také souvisí se smáčivostí těchto povrchů ve srovnání s nestrukturovaným povrchem.^[9, 10] Zde je výhoda v tom, že pouhou změnou např. průměru nanostruktury můžeme měnit jeho smáčivost, aniž bychom měnili povrchové chemické vlastnosti. Zde můžeme obecně říci, že buňky mají tendenci lépe interagovat a adherovat s hydrofilními povrchy. Další optimalizace povrchových vlastností nanostruktur může být v důsledku navázání různých bioaktivních látek, jako je hydroxyapatit zlepšující osteointegraci implantátů.^[11] Na druhou stranu bylo také prokázáno, že např. samotné nanotrubičky z oxidu titaničitého (TiO_2) podporují růst apatitu přírodní cestou v simulovaných tělních tekutinách ve srovnání s „hladkým“ povrchem.^[12] Taktéž přeměna amorfní formy TiO_2 na anatázovou či směs anatasu a rutilu podpořila bioaktivitu TiO_2 nanotrubiček.^[12]

Z hlediska antibakteriálních vlastností, samotné nanostruktury ve srovnání s nestrukturovaným povrchem vykazují více či méně antibakteriální vlastnosti. Nicméně řada těchto nanostruktur byla dále modifikována pro vylepšení antibakteriálního účinku.^[13] Na začátku lze opět říct, že

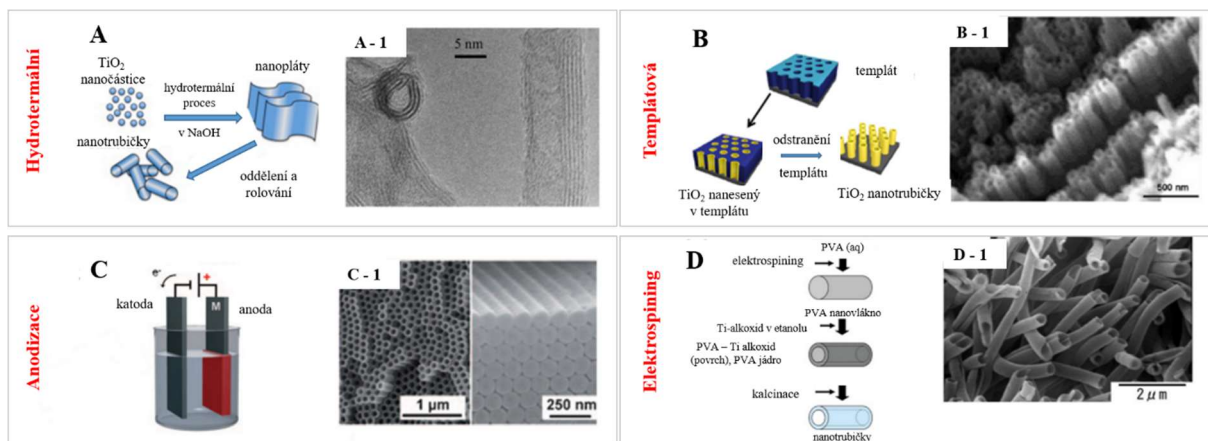
samotná geometrie nanostruktur má významný vliv na interakci s gram pozitivními a gram negativními bakteriemi. Další modifikace podporující antibakteriální vlastnosti zahrnují např. naplnění TiO₂ nanotrubiček antibiotiky, jejichž postupné uvolňování bylo dosaženo modulací jejich průměru a délky.^[14] Z obecného hlediska lze nanostrukturované povrchy dále dekorovat nanočásticemi mající antibakteriální vlastnosti. Příkladem jsou nanočástice zinku, stříbra nebo selenu.^[15, 16] Nicméně pokud tyto dekorované povrchy mají být aplikované jako potenciální biomateriály, je nezbytnou součástí optimalizovat a často tedy najít určitou rovnováhu mezi antibakteriálními účinky a netoxickými účinky na tkáňové buňky.

V dalších kapitolách se zaměříme na přípravu a aplikaci povrchů tvořených polem nanotrubiček z oxidu titanu, a dále na „nanotyčinky“ z oxidu tantalu, hafnia a zirkonia.

1.1 Nanotrubičky z oxidu titaničitého

V posledních letech byla vytvořena řada různých strategií pro přípravu polí nanotrubiček z oxidu titaničitého, které lze zhruba rozdělit na templátové (tj. za využití šablony), hydrotermální a anodickou oxidaci (Obr. 1 A-D).

Šablonami pro vytvoření trubičkových struktur mohou být např. definovaná organizovaná nanostruktura porézního oxidu hlinitého či jiné šablony ve formě např. membrán, micel, ZnO₂ nanodrátů apod.^[17] Tyto šablony jsou poté vyplněny různými metodami (sol-gel metoda nebo depozice atomové vrstvy (ALD)) oxidem titaničitým za vzniku TiO₂ nanotrubiček.^[18] Takovéto kompozitní struktury lze použít, když je TiO₂ v/na šabloně, ale nejčastěji je šablona odstraněna (selektivně rozpuštěna) za vzniku „volných“ nanotrubiček nebo trubičkového prášku o průměru 10 - 500 nm a délky v nm - μm. Na druhou stranu může být šablona potažena fyzikální depozicí z plynné fáze platinou, stříbrem nebo zlatem a TiO₂ může být elektrodeponován z prekurzoru. Tím se získají nanotrubičky stojící na kovovém substrátu. Přístupy bez šablon jsou založeny na (i) hydrotermálních metodách, kde se obvykle částice oxidu titaničitého autoklávají v hydroxidu sodném (NaOH) za vzniku nanoplátů, které se pak sestavují do tvaru nanotrubiček, netvořících však pole trubiček, ale zůstávají „volné“.^[19] Tímto způsobem jsou vytvářeny trubičky s průměrem 2 - 20 nm a délky do několika μm. (ii) Významněji, příprava pole samouspořádaných nanotrubiček, které vznikají elektrochemickou anodizací kovů jako je právě titan, probíhá obvykle ve vodných elektrolytech obsahující fluoridové ionty. Tímto lze vytvářet amorfní či krystalické formy nanotrubiček přímo z kovu o délce 100 nm - 100 μm a průměru 10 - 500 nm.^[20]



Obr. 1 Přehled různě připravovaných nanotrubiček z TiO_2 : Nanotrubičky TiO_2 připravené (A) hydrotermální metodou, (B) pomocí šablony, (C) anodickou oxidací a (D) elektrosponingem. Převzato a upraveno podle [21].

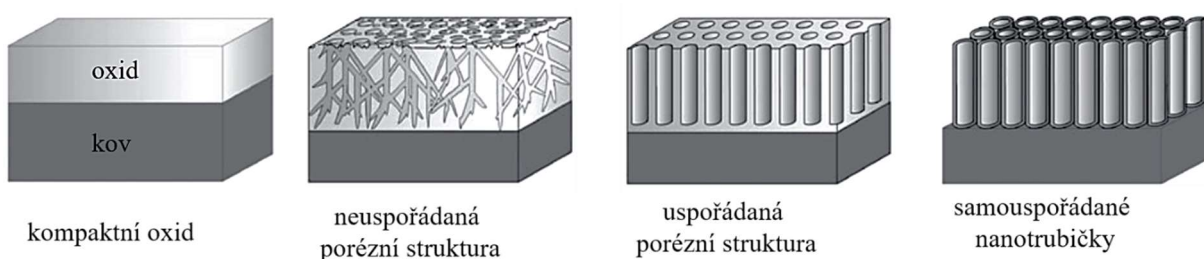
1.1.1 Elektrochemická anodizace TiO_2 nanotrubiček

Ve srovnání s jinými metodami přípravy TiO_2 nanotrubiček, se přímá anodická oxidace titanu ukazuje jako jednoduchá technika, při níž lze kontrolovatelně vytvářet požadované nanostruktury s určitou délkou, průměrem, tvarem a mírou uspořádání na základě optimalizace parametrů oxidace, jako je aplikovaný potenciál, čas, teplota, pH a složení elektrolytu.[22-24] Díky vysoce organizované struktuře trubiček a velkému poměru plochy povrchu vůči objemu, můžou získat samouspořádaná pole nanotrubiček z oxidů kovů jedinečné vlastnosti. Elektrochemická anodizace je navíc nízkonákladový proces, který se neomezuje pouze na titan, ale může být vhodný i pro jiné přechodné kovy včetně hafnia, zirkonu, niobu, tantalu, vanadu nebo jejich slitin.[25-28]

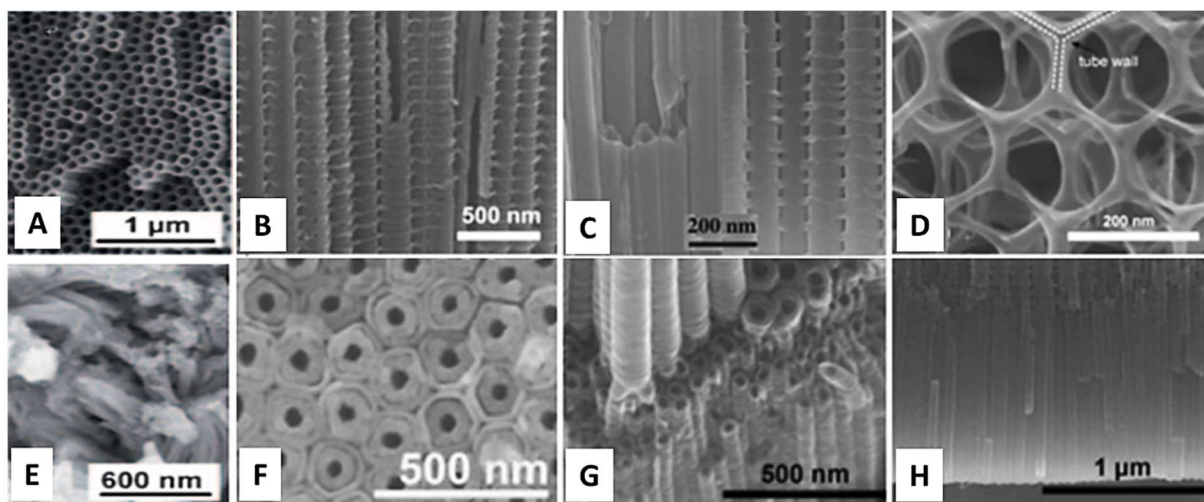
Samouspořádané TiO_2 nanotrubičky připravené elektrochemickou anodizací jsou nejčastěji vytvářeny přímo z titanové fólie jako základního substrátu. Nicméně je možné vytvářet TiO_2 nanotrubičky i z titanové vrstvy deponované na jiném, nejčastěji křemíkovém substrátu. Míru uspořádání TiO_2 nanotrubiček ovlivňují zhruba tyto důležité faktory, a tím je (i) vysoká čistota Ti substrátu nebo mechanické, chemické či elektroleštění Ti substrátu, (ii) aplikované napětí, (iii) opakovaná anodizace, která může být dvou- i tří-kroková a také (iv) před-texturování Ti substrátu před samotnou anodizací (např. nano-imprintingem nebo pomocí mikroobrábění).

Jak již bylo naznačeno, nanotrubičky z oxidu titanu lze vytvářet za specificky definovaných podmínek anodické oxidace. Samotný anodický proces může představovat jednoduchý systém (i) se dvěma elektrodami, a to titanové fólie jako anody a inertní kovové elektrody jako katody, (ii) elektrolytem obsahující fluoridové ionty, chloridové ionty, ionty chromu, bromidové ionty nebo perchlorát; a (iii) stejnosměrným napájecím zdrojem. Optimalizací podmínek anodizace a samotné formování TiO_2 nanotrubiček může tedy ovlivnit následné aplikace těchto nanotrubiček, tj. ve smyslu jejich geometrie (velikost, tvar, stupeň řádu, krystalickou fází atd.)

a jejich fyzikálně-chemické vlastnosti a použití v biomedicíně.^[29] Jinými slovy, kontrolou parametrů elektrochemické anodizace (aplikovaný potenciál, doba trvání anodizace, složení elektrolytu, teplota elektrolytu, pH elektrolytu), lze vyrobit různé nanostruktury z oxidu titanu, jako je rovnoměrná kompaktní vrstva oxidu (bez přítomnosti fluoridů)^[20], porézní vrstva^[29], neuspořádané vrstvy nanotrubiček TiO_2 rostoucích ve svazcích^[30], nebo vysoce organizované TiO_2 nanotrubičky^[31] či pokročilé nanotubulární vrstvy: rozvětvená trubice a bambusová struktura^[32], dvoustěnná^[33], nebo dvouvrstvá^[34] struktura (Obr. 2). Obr. 3 zobrazuje snímky z elektronové mikroskopie příkladů výše zmíněných morfologií nanotrubiček. V současné době lze získat pole nanotrubiček z TiO_2 s průměrem v rozmezí od 10 do 500 nm, tloušťkou vrstev v rozmezí od několika set nanometrů do 1000 μm a tloušťkou stěny v rozmezí od 2 do 80 nm.^[35]

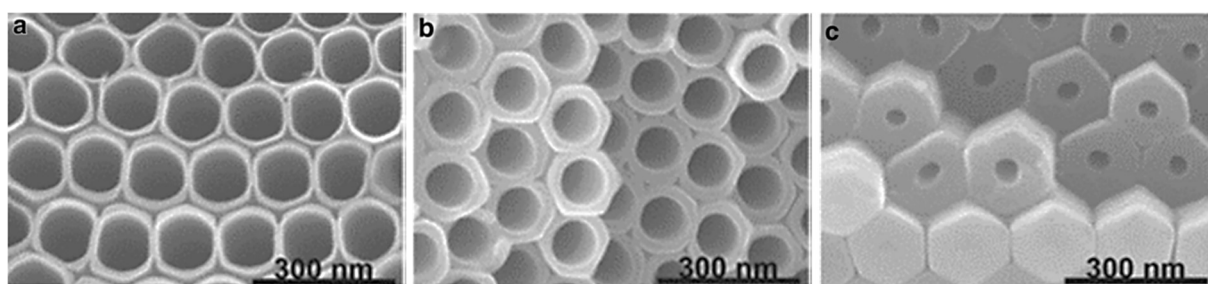


Obr. 2 Morfologie, které lze získat elektrochemickou anodizací kovů - kompaktní oxidový film, neuspořádaná nanoporézní vrstva, uspořádaná nanoporézní nebo samouspořádaná nanotrubičková vrstva. Převzato a upraveno podle [36].



Obr. 3 SEM snímky anodizovaných vrstev nanotrubiček z TiO_2 různými anodizačními procesy titanu. A) Vysoce uspořádané nanotrubičky TiO_2 . B) Bambusová struktura nanotrubiček. C) Přejít od hladkých k bambusovým nanotrubičkám. D) 2D nanokrajkové struktury. E) Neuspořádané nanotrubičky z TiO_2 . F) Dvoustěnné nanotrubičky. G) Rozvětvené nanotrubičky. H) Dvouvrstvé nanotrubičky se stejnými nebo dvěma různými průměry trubiček. Převzato z [37].

V procesu elektrochemické anodizace se pole nanotrubiček z TiO_2 tvoří samoorganizací oxidu titanu díky třem relativně nezávislým procesům: elektrochemická oxidace Ti na TiO_2 , elektrickým polem indukované rozpouštění TiO_2 a rozpouštění TiO_2 chemicky za přítomnosti nejčastěji fluoridových iontů. Vznik nanotrubiček lze pozorovat v čase, měřením proudové hustoty.^[38] V první části dochází k poklesu proudové hustoty způsobenému nově vytvořeným bariérovým oxidem. Ve druhé části začíná proud opět stoupat vlivem zvětšujícího se povrchu anody a vytvářejí se póry budoucích nanotrubiček. V poslední fázi proud dosáhne ustáleného stavu a vzniku samouspořádané vrstvy TiO_2 nanotrubiček. Výsledné nanotrubičky jsou ve tvaru písmene V, to znamená, že vrchní část stěn je podstatně tenčí než jejich spodní část (Obr. 4).^[37]



Obr. 4 SEM snímky TiO_2 nanotrubiček v polyetylenglykol elektrolytu s fluoridovými ionty vytvořené opakovanou anodizací titanu. a) Horní část nanotrubiček. b) Řez nanotrubiček uprostřed jejich délky. c) Spodní část nanotrubiček. Převzato z [37].

1.1.2 Vliv anodizačních podmínek na přípravu TiO_2 nanotrubiček

1. Typ elektrolytu

Složení, koncentrace a pH elektrolytu silně ovlivňuje délku a průměr výsledných nanotrubiček za určitých anodizačních podmínek. Na základě použitého elektrolytu může být vytváření polí nanotrubiček v zásadě rozdělen do tří skupin. První skupinou je použití vodných roztoků obsahující kyselinu fluorovodíkovou (HF). V HF vodném roztoku elektrolytů, kde je pH relativně nízké, což znamená vysokou koncentraci vodíkových iontů, hraje v anodizačním procesu dominantní postavení chemické rozpouštění TiO_2 indukované fluoridy iontů, čímž bylo dosaženo nízké uspořádanosti a maximální délky nanotrubiček okolo 500 nm.^[39] Druhou skupinou je použití pufrovaných elektrolytů, čímž se např. dosáhlo delších samouspořádaných nanotrubiček v řádu okolo 5 μm přidáním fluoridu sodného nebo draselného, a úpravou pH na slabě kyselé (pH $\sim 4,5$), popř. neutrální pH.^[40] Třetí skupinou jsou polární organické elektrolyty jako glycerol, dimethylsulfoxid, formamid nebo etylenglykol obsahující fluoridové sloučeniny (fluorid amonný NH_4F , fluorid sodný NaF či fluorid draselný KF) a malé množství vody. Při výrobě v těchto elektrolytech bylo dosaženo vysokého poměru délky vs. průměr (L/D) nanotrubiček, tj. byly syntetizovány samouspořádané trubičky v rozmezí délek 7 – 130 μm a

průměru od 40 – 160 nm, resp.^[41, 42] Bylo tedy prokázáno, že nanotrubičky TiO_2 s vyšším L/D mohou být připraveny v polárním organickém elektrolytu díky správné kontrole pH elektrolytu snižujícím chemické rozpouštění oxidu titaničitého. Kromě složení elektrolytu a pH hraje v procesu přípravy nanotrubiček obsah vody. Bylo zjištěno, že snížení množství vody na méně než 5% vede k tvorbě dlouhých nanotrubiček a snížení obsahu vody pod 2% je zárukou k vytvoření dobře organizovaných nanotrubiček z TiO_2 .^[43] Čtvrtou skupinou elektrolytů pak představují elektrolyty bez přítomnosti fluoridových iontů. Tyto vodné elektrolyty jsou tvořeny např. kyselinou chlorovodíkovou, peroxidem vodíku, perchlorovou kyselinou či jejich směsí.^[44, 45] Obecně tedy můžeme říci, že optimalizací složení elektrolytu, obsahu vody, a pH lze modulovat geometrii výsledných nanotrubiček, míru organizovanosti či tvorbu jednostěnných či dvoustěnných nanotrubiček.

2. Aplikované napětí

Anodizační napětí je kritickým faktorem, který má zásadní vliv na průměr trubiček.^[46] Rozměry nanotrubiček lze předpovědět jednoduše pouhým použitím vhodného rozsahu napětí zvaného napěťové okno.^[47] Při nízkém napětí dochází k tvorbě nanotrubiček s menšími průměry. Pokud je napětí ale příliš nízké, vrstva TiO_2 se stává kompaktní, a nelze pozorovat žádnou nanotubulární strukturu. Na druhou stranu, pokud je napětí příliš vysoké, lze získat houbovitou porézní strukturu. Obecně ale platí, že v určitém rozsahu aplikovaného napětí je průměr nanotrubiček úměrný napětí.^[46] Dále se ukázalo, že daný rozsah napětí souvisí také s použitým elektrolytem. Ve vodných elektrolytech by napěťové okno mělo být kontrolováno v rozsahu od 10 do 25 V, přičemž v organických elektrolytech je mnohem širšího rozsahu, mezi několika volty až stovkami voltů.^[48]

3. Doba anodizace

Doba anodizace ovlivňuje formaci nanotrubiček především ve dvou aspektech, a to zda vůbec dojde k tvorbě nanotrubiček, a pak v délce trubiček. To znamená, že v první fázi anodizace se vytvoří kompaktní film TiO_2 . Pokud je doba trvání příliš krátká lze místo nanotrubiček dosáhnout pouze neuspořádané porézní vrstvy.^[47] Se zvyšující se dobou anodizace porézní struktura postupně roste hlouběji a přechází na nanotubulární pole TiO_2 . Pokud jsou ostatní elektrochemické parametry ponechány konstantní, bylo pozorováno zvyšování délky nanotrubiček v průběhu času, aniž by to mělo významný vliv na průměr a tloušťku stěny nanotrubiček dokud nedošlo k ustálenému stavu.^[49]

4. Teplota elektrolytu

Teplota snižuje rychlost růstu a kvalitu polí nanotrubiček, jelikož má přímý vliv na rychlost růstu oxidu, délku a tloušťku stěny nanotrubiček.^[50] Například ve vodném elektrolytu bylo při zvyšování teploty pozorováno mírné zmenšení vnitřních průměrů, zatímco vnější průměry trubiček zůstaly stejné.^[51] V nevodném elektrolytu obsahujícím fluoridové ionty bylo např. zjištěno, že vnější průměr nanotrubiček je zvětšující se se zvyšující se teplotou elektrolytu.^[48] Nicméně lze říci, že pro stabilní pole nanotrubiček z TiO_2 je nejběžnější příprava při pokojové teplotě.

1.1.3 Modifikace vlastností TiO₂ nanotrubiček

Využití pole TiO₂ nanotrubiček je zejména studováno vzhledem k jejímu fotoelektrochemickému a biomedicínskému využití. V průběhu let došlo k modifikaci těchto polovodičových struktur za účelem např. zvýšení rychlosti přenosu elektronů a fotoelektrochemické aktivity nebo modifikace za účelem zvýšení biokompatibility nanotrubiček.

1. Tepelné žíhání

Krystalická struktura nanotrubiček a jejich vodivost, či optické vlastnosti závisí hlavně na teplotě žíhání a přítomné atmosféře.^[52] Běžně připravené nanotrubičky z TiO₂ jsou amorfni povahy, ale mohou být žíhány na anatasovou nebo rutilovou fázi nebo na směs obou fází při specifické teplotě. Bylo prokázáno, že amorfni fázi trubiček lze převést na anatazovou fázi za vyšší teploty (nad 300 °C) na vzduchu nebo na směs anatasu a rutilu při teplotách vyšších než 500 °C. Anatasová fáze TiO₂ se jeví jako nejvýhodnější krystalická struktura s nejlepšími fotoelektrochemickými vlastnostmi a nejnižším odporem při žíhání okolo 400 °C.^[53] Taktéž se jevila jako nejvíce biokompatibilní.

2. Dopování

Dopováním ionty nebo atomy do mřížky TiO₂ opět může přispět ke zlepšení fotoelektrochemických vlastností nanotrubiček či vlastností významných pro biomedicínské aplikace. Nanotrubičky z TiO₂ byly dopovány nejčastěji kovy jako je niob, železo, zinek, zirkonium a vanad^[54-57] nebo nekovovými materiály jako je dusík, fluor, bór, uhlík, síra či jód^[58-60].

3. Povrchové modifikace

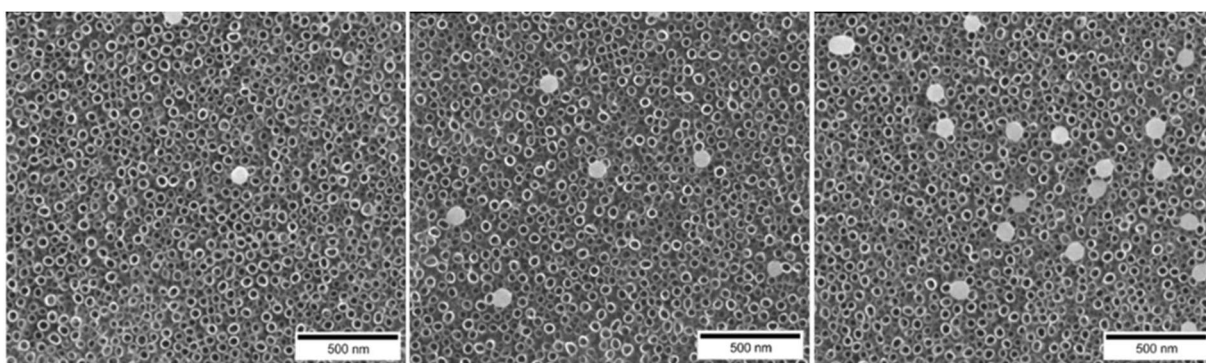
Povrchovou modifikací se rozumí dekorace povrchu nanotrubičkových polí z TiO₂ různými nanočásticemi nebo depozicí tenkých vrstev materiálu (kovy, polovodiče a organická barviva) za účelem vylepšení jejich vlastností. Nanotrubičky lze také modifikovat např. elektrodepozicí nanodrátků.^[61] Těmito modifikacemi se dosahuje např. zlepšení elektrokatalytických vlastností TiO₂ nanotrubiček a zlepšení vlastností pro biomedicínské aplikace. Příkladem lze uvést dekoraci nanotrubiček nanočásticemi stříbra^[62], kvantovými nanočásticemi^[63], nanočásticemi z TiO₂ a oxidu wolframového^[64, 65] nebo depozice paladia, oxidu zinečnatého, oxidu hlinitého (Al₂O₃) pomocí ALD techniky^[66-68].

1.1.4 Vědecké práce v oblasti TiO₂ nanotrubiček

V rámci vědecké práce jsem se se svými studenty zaměřila na přípravu a především modifikaci TiO₂ nanotrubiček vzhledem k vylepšení antibakteriálních vlastností a interakce s tkáňovými buňkami. V bakalářské práci Kateřiny Polákové byly optimalizovány podmínky anodické oxidace přípravy nanotrubiček (BP 2016; *Studium chování buněk na nanostrukturovaných TiO₂ površích*) a se studentem Ing. Ondřejem Bílkem jsem se zaměřila především na modifikace

TiO₂ nanotrubiček. Jeho diplomová práce (DP 2017: *Příprava a charakterizace TiO₂ nanotrubiček dekorovaných stříbrem pro biomedicínské účely*) navazovala na poznatky Kateřiny Polákové, nicméně byla nadstavena elektrodepozicí stříbrných nanočástic na TiO₂ nanotrubičky a studiem antibakteriálních vlastností a kompatibilitou těchto povrchů s tkáňovými buňkami. TiO₂ nanotrubičky byly připraveny pomocí anodické oxidace v dvouelektrodevém zapojení a v elektrolytu na organické bázi. V rámci optimalizace podmínek anodizace jsme získali nanotrubičky o průměru okolo 60 nm. Nanotrubičky byly poté žíhány při 450 °C. Dále byly optimalizovány podmínky elektrodepozice stříbra na TiO₂ povrchy, s cílem získat uniformní nanočástice a pokrytí povrchů různým počtem nanočástic na plochu.

Poznatky z této diplomové práce student dále využíval v rámci svého doktorského studia. Zde jsme se jako první zaměřili na optimalizaci dekorování TiO₂ nanotrubiček, připravených anodizací, chemicky syntetizovanými nanočásticemi selenu. Optimalizace dekorování povrchů na 50 nm TiO₂ nanotrubičky byla zaměřena na získání povrchů s různým počtem selenových nanočástic na plochu povrchu (Obr. 5). Nanočástice byly o velikosti kolem 80 nm. Povrchy byly dále studovány z hlediska kompatibility s nádorovými, nenádorovými a bakteriálními buňkami. Výsledek této studie naznačuje, že nanočástice selenu zlepšují antibakteriální vlastnosti nanotrubiček z oxidu titaničitého a potvrzují protinádorovou aktivitu. Antibakteriální i protinádorová aktivita se zvyšovala se zvyšujícím se počtem nanočástic na plochu. Vedle toho bylo zjištěno, že vysoký počet nanočástic na plochu měl zhoršující se vliv na buněčnou adhezi a životaschopnost nenádorových buněk, což může komplikovat integraci těchto potenciálních biomateriálů do hostitelské tkáně. Optimalizace povrchových vlastností biopovrchů by měla být tedy nezbytnou součástí výzkumu, aby byla zajištěna určitá rovnováha mezi kompatibilitou vůči tkáňovým buňkám a antibakteriální aktivitou. Tato práce byla publikována mým studentem v impaktovaném časopise a je uvedena jako součást této habilitační práce v kapitole 4 (Článek 1; *Enhanced antibacterial and anticancer properties of Se-NPs decorated TiO₂ nanotube film*. *PLoS ONE*, 2019).



Obr. 5 TiO₂ nanotrubičky dekorované selenovými nanočásticemi v různém počtu nanočástic na plochu. Převzato z (Článek 1: *Enhanced antibacterial and anticancer properties of Se-NPs decorated TiO₂ nanotube film*. *PLoS ONE*, 2019).

Druhá práce studenta Ing. Bílka v této oblasti studia využití TiO₂ nanotrubiček se zaměřila opět na dekorování nanotrubiček, ale komerčními nanočásticemi stříbra a studia antibakteriálních vlastností takto připravených povrchů. Zde jsme vzali v potaz především vliv různých stabilizačních činidel stříbrných nanočástic (polyvinylpyrolidon, rozvětvený polyetylenimin, citrát, lipoová kyselina a polyetylen glykol) při zachování parametrů geometrie nanotrubiček a velikosti nanočástic. Naše výsledky ukázaly, že dekorace nanočásticemi s různým stabilizačním činidlem hraje důležitou roli v antibakteriálních vlastnostech TiO₂ nanotrubiček, jelikož tento synergický efekt prokázal různý vliv na adhezi a životaschopnost selektovaných G- a G+ bakterií. Tato zjištění by mohla vědcům pomoci optimálně navrhnout jakékoli povrchy, které mají být použity jako antibakteriální, včetně implantovatelných titanových biomateriálů. Práce byla opět publikována v impaktovaném časopise a je součástí této práce v kapitole 4 (Článek 2; *Antibacterial activity of AgNPs-TiO₂nanotubes: influence of different nanoparticle stabilizers. RSC Advances, 2020*).

1.2 Templátová metoda přípravy „nanotyčinek“ z oxidů kovů

Jak již bylo zmíněno, elektrochemická anodizace se neomezuje pouze na titan, ale může být vhodná i pro přechodné kovy jako jsou hafnium, zirkonium, niobium, tantal, vanad či jejich slitiny. Kromě nanotrubiček z TiO₂ byly z pohledu studia biorozhraní dále připraveny nanotyčinky z oxidu tantalu, hafnia a zirkonia. Především nanotyčinky z oxidu hafnia a zirkonia byly jako první vyrobené a charakterizované v rámci naší skupiny, tak jako vliv těchto nanostruktur na buněčné systémy. Níže bude tedy popsána technologie výroby těchto struktur. Z důvodů podobnosti a optimalizace specifických podmínek jak bylo popsáno u TiO₂ nanotrubiček, nebudou již tyto kapitoly popsány více dopodrobna.

Templátové metody nesouvisí pouze s přípravou nanotrubiček, ale hrají významnou roli ve výrobě dalších nanostruktur, jako jsou nanotečky, nanotyčinky, nanodráty, membrány apod. Jako šablona se nejvíce používá porézní anodická alumina (PAA nebo také v literatuře označovaná jako anodický oxid hlinitý AAO), která tvoří v podstatě jednoduchou, dobře kontrolovanou a tedy i reprodukovatelnou metodu pro vytváření nanostruktur.^[69] Tento nanoporézní templát lze snadno připravit dvoukrokovou anodizací hliníku za stejných a definovaných podmínek anodizace. Kromě toho, při anodické oxidaci je možné vytvořit v jednom procesu jak aluminovou šablonu, tak zoxidovanou nanostrukturu z jiného kovu ve stejném elektrolytu (tzv. PAA asistovaná anodizace na substrátu).^[70] PAA se v podstatě vytváří obdobně jako porézní nebo tubulární struktury např. z TiO₂, avšak je méně citlivá na parametry elektrolytu. Napětí a elektrolyt, které jsou použity při vytváření aluminové šablony ovlivňuje velikost pórů. Odstranění PAA po výrobě nanostruktur lze dosáhnout chemickým leptáním pomocí kyselých nebo alkalických roztoků. Definované, periodicky uspořádané nanopóry aluminy tedy poskytují šablony pro růst nanostruktur, jejichž průměr a délku, stejně jako vzdálenost mezi dvěma sousedními strukturami, lze řídit změnou odpovídajících rozměrů

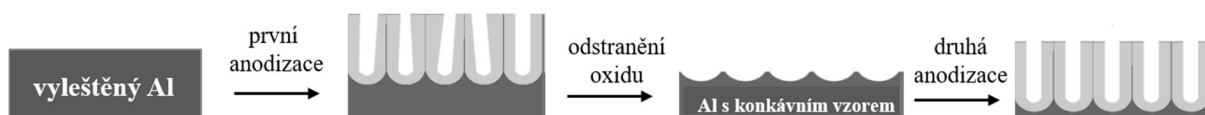
šablony, což je realizováno změnou podmínek anodizace.^[71] Vedle toho může být i samotná PAA použita jako porézní filtrační membrána.

1.2.1 Elektrochemická výroba PAA šablony

Obecně existují dvě rozšířené metody tvorby vysoce uspořádané šablony PAA: (i) dvoukroková anodizace a (ii) před-texturování povrchu s následnou anodizací hliníku vedoucímu k vysoce uspořádanému uskupení nanopórů.^[72] Před-texturování povrchu hliníku lze provést přímo pomocí hrotu mikroskopu se skenovací sondou či mikroskopu atomárních sil nebo speciálními litografickými technikami, nicméně se jedná o časově náročné techniky přípravy PAA. Proto se pro před-texturování hliníku častěji používá litografické techniky pro výrobu „razítka“ s definovanou topografií a ta se otiskne do hliníkového substrátu (Obr. 6). Razítka jsou obvykle vyrobena z karbidu křemíku, nitridu křemíku nebo niklu.



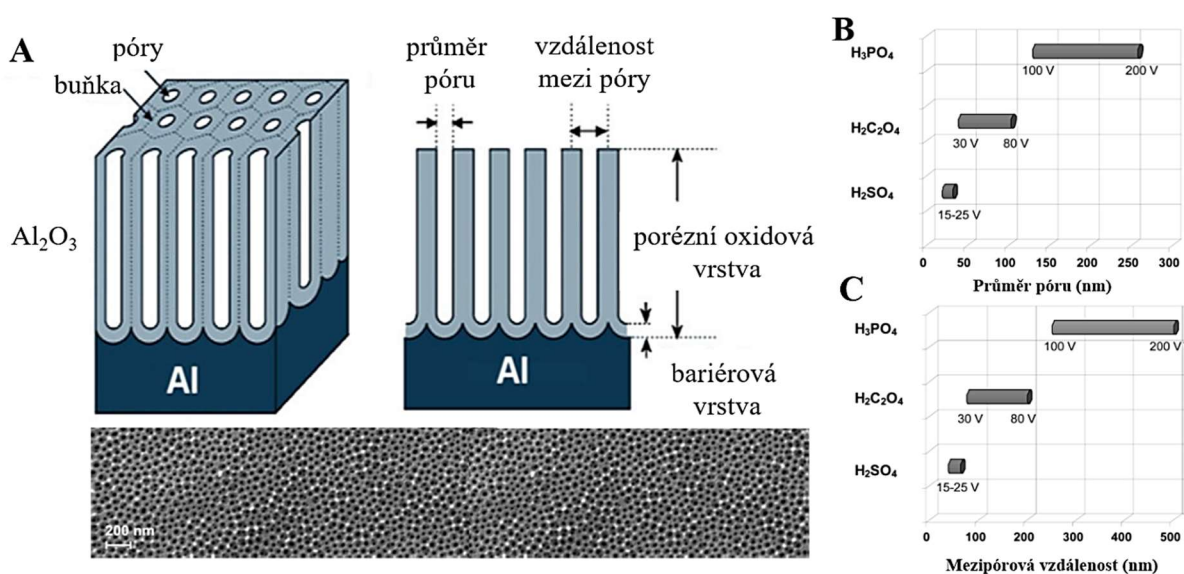
Obr. 6 Výroba ideálně uspořádaného anodického porézního oxidu hlinitého pomocí razítka. Převzato a upraveno podle [72].



Obr. 7 Dvoukroková anodizace hliníku za vzniku porézní aluminu. Převzato a upraveno podle [72].

Při procesu výroby samoorganizované PAA šablony dvoukrokovou anodizací hliníku v elektrolytu, který rozpouští oxid hlinitý, se vytváří vrstva oxidu s jedinečnou porézní strukturou na kovovém povrchu (Obr. 7). Vysoce uspořádané póry jsou kolmé k základně a procházejí téměř celou tloušťkou vrstvy oxidu. Na rozhraní s kovem nicméně roste neporézní bariérová vrstva, která má obvykle tloušťku několik desítek nanometrů. Při použití hliníkového substrátu s vysokou čistotou a uniformní strukturou, lze kontrolou parametrů elektrochemické oxidace dosáhnout homogenní distribuce pórů v hexagonálním uspořádání. Průměry pórů jsou uniformní; záleží na oxidačních podmínkách a lze je regulovat v rozmezí od 10 do několika set nanometrů. Celková tloušťka vrstvy oxidu je určena dobou oxidace. Obvykle se pohybuje v

rozmezí desetin po desítky mikrometrů.^[73] Schematický nákras struktury PAA je uveden na Obr. 8. Mechanismus procesu anodické oxidace hliníku a vytváření porézní oxidové vrstvy je stále předmětem výzkumu. Předpokládá se, že porézní struktura je výsledkem dvou konkurenčních reakcí: tvorby Al_2O_3 a rozpuštění tohoto oxidu. Oxidová vrstva s porézní strukturou se získá za použití roztoků dvojsytných a trojsytných kyselin, ve kterých je oxid snadno rozpouštěn (např. kyselina fosforečná, šťavelová, oxalocetová, sírová, chromová). Porézní anodickou vrstvu lze také získat z roztoků mnoha organických kyselin, zejména vícesytných kyselin, jako je kyselina vinná, citronová, sulfosalicylová, maleinová a jantarová. Tloušťka bariérové vrstvy, průměr pórů, vzdálenost mezi póry a jejich povrchová hustota, se značně liší v závislosti na typu elektrolytů, napětí a teplotě. Pro daný elektrolyt jsou geometrické parametry pórů řízeny změnou napětí během anodické oxidace. Tloušťka bariérové vrstvy a průměr pórů jsou víceméně úměrné použitému napětí. Póry mající větší průměr lze získat z roztoků kyseliny fosforečné nebo organických kyselin při vysokém napětí.^[74]



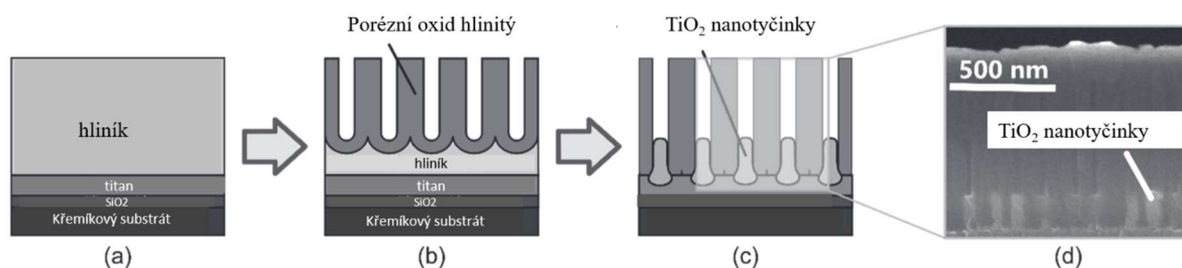
Obr. 8 (A) Schematické znázornění struktury PAA připravené elektrochemickou oxidací Al. (B, C) Vliv elektrolytu (kyselina sírová H_2SO_4 , šťavelová $\text{H}_2\text{C}_2\text{O}_4$ a fosforečná H_3PO_4) na průměr pórů a mezipórovou vzdálenost při určitém napětí. Převzato a upraveno podle [71, 72, 74].

1.2.2 Příprava „nanotyčinek“ PAA asistovanou anodizací

Jak již bylo zmíněno, šablonu z PAA a vytváření nanoteček až po různě veliké nanotyčinky z oxidů kovů lze realizovat současně více-krokovou anodizací na substrátu. Klíčovým parametrem pro dosažení „nanotyčinek“ je použité napětí a také čas potřebný k průrazu spodní bariérové vrstvy aluminové šablony. Obecně lze říci, že se zvyšujícím se napětím roste průměr pórů šablony a následně dalším zvýšením napětí či regulací času anodizace lze ovlivňovat

výslednou velikost „teček či tyčinek“. Teplota při procesu by se měla pohybovat pod 25 °C. Nižší teplota totiž zajišťuje větší stabilitu výsledné struktury. Závěrem můžeme konstatovat, že vytváření nanostruktur pomocí PAA šablony, tzv. bottom-up technikou, je ovlivněno použitým elektrolytem, teplotou, napětím a časem anodické oxidace. Jde o jednodušší přístup výroby nanostruktur, nevyžadující žádné nákladné procesy a techniky, jako v případě top-down technik s použitím různých litografických metod (elektronová, iontová atd.).

Anodickou oxidací přípravy vysoce uspořádané struktury „nanotyčinek“ na substrátu pomocí PAA šablony lze obecně znázornit na příkladu TiO₂ nanotyčinek (Obr. 9).^[75] Oxidace probíhala v elektrolytu tvořeném kyselinou šťavelovou při chlazení na 10 °C. Aluminová pórovitá šablona byla vytvářena při napětí 40 V. Poté bylo napětí zvýšeno na 80 V, aby došlo k průrazu bariérové vrstvy na dně aluminy. Po nárůstu nanotyčinek byla aluminová šablona odleptána ve směsi oxidu chromového, kyseliny fosforečné a vody. Přípravou TiO₂ nanotyčinek se ve své diplomové práci také zabývala studentka Kateřina Poláková (DP 2016: *Studium chování buněk na nanostrukturovaných TiO₂ površích*).



Obr. 9. Příprava nanotyčinek z TiO₂ anodickou oxidací za pomoci PAA šablony na křemíkovém substrátu. Převzato a upraveno z [75].

1.2.3 Vědecká činnost v PAA asistované anodizaci

Elektrochemická anodizace procesu tvorby „nanotyčinek“ z oxidů kovů pomocí PAA šablony se neomezuje pouze na titan, ale může být vhodný i pro jiné přechodné kovy jako je hafnium^[25], zirkonium^[76], niobium^[26], tantal^[27], vanad^[77] nebo jejich slitiny^[78]. Nejenomže řada těchto kovů je biokompatibilním materiálem využívaným v biomedicíně, jejich strukturováním a vytvářením jejich oxidů lze mimikovat komplexní bionanostruktury a vylepšovat jejich vlastnosti pro specifické aplikace vzhledem k neoxidovaným a nestrukturovaným kovovým materiálům. V poslední době se biologicky související aspekty nanomateriálových aplikací zaměřily na bioseparaci, pro doručování léčiv a vývoj nových pokročilých bioimplantátových materiálů. Z posledně zmíněného vycházely další vědecké práce, které byly zaměřeny na PAA asistovanou anodickou oxidaci organizovaného pole „nanotyčinek“ z oxidu tantalu, hafnia a zirkonia, jež byly následně otestované z hlediska jejich biokompatibility a antibakteriálním vlastnostem. Náš zájem především vycházel z faktu vlivu topografie nanostrukturovaného povrchu na buněčné systémy ve srovnání s „nestrukturovaným“ povrchem.

Výroba a biorozhraní nanotyčinek z oxidu tantalu

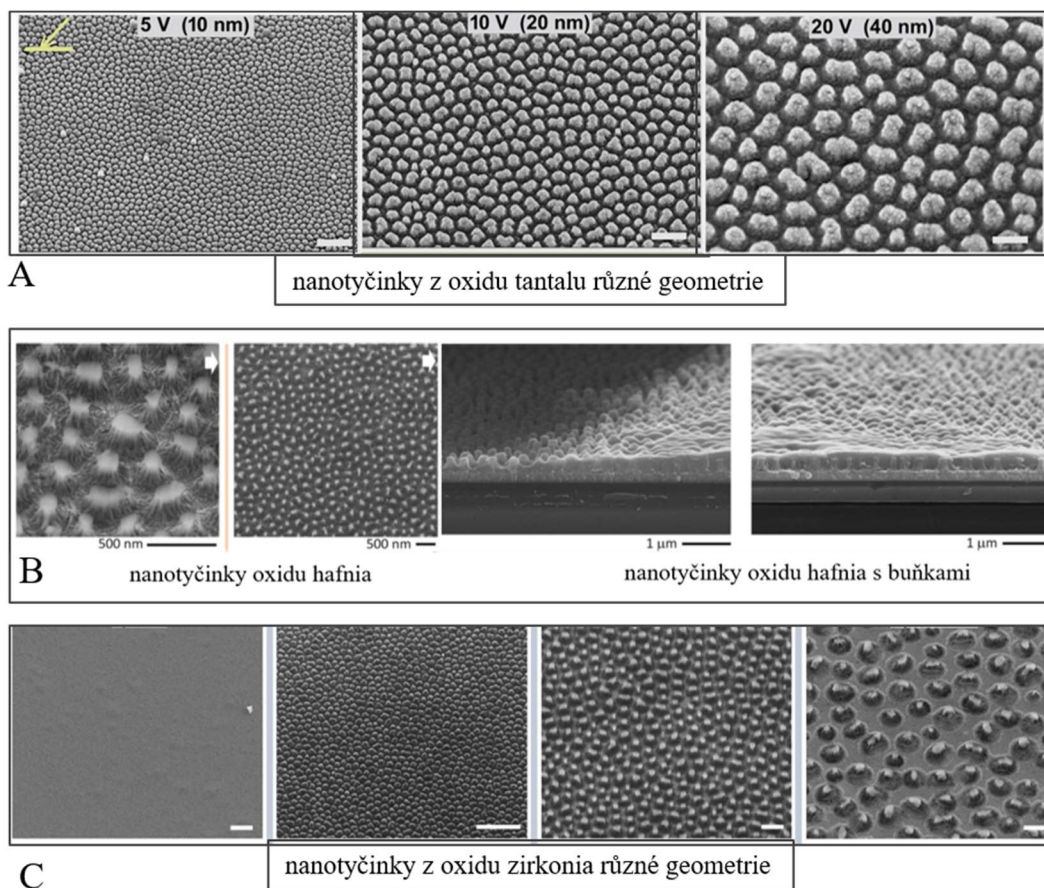
Ačkoliv je titan a TiO_2 v posledních letech nejvíce prostudovaným materiálem, v poslední době se do popředí dostávají i vzácnější kovy včetně tantalu a jeho oxidu, který může sloužit jako alternativní materiál pro implantáty nebo jako povlak, vzhledem k jeho vynikajícím antikorozním vlastnostem a dobré biokompatibilitě. My jsme se zaměřili na výrobu samoorganizovaného filmu „nanotyčinek“ z oxidu tantalu (Ta_2O_5) pomocí elektrochemické anodizace Al/Ta vrstvy na křemíkovém substrátu (Obr. 10A). Nejsvrchnější vrstva hliníku byla prvně anodizována při pokojové teplotě v kyselině sírové za vzniku porézní aluminy, obsahující samoorganizovanou porézní strukturu dosahující k vrstvě tantalu. Při stejném potenciálu následně docházelo i k oxidaci tantalové vrstvy. Poté byla vrstva re-oxidována, přičemž vznikající oxid tantalu překonal bariéru porézní aluminy a prostoupil do jejích pórů. V závislosti na složení elektrolytu a hodnotě anodizačního a re-anodizačního napětí byla regulována velikost nanotyčinek. Porézní alumina byla odstraněna v horkém roztoku kyseliny chromové a kyseliny fosforečné. Tímto způsobem byly vytvořeny „nanotyčinky“ z oxidu tantalu o průměru 10, 20 a 40 nm. Cílem bylo následně studovat, zda tyto rozdíly v geometrii tyčinek má vliv na chování buněk. Naše výsledky mohou přispívat k lepšímu porozumění biorozhraní mezi živočišnými buňkami a nanostrukturovanými povrchy z oxidů kovů, a jejich uplatnění v tkáňovém inženýrství. Tato práce byla publikována v impaktované časopise a je součástí této habilitační práce v kapitole 4 (Článek 3: *Tuning the response of osteoblast-like cells to the porous-alumina-assisted mixed-oxide nano-mound arrays*, *Journal of Biomedical Materials Research - Part B Applied Biomaterials*, 2018).

Výroba a biorozhraní nanotyčinek z oxidu hafnia

Další ze zajímavých materiálů, který byl studován, byl oxid hafnia (HfO_2). Hafnium (Hf) je přechodný kov, podobně jako titan nebo zirkon. Hafnium má výbornou mechanickou odolnost, je termostabilní, tvrdý a vysoce biokompatibilní kov. Dosavadní výzkumy, které byly publikovány, pracují pouze s čistým hafniem, a to in vivo (tj. jeho implantací do živých zvířat) nebo se studují jeho antikorozní vlastnosti v biotekutinách. Více často se můžeme setkat se studiem hafnia jako součástí slitin titanu, tantalu nebo niobu. Doposud byl oxid hafnia syntetizován různými metodami ve formě nanoporézních filmů či nanotrubiček. V této práci jako první pracujeme s nanotyčinkami z oxidu hafnia, o výšce ~250 nm a průměru mezi 200 - 350 nm (Obr. 10B). Nanotyčinky byly připraveny metodou elektrochemické anodizace pomocí porézní aluminy obdobně jako v případě nanostruktur z oxidu tantalu. In vitro interakce strukturovaného a nestrukturovaného povrchu oxidu hafnia s buňkami MG-63 (osteoblastová linie) a Gram-negativními bakteriemi *E. coli* byla studována poprvé. Současné poznatky prohlubují znalosti biologických procesů na biorozhraní živých buněk/oxidu kovů, vycházejících z role povrchové chemie a morfologie povrchů. Práce opět byla publikována v impaktovaném časopise a je uvedena v kapitole 4 (Článek 4: *Anodic formation and biomedical properties of hafnium-oxide nanofilms*, *Journal of Materials Chemistry B*, 2019).

Výroba a biorozhraní nanotyčinek z oxidu zirkonia

Biokeramika na bázi ZrO_2 se dnes aktivně zavádí do komerčního využití díky své vynikající stabilitě, antikorozním vlastnostem a biokompatibilitě. Strukturování keramiky z oxidu zirkonia v nanoměřítku může dále vylepšit jejich užitečné vlastnosti. Příprava vysoce organizovaných nanostruktur ZrO_2 prostřednictvím anodizace vrstvy zirkonu pomocí porézní anodické aluminy vedla k výrobě tří typů nanostruktur vyčnívajících nad tenkou vrstvou oxidu, a lišících se tvarem, velikostí, rozestupy a hustotou (struktury byly označeny jako nanotečky (~ 70 nm), nanosloupky (~ 150 nm) a nanopářezy (~ 250 nm)). Tyto nanostrukturované povrchy byly srovnávány k „nestrukturovanému“ anodickému filmu ZrO_2 ve smyslu interakce s tkáňovými buňkami a tedy jako potenciální biomateriál (Obr. 10C). *Práce je momentálně v procesu zaslání do časopisu k jeho posouzení, a je součástí jako manuskript v kapitole 4 (Článek 5: Nanostructured ZrO_2 bioceramic coatings derived from the anodically oxidized Al/Zr metal layers).*



Obr. 10 SEM mikroskopie nanostruktur z oxidu tantalumu (A), hafnia (B) a zirkonia (C). Převzato viz kapitola 4 (Článek 3,4,5).

2 Mikrostrukturované povrchy z polymerů

Polymerní mikro- a nanosloupky, a to především s vysokým „aspect ratio“ (AR; poměr výšky k průměru sloupku), s definovanou geometrií nabyly významu v řadě aplikací, včetně modulace smáčivosti povrchů, doručování léčiv, vytváření biomimetických povrchů (gekon, lotosové listy aj.), jako substráty pro měření buněčné síly, či jako MEMS aktuátory.^[79-83] Nabízejí výhody, jako je velká povrchová plocha, dobrá linearita odezvy v mechanické transdukcii a efekt povrchové topografie. Řada polymerů je také transparentních, poddajných a biokompatibilních a/nebo biologicky odbouratelných, což opět nese výhody pro specifické aplikace. Navíc, polymery jsou levné, což je velmi žádoucí pro nízkonákladové aplikace.

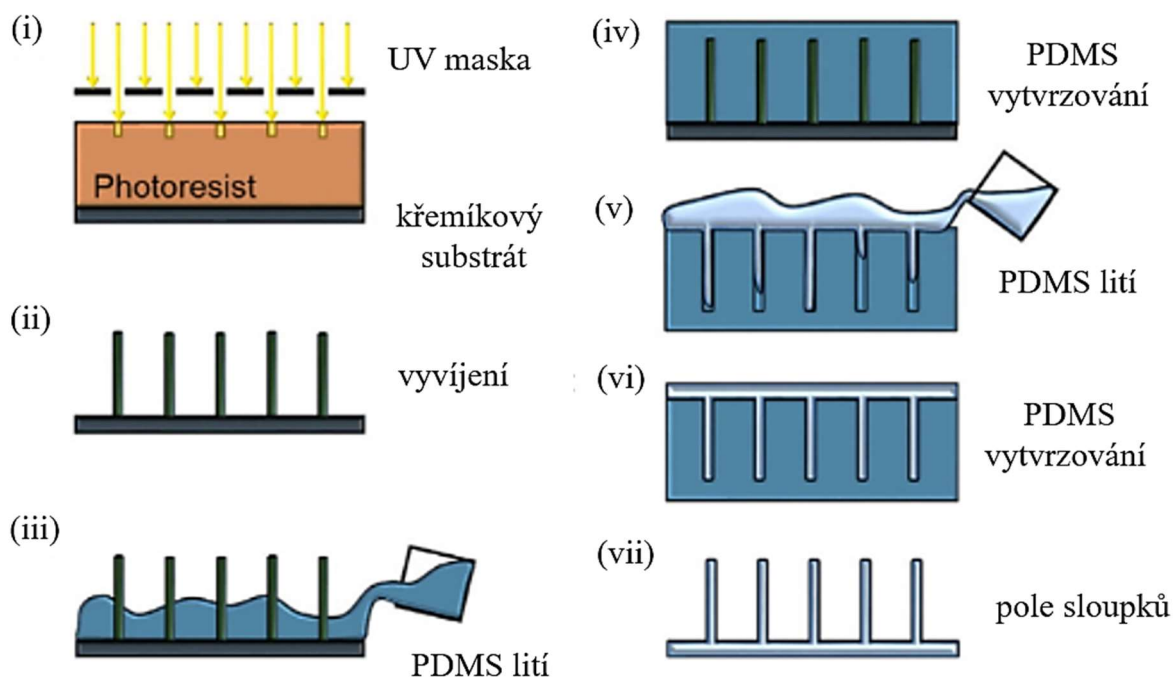
Sloupky s AR hodnotou vyšší než 10 byly vyrobeny pro tvrdší materiály, včetně kovových a uhlíkových.^[84-86] Výzvou však zůstává výroba polymerních sloupků s vysokou AR hodnotou a vysokou hustotou jejich distribuce na povrchu substrátu. Polymerní sloupky s vysokým AR (až 15) byly vyrobeny pomocí litografických technik s rozměry struktur v rozmezí desítek až stovek mikronů.^[87, 88] Pokud se rozměry struktur sníží na stovky nanometrů a zvýší se hustota uspořádání, vysoké a hustě uspořádané polymerní nanosloupky mohou mít tendenci ke kolapsu, především u „měkkých“ polymerů jako je polydimetylsiloxan (PDMS). A právě PDMS je nejčastěji používaným materiálem ve výrobě pole sloupků pro měření buněčné síly, o které budeme níže dále mluvit. PDMS polymerní sloupky s vysokým AR mají tendenci kolabovat z důvodu poměrně nízkého Youngova modulu pružnosti, velké povrchové adhezni síle mezi sousedními sloupky a vznikají problémy při soft litografii v rámci de-moldingu, tj. odlupování polymerních struktur od šablony.^[89, 90]

I když existují relativně jednoduché způsoby výroby sloupků v mikroskopickém měřítku, k výrobě sloupkových polí s vysokou hodnotou AR a prostorovou hustotou s rozměry v nanoměřítku se používají pokročilé výrobní techniky. Obecně lze ale říci, že výroba je vždy spojena s použitím litografických technik. V následující části si uvedeme několik nejběžnějších příkladů výroby ohebných sloupkových polí z PDMS polymeru pro aplikace v mechanotransdukcii, tj. jako flexibilní substrát pro měření síly generované živými buňkami, kde vertikální sloupky fungují podobně jako horizontální kantilevery („jazýčky“). PDMS je poměrně dost „měkkým“ polymerem (např. poměr síťovadla a monomeru 1:10 vytvrzeného při 65 °C po dobu cca 12 hodin dává Youngův modul kolem 2 MPa), a výroba sloupků s vysokým AR a hustotou je poměrně komplikovaná v rámci často používaných tzv. „replica molding technik“, jelikož je obtížné ho odloupnout od šablony.^[91] Nicméně tyto techniky i přesto umožňují výrobu PDMS mikrosoupků různé tuhosti, a to modulací AR hodnoty, geometrie, UV světlem či stupněm polymerace.

2.1 Výroba PDMS sloupků

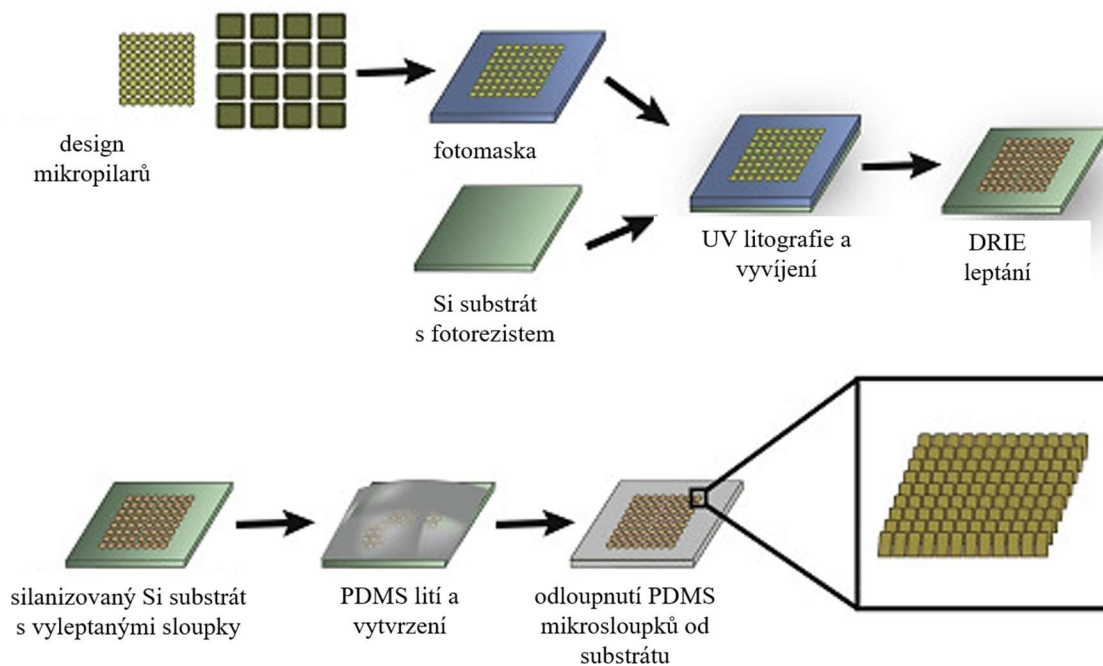
„Replica molding“ je často brána jako zlatý standard pro výrobu polí mikrosloupků. Při této technice se do šablony s požadovanou geometrií a rozměry struktur odlije polymer a po vytvrzení polymeru se výsledné pole sloupků odloupe od šablony. I když jsou základní principy protokolů pro „replica molding“ v publikované literatuře podobné, existují různé techniky pro výrobu šablon sloupků.^[92]

a) Standardní postup vytváření šablony byl použit v literatuře pro výrobu mikrosloupků s rozměry v rozmezí od 2 do 10 μm v průměru a 3 μm až 50 μm na výšku a vzdáleností mezi sloupky až 9 μm ; tj. s nízkou hodnotou AR a prostorovou hustotou sloupků.^[93-95] Příkladem může být výroba šablony z negativního SU-8 fotorezistu deponovaném na křemíkové destičce, do něhož se pomocí fotolitografie vytvoří díry dle příslušného motivu masky s následným procesem vyvíjení. Hloubka litografického procesu je v podstatě limitována vlnovou délkou ozáření a tloušťkou fotorezistu. Následně je PDMS nalit na sloupy z SU-8, vytvrzen a odloupen za vzniku šablony. Tato šablona je ošetřena povrchovou oxidací v plazmě a silanizována ve vakuu, aby se usnadnila snadná separace PDMS sloupků od šablony. Poté je opět PDMS nalit na šablonu, odplyněn ve vakuu, vytvrzen a odloupen. Obr. 11 znázorňuje schéma typického „replica molding“ procesu.



Obr. 11 Výroba mikrosloupků pomocí „replica molding“ techniky. (i) Vytváření obrazců pomocí fotomasky na fotorezistním materiálu (např. SU-8) prostřednictvím fotolitografie; (ii) vyvíjení fotorezistu; (iii) odlévání PDMS; (iv) vytvrzování PDMS; (v) druhý odlitek PDMS; (vi) vytvrzení PDMS a (vii) finální sloupkové pole. Převzato a upraveno podle [92].

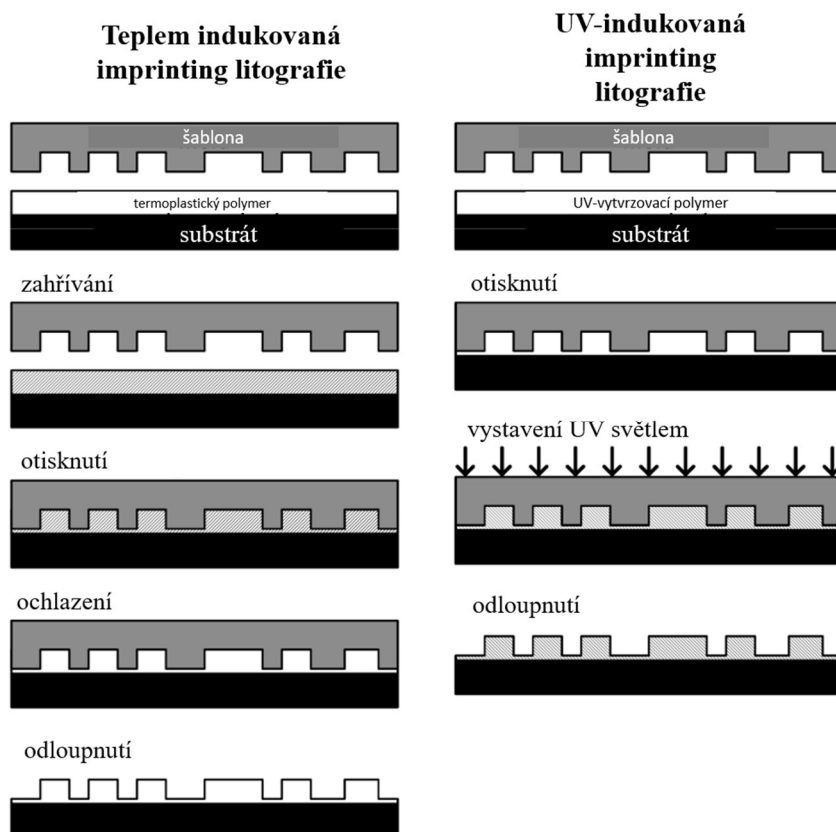
b) „Replica molding“ proces byl také použit k získání mikrosloupeků o vyšší AR a prostorové hustotě (např. o rozměrech od 1 μm do 2 μm v průměru, 3 μm až 8 μm na výšku a vzdáleností sloupeků od 2 μm do 4 μm).^[96, 97] V těchto studiích byla vytvořena negativní šablona, pomocí kontaktní fotolitografie dle designu fotomasky, s požadovaným vzorem a hloubkou na křemíkových destičkách procesem hlubokého iontového leptání (DRIE, Bosch proces). Po silanizaci šablony byl PDMS vylit, vytvrzen a odloupen od této šablony (Obr. 12).



Obr. 12 Výroba PDMS sloupeků pomocí „replica molding“ metody a DRIE leptání. Převzato a upraveno podle [98].

c) Dalším příkladem výroby sloupeků, a to i v nanoměřítku je imprinting nanolitografie.^[99] Tato technika využívá řadu přístupů výroby sloupeků. Na Obr. 13 je znázorněna imprinting litografie indukovaná teplem a UV zářením, přičemž je nutno brát v potaz vlastnosti polymeru, jako termoplastické či UV vytvrzovací polymery, resp. Jako příklad zde uvedu výrobu nanosloupeků z polykarbonátu.^[100] Požadovaná silikonová šablona byla vyrobena standardním fotolitografickým procesem a DRIE leptáním, jak již bylo zmíněno výše v bodě b). Tato šablona byla chemicky ošetřena silanem pro finální odlepení polymeru. Otisk šablony byl proveden pomocí nanoimprinteru po nanesení substrátu na šablonu, v tomto případě polykarbonátu o určité tloušťce v řádech stovek mikrometrů. K otisku došlo při 180 °C a tlaku 6 barů po dobu 20 minut. Poté došlo k vychladnutí vrstev na 80 °C a bylo provedeno odloupení polymeru od šablony.

Na závěr je také nutné zmínit, že ačkoliv s rozvojem technologií existuje celá řada výroby mikro- a nanosloupků z polymerních materiálů, tyto sloupky lze dále modifikovat pro specifické aplikace. Například je lze modifikovat přidáním magnetických nanočástic^[101] nebo nanodrátků z kobaltu^[95], povrch těchto sloupků lze dekorovat pomocí proteinů či zlatem^[102].



Obr. 13 Výroba polymerních mikro- a nanosloupků metodou UV- a teplem indukovaného imprintingu. Převzato a upraveno z [99].

2.2 Vědecká činnost v oblasti výroby polymerních mikrosloupků

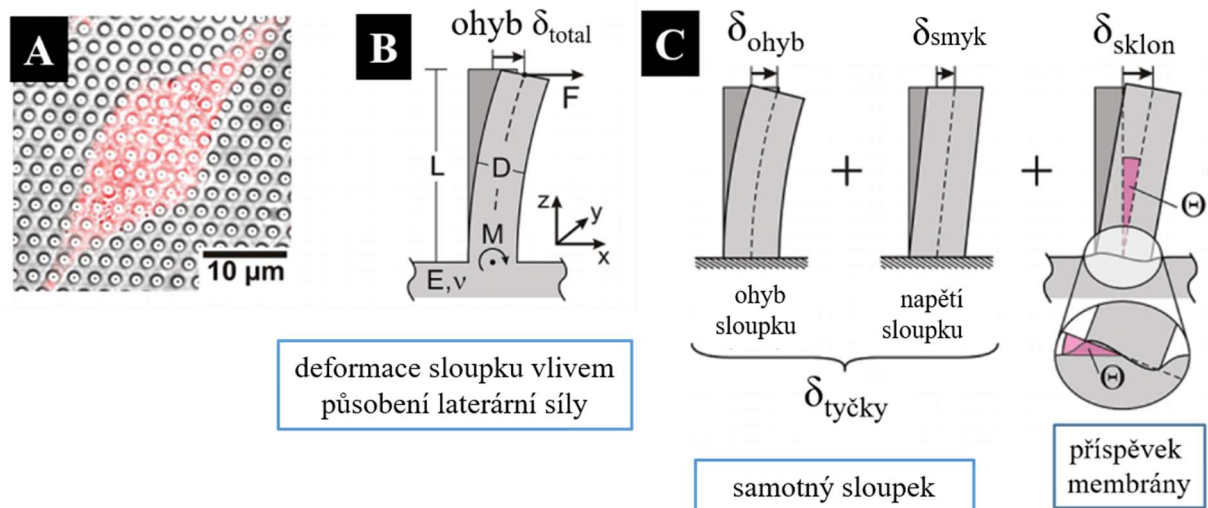
V této části práce se zaměřím na výrobu ohebných mikrosloupků z parylenu C a jejich povrchovou dekorací tenkou vrstvičkou oxidu křemičitého (SiO_2). Tyto sloupky byly navrženy pro biofyzikální aplikaci v oblasti mechanotransdukce, tj. k měření síly generované buňkami.

Síla generovaná buňkou (tzv. trakční síla) vlivem působení různých fyzikálních a biochemických podnětů je známý jev, tak jako studie měření této síly pomocí ohybu polymerních mikro-/nanosloupků, nejčastěji vyrobených z PDMS polymeru. Tyto mechanické síly v podstatě hrají zásadní úlohu v buněčném vývoji, interakci buněk s okolím, v diferenciaci kmenových buněk, za patologických stavů včetně aterosklerózy, rakoviny atd.^[94, 103] Měřit přesně trakční sílu buněk v reálném čase je docela složité. Měření pomocí ohybu flexibilních

sloupeků se zdá být určitým přiblížením a řešením. Mikro- a nanosloupky jsou vertikální adaptací horizontálních kantilevrů neboli jazýčků, které jsou modifikovány bílkoviny tak, aby v podstatě tvořily substrát pro adhezi buněk.^[104] Buňky mohou adherovat a migrovat na povrchu sloupeků působením tažných laterálních sil, jež jsou výsledkem interakce buněčného cytoskeletu přes fokální kontakty a povrchu substrátu (sloupeků). Tato síla má za následek ohyb sloupku, který se chová v podstatě jako pružina. V rámci usnadnění a na základě parametrů sloupeků, tj. definováním poměru délky a průměru sloupeků (L/D nebo také AR poměr) lze spočítat jejich konstantu pružnosti a výslednou sílu na základě Hookova zákona^[105]:

$$F = k \times \Delta\delta = \left(\frac{3}{4}\pi E \frac{r^4}{L^3}\right) \times \Delta\delta,$$

kde F je síla, k je konstanta pružnosti a $\Delta\delta$ je míra ohybu sloupku, E je Youngův modul polymeru, L je délka sloupku a r je jejich poloměr. Trakční síly buněk jsou podélné, a můžou být velmi slabé, v řádech pN až μ N. Vyhodnocení této síly se provádí analýzou mikroskopických obrazů, přičemž u sloupeků s různým L/D poměrem a Youngovým modulem polymeru, se bere v potaz lineární platnost Hookova zákona. Nicméně, z praktického hlediska se určitým způsobem zanedbává např. možné smykové napětí na sloupcích a vliv tohoto stresu a ohybu sloupeků na základní substrát (membránu), na kterém jsou sloupky ukotveny (Obr. 14). Pokud vezmeme v úvahu nejčastěji vyráběné sloupky z měkkého PDMS polymeru, a tedy i membrány z PMDS jako jednoho celku a velmi nízký AR poměr sloupku, je vhodné určitá fakta brát v úvahu a provést možnou korekci. Proto je nasnadě vyrábět sloupky s vysokou hodnotou AR, kde smykové napětí a vliv deformace membrány na výslednou sílu je nejmenší.

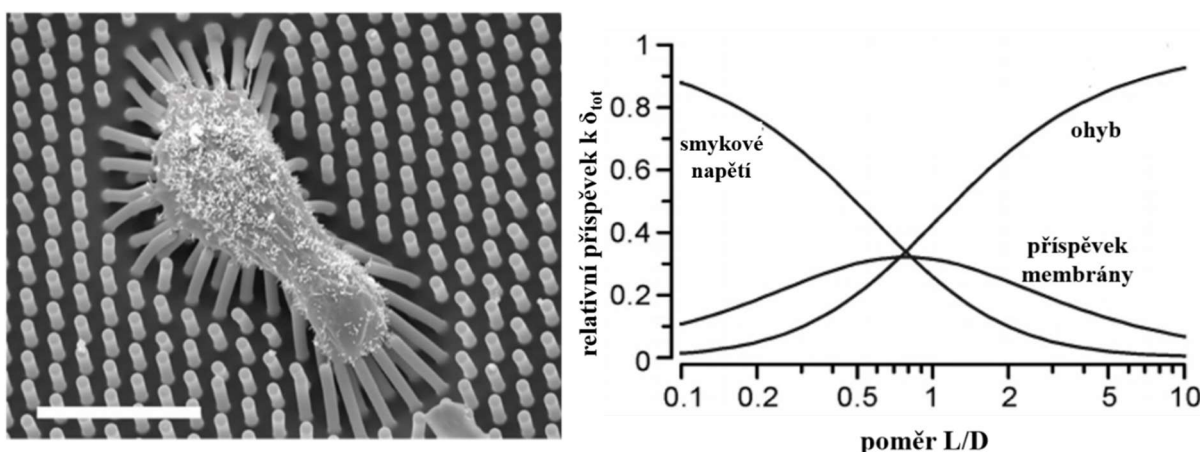


Obr. 14 Mikroslopky a buňka s fluorescenčně značenou buněčnou membránou (A). Ohyb mikroslopku vlivem síly kolmé k ose sloupeků (B). Schéma ohybu, smykového napětí a deformace membrány vlivem působení síly kolmé k ose mikroslopků (C). Převzato a upraveno podle [106].

Ze simulačních výsledků prováděných na PDMS mikrosloupcích, s L/D poměrem od 0.1 do 10, bylo zjištěno, že u vysokých hodnot L/D je dominantní ohyb sloupků. Naopak u nízkých hodnot dominuje smykové napětí sloupků. Okolo hodnoty L/D 1 se také projevuje největší vliv deformace podkladové membrány. Tento příspěvek membrány, tak jako smykové napětí sloupků nezanedbatelně zkreslují výslednou měřenou sílu (až do 40%), což se téměř vždy ve studiích zanedbává. To znamená, že Hookův zákon by měl být doplněn o korekční faktor, jehož hodnoty pro PDMS materiál, L/D poměr a Poissonovu konstantu byly vypočteny v publikaci [106]:

$$F = kor. \times k_{ohyb} \times \Delta\delta$$

Popřípadě je lze odhadnout z grafu Obr. 15 (demonstrováno pro Poissonovu konstantu 0,45).



Obr. 15 Snímek ohybu mikrosloupků buňkou zachyceným elektronovým mikroskopem (vpravo). Korekční faktor uplatňovaný pro ohyb mikrosloupků z PDMS (vlevo). Převzato a upraveno podle [106].

Při měření buněčné síly na flexibilních sloupcích se ve velké míře provádí mikrokontaktní tisk bílkovin.^[98] Tato metoda umožňuje „tisknout“ na povrch sloupků bílkoviny podporující buněčnou adhezi a dalším chemickým modifikováním stran sloupků se dosahuje adheze buněk „pouze“ na povrchu sloupků, a tím i přesnější měření síly generované buňkou. Z praktického hlediska je to krok vyžadující litografii pro vytvoření PDMS razítka, přičemž se poté nechá razítko krátce inkubovat s bílkoviny a následně se otiskne na kyslíkovou plazmou aktivovaný povrch pole sloupků. Z hlediska metodiky může být nepřesný, nekontrolovatelný a nereprodukovatelný, jelikož tisk vyžaduje aplikaci určité síly, což může způsobovat kolaps struktur razítka i sloupků. Dále, ne vždy všechny bílkoviny lze tisknout. Tisk je často omezen jen na bílkoviny, které lze sorbovat na hydrofobní povrch PDMS a tisknout se na povrchy hydrofilní.^[107]

Z dalšího pohledu aplikace těchto PDMS sloupků pro měření buněčné síly vyplývá, že by bylo vhodné vyrábět sloupky s vysokou hodnotou AR a s vysokou hustotou sloupků, což z pohledu PDMS polymeru je problematické i přesto, že lze zvýšit tuhost PDMS pomocí UV záření či polymerizací.^[108] Navíc, vytvořit gradient tuhosti z PDMS je limitováno a pokud by se měla měřit síla buněk na základě různé tuhosti substrátu, za konstantních podmínek AR hodnoty by nemusela pokrývat velký rozsah tuhostí biologického materiálu včetně tvrdých kostí. Proto je dobré hledat další biokompatibilní polymery, které by mohly poskytovat tužší substrát a vyrábět se s vysokou hodnotou AR a nejlépe na pevném substrátu, kde by se neuplatňovala deformace membrány.

Ve vědeckém příspěvku v této oblasti, který je financován GAČR agenturou v rámci juniorského výzkumu uchazečky, přicházím s alternativním přístupem výroby sloupků pro měření buněčné síly, na rozdíl od běžně vyráběných PDMS sloupků. V práci jsme se zaměřili na „top-down“ výrobu vysoce uspořádaného pole mikrosloupků z parylenu C, dekorovaných tenkou vrstvou SiO₂ na povrchu sloupků, a stojících na křemíkovém substrátu. Sloupky byly vyrobeny s vysokou a nižší AR hodnotou 6 a 3,5 a konstantou pružnosti 4.7 μN μm⁻¹ a 28 μN μm⁻¹, resp. Příspěvkem této práce je jednak možnost vytvořit sloupky s poměrně vyšší hodnotou AR a eliminovat příspěvek deformace polymerních membrán vlivem ohybu sloupků, jelikož naše sloupky stojí na pevném křemíkovém substrátu. Déle, SiO₂ vrstva umožňuje kovalentně vázat jakékoliv adhezivní bílkoviny a nemusí se vyrábět PDMS razítko pro mikrokontaktní tisk těchto bílkovin. Parylen C je polymer s několika násobně vyšší hodnotou Youngova modulu, což by mohlo umožňovat vyrábět sloupky ve velkém rozmezí AR hodnot, a ve výsledku může poskytovat i tužší substrát pro buňky ve srovnání s PDMS. Detaily této práce, která byla publikována v impaktovaném časopise, lze najít jako součást této habilitační práce v kapitole 4 (Článek 6: *SiO₂-decorated Parylene C micropillars designed to probe cellular force, Advanced Materials Interfaces*).

3 Perspektiva uchazeče

Pedagogická perspektiva

V tomto směru bych ráda, po diskuzi s garantem, i nadále inovovala přednášky a cvičení k předmětu Elektronika a biosenzory (BSN). Mým cílem je obohatit přednášky o moderní trendy v této oblasti, včetně technologických přístupů výroby mikrofluidních MEMS a lab-on-chip systémů, jejich bioaplikace a tím udělat přednášky studentům záživnější, a z mého pohledu mnohem zajímavější. V rámci akreditace nového oboru na FEKT, který začne probíhat v dohledné době, jsem se také stala garantkou anglické verze BSN: Electronics and Biosensors.

I nadále plánuji se aktivně podílet na vzdělávání studentů v rámci bakalářských a diplomových prací. V tomto roce také mám úspěšně dokončeného Ph.D. studenta (Ing. Ondřej Bílek) a jeden student, který momentálně pro mě pracuje na pozici technického pracovníka, nastoupí v akademickém roce 2021/2022 na doktorské studium (Mgr. Zuzana Košelová).

Vědecká perspektiva

Zde bych nastínila několik vizí do budoucna týkající se mé vědecké práce:

1. V rámci svého GAČR projektu (Mapování trakční síly buněk) budu nadále rozvíjet toto zajímavé téma především v rámci výrobního procesu a zajímat se o limitace a výhody výroby námi navržených sloupků. Určitým cílem je vyrobit tyto sloupky v nanoměřítku s vysokou AR hodnotou. Dále bych ráda pokračovala v bioaplikacích těchto sloupků, na nichž usilovně pracuji již nyní.
2. V rámci nově přijatého MVČR projektu na FEKT VUT na detekci SARS-Covid se budu podílet se na řešení tohoto projektu jako člen týmu, tak jako manažer tohoto projektu.
3. Dále budu pokračovat v charakterizaci biorozhraní nanostrukturovaných povrchů z oxidu kovů. Chtěla bych se zaměřit na nanostrukturované povrchy z oxidu kovů dopovaných dalšími materiály významnými pro především biomedicínské aplikace. V současnosti pracujeme s kolegou Dr. Mozalemem na myšlence dopování zirkoniových nanostruktur selenem.
4. Posledním tématem mého zájmu jsou biosenzory. Již v současnosti s Mgr. Zuzanou Košelovou rozvíjíme téma enzymového biosenzoru s impedančním převodníkem a vlivu adsorbovaných nanočástic na povrchu elektrody na výslednou odezvu.

Celkově bude ale mým hlavním úkolem snaha pro získávání nových projektů, a to nejen tuzemských, ale i evropských.

Závěr

Práce shrnuje teoretické a experimentální poznatky uchazečky zaměřené na vybrané nanostrukturované povrchy z oxidu kovů (oxid titanu, oxid tantalu, oxid hafnia a oxid zirkonia) a jejich biomedicínskou aplikaci. V druhé části se autorka zaměřuje na výrobu flexibilních polymerních mikrosloupků a jejich biofyzikální aplikaci jako substrátu a senzoru pro měření síly generované buňkami.

První dvě publikace jsou věnovány výrobě TiO_2 nanotrubiček dekorovaných nanočásticemi selenu a stříbra. I když bylo prokázáno, že TiO_2 nanotrubičky vykazují v určité míře antibakteriální vlastnosti, v synergickém působení se selenovými nanočásticemi byla antibakteriální aktivita několikanásobně zvýšena. Taktéž došlo ke snížené adhezi a množení nádorových buněk. Ačkoliv selenové nanočástice byly prezentovány v řadě publikací jako netoxické vůči nenádorovým buňkám v širokém rozsahu koncentrací, v kombinaci s nanotrubičkami byla upozorována snížená adheze a množení při vyšším počtu nanočástic na plochu pole nanotrubiček. Z hlediska vyvíjení pokročilých funkčních materiálů pro tkáňové inženýrství je toto informace nutností optimalizovat parametry nanotrubiček a nanočástic, včetně počtu nanočástic na plochu, k vybalancování jejich antibakteriálního účinku, protinádorového účinku a zároveň nebyť toxický vůči nenádorovým buňkám.

V druhém případě byly nanotrubičky dekorovány nanočásticemi stříbra s různým stabilizačním činidlem. V našem případě to byl polyvinylpyrolidon, rozvětvený polyetylenimin, citrát, polyetylglykol a kyselina lipoová. K této práci vedla řada podnětů; často v podobně zaměřených publikacích s využitím antibakteriálních nanočástic se neřešilo stabilizační činidlo. Proto jsem se se svým studentem zaměřila na antibakteriální aktivitu TiO_2 nanotrubiček dekorovaných různými stříbrnými nanočásticemi vůči gram pozitivním a gram negativním bakteriím. Ukázali jsme, že stabilizační činidlo nanočástice hrálo důležitou roli v antibakteriálních vlastnostech takto dekorovaných nanotrubiček. Pro detailnější studium je nicméně nutné dále zhodnotit různé počty nanočástic na plochu, vliv velikosti nanočástic, zkombinovat to s geometrií nanotrubiček a také zhodnotit kompatibilitu vůči tkáňovým buňkám.

Při výrobě „nanotyčinek“ z oxidu kovů jsem se s mým kolegou zaměřila na nanostrukturované povrchy z oxidu tantalu, hafnia a zirkonia. Všechno tyto oxidy jsou z medicínského hlediska biokompatibilními a mým zájmem bylo hlavně studovat vliv topografie na chování buněk, popř. bakterií. Z hlediska chemie bylo upozorováno, že různorodost v typu biomateriálu nemá podstatný vliv na buňky, nicméně změna topografie je vnímána buňkami zcela významně. Proto byly vytvořeny různé geometrie nanotyčinek a studoval se vliv topografie na chování buněk. Z řad našich výsledků bylo prokázáno, že nanostrukturování může mít pozitivní vliv na buňky ve srovnání s nestrukturovaným povrchem. Nicméně byly i strukturované povrchy, které se nejevily pro buňky jako příznivé. Na základě toho je opět nutné optimalizovat strukturování těchto povrchů tak, aby se dosáhlo požadovaných vlastností.

Druhá část práce je věnována výrobě pole polymerních mikrosloupků z parylenu C a jeho aplikaci pro měření buněčné síly. Tyto sloupky se vyrábějí běžně z polydimetylsiloxanu, jako polymeru s nízkým Youngovým modulem pružnosti. Problematické je vyrobit z tohoto polymeru vysoké a tenké sloupky, také podkladová membrána ze stejného polymeru může mít nežádoucí vliv na výslednou měřenou sílu. Vzhledem k tomu jsem se zaměřila na výrobu vysokých sloupků z parylenu C, stojících na křemíkovém substrátu, čímž se eliminoval vliv deformace membrány. Dále jsou sloupky dekorované tenkou vrstvou oxidu křemičitého, což umožňuje kovalentně vázat proteiny, přičemž není nutná výroba polymerního razítka pro mikrokontaktní tisk bílkovin na povrch sloupků. Dále je parylen poměrně tužším polymerem, což teoreticky umožňuje biomimikovat tvrdší substráty pro buňky.

Výše zmíněné práce jsou shrnuty v šesti publikacích a jsou součástí této habilitační práce. Tímto děkuji i svým spoluautorům, že mi pomohli v určitém rozsahu realizovat tyto myšlenky.

Reference

- [1] E. Luong-Van, I. Rodriguez, H.Y. Low, N. Elmouelhi, B. Lowenhaupt, S. Natarajan, C.T. Lim, R. Prajapati, M. Vyakarnam, K. Cooper, *Journal of Materials Research*, 28 (2012) 165-174.
- [2] D.-H. Lien, J.R. Durán Retamal, J.-J. Ke, C.-F. Kang, J.-H. He, *Nanoscale*, 7 (2015) 19874-19884.
- [3] K. Kannan, D. Radhika, K.K. Sadasivuni, K.R. Reddy, A.V. Raghu, *Advances in Colloid and Interface Science*, 281 (2020) 102178.
- [4] A. Majeed, J. He, L. Jiao, X. Zhong, Z. Sheng, *Nanoscale Research Letters*, 10 (2015) 56.
- [5] J. Gallo, M. Holinka, C.S. Moucha, *Int J Mol Sci*, 15 (2014) 13849-13880.
- [6] J. Park, S. Bauer, K. von der Mark, P. Schmuki, *Nano Letters*, 7 (2007) 1686-1691.
- [7] S. Oh, K.S. Brammer, Y.S.J. Li, D. Teng, A.J. Engler, S. Chien, S. Jin, *Proceedings of the National Academy of Sciences of the United States of America*, 106 (2009) 2130-2135.
- [8] J. Park, S. Bauer, K.A. Schlegel, F.W. Neukam, K. von der Mark, P. Schmuki, *Small*, 5 (2009) 666-671.
- [9] J.M. Łopacińska, C. Grădinaru, R. Wierzbicki, C. Købler, M.S. Schmidt, M.T. Madsen, M. Skolimowski, M. Dufva, H. Flyvbjerg, K. Mølhav, *Nanoscale*, 4 (2012) 3739-3745.
- [10] S. Bauer, J. Park, K.v.d. Mark, P. Schmuki, *Acta Biomaterialia*, 4 (2008) 1576-1582.
- [11] A. Kodama, S. Bauer, A. Komatsu, H. Asoh, S. Ono, P. Schmuki, *Acta Biomaterialia*, 5 (2009) 2322-2330.
- [12] H. Tsuchiya, J.M. Macak, L. Müller, J. Kunze, F. Müller, P. Greil, S. Virtanen, P. Schmuki, *Journal of Biomedical Materials Research Part A*, 77A (2006) 534-541.
- [13] L. Zhao, P.K. Chu, Y. Zhang, Z. Wu, *Journal of Biomedical Materials Research Part B: Applied Biomaterials*, 91B (2009) 470-480.
- [14] K.C. Popat, M. Eltgroth, T.J. LaTempa, C.A. Grimes, T.A. Desai, *Small*, 3 (2007) 1878-1881.
- [15] H. Cheng, Y. Li, K. Huo, B. Gao, W. Xiong, *Journal of Biomedical Materials Research Part A*, 102 (2014) 3488-3499.
- [16] G. Jin, H. Cao, Y. Qiao, F. Meng, H. Zhu, X. Liu, *Colloids and Surfaces B: Biointerfaces*, 117 (2014) 158-165.
- [17] M.S. Sander, M.J. Côté, W. Gu, B.M. Kile, C.P. Tripp, *Advanced Materials*, 16 (2004) 2052-2057.
- [18] H. Shin, D.K. Jeong, J. Lee, M.M. Sung, J. Kim, *Advanced Materials*, 16 (2004) 1197-1200.
- [19] D.V. Bavykin, V.N. Parmon, A.A. Lapkin, F.C. Walsh, *Journal of Materials Chemistry*, 14 (2004) 3370-3377.
- [20] P. Roy, S. Berger, P. Schmuki, *Angewandte Chemie International Edition*, 50 (2011) 2904-2939.
- [21] K. Nakane, N. Ogata, 2010.
- [22] Z. Jedi-soltanabadi, N. Pishkar, M. Ghoranneviss, *Journal of Theoretical and Applied Physics*, 12 (2018) 135-139.
- [23] X. Zhao, Y. Zhu, Y. Wang, L. Zhu, L. Yang, Z. Sha, *Journal of Nanomaterials*, 2015 (2015) 104193.
- [24] H. Li, G. Wang, J. Niu, E. Wang, G. Niu, C. Xie, *Results in Physics*, 14 (2019) 102499.
- [25] X. Qiu, J.Y. Howe, M.B. Cardoso, O. Polat, W.T. Heller, M. Parans Paranthaman, *Nanotechnology*, 20 (2009) 455601.
- [26] X. Liu, R. Yuan, Y. Liu, S. Zhu, J. Lin, X. Chen, *New Journal of Chemistry*, 40 (2016) 6276-6280.
- [27] R.V. Gonçalves, P. Migowski, H. Wender, D. Eberhardt, D.E. Weibel, F.C. Sonaglio, M.J.M. Zapata, J. Dupont, A.F. Feil, S.R. Teixeira, *The Journal of Physical Chemistry C*, 116 (2012) 14022-14030.
- [28] K. Yasuda, P. Schmuki, *Electrochemistry Communications*, 9 (2007) 615-619.
- [29] S. Berger, R. Hahn, P. Roy, P. Schmuki, *physica status solidi (b)*, 247 (2010) 2424-2435.
- [30] H. Jha, P. Roy, R. Hahn, I. Paramasivam, P. Schmuki, *Electrochemistry Communications*, 13 (2011) 302-305.

- [31] S. Li, G. Zhang, D. Guo, L. Yu, W. Zhang, *The Journal of Physical Chemistry C*, 113 (2009) 12759-12765.
- [32] S.P. Albu, D. Kim, P. Schmuki, *Angewandte Chemie International Edition*, 47 (2008) 1916-1919.
- [33] S.P. Albu, A. Ghicov, S. Aldabergenova, P. Drechsel, D. LeClere, G.E. Thompson, J.M. Macak, P. Schmuki, *Advanced Materials*, 20 (2008) 4135-4139.
- [34] Y.-Y. Song, P. Schmuki, *Electrochemistry Communications*, 12 (2010) 579-582.
- [35] K. Lee, A. Mazare, P. Schmuki, *Chemical Reviews*, 114 (2014) 9385-9454.
- [36] L.-N. Wang, M. Jin, Y. Zheng, Y. Guan, X. Lu, J.-L. Luo, *Int J Nanomedicine*, 9 (2014) 4421-4435.
- [37] Y. Fu, A. Mo, *Nanoscale Research Letters*, 13 (2018) 187.
- [38] D. Regonini, C.R. Bowen, A. Jaroenworarluck, R. Stevens, *Materials Science and Engineering: R: Reports*, 74 (2013) 377-406.
- [39] O.K. Varghese, D. Gong, M. Paulose, K.G. Ong, E.C. Dickey, C.A. Grimes, *Advanced Materials*, 15 (2003) 624-627.
- [40] Q. Cai, M. Paulose, O.K. Varghese, C.A. Grimes, *Journal of Materials Research*, 20 (2011) 230-236.
- [41] J.M. Macak, H. Tsuchiya, L. Taveira, S. Aldabergerova, P. Schmuki, *Angewandte Chemie International Edition*, 44 (2005) 7463-7465.
- [42] J. Wan, X. Yan, J. Ding, M. Wang, K. Hu, *Materials Characterization*, 60 (2009) 1534-1540.
- [43] K.S. Raja, T. Gandhi, M. Misra, *Electrochemistry Communications*, 9 (2007) 1069-1076.
- [44] N.K. Allam, C.A. Grimes, *The Journal of Physical Chemistry C*, 111 (2007) 13028-13032.
- [45] N.K. Allam, K. Shankar, C.A. Grimes, *Journal of Materials Chemistry*, 18 (2008) 2341-2348.
- [46] Z. Lockman, S. Sreekantan, S. Ismail, L. Schmidt-Mende, J.L. MacManus-Driscoll, *Journal of Alloys and Compounds*, 503 (2010) 359-364.
- [47] J.M. Macak, H. Hildebrand, U. Marten-Jahns, P. Schmuki, *Journal of Electroanalytical Chemistry*, 621 (2008) 254-266.
- [48] J. Wang, Z. Lin, *The Journal of Physical Chemistry C*, 113 (2009) 4026-4030.
- [49] G.A. Crawford, N. Chawla, K. Das, S. Bose, A. Bandyopadhyay, *Acta Biomaterialia*, 3 (2007) 359-367.
- [50] V.M. Prida, E. Manova, V. Vega, M. Hernandez-Velez, P. Aranda, K.R. Pirola, M. Vázquez, E. Ruiz-Hitzky, *Journal of Magnetism and Magnetic Materials*, 316 (2007) 110-113.
- [51] M. Enachi, I. Tiginyanu, V. Sprincean, V. Ursaki, *physica status solidi (RRL) – Rapid Research Letters*, 4 (2010) 100-102.
- [52] A. Tighineanu, T. Ruff, S. Albu, R. Hahn, P. Schmuki, *Chemical Physics Letters*, 494 (2010) 260-263.
- [53] S. Das, R. Zazpe, J. Prikryl, P. Knotek, M. Krbal, H. Sopha, V. Podzemna, J.M. Macak, *Electrochimica Acta*, 213 (2016) 452-459.
- [54] T. Cottineau, N. Béalu, P.-A. Gross, S.N. Pronkin, N. Keller, E.R. Savinova, V. Keller, *Journal of Materials Chemistry A*, 1 (2013) 2151-2160.
- [55] P. Benjwal, K.K. Kar, *Materials Chemistry and Physics*, 160 (2015) 279-288.
- [56] H. Liu, G. Liu, Q. Zhou, *Journal of Solid State Chemistry*, 182 (2009) 3238-3242.
- [57] M.M. Momeni, Y. Ghayeb, Z. Ghonchehi, *Ceramics International*, 41 (2015) 8735-8741.
- [58] H.-i. Kim, D. Monllor-Satoca, W. Kim, W. Choi, *Energy & Environmental Science*, 8 (2015) 247-257.
- [59] M. Szkoda, A. Lisowska-Oleksiak, K. Siuzdak, *Journal of Solid State Electrochemistry*, 20 (2016) 1765-1774.
- [60] K. Siuzdak, M. Szkoda, M. Sawczak, A. Lisowska-Oleksiak, J. Karczewski, J. Ryl, *RSC Advances*, 5 (2015) 50379-50391.
- [61] Y. Kang, J. Zhao, J. Tao, X. Wang, Y. Li, *Applied Surface Science*, 254 (2008) 3935-3938.
- [62] L. Zhao, H. Wang, K. Huo, L. Cui, W. Zhang, H. Ni, Y. Zhang, Z. Wu, P.K. Chu, *Biomaterials*, 32 (2011) 5706-5716.
- [63] L. Yang, S. Luo, R. Liu, Q. Cai, Y. Xiao, S. Liu, F. Su, L. Wen, *The Journal of Physical Chemistry C*, 114 (2010) 4783-4789.

- [64] A. Benoit, I. Paramasivam, Y.C. Nah, P. Roy, P. Schmuki, *Electrochemistry Communications*, 11 (2009) 728-732.
- [65] P. Roy, D. Kim, I. Paramasivam, P. Schmuki, *Electrochemistry Communications*, 11 (2009) 1001-1004.
- [66] L. Assaud, N. Brazeau, M.K.S. Barr, M. Hanbücken, S. Ntais, E.A. Baranova, L. Santinacci, *ACS Applied Materials & Interfaces*, 7 (2015) 24533-24542.
- [67] S. Ng, P. Kuberský, M. Krbal, J. Prikryl, V. Gärtnerová, D. Moravcová, H. Sopha, R. Zazpe, F.K. Yam, A. Jäger, L. Hromádka, L. Beneš, A. Hamáček, J.M. Macak, *Advanced Engineering Materials*, 20 (2018) 1700589.
- [68] R. Zazpe, M. Knaut, H. Sopha, L. Hromádka, M. Albert, J. Prikryl, V. Gärtnerová, J.W. Bartha, J.M. Macak, *Langmuir*, 32 (2016) 10551-10558.
- [69] Z. Zhou, S.S. Nonnenmann, *Materials (Basel)*, 12 (2019) 2535.
- [70] A. Mozalev, J. Hubalek, *Electrochimica Acta*, 297 (2019) 988-999.
- [71] W.J. Stępniewski, Z. Bojar, *Nanoporous Anodic Aluminum Oxide: Fabrication, Characterization, and Applications*, in: M. Aliofkhae, A.S.H. Makhlof (Eds.) *Handbook of Nanoelectrochemistry: Electrochemical Synthesis Methods, Properties and Characterization Techniques*, Springer International Publishing, Cham, 2016, pp. 1-47.
- [72] G. Sulka, L. Zaraska, W. Stępniewski, *Anodic porous alumina as a template for nanofabrication*, 2011, pp. 261-349.
- [73] S. Ateş, E. Baran, B. Yazıcı, *Thin Solid Films*, 648 (2018) 94-102.
- [74] P. Tomassi, Z. Buczko, 2015.
- [75] T.M. Lednický, A.; Bendova, M, *Conference Proceedings of 8th International Conference on Nanomaterials - Research & Application (Nanocon)*, Ostrava, Czech Republic, 2017.
- [76] W. Jiang, J. He, J. Zhong, J. Lu, S. Yuan, B. Liang, *Applied Surface Science*, 307 (2014) 407-413.
- [77] Y. Yang, S.P. Albu, D. Kim, P. Schmuki, *Angewandte Chemie International Edition*, 50 (2011) 9071-9075.
- [78] S. Berger, H. Tsuchiya, P. Schmuki, *Chemistry of Materials*, 20 (2008) 3245-3247.
- [79] U. Mock, R. Förster, W. Menz, J. Rühle, *Journal of Physics: Condensed Matter*, 17 (2005) S639-S648.
- [80] D.V. McAllister, P.M. Wang, S.P. Davis, J.-H. Park, P.J. Canatella, M.G. Allen, M.R. Prausnitz, *Proceedings of the National Academy of Sciences*, 100 (2003) 13755.
- [81] A.K. Geim, S.V. Dubonos, I.V. Grigorieva, K.S. Novoselov, A.A. Zhukov, S.Y. Shapoval, *Nature Materials*, 2 (2003) 461-463.
- [82] K. Kim, S. Park, J.-B. Lee, H. Manohara, Y. Desta, M. Murphy, C.H. Ahn, *Microsystem Technologies*, 9 (2002) 5-10.
- [83] S. Nomura, H. Kojima, Y. Ohyabu, K. Kuwabara, A. Miyauchi, T. Uemura, *Japanese Journal of Applied Physics*, 44 (2005) L1184-L1186.
- [84] T.N. Krupenkin, J.A. Taylor, T.M. Schneider, S. Yang, *Langmuir*, 20 (2004) 3824-3827.
- [85] W. Chunlei, J. Guangyao, L.H. Taherabadi, M.J. Madou, *Journal of Microelectromechanical Systems*, 14 (2005) 348-358.
- [86] K. Ansari, J.A. van Kan, A.A. Bettiol, F. Watt, *Applied Physics Letters*, 85 (2004) 476-478.
- [87] X.M. Zhao, Y. Xia, D. Qin, G.M. Whitesides, *Advanced materials*, 9 (1997) 251-254.
- [88] C.N. LaFratta, T. Baldacchini, R.A. Farrer, J.T. Fourkas, M.C. Teich, B.E. Saleh, M.J. Naughton, *The Journal of Physical Chemistry B*, 108 (2004) 11256-11258.
- [89] K.G. Sharp, G.S. Blackman, N.J. Glassmaker, A. Jagota, C.-Y. Hui, *Langmuir*, 20 (2004) 6430-6438.
- [90] P. Roca-Cusachs, F. Rico, E. Martinez, J. Toset, R. Farré, D. Navajas, *Langmuir*, 21 (2005) 5542-5548.
- [91] Y. Zhang, C.-W. Lo, J.A. Taylor, S. Yang, *Langmuir*, 22 (2006) 8595-8601.
- [92] Y. Alapan, K. Icoz, U.A. Gurkan, *Biotechnology Advances*, 33 (2015) 1727-1743.
- [93] L.H. Ting, J.R. Jahn, J.I. Jung, B.R. Shuman, S. Feghhi, S.J. Han, M.L. Rodriguez, N.J. Sniadecki, *Am J Physiol Heart Circ Physiol*, 302 (2012) H2220-H2229.

- [94] J.L. Tan, J. Tien, D.M. Pirone, D.S. Gray, K. Bhadriraju, C.S. Chen, *Proceedings of the National Academy of Sciences*, 100 (2003) 1484.
- [95] N.J. Sniadecki, A. Anguelouch, M.T. Yang, C.M. Lamb, Z. Liu, S.B. Kirschner, Y. Liu, D.H. Reich, C.S. Chen, *Proceedings of the National Academy of Sciences*, 104 (2007) 14553.
- [96] O. du Roure, A. Saez, A. Buguin, R.H. Austin, P. Chavrier, P. Siberzan, B. Ladoux, *Proceedings of the National Academy of Sciences of the United States of America*, 102 (2005) 2390.
- [97] A. Rabadzey, P. Alcaide, F.W. Lusckas, B. Ladoux, *Biophysical Journal*, 95 (2008) 1428-1438.
- [98] M. Gupta, L. Kocgozlu, B.R. Sarangi, F. Margadant, M. Ashraf, B. Ladoux, Chapter 16 - Micropillar substrates: A tool for studying cell mechanobiology, in: E.K. Paluch (Ed.) *Methods in Cell Biology*, Academic Press 2015, pp. 289-308.
- [99] K.-S. Kim, J.-H. Kim, H.-J. Lee, S.-R. Lee, *Journal of Mechanical Science and Technology*, 24 (2010) 5-12.
- [100] F. Viela, D. Granados, A. Ayuso-Sacido, I. Rodríguez, *Advanced Functional Materials*, 26 (2016) 5599-5609.
- [101] X. Yang, Z. Zhong, *Journal of Applied Polymer Science*, n/a (2021) 50460.
- [102] S. Ghassemi, O. Rossier, M.P. Sheetz, S.J. Wind, J. Hone, *Journal of Vacuum Science & Technology B: Microelectronics and Nanometer Structures Processing, Measurement, and Phenomena*, 27 (2009) 3088-3091.
- [103] Z. Li, H. Persson, K. Adolfsson, L. Abariute, M.T. Borgström, D. Hessman, K. Åström, S. Oredsson, C.N. Prinz, *Nanoscale*, 9 (2017) 19039-19044.
- [104] N.Q. Balaban, U.S. Schwarz, D. Riveline, P. Goichberg, G. Tzur, I. Sabanay, D. Mahalu, S. Safran, A. Bershadsky, L. Addadi, B. Geiger, *Nature Cell Biology*, 3 (2001) 466-472.
- [105] J. le Digabel, M. Ghibaudo, L. Trichet, A. Richert, B. Ladoux, *Medical & Biological Engineering & Computing*, 48 (2010) 965-976.
- [106] I. Schoen, W. Hu, E. Klotzsch, V. Vogel, *Nano Letters*, 10 (2010) 1823-1830.
- [107] S.G. Ricoult, A. Sanati Nezhad, M. Knapp-Mohammady, T.E. Kennedy, D. Juncker, *Langmuir*, 30 (2014) 12002-12010.
- [108] Y. Sun, L.-T. Jiang, R. Okada, J. Fu, *Langmuir*, 28 (2012) 10789-10796.

4 Publikační činnost v rámci habilitační práce

Vybrané publikační práce související s výzkumnou činností v rámci předložené habilitační práce za posledních 5 let na VUT.

Článek 1 Enhanced antibacterial and anticancer properties of Se-NPs decorated TiO₂ nanotube film, Bilek, O., Fohlerova, Z., Hubalek, J., PLoS ONE, 2019, 14(3), e0214066.

Korespondeční autor (podíl 45%)

Článek 2 Antibacterial activity of AgNPs-TiO₂ nanotubes: Influence of different nanoparticle stabilizers, Bilek, O., Fialova, T., Otahal, A., Smerkova, K., Fohlerova, Z., RSC Advances, 2020, 10(72), pp. 44601– 44610.

Korespondeční autor (podíl 45%)

Článek 3 Tuning the response of osteoblast-like cells to the porous-alumina-assisted mixed-oxide nanomound arrays, Fohlerova, Z., Mozalev, A., Journal of Biomedical Materials Research - Part B Applied Biomaterials, 2018, 106(5), pp. 1645–1654.

První a korespondeční autor (podíl 50%)

Článek 4 Anodic formation and biomedical properties of hafnium-oxide nanofilms Fohlerova, Z., Mozalev, A., Journal of Materials Chemistry B, 2019, 7(14), pp. 2300 – 2310.

První a korespondeční autor (podíl 50%)

Článek 5 Nanostructured ZrO₂ bioceramic coatings derived from the anodically oxidized Al/Zr metal layers, Fohlerova Z., Sepulveda M., Kamnev K., Mozalev A., zasláno do časopisu.

První autor (podíl 40%)

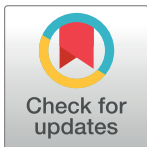
Článek 6 SiO₂-decorated Parylene C micropillars designed to probe cellular force, Fohlerova Z., Gablech I., Otahal A., Fecko P., Advanced Materials Interfaces, 2021, 2001897.

První a korespondeční autor (podíl 50%)

Článek 1

**Enhanced antibacterial and anticancer properties of Se-NPs
decorated TiO₂ nanotube film**

RESEARCH ARTICLE

Enhanced antibacterial and anticancer properties of Se-NPs decorated TiO₂ nanotube filmOndrej Bilek¹, Zdenka Fohlerova^{1,2*}, Jaromir Hubalek^{1,2}¹ Central European Institute of Technology, Brno University of Technology, Brno, Czech Republic,² Department of Microelectronics, Brno University of Technology, Brno, Czech Republic* zdenka.fohlerova@ceitec.vutbr.cz

OPEN ACCESS

Citation: Bilek O, Fohlerova Z, Hubalek J (2019) Enhanced antibacterial and anticancer properties of Se-NPs decorated TiO₂ nanotube film. PLoS ONE 14(3): e0214066. <https://doi.org/10.1371/journal.pone.0214066>

Editor: Thomas Webster, Northeastern University, UNITED STATES

Received: December 7, 2018

Accepted: March 6, 2019

Published: March 22, 2019

Copyright: © 2019 Bilek et al. This is an open access article distributed under the terms of the [Creative Commons Attribution License](https://creativecommons.org/licenses/by/4.0/), which permits unrestricted use, distribution, and reproduction in any medium, provided the original author and source are credited.

Data Availability Statement: All relevant data are within the manuscript and Supporting Information files.

Funding: Research described in this paper was financed by Czech Ministry of Education in frame of National Sustainability Program under grant LO1401. For research, infrastructure of the SIX Center was used. The funders had no role in study design, data collection and analysis, decision to publish, or preparation of the manuscript.

Competing interests: The authors have declared that no competing interests exist.

Abstract

Selenium nanoparticle modified surfaces attract increasing attention in the field of tissue engineering. Selenium exhibits strong anticancer, antibacterial and anti-inflammatory properties and it maintains relatively low off-target cytotoxicity. In our paper, we present the fabrication, characterization and cytocompatibility of titanium oxide (TiO₂) nanotube surface decorated with various surface densities of chemically synthesized selenium nanoparticles. To evaluate antibacterial and anti-cancer properties of such nanostructured surface, gram negative bacteria *E. coli*, cancerous osteoblast like MG-63 cells and non-cancerous fibroblast NIH/3T3 were cultured on designed surfaces. Our results suggested that selenium nanoparticles improved antibacterial properties of titanium dioxide nanotubes and confirmed the anticancer activity towards MG-63 cells, with increasing surface density of nanoparticles. Further, the selenium decorated TiO₂ nanotubes suggested deteriorating effect on the cell adhesion and viability of non-cancerous NIH/3T3 cells. Thus, we demonstrated that selenium nanoparticles decorated TiO₂ nanotubes synthesized using sodium selenite and glutathione can be used to control bacterial infections and prevent the growth of cancerous cells. However, the higher surface density of nanoparticles adsorbed on the surface was found to be cytotoxic for non-cancerous NIH/3T3 cells and thus it might complicate the integration of biomaterial into the host tissue. Therefore, an optimal surface density of selenium nanoparticles must be found to effectively kill bacteria and cancer cells, while remaining favorable for normal cells.

Introduction

The widespread use and persisting negative properties of some metallic biomaterials for tissue engineering or surgical instruments aimed researches to modulate the surface characteristics of biomaterials into the form with desired functional surface properties. The rapid progress in nanotechnology enabled us to approach and mimic the tissue environment via surface modifications including chemistry, topography or roughness that can significantly change the interface between individual material and tissue cells or bacteria and thus, results in different

responses in cell adhesion, viability, metabolism, antibacterial or anti-inflammatory activity. For instance, it was previously reported in independent *in vitro* studies that the nanotopography plays a crucial role in the character and strength of the cellular interaction to such a modified surface with a positive impact on the resulting cellular responses [1–5]. Moreover, nanostructured biomaterials were considered to exhibit various qualities, such as antibacterial activity [6, 7] or improved bioactivity [8, 9] that were not observed for their non-structured forms.

Materials such as titanium (Ti) and its alloys are widely used in many replacements including orthopaedic, dental and cardiovascular implants and medical devices [10]. The favorable mechanical properties, exceptional corrosion resistance and biocompatibility of titanium [11] were attributed to a passive thin film of titanium dioxide (TiO₂) formed on Ti surface [8]. This thin layer was also considered to impart bioactivity and chemical bonding between implant and the bone [2]. Nanostructuring of titanium film into the form of nanotubes (TNTs) has attracted great attention for improving cell adhesion, growth and differentiation [9, 12, 13]. Later findings proved the strong relation between the cell responses and nanotube dimensions [4, 14, 15]. For example, mesenchymal stem cells showed the improved response on nanotubes with smaller diameters (~15 nm) [4, 16], while osteoblasts preferred nanotubes with bigger diameters (~70 nm) [12]. The adhesion was faster and stronger compared to the control, which was thought to avoid formation of fibrous tissue caused by a weak cell-surface interaction [2].

Many approaches were subsequently introduced to enhance the performance of TNT surfaces. Some aimed to increase the antibacterial activity through loading the nanotubes with various antibiotics, such as vancomycin [17] and gentamicin [18] or their decoration/doping with various nanoparticles, including gold [19, 20], silver [8, 21] and zinc oxide [22]. Other addressed the biocompatibility through coating with bioactive compounds, such as PLGA [23], chitosan [23], hydroxyapatite [24] or growth factors [25].

Recently, treatment of bio-surfaces with selenium attracted attention. Selenium is an important element that plays crucial role in preventing cancer and protecting cells from oxidative damage [26, 27]. It has been reported to exhibit not only antibacterial [28–31], but also anti-cancer [28, 32] and anti-inflammatory [29, 33] properties that make selenium interesting for various applications including oncology [28, 32], regenerative medicine [34] and tissue engineering [29, 30, 35–37]. Selenium nanoparticle (SeNPs) decorated TNTs were studied and reported previously for its antibacterial and anti-inflammatory properties [29]. Results suggested that selenium nanoparticles enhanced antibacterial properties of TNTs which caused the decrease in colony forming units of both gram-positive and gram-negative bacteria. How such a surface effected cancerous and non-cancerous cells remained unanswered. In another reported research [28], the release of selenium nanoparticles from TiO₂ nanotubes covered with chitosan was studied for antibacterial activity. Authors declared that such a fabricated and designed surface positively influenced the viability of osteoblasts and negatively affected cancerous cells, while promoted the antibacterial activity of TNTs. However, this antibacterial effect could be attributed to chitosan, which is, in the fact, antimicrobial [38] and biocompatible [39]. Authors in this study also admitted, that no discernable layer of Se or Se nanoparticles was observed on their samples.

In our work, we introduced the fabrication of TiO₂ nanotubes of 50 nm in diameter via anodic oxidation of titanium layer deposited on silicon wafer. Nanotubes were decorated with chemically synthesized selenium nanoparticles of three different surface densities. Designed films were characterized with contact angle measurement, SEM, XPS and AFM techniques. Due to the absence of reports regarding the interaction of such a surface with tissue cells, we studied mutual effect of selenium nanoparticles and TiO₂ nanotubes on antibacterial

properties against *E. coli* and viability of osteosarcoma MG-63 cells and non-cancerous NIH/3T3 fibroblasts.

Materials and methods

Preparation of nanotubes via anodic oxidation

TiO₂ nanotubes were fabricated from 500 nm thick titanium layer sputter-deposited on silicon wafer via electrochemical anodization according to protocol established previously [40]. The fabrication process is schematically depicted in Fig 1. Briefly, electrochemical anodization was performed with voltage ramp from 0 V to 15 V and the step of 1 volt per second in the electrolyte solution of ethylene glycol (C₂H₆O₂, p.a., Penta, CZ), 1.2 wt% ammonium fluoride (NH₄F, Sigma Aldrich, DE) and 2 vol% of deionized water (Millipore Corp., USA, 18,2 MΩ). When the voltage reached the maximum set value, the voltage was maintained until the current reached zero value. Samples were then rinsed with deionized water, dried with stream of nitrogen and subsequently annealed in vacuum furnace at 450°C for 3 hours, with the heating ramp of 5°C per minute.

Decoration with selenium nanoparticles. The protocol for preparation of selenium nanoparticle solution was inspired by previous study carried by Liu et al. [29]. The 3 mL of 100 mmol L⁻¹ L-glutathione (Sigma-Aldrich) and 3 mL of 100 mmol L⁻¹ sodium selenite (Sigma-Aldrich) were blended together. To control the amount of selenium nanoparticles decorated onto the surface, different volumes of ultrapure water were added to individual mixtures— 9 mL for low, 6 mL for medium and 3 mL for high selenium nanoparticle concentration. Finally, 50 μL of 1 mol L⁻¹ NaOH solution was added to initiate the reaction at room temperature. The formation of nanoparticles was optically observed as a gradual change in the color from transparent to red. 100 μL of nanoparticle suspension was then introduced onto the nanostructured surface and incubated for 20 minutes. After that, samples were rinsed several times, and

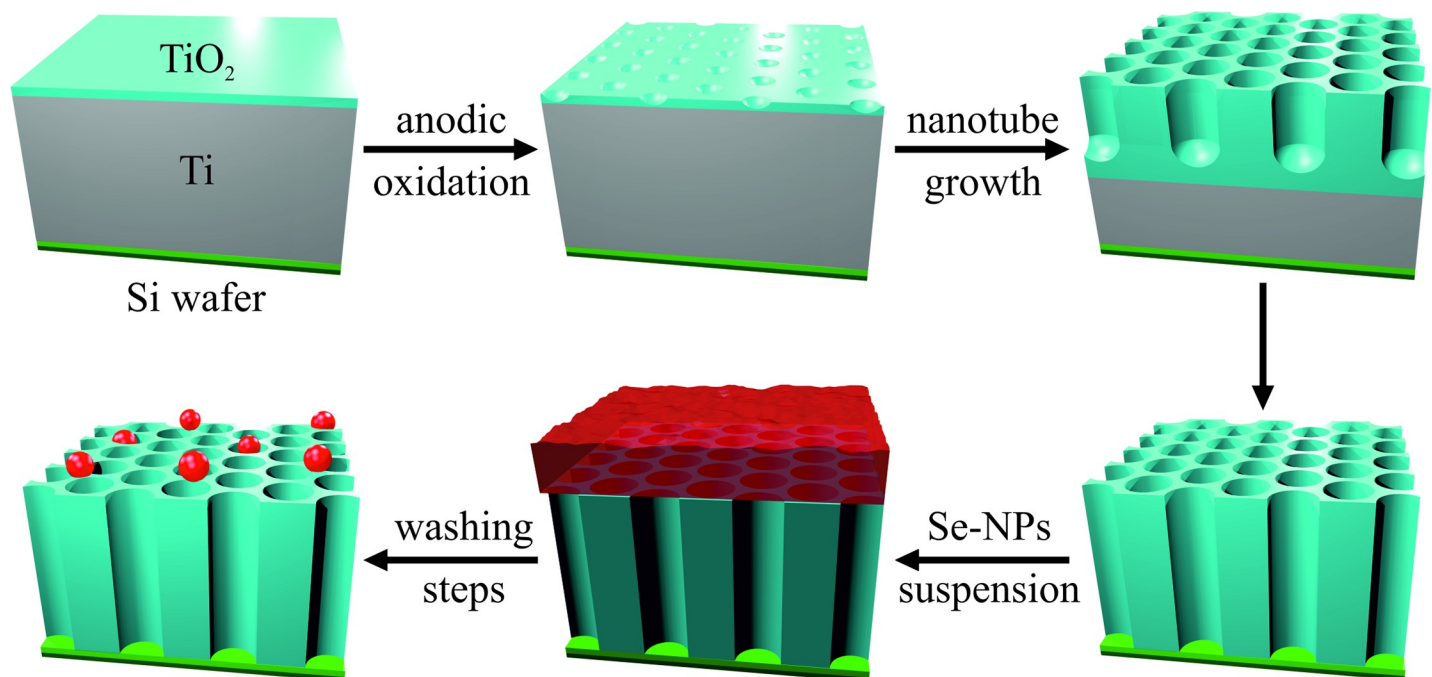


Fig 1. Fabrication scheme of Se-NP decorated TiO₂ nanotube film. TiO₂ nanotubes were fabricated via anodic oxidation of 500 nm thick titanium layer deposited on silicon wafer. Nanotubes were decorated with different concentrations of selenium nanoparticles.

<https://doi.org/10.1371/journal.pone.0214066.g001>

subsequently soaked in ultrapure water to remove non-adsorbed particles. Scanning electron microscopy and atomic force microscopy was used to check the quality of nanoparticle decoration, and to analyze the amount and diameter of selenium nanoparticles. Prior to bio-characterizations, fabricated surfaces were sterilized with UV irradiation for 15 minutes.

Characterization of nanostructured film

The wettability of samples was measured at room temperature by determination of water contact angle of 5 μ L water drop introduced on sample surface after UV irradiation (Phoenix 300, Surface & Electro Optics Co.,Ltd, KOR). Contact angle was evaluated using tangent line method 2 (higher angles) and trigonometric functions method (lower angles) implemented in software Surfaceware 8. The surface morphology and nanoparticles size was characterized with scanning electron microscope (SEM, Mira II, Tescan, CZ) and the roughness was calculated by atomic force microscopy in dry non-contact mode (AFM, NanoWizzard3, JPK). Chemical composition of samples was determined with X-ray photoelectron spectroscopy (XPS, AXIS Supra, Kratos Analytical Ltd, UK). The XPS spectra were analyzed by a peak fitting software (CasaXPS version 2.3.18PR1.0) provided by SPECS GmbH (Berlin, Germany). Raw data were processed by the subtraction of a Shirley background for secondary electrons and element peak fitting was used to estimate the relative element molar fraction. The integral of the peak was divided by a relative sensitivity factor (R.S.F.), which is characteristic for each element. Finally, the concentration profile of selenium released from the surface was determined with inductively coupled plasma mass spectrometry (ICP-MS). Decorated samples were immersed into 3 mL of ultrapure water for 15 days. At selected time points, 1.5 mL of solution was collected. Samples were subsequently dried with nitrogen stream and immersed into 3 mL of fresh ultrapure water.

Antibacterial test

Antibacterial properties of selenium NPs decorated nanotubes were evaluated through the bacterial viability assay with gram negative *E. coli*. Non-decorated nanotube surface was used as a control. The samples were rinsed with water and sterilized with UV for 15 minutes before each experiment. Briefly, 50 μ L of bacterial suspension was spread onto the surface and incubated 4 hours at 37°C. Subsequently, adhered bacteria were washed out with phosphate buffer saline (PBS) and collected bacterial suspension was diluted 100 times with PBS. Bacteria cultured plates were prepared using agar, yeast extract, NaCl and tryptone. The 200 μ L of diluted solution was inoculated on prepared agar plates and incubated for 24 hours at 37°C and 80% humidity. Agar plates were then photographed and colony forming units were calculated (CFU mL⁻¹).

Cell culture

The cancerous MG-63 cells and non-cancerous NIH/3T3 cells were maintained in complete Dulbecco's Modified Eagle's medium (DMEM) supplemented with 10% fetal bovine serum (FBS), 2 mmol L⁻¹ L-glutamine, and 5% penicillin/streptomycin (50 U mL⁻¹ and 50 μ g mL⁻¹) at 37°C in a humidified 5% CO₂ incubator. Cells were harvested by trypsinization with 0.25% trypsin-EDTA solution at 75% confluency and seeded with a defined density onto the sterile samples placed in a polystyrene microplate.

Cell adhesion and viability

The adhesion of MG-63 and NIH/3T3 cells onto TiO₂ nanotubes decorated with selenium NPs and onto the control (TiO₂ nanotubes without selenium nanoparticles) was qualitatively

evaluated from images taken by an optical microscope (Axio Imager M2m, Zeiss). TiO₂ and TiO₂-SeNPs samples were placed in a 24-well plate and used as the surface for cell seeding at a density of $1 \cdot 10^3$ cells per area. The images of cells were taken at 3 hours. Viability of MG-63 cells was measured with XTT assay and evaluated on days 1, 2, and 6 after the seeding; the initial cell density was $1 \cdot 10^3$ cells per area. Briefly, the cells were incubated for a defined period of time and then gently washed twice with pre-heated phosphate buffer saline (PBS). The mixture of 100 μ L culture medium and 50 μ L of tetrazolium dye (XTT, 1 mg mL⁻¹ in DMEM and 25 μ mol L⁻¹ PMS in PBS) was added into each well containing the samples and incubated 2 hours in CO₂ incubator. 100 μ L solution were transferred from each well into a new 96-well plate and the absorbance was measured at 450 nm with a microplate spectrophotometer (Beckman Coulter Paradigm). The live/dead staining of MG-63 cells and 3T3 fibroblasts was performed at the day 6. The cells were gently rinsed with pre-warmed PBS and incubated 15 min with 2 μ M Calcein-AM and 1.5 μ M propidium iodide solution in PBS. The cells were finally rinsed twice in PBS before imaging with a fluorescent microscope coupled to a CCD camera (Zeiss, Germany).

Statistical analysis

Mean values and standard deviations of obtained data were calculated. Statistically significant differences ($p < 0.05$) were confirmed using Student's t-test. All shown data are expressed as the mean \pm standard deviation.

Results and discussion

Surface characterization

Selenium NPs decorated TiO₂ nanotubes were fabricated via anodic oxidation of titanium layer deposited on silicon wafer followed by the adsorption of chemically synthesized selenium nanoparticles. Fabrication of nanostructured surface resulted in TNTs with the diameter of 51.72 ± 5.55 nm (Fig 2A) and length of 500 nm (Fig 2B). The surface was decorated with spherical selenium nanoparticles (Fig 2C) of 88.93 ± 6.87 nm in size, which is significantly bigger than nanotube diameter. Thus the nanoparticles covered the top of the nanotubes at Se-Low (Fig 2D), Se-Medium (Fig 2E) and Se-High (Fig 2F) densities corresponding to number of 3.2 ± 1.14 (low), 9.1 ± 1.20 (medium) and 18.5 ± 2.37 (high) particles per $4 \mu\text{m}^2$, respectively. According to Boxplot of obtained data (Fig 3) and Shapiro-Wilk test of normality, both nanoparticle and nanotube size have normal distributions

SEM analysis also revealed the discrete TiO₂ nanotubes with the nanoparticle density and nanotube diameter consistent over the whole surface of the sample. AFM analysis further showed the increase in root mean squared (RMS) roughness of samples with increasing surface density of nanoparticles. The RMS value from bare TNTs to Se-High TNTs ranged from 16.6 nm to 24.1 nm.

Measurement of UV-treated TNTs wettability showed significant difference between decorated and non-decorated TiO₂ nanotubes. The contact angle of bare nanotubes and nanoparticle decorated nanotubes was assessed to values $\sim 20^\circ$ and $\sim 48^\circ$, respectively. The difference between individual nanoparticle surface densities was $\sim 1.5^\circ$. Selenium nanoparticles can slightly increase the contact angle of TiO₂ surfaces as was previously reported [41] and this effect was also retained after the UV irradiation.

X-ray photoelectron spectroscopy of selenium decorated TiO₂ nanotubes was done to confirm the presence selenium in the samples. There was no significant change in bonding states of Ti2p and O1s after the decoration with nanoparticles. The XPS quantitative analysis of selected elements was summarized in Table 1. The percentage of selenium Se3d proportionally

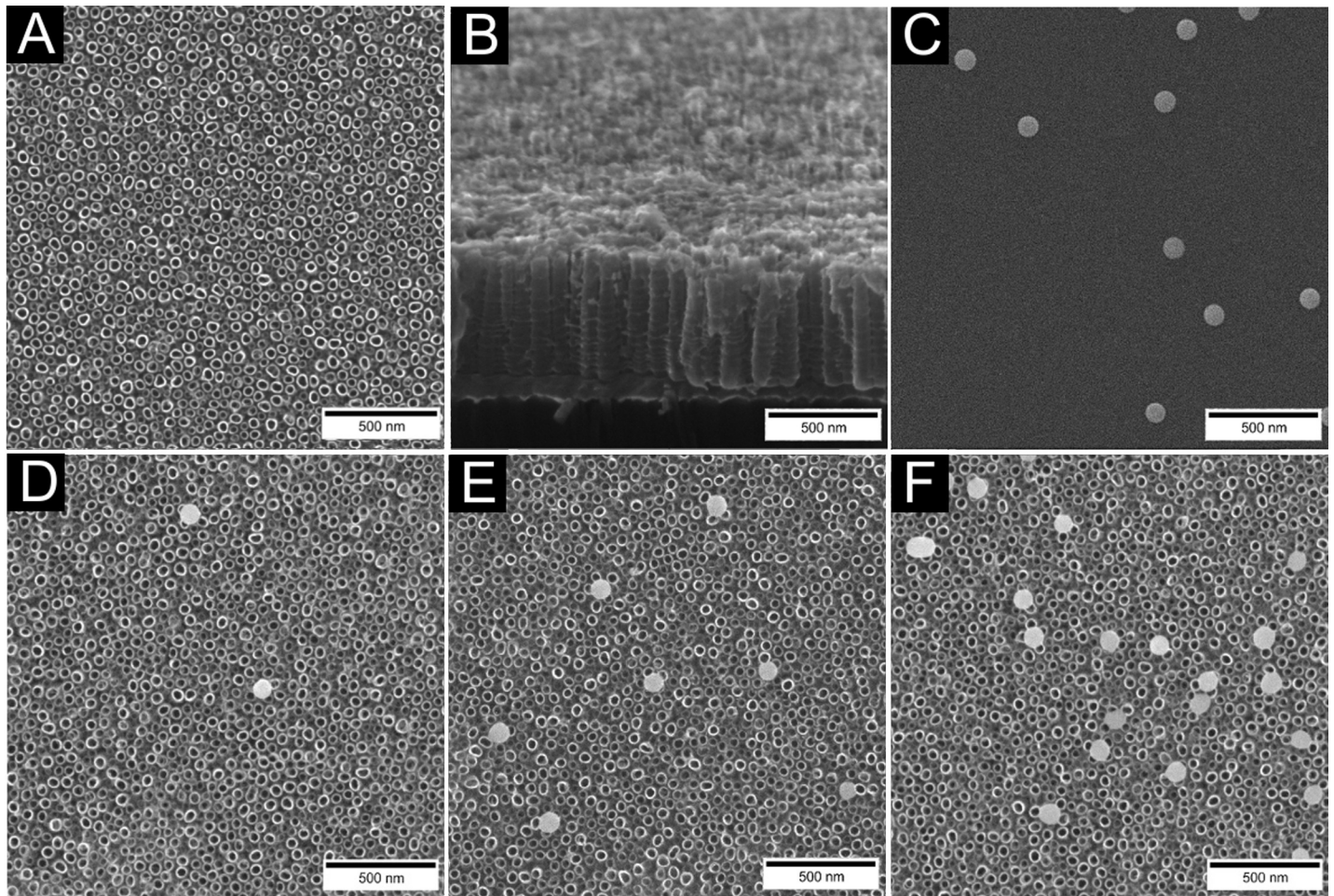


Fig 2. SEM images of fabricated nanostructures. Annealed TiO₂ nanotubes (A), their cross section (B), and selenium nanoparticles (C). TiO₂ nanotubes decorated with Se-Low (D), Se-Medium (E) and Se-High (F) concentrations of nanoparticles.

<https://doi.org/10.1371/journal.pone.0214066.g002>

increased with increasing surface density of nanoparticles. We also observed a peak corresponding to the presence of sulfur. The sulfur peak was observed for all nanoparticle decorated samples even after multiple washing steps and 24 hours immersion in ultrapure water. It could

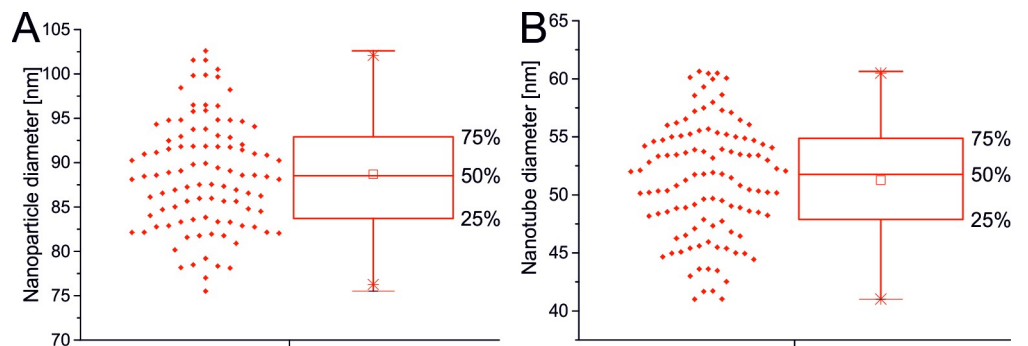


Fig 3. Boxplot of normal size distributions of nanoparticle (A) and nanotube (B). Both the boxplot and Shapiro-Wilk test of normality suggested normal distributions.

<https://doi.org/10.1371/journal.pone.0214066.g003>

Table 1. XPS analysis of selenium decorated TiO₂ nanotubes. Relative percentage of selected elements calculated from narrow spectra.

	TNTs [%]	Se-Low [%]	Se-Medium [%]	Se-High [%]
O1s	55,93	56,12	55,89	51,92
Ti2p	12,75	11,69	11,98	11,11
C1s	31,31	32,19	31,76	35,24
Se3d	0,00	0,08	0,46	1,73

<https://doi.org/10.1371/journal.pone.0214066.t001>

correspond with the adsorption of glutathione, or other product of reaction containing sulfur on the fabricated surface.

The ICP-MS analysis introduce powerful and sensitive technique capable of detecting metals and several non-metals at concentrations as low as one part in 10¹⁵ (part per quadrillion, ppq). We used this technique to obtain the release profile of selenium from the nanotube surface. The analysis showed the minimal release rate of selenium at maximum tens of ppb (Fig 4), suggesting a strong bond between SeNPs and nanotubes. The biggest contribution to the total release was during the first 24 hours, which can be still attributed to the washing selenium out from the nanotubes. Over period of time, the released amount of selenium steadily decreased. Samples were then checked with SEM microscope. Compared to images taken before the measurement, no significant difference in SeNP surface density was found. Further, the release rate was significantly lower than in research done by Liu et al. [29], in which authors attributed the importance of release to the cytotoxicity of selenium. The question is whether such a low concentration of selenium can result in the toxicity for some bacteria and tissue cells. Taking into the consideration it beneficial properties in the human body at higher concentration than our measurable ppb values, we believe that there is another mechanism of toxicity via the interaction of cell membrane with combination of nanoparticle and nanotube properties, nanoparticle size and surface density.

Antibacterial properties of Se NPs—TiO₂ nanotubes

To protect the adhesion and proliferation of pathogenic bacteria on biomaterials consist in coatings with antibiotics, biocidal agents or antibacterial nanoparticles. Selenium nanoparticles are well-known for antibacterial properties to the wide range of bacteria even if the mechanism of action is still unknown [42]. It has been reported by Tran et al. [30] that selenium nanoparticles inhibited the growth of gram-positive *Staphylococcus aureus*. Liu et al. [29] incorporated these nanoparticles into TNTs to enhance the antibacterial activity of TNT surface to *Escherichia coli* with 50% efficiency compared to bare TNTs in 24 hours. In our experiment, we compared the antibacterial efficiency of selenium decorated TiO₂ nanotubes at different selenium nanoparticle surface density against *E. coli* in a short four-hour incubation. Compared to the bare nanotubes, selenium decorated TNTs exhibited enhanced antibacterial properties (Fig 5). Short time interaction of surface with bacteria was efficient to decrease the number of *E. coli* colonies for Se-Low and Se-High about 60% and 90%, respectively. Even if we confirmed the antibacterial properties of Se-TNTs surface, the question is whether bacteria were killed by selenium release in ppb concentration, as indicated by ICP-MS at the first 24 hours or by the nanoscale surface topography and chemistry of Se-TiO₂-TNTs which can be non-adhesive, anti-proliferative or membrane damaging for some bacteria [29, 30, 36, 43]. Selenium nanoparticles and TiO₂ are negatively charged at physiological pH and thus repulsive for the negatively charged membrane of *E. coli* [44]. This might also suggest the inhibition mechanism of *E. coli* adhesion and proliferation on Se-TiO₂-TNTs surface at a short time incubation.

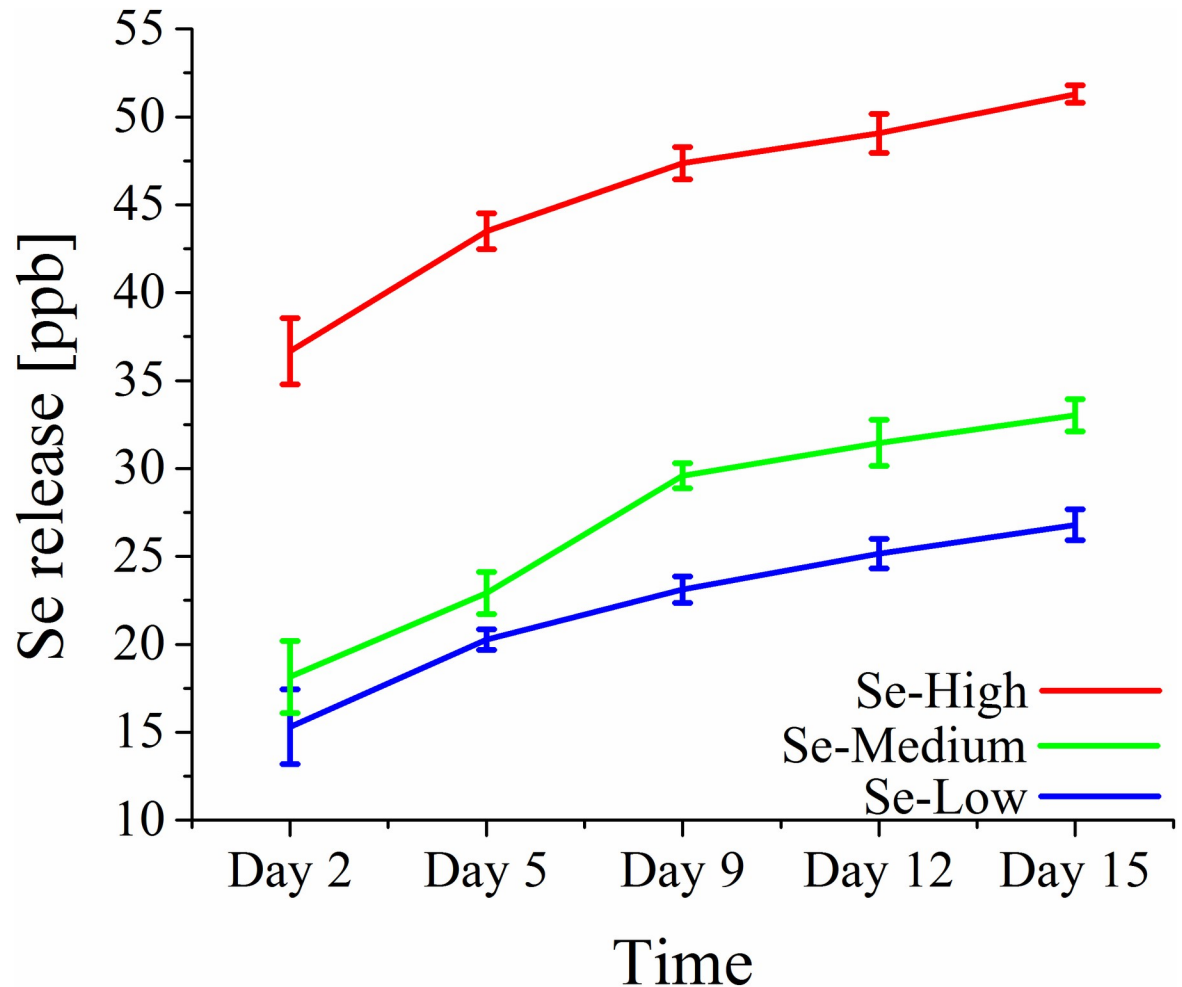


Fig 4. The cumulative release profile of selenium. Individual samples were measured with ICP-MS technique. Measured release was highly dependent on initial SeNPs concentrations.

<https://doi.org/10.1371/journal.pone.0214066.g004>

Viability assay of normal and cancer cells

Adhesion plays a fundamental role in cell development, differentiation, communication and migration, and during the pathogenesis of a wide range of diseases including cancer [45], osteoporosis [46], and atherosclerosis [47]. The strength of cell adhesion to substrate is a crucial consideration in biomaterial design and development. On the other hand, selenium is known to be involved in anti-cancer activity while protecting the benign cells [27, 28, 32, 48]. Thus we studied the effect of selenium nanoparticle decorated TiO₂ nanotubes on adhesion and proliferation of cancer (MG-63 cells) and normal (NIH/3T3 cells) cells. The adhesion and morphology of both cells was qualitatively evaluated by taking DIC images 3 and 24 hours after cell seeding as shown in Fig 6. The NIH/3T3 cells adhered on control TNTs and Se-Low TNTs surface with fibroblastic well spread elongated morphology. Se-Medium surface showed a little deterioration in cells morphology turning the elongated morphology to the rounded shape but still well adhered. The NIH/3T3 cells on Se-High surface were completely round in shape with obvious apoptotic cells. The unfavorable conditions reflecting the change in cell morphology resulted in lower number of attached cells. The similar effect of selenium decorated nanotubes was observed for adhesion and morphology of cancerous MG-63 cells (Fig 6). These cells at

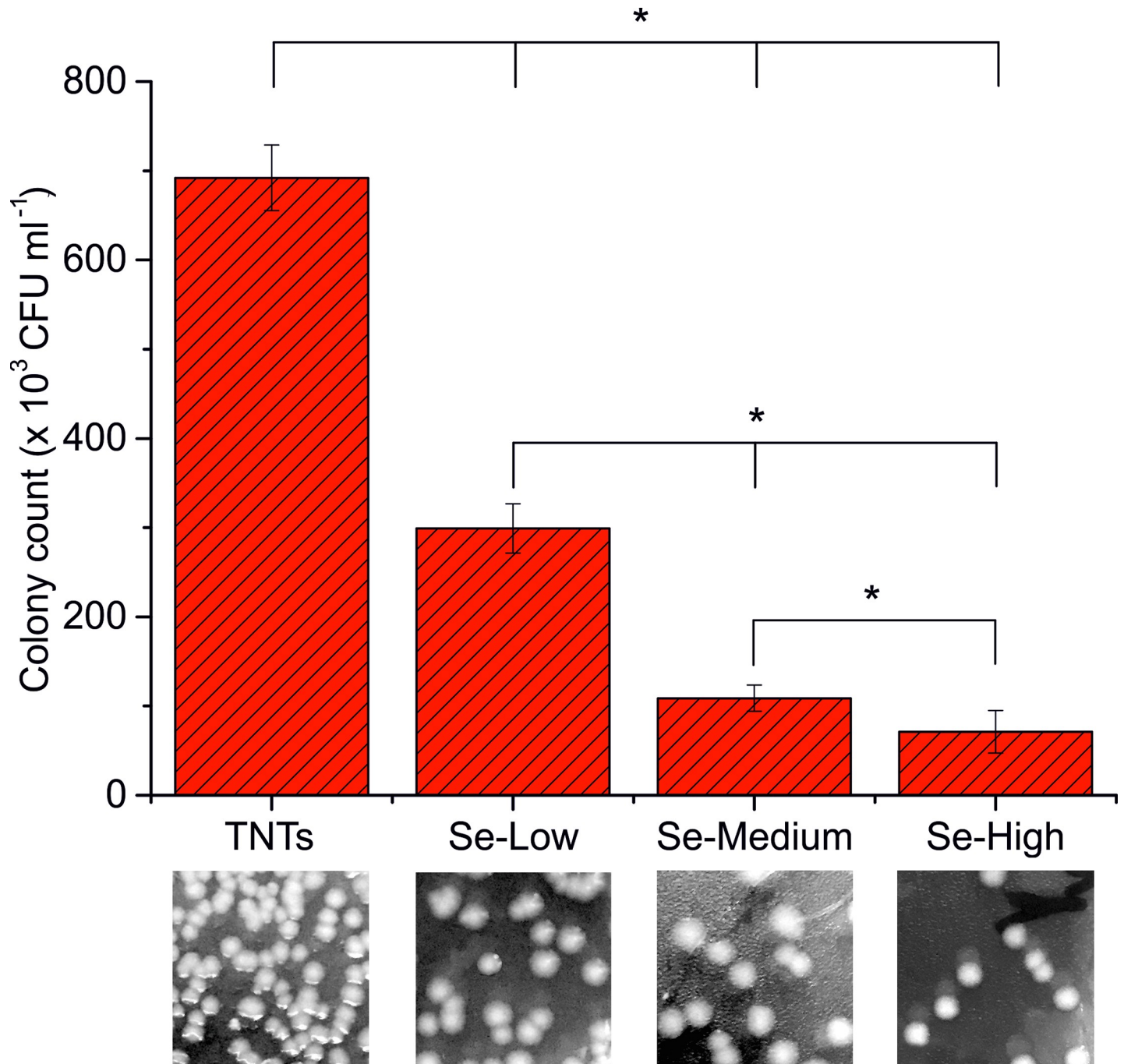


Fig 5. Bacterial assay of viability expressed in colony forming units. Se nanoparticle decorated TiO₂ -TNTs were exposed to gram negative bacteria *E. coli* for 4 hours and the antibacterial effect Se-TNTs was compared with undecorated TNTs. * indicates significant difference between compared samples (p = 0.05).

<https://doi.org/10.1371/journal.pone.0214066.g005>

the day 1 attached to the control and Se-Low surfaces but exhibited more rounded shape compared to the noncancerous cells (Fig 6). Cell adhesion experiment demonstrated that the selenium nanoparticle decorated TiO₂ nanotubes caused unfavorable conditions for cancer MG-63 and normal NIH/3T3 cells, particularly at Se-Medium and Se-High TNTs surface, compared to the control TNTs and Se-Low surface. In order to know whether these microscopic

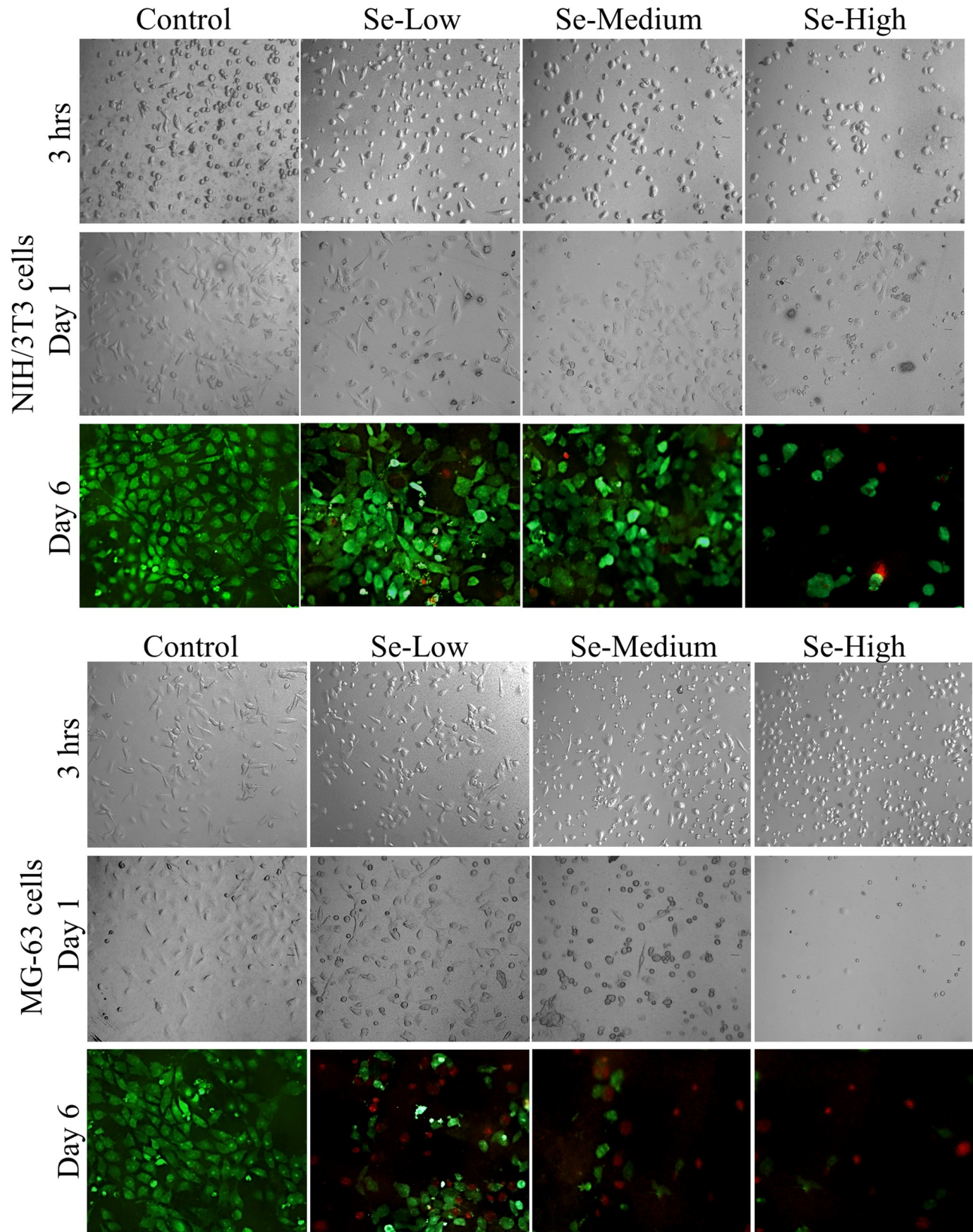


Fig 6. Adhesion and morphology of MG-63 (cancer) and NIH/3T3 (normal) cells cultured on Se-NPs decorated TiO₂ nanotubes. DIC images were taken after 3 and 24 hours cultivation. Live/dead staining of cells was performed with calcein (green color) and propidium iodide (red color) at the day 6.

<https://doi.org/10.1371/journal.pone.0214066.g006>

observations were not done by the slow adhesion rate, we performed proliferation assay by measurement of cellular activity using XTT assay. Our results with NIH/3T3 cells suggested that there was no significant difference in proliferation rate at day 1 and 2 for Se-Low and Se-Medium TNTs surfaces compared to the control group (Fig 7A). At the day 6, XTT assay showed increased proliferation rate of NIH/3T3 cells. The decreasing tendency of measured values at this day towards Se-Medium can be attributed to the slower adhesion, activity or proliferation of cells on such surfaces. Anyway, the Se-Low and Se-Medium surface promoted activity and proliferation of NIH/3T3 cells. Proliferation rate in NIH/3T3 cells cultured on Se-High TNTs surface was significantly decreased at day 1, 2 and 6. It came out from the smaller initial number of cells adhered well on Se-High surface as observed with adhesion assay and suggests that this selenium nanoparticle surface density was not compatible with the adhesion and proliferation of noncancerous NIH/3T3 cells compared to the Se-lower surface densities and control TNTs surfaces. The similar results were obtained for the cancerous MG-63 cells (Fig 7B). The unfavorable effect of selenium nanoparticle density for cancerous cells was stronger at Se-Medium surface compared to the noncancerous cells and maximal at Se-High surface. We can also observe from our results that MG-63 cells did not adhere well selenium decorated surfaces but when adhered, they did not increase activity or proliferation rate since no significant change in absorbance was observed at day 6 compared to day 1 and 2. Finally, we did live/dead staining of both cells to check the viability of cells at the day 6. The images (Fig 6) confirmed our quantitative results obtained from the proliferation test. The cancerous cells gradually detached the selenium decorated surface and compared with the control, mostly dying cells occurred attached the surface (Fig 6, red color). Fibroblasts showed significant decrease in a number of adhered cells on Se-High surface and a few dying cells on Se-Medium surface which again supported our results from proliferation assay.

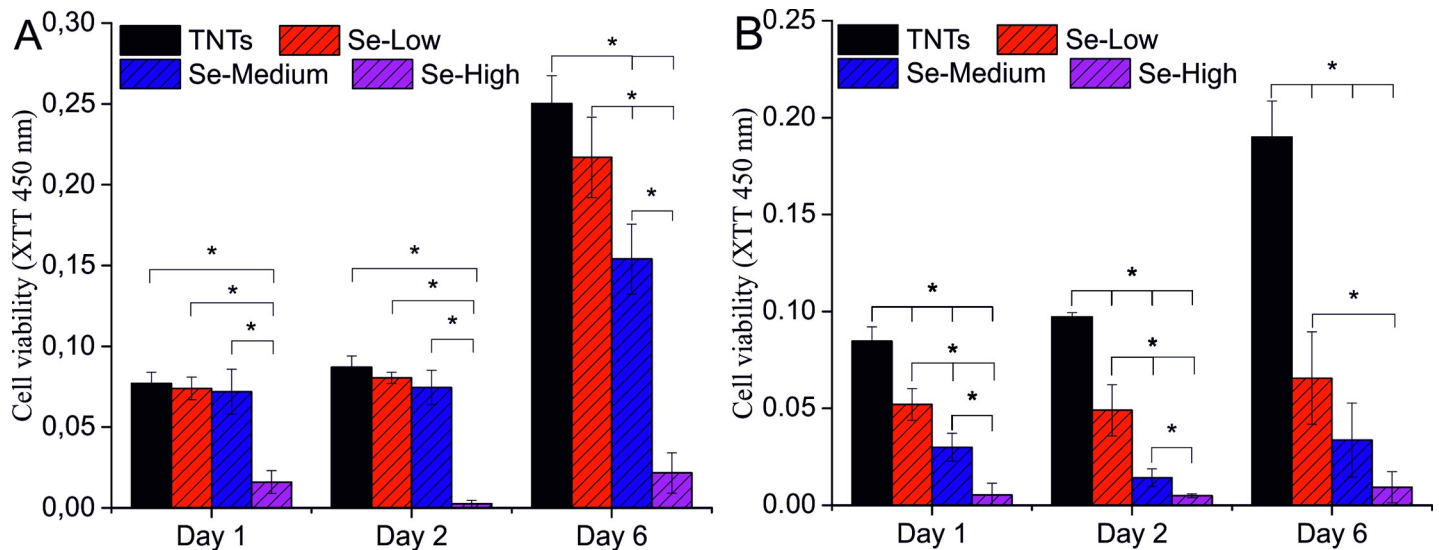


Fig 7. XTT viability assay of MG-63 (B) and NIH/3T3 (A) cells cultured on Se-NPs decorated TiO₂ nanotubes. * indicates significant difference between compared samples ($p = 0.05$).

<https://doi.org/10.1371/journal.pone.0214066.g007>

Our observation is consistent with other similar report of Chen et al. [28] in which the selenium nanoparticles released from TiO₂ nanotubes and diffused through the chitosan layer, decreased adhesion and viability of cancerous osteoblasts. Other reports suggesting selenium as a promising and favorable for noncancerous cells [28, 32] was not confirmed in our experiments since the Se-High TNTs surface was significantly suppressing the noncancerous NIH/3T3 cells adhesion and viability. To conclude these results, the exact mechanism that makes the anti-cancer action of selenium work is still a subject of research as well as much work must be done regarding the influence of selenium towards noncancerous cells. However, selenium nanoparticle decorated TiO₂ nanotubes can be promising biomaterial surface for tissue engineering since the mechanisms of action combining the antibacterial selenium nanoparticles and nanostructured TiO₂ surface is still unknown.

Conclusion

In this paper, TiO₂ nanotubes with $51,72 \pm 5,55$ nm diameter decorated with different surface densities of spherical selenium nanoparticles with $88,93 \pm 6,87$ nm diameter were fabricated via anodic oxidation and characterized with SEM, XPS and AFM. The release rate of selenium measured with ICP-MS was found out very low for a long period of time, which indicates for the strong and stable adsorption of selenium nanoparticles on TiO₂ nanotubes. The antibacterial activity of Se-NPs decorated TNTs was significantly enhanced in 4 hours incubation for gram negative *E. coli* which suggest the strong antibacterial effect of selenium compared to the bare TNTs surface. The cell adhesion and proliferation of cancerous MG-63 cells was obviously decreased on selenium decorated surface, confirming the anti-cancer activity of selenium compared to the bare TiO₂ nanotubes. The NIH/3T3 fibroblasts adhered and proliferated on bare, Se-Low and Se-Medium TNTs surfaces. The Se-High surface density of nanoparticles was found to be incompatible with NIH/3T3 cell adhesion and proliferation. Therefore, it is important and desirable to find an optimal surface density of selenium nanoparticles to be decorated on TiO₂ nanotubes including the nanoparticle and nanotube diameters that effectively kill bacteria, cancer cells and remains favorable to the normal cells.

Supporting information

S1 File. Individual datasets. File contains raw data from which the graphs were drawn. (DOCX)

Acknowledgments

Research described in this paper was financed by Czech Ministry of Education in frame of National Sustainability Program under grant LO1401. For research, infrastructure of the SIX Center was used.

Author Contributions

Formal analysis: Ondrej Bilek.

Investigation: Ondrej Bilek, Zdenka Fohlerova.

Methodology: Ondrej Bilek.

Supervision: Jaromir Hubalek.

Writing – original draft: Ondrej Bilek.

Writing – review & editing: Zdenka Fohlerova, Jaromir Hubalek.

References

1. Lamers E, Horssen Rv, Riet Jt, Delft Fv, Lutttge R, Walboomers XF, et al. The influence of nanoscale topographical cues on initial osteoblast morphology and migration. *Eur Cells Mater.* 2010;329–43.
2. Oh S, Daraio C, Chen L-H, Pisanic TR, Fiñones RR, Jin S. Significantly accelerated osteoblast cell growth on aligned TiO₂ nanotubes. *J Biomed Mater Res, Part A.* 2006; 78A(1):97–103.
3. Kummer KM, Taylor E, Webster TJ. Biological applications of anodized TiO₂ nanostructures: a review from orthopedic to stent applications. *Nanosci Nanotechnol Lett.* 2012; 4(5):483–93.
4. Park J, Bauer S, von der Mark K, Schmuki P. Nanosize and vitality: TiO₂ nanotube diameter directs cell fate. *Nano Lett.* 2007; 7(6):1686–91. <https://doi.org/10.1021/nl070678d> PMID: 17503870
5. Fohlerova Z, Mozalev A. Tuning the response of osteoblast-like cells to the porous-alumina-assisted mixed-oxide nano-mound arrays. *Journal of biomedical materials research Part B, Applied biomaterials.* 2018; 106(5):1645–54. <https://doi.org/10.1002/jbm.b.33971> PMID: 28837748
6. Tam KH, Djurišić AB, Chan CMN, Xi YY, Tse CW, Leung YH, et al. Antibacterial activity of ZnO nanorods prepared by a hydrothermal method. *Thin Solid Films.* 2008; 516(18):6167–74.
7. Kang S, Herzberg M, Rodrigues DF, Elimelech M. Antibacterial Effects of Carbon Nanotubes: Size Does Matter! *Langmuir.* 2008; 24(13):6409–13. <https://doi.org/10.1021/la800951v> PMID: 18512881
8. Lan M-Y, Liu C-P, Huang H-H, Lee S-W. Both enhanced biocompatibility and antibacterial activity in Ag-decorated TiO₂ nanotubes. *PLoS One.* 2013; 8(10):e75364. <https://doi.org/10.1371/journal.pone.0075364> PMID: 24124484
9. Brammer KS, Oh S, Cobb CJ, Bjursten LM, Heyde Hvd, Jin S. Improved bone-forming functionality on diameter-controlled TiO₂ nanotube surface. *Acta Biomater.* 2009; 5(8):3215–23. <https://doi.org/10.1016/j.actbio.2009.05.008> PMID: 19447210
10. Geetha M, Singh AK, Asokamani R, Gogia AK. Ti based biomaterials, the ultimate choice for orthopaedic implants—a review. *Prog Mater Sci.* 2009; 54(3):397–425.
11. Liu X, Chu PK, Ding C. Surface modification of titanium, titanium alloys, and related materials for biomedical applications. *Materials Science and Engineering: R: Reports.* 2004; 47(3):49–121.
12. Brammer KS, Frandsen CJ, Jin S. TiO₂ nanotubes for bone regeneration. *Trends Biotechnol.* 2012; 30(6):315–22. <https://doi.org/10.1016/j.tibtech.2012.02.005> PMID: 22424819
13. Popat KC, Leoni L, Grimes CA, Desai TA. Influence of engineered titania nanotubular surfaces on bone cells. *Biomaterials.* 2007; 28(21):3188–97. <https://doi.org/10.1016/j.biomaterials.2007.03.020> PMID: 17449092
14. Oh S, Brammer KS, Li YJ, Teng D, Engler AJ, Chien S, et al. Stem cell fate dictated solely by altered nanotube dimension. *Proc Natl Acad Sci.* 2009; 106(7):2130–5. <https://doi.org/10.1073/pnas.0813200106> PMID: 19179282
15. Park J, Bauer S, Schmuki P, von der Mark K. Narrow Window in Nanoscale Dependent Activation of Endothelial Cell Growth and Differentiation on TiO₂ Nanotube Surfaces. *Nano Lett.* 2009; 9(9):3157–64. <https://doi.org/10.1021/nl9013502> PMID: 19653637
16. Bauer S, Park J, Faltenbacher J, Berger S, von der Mark K, Schmuki P. Size selective behavior of mesenchymal stem cells on ZrO₂ and TiO₂ nanotube arrays. *Integr Biol.* 2009; 1(8–9):525–32.
17. Zhang H, Sun Y, Tian A, Xue XX, Wang L, Alquhali A, et al. Improved antibacterial activity and biocompatibility on vancomycin-loaded TiO₂ nanotubes: in vivo and in vitro studies. *Int J Nanomed.* 2013; 8:4379.
18. Popat KC, Eltgroth M, LaTempa TJ, Grimes CA, Desai TA. Decreased Staphylococcus epidermis adhesion and increased osteoblast functionality on antibiotic-loaded titania nanotubes. *Biomaterials.* 2007; 28(32):4880–8. <https://doi.org/10.1016/j.biomaterials.2007.07.037> PMID: 17697708
19. Li J, Zhou H, Qian S, Liu Z, Feng J, Jin P, et al. Plasmonic gold nanoparticles modified titania nanotubes for antibacterial application. *Appl Phys Lett.* 2014; 104(26):261110.
20. Yang T, Qian S, Qiao Y, Liu X. Cytocompatibility and antibacterial activity of titania nanotubes incorporated with gold nanoparticles. *Colloids Surf, B.* 2016; 145:597–606.
21. Mei S, Wang H, Wang W, Tong L, Pan H, Ruan C, et al. Antibacterial effects and biocompatibility of titanium surfaces with graded silver incorporation in titania nanotubes. *Biomaterials.* 2014; 35(14):4255–65. <https://doi.org/10.1016/j.biomaterials.2014.02.005> PMID: 24565524
22. Liu W, Su P, Chen S, Wang N, Ma Y, Liu Y, et al. Synthesis of TiO₂ nanotubes with ZnO nanoparticles to achieve antibacterial properties and stem cell compatibility. *Nanoscale.* 2014; 6(15):9050–62. <https://doi.org/10.1039/c4nr01531b> PMID: 24971593
23. Kumeria T, Mon H, Aw MS, Gulati K, Santos A, Griesser HJ, et al. Advanced biopolymer-coated drug-releasing titania nanotubes (TNTs) implants with simultaneously enhanced osteoblast adhesion and antibacterial properties. *Colloids Surf, B.* 2015; 130:255–63.

24. Kim H-W, Koh Y-H, Li L-H, Lee S, Kim H-E. Hydroxyapatite coating on titanium substrate with titania buffer layer processed by sol-gel method. *Biomaterials*. 2004; 25(13):2533–8. PMID: [14751738](#)
25. Subramani K, Ahmed W. Chapter 7—Titanium Nanotubes as Carriers of Osteogenic Growth Factors and Antibacterial Drugs for Applications in Dental Implantology. In: Subramani K, Ahmed W, editors. *Emerging Nanotechnologies in Dentistry*. Boston: William Andrew Publishing; 2012. p. 103–11.
26. Tapiero H, Townsend DM, Tew KD. The antioxidant role of selenium and seleno-compounds. *Biomed Pharmacother*. 2003; 57(3):134–44.
27. El-Bayoumy K. The protective role of selenium on genetic damage and on cancer. *Mutat Res, Fundam Mol Mech Mutagen*. 2001; 475(1):123–39.
28. Chen X, Cai K, Fang J, Lai M, Hou Y, Li J, et al. Fabrication of selenium-deposited and chitosan-coated titania nanotubes with anticancer and antibacterial properties. *Colloids Surf, B*. 2013; 103:149–57.
29. Liu W, Golshan NH, Deng X, Hickey DJ, Zeimer K, Li H, et al. Selenium nanoparticles incorporated into titania nanotubes inhibit bacterial growth and macrophage proliferation. *Nanoscale*. 2016; 8(34):15783–94. <https://doi.org/10.1039/c6nr04461a> PMID: [27533297](#)
30. Tran PA, Webster TJ. Selenium nanoparticles inhibit *Staphylococcus aureus* growth. *Int J Nanomed*. 2011; 6:1553.
31. Tran PA, Webster TJ. Antimicrobial selenium nanoparticle coatings on polymeric medical devices. *Nanotechnology*. 2013; 24(15):155101. <https://doi.org/10.1088/0957-4484/24/15/155101> PMID: [23519147](#)
32. Tran P, Webster TJ. Enhanced osteoblast adhesion on nanostructured selenium compacts for anti-cancer orthopedic applications. *Int J Nanomed*. 2008; 3(3):391.
33. El-Ghazaly M, Fadel N, Rashed E, El-Batal A, Kenawy S. Anti-inflammatory effect of selenium nanoparticles on the inflammation induced in irradiated rats. *Can J Physiol Pharmacol*. 2016; 95(2):101–10. <https://doi.org/10.1139/cjpp-2016-0183> PMID: [27936913](#)
34. Shurygina IA, Shurygin MG. *Nanoparticles in Wound Healing and Regeneration. Metal Nanoparticles in Pharma*: Springer; 2017. p. 21–37.
35. Shakibaie M, Forootanfar H, Golkari Y, Mohammadi-Khorsand T, Shakibaie MR. Anti-biofilm activity of biogenic selenium nanoparticles and selenium dioxide against clinical isolates of *Staphylococcus aureus*, *Pseudomonas aeruginosa*, and *Proteus mirabilis*. *J Trace Elem Med Biol*. 2015; 29:235–41. <https://doi.org/10.1016/j.jtemb.2014.07.020> PMID: [25175509](#)
36. Huang X, Chen X, Chen Q, Yu Q, Sun D, Liu J. Investigation of functional selenium nanoparticles as potent antimicrobial agents against superbugs. *Acta Biomater*. 2016; 30:397–407. <https://doi.org/10.1016/j.actbio.2015.10.041> PMID: [26518106](#)
37. Forootanfar H, Adeli-Sardou M, Nikkhoo M, Mehrabani M, Amir-Heidari B, Shahverdi AR, et al. Antioxidant and cytotoxic effect of biologically synthesized selenium nanoparticles in comparison to selenium dioxide. *J Trace Elem Med Biol*. 2014; 28(1):75–9. <https://doi.org/10.1016/j.jtemb.2013.07.005> PMID: [24074651](#)
38. Raafat D, Sahl HG. Chitosan and its antimicrobial potential—a critical literature survey. *Microb Biotechnol*. 2009; 2(2):186–201. <https://doi.org/10.1111/j.1751-7915.2008.00080.x> PMID: [21261913](#)
39. Cheung RCF, Ng TB, Wong JH, Chan WY. Chitosan: an update on potential biomedical and pharmaceutical applications. *Mar Drugs*. 2015; 13(8):5156–86. <https://doi.org/10.3390/md13085156> PMID: [26287217](#)
40. Příkrylová K, Drbohlavová J, Svatoš V, Gablech I, Kalina L, Pytlíček Z, et al. Fabrication of highly ordered short free-standing titania nanotubes. *Monatsh Chem*. 2016; 147(5):943–9.
41. Tran PA, Webster TJ. Understanding the wetting properties of nanostructured selenium coatings: the role of nanostructured surface roughness and air-pocket formation. *Int J Nanomed*. 2013; 8:2001–9.
42. Stolzoff M, Wang S, Webster T, editors. Efficacy and mechanism of selenium nanoparticles as antibacterial agents. *Front Bioeng Biotechnol Conference Abstract: 10th World Biomaterials Congress 103389/conf FBIOE*; 2016.
43. Gallo J, Holinka M, Moucha CS. Antibacterial Surface Treatment for Orthopaedic Implants. *Int J Mol Sci*. 2014; 15(8):13849–80. <https://doi.org/10.3390/ijms150813849> PMID: [25116685](#)
44. Tran PA, O'Brien-Simpson N, Reynolds EC, Pantarat N, Biswas DP, O'Connor AJ. Low cytotoxic trace element selenium nanoparticles and their differential antimicrobial properties against *S. aureus* and *E. coli*. *Nanotechnology*. 2015; 27(4):045101. <https://doi.org/10.1088/0957-4484/27/4/045101> PMID: [26656836](#)
45. Bendas G, Borsig L. Cancer cell adhesion and metastasis: selectins, integrins, and the inhibitory potential of heparins. *Int J Cell Biol*. 2012;2012.

46. Perinpanayagam H, Zaharias R, Stanford C, Brand R, Keller J, Schneider G. Early cell adhesion events differ between osteoporotic and non-osteoporotic osteoblasts. *J Orthop Res*. 2001; 19(6):993–1000. [https://doi.org/10.1016/S0736-0266\(01\)00045-6](https://doi.org/10.1016/S0736-0266(01)00045-6) PMID: 11781027
47. Blankenberg S, Barbaux S, Tiret L. Adhesion molecules and atherosclerosis. *Atherosclerosis*. 2003; 170(2):191–203. PMID: 14612198
48. Rayman MP. Selenium in cancer prevention: a review of the evidence and mechanism of action. *Proc Nutr Soc*. 2005; 64(4):527–42. PMID: 16313696

Článek 2

Antibacterial activity of AgNPs-TiO₂ nanotubes: influence of different nanoparticle stabilizers


 Cite this: *RSC Adv.*, 2020, 10, 44601

Antibacterial activity of AgNPs–TiO₂ nanotubes: influence of different nanoparticle stabilizers

 Ondrej Bilek,^a Tatiana Fialova,^b Alexandr Otahal,^c Vojtech Adam,^{id} ^{ab}
 Kristyna Smerkova^{ab} and Zdenka Fohlerova^{id} ^{*acd}

Enhanced antibacterial properties of nanomaterials such as TiO₂ nanotubes (TNTs) and silver nanoparticles (AgNPs) have attracted much attention in biomedicine and industry. The antibacterial properties of nanoparticles depend, among others, on the functionalization layer of the nanoparticles. However, the more complex information about the influence of different functionalization layers on antibacterial properties of nanoparticle decorated surfaces is still missing. Here we show the array of ~50 nm diameter TNTs decorated with ~50 nm AgNPs having different functionalization layers such as polyvinylpyrrolidone, branched polyethyleneimine, citrate, lipoic acid, and polyethylene glycol. To assess the antibacterial properties, the viability of Gram-positive (*Staphylococcus aureus*) and Gram-negative bacteria (*Escherichia coli* and *Pseudomonas aeruginosa*) has been assessed. Our results showed that the functional layer of nanoparticles plays an important role in antibacterial properties and the synergistic effect such nanoparticles and TiO₂ nanotubes have had different effects on adhesion and viability of G⁻ and G⁺ bacteria. These findings could help researchers to optimally design any surfaces to be used as an antibacterial including the implantable titanium biomaterials.

 Received 25th August 2020
 Accepted 1st December 2020

DOI: 10.1039/d0ra07305a

rsc.li/rsc-advances

Introduction

Antibacterial properties of metals,¹ metal oxides² and alloys³ have found significant use in clinics and industry. The protection of medical and surgical devices, clothes, or implantable materials from the growth and colonization of bacteria becomes the key factor for avoiding the transmission of infectious diseases or the acceptance of foreign materials in the host body.⁴ However, bacterial contamination, resistance to antibiotics, and the development of biofilms still pose hard-to-solve problems with many implants and medical devices.

The inhibition of bacterial adhesion and growth comes from the natural antibacterial properties of materials such as copper, titanium, zinc, silver, and their alloys.⁵ Nevertheless, many materials must be extra-modified to introduce the antibacterial coating based on chemically attached antibacterial peptides,⁶ metal oxides,² organosilanes⁷ or polymers⁸ in order to inhibit the bacteria adhesion, growth and plaque formation. Besides, bacteria can also be killed based on photocatalytic properties of specific materials that have been successfully applied in water

purification or air cleaning.⁹ The inorganic nanomaterials such as metal/metal oxide nanoparticles (NPs) and the nanostructured surface of metallic biomaterials have a great impact on their ability to be utilized for the bacterial growth inhibition and the prevention of biofilm formation that protects bacteria against antibiotics.¹⁰ The NPs size and shape¹¹ and the topography of the nanostructured surface, including the type of the material can effectively modulate the antibacterial properties.¹² Nevertheless, the mechanism of action is still being under the investigation. Some proposed theories speak about dissolved metal ion toxicity or generation of reactive oxygen species on the nanomaterial surface.¹³ Apart from these, the anti-adhesive surface may arise from the morphological and physico-chemical properties of materials.¹⁴ Even if the antibacterial properties of specific nanoparticles synthesized from Ag, Ti, Au, Zn, and its oxides are well known against both Gram-positive (*Bacillus subtilis*, *Staphylococcus aureus*) and Gram-negative bacteria (*Escherichia coli*, *Pseudomonas aeruginosa*), the impact of nanostructured surfaces has got attention in the last decades.¹⁵

Ti and its alloys have been applied in biomedicine for many years.¹⁶ The smooth surface of titanium implants does not appear to be sufficiently bioactive and suffer from infections and fibrous tissue development. Therefore, the TiO₂ nanotubes with nanoscaled topography become an interesting nanomaterial to be recognized as an attractive and promising for biomedicine.^{17,18} TNTs have been found to have good corrosion resistance, biocompatibility, hemocompatibility, and enhanced

^aCentral European Institute of Technology, Brno University of Technology, Purkynova 123, Brno, Czech Republic. E-mail: zdenka.fohlerova@ceitec.vutbr.cz

^bDepartment of Chemistry and Biochemistry, Mendel University in Brno, Zemedelska 1, Brno, Czech Republic

^cDepartment of Microelectronics, Brno University of Technology, Technicka 10, Brno, Czech Republic

^dDepartment of Biochemistry, Faculty of Medicine, Masaryk University, Kamenice 753/5, 625 00 Brno, Czech Republic


bioactivity.^{19,20} Moreover, a nanostructured surface can modulate the protein adsorption and cellular responses such as adhesion, proliferation, or differentiation and antibacterial properties.²¹ In a positive way, the enhanced or stimulated biological response due to the nanostructured TiO₂ surface may be considered to mimic the natural cellular environment.

The TNTs have been demonstrated to be a promising platform for a drug loading and delivery administration.²² The simple and controllable fabrication of highly ordered TNTs *via* electrochemical anodization process has been found to perform tunable drug-release of vancomycin²³ or gentamicin.²⁴ In addition to antibiotics loading, the doping with strontium and samarium²⁵ or decoration with nanoparticles such as gold,^{26,27} zinc oxide,²⁸ selenium,^{29,30} and silver^{31,32} have been demonstrated to enhance the antibacterial properties of TNTs.^{33–38} The antimicrobial properties of nanoparticles depend on the surface charge, nanoparticle size, shape, and surface coating (stabilizers/functional layers). Lately, the role of nanoparticle surface coatings became more apparent.³⁹ To date, colloidal nanoparticles with different surface coatings have been synthesized and evaluated for their antibacterial action.^{40,41} However, the antibacterial properties of a free and decorated nanoparticles are supposed to significantly differ. To our knowledge, there is no information about the synergistic antibacterial effect of TiO₂ nanotubes and Ag nanoparticles with different functional layers.

In our work, the array of ~50 nm diameter TiO₂ nanotubes has been fabricated *via* anodic oxidation of polished titanium foil. Subsequently, the nanotubes were decorated with commercial silver nanoparticles of ~50 nm diameter. Nanoparticles were functionalized by polyvinylpyrrolidone, branched polyethyleneimine, citrate, lipoic acid and polyethylene glycol. Ag-decorated TNT arrays were characterized by scanning electron microscopy, atomic force microscopy and X-ray

photoelectron spectroscopy. To assess the antibacterial properties, the adhesion and viability of Gram-positive (*S. aureus*) and Gram-negative bacteria (*E. coli* and *P. aeruginosa*) were performed. Our results showed that the functionalization layers of nanoparticles play an important role in antibacterial properties and should be considered when designing antibacterial surfaces.

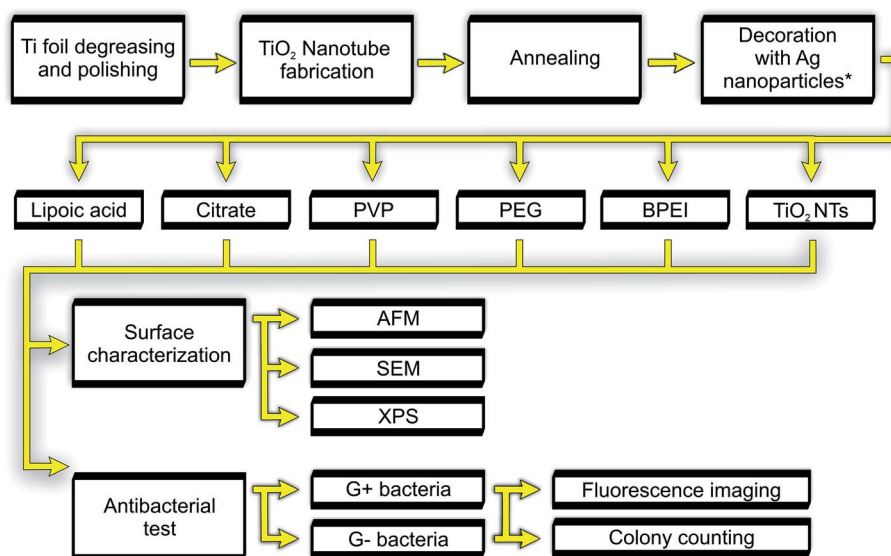
Materials and methods

Anodic oxidation of titanium foil

The 0.125 mm thick titanium foil sheets (GoodFellow, 99.6+%, annealed) were degreased in acetone and isopropyl alcohol and polished with fabric disks and diamond suspension. TiO₂ nanotubes were fabricated by single-step anodic oxidation in the electrolyte solution composed of ethylene glycol (Penta, CZ), 1.2 wt% ammonium fluoride (Sigma Aldrich) and 2 vol% of deionized water (Millipore Corp., USA, 18.2 MΩ).⁴² Electrochemical anodization was performed with a voltage ramp between 0 V and 30 V with a ramp speed of 1 V s⁻¹. The anodization time was 30 minutes per sample. After the anodization, samples were rinsed with deionized water and dried with a nitrogen stream. The TNTs samples were subsequently annealed in a vacuum furnace at 450 °C for 3 hours.

Decoration of TNTs with Ag-NPs

The array of TiO₂ nanotubes was decorated with commercial silver nanoparticles functionalized with polyvinylpyrrolidone (PVP), citrate, branched polyethyleneimine (BPEI), polyethylene glycol (PEG), and lipoic acid (Sigma-Aldrich; 0.02 mg mL⁻¹ stock solutions) as depicted in Fig. 1. Because different nanoparticles exhibited different degree of adsorption rates onto the TiO₂ nanotubes, we optimized the dilution of stock solution for each nanoparticle to achieve the same number of nanoparticles



* with suitable dilution of stock nanoparticle suspension

Fig. 1 General experimental flow chart.



per surface area. Then, 15 μL of diluted nanoparticle suspension was dropped onto the heated TNTs surface until drying. Decorated samples were rinsed five times in deionized water and soaked in ultrapure water to remove any un-adsorbed nanoparticles. The morphology of AgNPs-TNTs array was characterized with scanning electron microscope (SEM, Mira II, Tescan, CZ), surface roughness was analyzed using atomic force microscopy (AFM) in dry non-contact mode (SPM, Dimension Icon, Bruker), and X-ray photoelectron spectroscopy has been used to analyze surface chemistry (XPS, AXIS Supra, Kratos Analytical Ltd, UK). XPS spectra were analyzed by a peak fitting software (CasaXPS version 2.3.18PR1.0) provided by SPECS GmbH (Berlin, Germany).

Bacterial cultures and SEM microscopy

Bacterial strains of *S. aureus* (CCM 4223), *E. coli* (CCM 3954), and *P. aeruginosa* (CCM 3955) were purchased from the Czech Collection of Microorganisms (CZ). After overnight cultivation at 37 °C on blood agar, the strains were diluted in Mueller Hinton broth (Oxoid, UK) to the concentration of 1×10^6 CFU mL^{-1} (where CFU is colony-forming unit), measured by optical density at 600 nm (OD600). To image the bacteria on the TNTs surface using the SEM microscopy, 2 mL of bacterial suspension was dropped on TNTs (control) and AgNPs-TNTs array and incubated at 37 °C for 5 hours. Then, the samples were three-times gently washed with sterile physiological solution. Bacteria were fixated in 2% glutaraldehyde for 1 hour. The dehydration step was performed using graded ethanol concentration of 30%, 50%, 70%, 80%, 90%, 95% and 100%, one time for each and twice in 100% for 15 min each. Dried samples were coated with a 10 nm thick gold layer in order to achieve a better contrast of bacteria.

Antibacterial test

Live/dead fluorescence staining was performed to image and count the live and dead bacteria on the TNTs and AgNPs-TNTs surface. Samples were rinsed with sterile ultrapure water and left to dry in sterile conditions. The dried samples were subsequently placed in sterile 12-well plate, bathed in 2 mL of bacterial inoculum and incubated for 24 hours at 37 °C. After the incubation, samples were washed five times with sterile saline. The staining of bacteria with Live/Dead BacLight Bacterial Viability and Counting Kit (Thermo Fisher Scientific) was performed as recommended by the manufacturer. The samples were observed by inverted fluorescence microscope Olympus IX71 (Olympus, Japan) at a magnification of 20 \times . Captured images were analyzed with ImageJ software. The contrast, brightness, and the displayed range (max, min) were adjusted with the brightness/contrast tool until individual bacteria became clearly visible. The area occupied by red (or green) color was selected using the color threshold and calculated using the measurement module. The value in pixels was divided by the total number of pixels present in the analyzed image, and the area of bacterial coverage (in percentage) specific for live and dead bacteria was calculated.

Antibacterial properties of silver NPs decorated nanotubes were further evaluated *via* colony counting method. A bacterial inoculum with a density of 10^8 CFU mL^{-1} was prepared as the stock solution. Samples were rinsed in sterile water and 100 μL of bacterial suspension was spread onto the surface, followed by 4 hours' incubation at 37 °C. Subsequently, the samples were gently rinsed in PBS and adhered bacteria were de-attached by vortexing and sonication. Collected bacterial suspension was diluted 100 times with PBS. The 200 μL of diluted solution was inoculated on agar plates and incubated for 24 hours at 37 °C and 80% humidity. Bacteria colonies were then counted and colony forming unit was calculated (CFU mL^{-1}).

Statistical analysis

Mean values and standard deviations of obtained data were calculated. Statistically significant differences ($p < 0.05$) were confirmed using Student's *t*-test. All shown data are expressed as the mean \pm standard deviation. Coverage values are calculated from 5 images with the area of $558.7 \times 419 \mu\text{m}$ per each sample and bacterium. Colony counting method was performed in duplicate.

Results and discussion

Characterization of TNTs and AgNPs-TNTs surface

TiO₂ nanotubes decorated with silver nanoparticles were fabricated *via* single-step anodic oxidation of titanium foil, followed by adsorption of commercially available silver nanoparticles of similar diameter but having a different functionalization layer (PVP, BPEI, citrate, PEG and lipoic acid). TNTs array without nanoparticles was taken as a control. SEM image analysis of nanostructured surface resulted in highly ordered TNTs with a diameter of 51.11 ± 5.77 nm as depicted in Fig. 2.

The surface roughness of the undecorated TiO₂ nanotubes was characterized using AFM. Fig. 3A shows the 3D morphology of TNTs. The surface roughness measured by AFM was approximately 24.34 nm. In order to confirm the uniform distribution of Ag nanoparticles on the TNTs surface, several

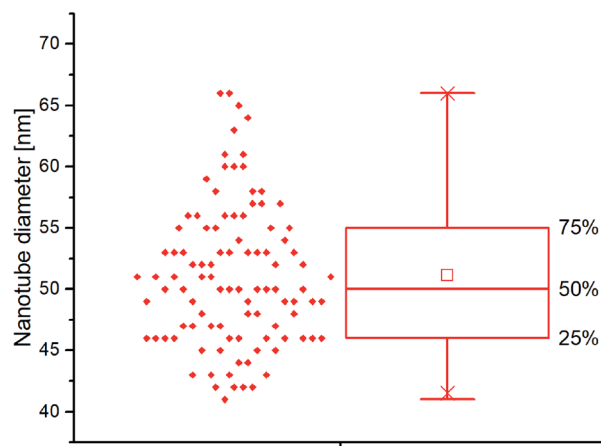


Fig. 2 Boxplot of nanotube diameter distributions calculated from SEM images.



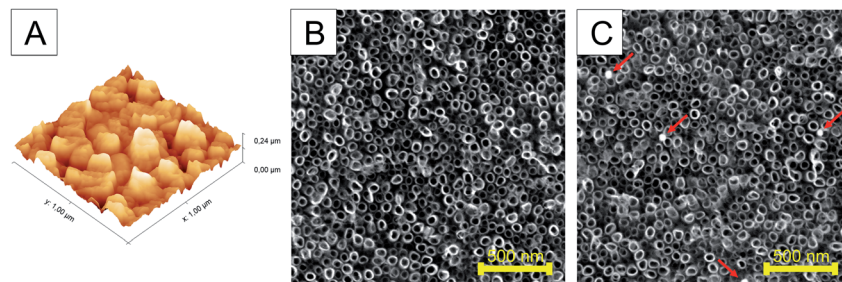


Fig. 3 AFM image showing root-mean-square (RMS) surface roughness of TNTs (A) and SEM image of as-annealed non-decorated TiO₂ nanotubes prepared by single-step anodic oxidation (B) and silver-decorated TiO₂ nanotubes (C). The nanoparticles are indicated by arrows.

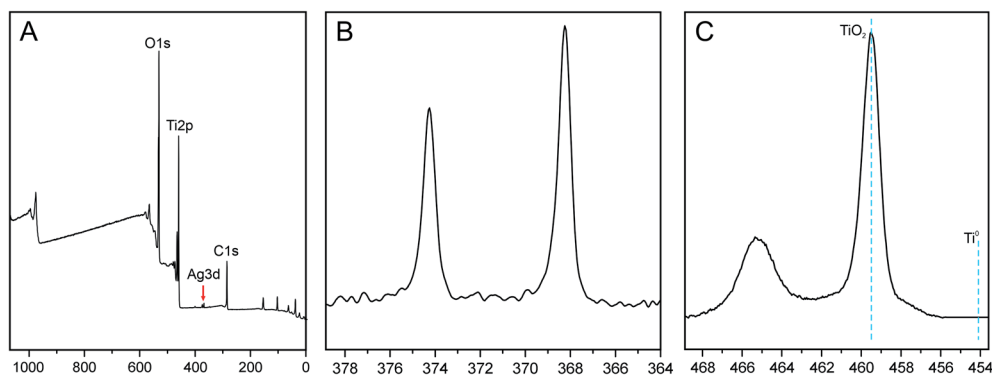


Fig. 4 XPS survey of TiO₂ nanotubes decorated with AgNPs (A), high resolution Ag 3d spectra (B) and high resolution spectra Ti 2p (C).

independent SEM images were evaluated for the number of nanoparticles per scanned area. The analysis of SEM images confirmed the decoration of TNTs surface with 3–4 nanoparticles on the area of 4 μm² for each of differently functionalized Ag nanoparticles (Fig. 3B and C). The size of nanoparticles of ~50 nm also guaranteed their deposition on the top of nanotubes.

The presence of silver nanoparticles and chemical composition of TiO₂ surface for bare- and silver-modified samples was investigated by X-ray photoelectron spectroscopy (XPS). In Fig. 4A, a typical XPS survey of the TiO₂ surface after AgNPs decoration is shown. The survey shows the Ti, C, O and Ag signals, indicating that silver nanoparticles are adsorbed on the TiO₂ nanotubes. Four main elements, *i.e.* Ti 2p, O 1s, C 1s and Ag 3d were quantitatively analyzed in details and XPS data is summarized in Table 1. Data shows that samples did not differ significantly in their compositions and chemical state of elements. All the samples possessed high carbon level on the surface in the range of 31–33%, which could be attributed to used electrolyte, or/and adsorbed CO₂ from the air. The silver content ~0.2% was indicated for all AgNPs decorated samples and no silver peak was observed for bare nanotubes. Similar Ag values on all samples also indicate that nanotubes were coated with nanoparticles evenly.

The characteristic high resolution XPS spectra of the Ag 3d region is shown in Fig. 4B. The signals at binding energies of 368 eV and 374 eV were corresponding to the 3d_{5/2} and 3d_{3/2} orbits of Ag⁰ (metallic silver). The nanoparticles are not

oxidized, as no further peaks at lower BE energy were needed for the fit. Additionally, high resolution XPS spectra of the Ti 2p is shown in Fig. 4C. The Ti 2p_{3/2} peak has a maximum at 459 eV which can be assigned to TiO₂. There is no contribution from metallic Ti (BE = 453.8 eV) which could be attributed to a thickness of oxide layer (> 10 nm).

Antibacterial properties of AgNPs-TNTs surfaces

The array of TiO₂ nanotubes has been previously found to exhibit antibacterial action in a certain extent compared to the flat surface but it still has been clearly insufficient for use as an antibacterial surface. On the other hand, the silver nanoparticles exhibited strong antimicrobial performance against wide spectra of microorganisms.⁴³ Although the mechanism of their antimicrobial action is not clearly understood, several mechanisms have been proposed. Those include the continual

Table 1 XPS analysis of bare-(control) and AgNPs decorated TiO₂ nanotubes. Relative percentage of selected elements calculated from narrow spectra

	BPEI [%]	Citrate [%]	Lipoic [%]	PEG [%]	PVP [%]	Control [%]
O 1s	51.42	50.28	50.74	51.49	51.29	51.07
Ti 2p	16.95	16.02	15.66	16.75	15.98	16.42
C 1s	31.44	33.5	33.41	31.56	32.52	32.51
Ag 3d	0.19	0.19	0.19	0.2	0.21	0



release of silver ions, disruption of the bacterial envelope, deactivation of respiratory enzymes, and generation of intracellular reactive oxygen species; consequently, cell death occurs.^{44,45} The antimicrobial activity of nano-sized silver particles was also found size- and shape-dependent, one of the reasons could be that different morphologies provide different areas to interact with bacteria and thus results in different antibacterial efficiency. In accordance with most reported data, the smallest-sized spherical AgNPs (<50 nm) were more efficient to kill G^- bacteria as compared to larger spherical AgNPs. Moreover, nanoparticles are usually stabilized in solution with a wide spectrum of chemicals such as citrate, polyvinylpyrrolidone *etc.* A few stabilization agents and/or functional layers of nanoparticles have been previously reported to affect the cell-surface interaction resulting in different antibacterial action.^{39,46} Since the nanoparticle stabilizers have not been extensively investigated for their antibacterial action of adsorbed nanoparticles, here we compared five different NPs stabilizing agents by the decoration of AgNPs on TNTs nanotubes. The synergistic antibacterial activity was evaluated for three bacteria such as *E. coli*, *P. aeruginosa* and *S. aureus*.

Adhesion and viability assay of G^- bacteria

The evaluation of the adhesion and viability of bacteria on AgNPs-TNTs surfaces, *E. coli* was chosen as a first representative model of Gram-negative bacteria. Some strains of *E. coli* are known for biofilm formation, which can be the source of persistent medical-device related infections.^{47,48} SEM microphotograph (Fig. 5A) shows *E. coli* growing and colonizing control TNTs surface. Live/dead images and image analysis of *E. coli* after 24 hours' incubation shows the antibacterial activity of AgNPs-TNTs depending on the variability of nanoparticle functionalization layers (Fig. 5B and 6). The bacterial nucleic acid was stained with two fluorescence dyes, SYTO9 and propidium iodide with two fluorescence dyes, SYTO9 and propidium iodide, respectively. Green stain SYTO9 is cell membrane permeant, thus it stains nucleic acids of viable cells. On the contrary, red stain propidium iodide is membrane impermeable, it is commonly used to detect dead cells in a population. However, when the DNA is exposed to both stains, propidium iodide shows higher affinity to intercalate DNA and

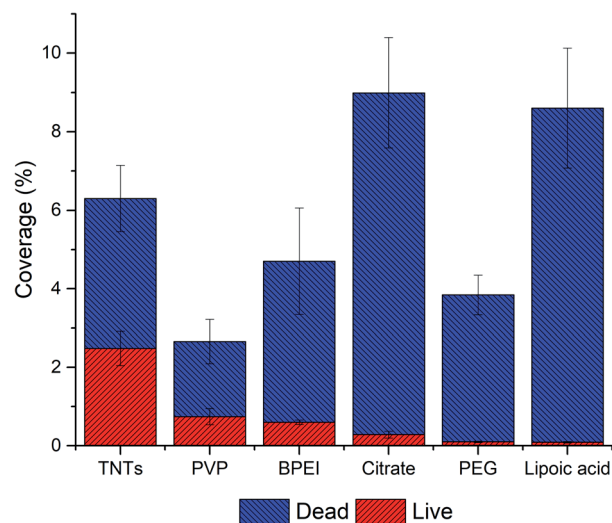


Fig. 6 The adhesion and live/dead assay of *E. coli* on AgNPs-TNTs surfaces. Data is expressed in % of total image area. All samples showed statistically significant difference ($p < 0.05$).

it is able to replace SYTO9. Therefore, the red fluorescence signal is generally considered as dead cell and green signal as live cell.^{49,50} The non-decorated TNTs surface (control) showed almost 40% of dead *E. coli* bacteria, whereas nanoparticle-coated TNTs exhibited enhanced antibacterial activity as it is shown in Fig. 6. The live/dead ratio obtained from the image analysis determined the enhanced antibacterial activity of the sample as follows: TNTs > PVP > BPEI > citrate > PEG > lipoic acid (Table 2). The antibacterial activity of TNTs as control is in a good agreement with previous studies suggesting the antibacterial properties of annealed unmodified TiO_2 nanotubes.^{32,51,52}

Generally, Ag nanoparticles significantly enhanced the antibacterial properties of TNTs in term of the amount of dead *E. coli* bacteria. Especially, lipoic acid and citrate functionalized AgNPs-TNTs samples showed a very low value of live/dead ratio (Table 2). However, when considering the total coverage of the surface with *E. coli*, which corresponds with the adhesion of

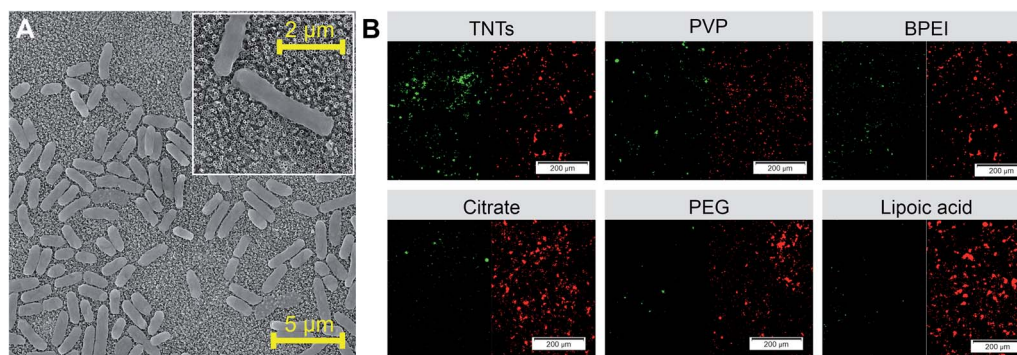


Fig. 5 SEM image of *E. coli* grown on control TNTs surface with bacteria detail showed in the insert (A). Live/dead fluorescence staining of *E. coli* performed on differently functionalized Ag-NPs decorating TNTs nanotubes ((B) red color represents dead cells and green color represents live cells). Abbreviations: PVP (polyvinylpyrrolidone), BPEI (branched polyethyleneimine), PEG (polyethylene glycol).



Table 2 The live/dead ratio of G^- and G^+ bacteria on TiO_2 nanotubes decorated with differently functionalized Ag-NPs after 24 hour incubation

	Live/dead ratio		
	<i>E. coli</i>	<i>P. aeruginosa</i>	<i>S. aureus</i>
TNTs	0.652 ± 0.012	1.161 ± 0.05	1.168 ± 0.003
PVP	0.381 ± 0.008	0.099 ± 0.011	0.926 ± 0.012
BPEI	0.151 ± 0.004	0.093 ± 0.001	1.021 ± 0.020
Citrate	0.033 ± 0.002	0.101 ± 0.013	2.457 ± 0.035
PEG	0.026 ± 0.001	0.009 ± 0.0002	0.447 ± 0.011
Lipoic acid	0.010 ± 0.001	0.019 ± 0.001	0.621 ± 0.008

bacteria, “lipoic acid” and “citrate” samples showed significantly higher surface coverages compared to other samples. Contrary, the PVP sample showed the lowest total surface coverage but exhibited good bacteria survival. It is generally considered that the electrostatic interaction between negatively charged bacteria membrane and positively charged nanoparticles increases the antibacterial efficiency.⁵⁸ For instance, since the lipoic acid, citrate, and PVP have a negative charge at physiological pH,^{53–55} the repulsiveness between negatively charged NPs and bacterial cells is supposed to dominate. However, a significantly high surface coverage on citrate and lipoic acid functionalized AgNPs–TNTs surface compared to PVP was observed. Further, the pKa value of TiO_2 is between 5.3–6.2.⁵⁶ It means that under the physiological pH, the surface is negatively charged, and thus it should also behave repulsively to bacteria. Contrary, when combining negatively charged TNTs and positively charged BPEI functionalized NPs, the surface coverage is lower than citrate, and lipoic acid functionalized AgNPs–TNTs surface. Thus, we did not find any correlation in bacteria adhesion depending on the surface charge and charge of bacterial membrane. It leads us to the conclusion that instead of electrostatic interaction, the topography and the chemical character AgNPs–TNT surfaces must be the key factor not only in cell–surface interaction and adhesion but also in viability of bacteria on such surfaces. The nanoparticles enhanced the antibacterial properties of TNTs, and more

importantly, the nanoparticle functionalization layers significantly contributed to the antibacterial effect of AgNPs–TNTs surface against *E. coli*.

Further, we tested all samples against Gram-negative *P. aeruginosa*, which is also known for the biofilm formation. It is the second most common Gram-negative bacteria causing orthopedic implant infection⁵⁷ and multidrug resistance.⁵⁸ Fig. 7A and B shows the SEM image of *P. aeruginosa* on the control TNTs surface and live/dead staining of bacteria on AgNPs decorated TNTs with different nanoparticle functionalization layers, respectively.

The data from image analyses of live/dead staining of *P. aeruginosa* (Fig. 8 and Table 2) showed a significant decrease in bacteria adhesion on NPs decorated TNTs compared to the control TNTs and also compared to the results obtained from *E. coli* experiment. Results can be attributed to several factors, including the charge repulsiveness, different composition of bacteria membrane, topography and chemistry of TiO_2

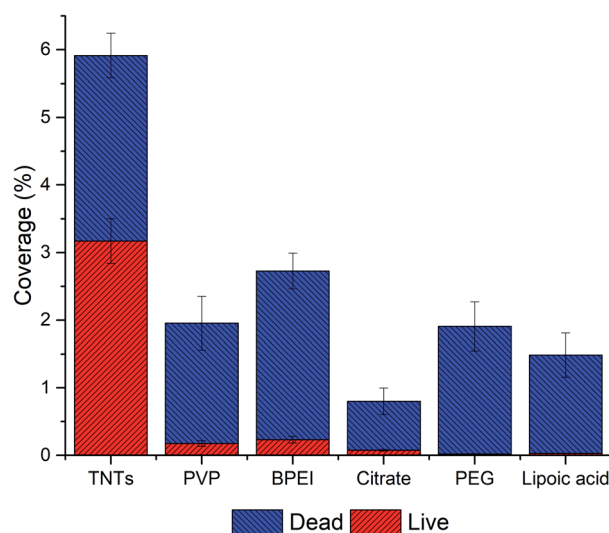


Fig. 8 Adhesion and live/dead assay of *P. aeruginosa* on AgNPs–TNTs surfaces. Data is expressed in percentage of total image area. All samples showed statistically significant difference ($p < 0.05$).

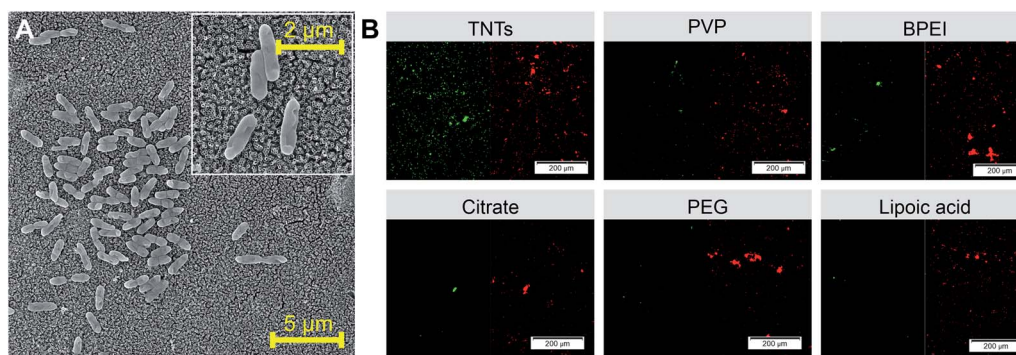


Fig. 7 SEM images of *P. aeruginosa* adhered on control TNTs sample and bacteria detail showed in the insert (A). Live/dead fluorescence images of *P. aeruginosa* adhered on differently functionalized Ag-NPs decorated on TNTs nanotubes ((B) red = dead cells; green = live cells). Abbreviations: PVP (polyvinylpyrrolidone), BPEI (branched polyethyleneimine), PEG (polyethylene glycol).



nanotubes and Ag nanoparticles.^{59,60} These factors probably acted synergistically, as was demonstrated by our results. Additionally, the viability of *P. aeruginosa* on TNTs control was enhanced (~50%) compared to *E. coli* bacteria, and the lowest live/dead ratio has been found on PEG and lipoic acid samples which was also observed for *E. coli* bacteria. The similar live/dead ratio ~0.1 was calculated for PVP, BPEI, and citrate functionalized NPs.

Adhesion and viability assay of G⁺ bacteria

S. aureus was chosen as a representative bacterial model for the evaluation of the adhesion and viability of Gram-positive bacteria on AgNPs-TNTs surfaces. In comparison to *E. coli* and *P. aeruginosa*, the primary source of hospital-acquired infections dwells in already infected people. *S. aureus* is biofilm-forming bacteria on bones, heart valves, or implanted materials.⁶¹ Results obtained from live/dead assay suggested that *S. aureus* adhered well on nanoparticle decorated TNTs surfaces as well as on the control TNTs (Fig. 9 A and B). The bacterial coverage of surfaces with *S. aureus* (>32%) was several times higher than it was observed for Gram-negative bacteria (<9%). Moreover, the ratio of live/dead cells significantly increased, as shown in Fig. 10 and Table 2. For instance, the citrate functionalized NPs decorating TNTs showed a two-folded increase in live/dead ratio compared to the control TNTs.

The results demonstrated on *S. aureus* suggested that bacteria interact differently on AgNPs decorated TNTs surfaces as the increased adhesion and viability were observed compared to the G⁻ bacteria. *S. aureus* was also more resistant to the character of NPs functionalized layers. To get better antibacterial properties of AgNPs-TNTs surface against *S. aureus*, the increased number of nanoparticles on TNTs nanotubes should be performed and tested. On the other hand, it is also possible to think about absolutely different design of antibacterial surface for such resistant G⁺ bacteria.

Colony counting assay of G⁺ and G⁻ bacteria

Results from fluorescence staining showed the degree of bacterial adhesion after 24 hours and the living/dead cell ratio. Colony counting method performed in this work reflects the

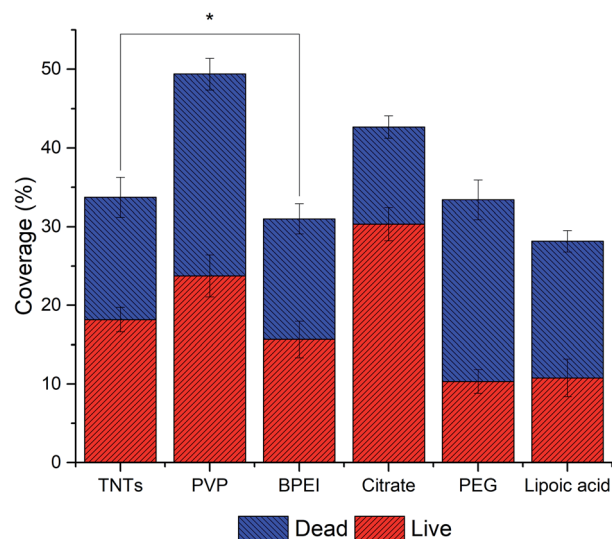


Fig. 10 Adhesion and live/dead assay of *S. aureus* on AgNPs-TNTs surfaces. Data is expressed in % of total image area. * indicates that there is no statistical significance ($p > 0.05$).

bacterial adhesion and viability after 4 hours' incubation of bacteria with AgNP-TNTs surfaces. Here, we performed colony counting assay for *E. coli* and *S. aureus* as representatives. Fig. 11A shows data obtained for *E. coli* bacteria, in which the adhesion and viability of bacteria decreased as follows: TNTs \geq PVP \geq BPEI $>$ citrate $>$ PEG $>$ lipoic acid. The viability of bacteria corresponds with live/dead staining obtained for 24 hours, where the portion of living bacteria had the similar trend. Different results could be observed for bacterial adhesion at 4 hours and 24 hours. The shorter time of interaction between bacteria and surface followed the trend of bacteria viability. However, it was significantly changed when *E. coli* was exposed to the surface for 24 hours, in which the adhesion was increased on citrate and lipoic acid samples; although at the expense of more dead cells. The results obtained for *S. aureus* (Fig. 11B) after 4 hours' incubation of bacteria on the samples showed increased adhesion and viability as follows: TNTs \geq PVP $>$ BPEI \geq PEG \geq lipoic acid $>$ citrate. Here we can see, that there is

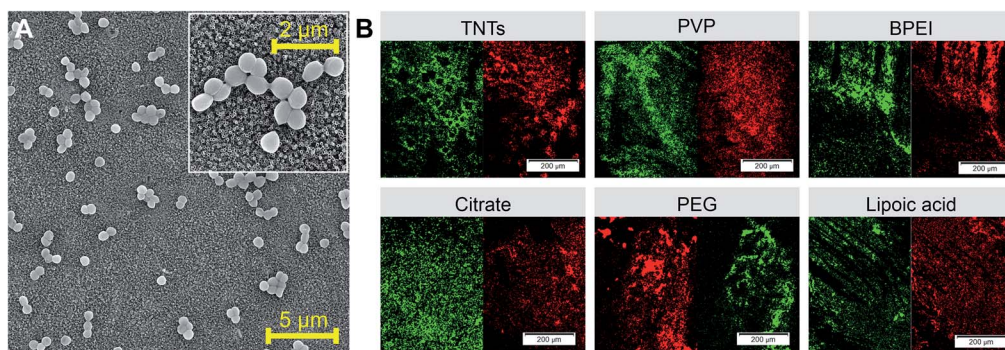


Fig. 9 SEM images of *S. aureus* adhered on the control TNTs sample with bacteria detail showed in the inset (A). Live/dead fluorescence staining of *S. aureus* performed on differently functionalized Ag-NPs decorated on TNTs nanotubes ((B) red color represents dead cells and green color represents live cells). Abbreviations: PVP (polyvinylpyrrolidone), BPEI (branched polyethyleneimine), PEG (polyethylene glycol).



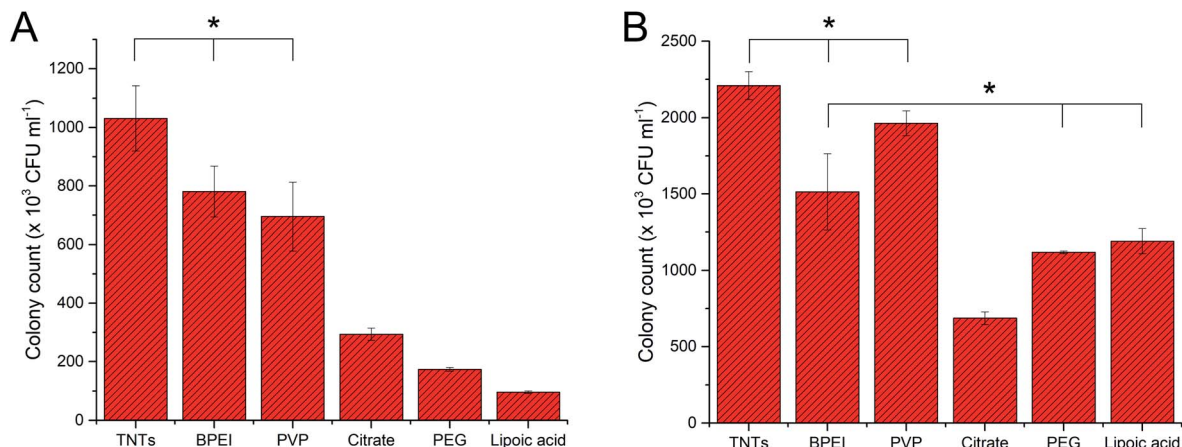


Fig. 11 The graphs of colony counting experiments expressed in colony forming units for *E. coli* (A) and *S. aureus* (B). Bacteria was exposed to surfaces for 4 hours, and the antibacterial effect was compared between individual samples. * indicates that there is no statistical significance.

a significant difference of results obtained for two incubation times. The explanation for this observation could be that bacteria sense, adhere and grow on different surfaces with different speed.

Conclusion

In this paper, the arrays of TiO₂ nanotubes were fabricated *via* single-step anodization of polished titanium foil. The nanotubes were decorated with silver nanoparticles stabilized with different functionalization layer such as polyvinylpyrrolidone, branched polyethyleneimine, citrate, polyethylene glycol, and lipoic acid. The antibacterial activity of Ag-decorated TiO₂ nanotubes was tested against three biofilm-forming bacteria, such as Gram-positive *S. aureus* and Gram-negative *E. coli* and *P. aeruginosa* using fluorescence microscopy-based live/dead assay and colony counting method. We showed that the stabilizing agent play important role in antibacterial properties of AgNPs as was confirmed by the synergistic effect of particular nanoparticles and TiO₂ nanotubes on adhesion and viability of G⁻ and G⁺ bacteria. For future work, the antibacterial properties of TiO₂ nanotubes will be evaluated for different AgNPs concentrations and size and the cytocompatibility of such decorated nanotubes will also be in our interest.

Conflicts of interest

There are no conflicts to declare.

Acknowledgements

The authors wish to acknowledge the financial support of the GACR Project Number GA19-04270Y from the Czech Republic. This study was also supported by IGA MENDELU AFIGA2020-IP029 and ERDF "Multidisciplinary research to increase application potential of nanomaterials in agricultural practice" (No. CZ.02.1.01/0.0/0.0/16_025/0007314). We also thank to CEITEC Nano Research Infrastructure (LM2018110) and to Jan Prášek

and Tomáš Lednický from CF Nano for AFM and XPS measurements.

References

- 1 R. J. Turner, Metal-based antimicrobial strategies, *J. Microb. Biotechnol.*, 2017, (10), 1062–1065.
- 2 A. Azam, *et al.*, Antimicrobial activity of metal oxide nanoparticles against Gram-positive and Gram-negative bacteria: a comparative study, *Int. J. Nanomed.*, 2012, (7), 6003.
- 3 A. Róžańska, *et al.*, Antimicrobial properties of selected copper alloys on Staphylococcus Aureus and Escherichia Coli in different simulations of environmental conditions: with vs. without organic contamination, *Int. J. Environ. Res. Publ. Health*, 2017, (14), 813.
- 4 J. Hasan, *et al.*, Antibacterial surfaces: the quest for a new generation of biomaterials, *Trends Biotechnol.*, 2013, (31), 295–304.
- 5 J. A. Lemire, *et al.*, Antimicrobial activity of metals: mechanisms, molecular targets and applications, *Nat. Rev. Microbiol.*, 2013, (11), 371–384.
- 6 M. Mahlapuu, *et al.*, Antimicrobial Peptides: An Emerging Category of Therapeutic Agents, *Front. Cell. Infect. Microbiol.*, 2016, (6).
- 7 E. N. Gkana, *et al.*, Anti-adhesion and Anti-biofilm Potential of Organosilane Nanoparticles against Foodborne Pathogens, *Front. Microbiol.*, 2017, (8).
- 8 N. F. Kamaruzzaman, *et al.*, Antimicrobial polymers: The potential replacement of existing antibiotics?, *Int. J. Mol. Sci.*, 2019, (20), 2747.
- 9 V. Likodimos, Advanced Photocatalytic Materials, *Materials*, 2020, (13), 821.
- 10 A. Khezroulou, *et al.*, Nanoparticles and their antimicrobial properties against pathogens including bacteria, fungi, parasites and viruses, *Microb. Pathog.*, 2018, (123), 505526.
- 11 C. Buzea, *et al.*, Nanomaterials and nanoparticles: Sources and toxicity, *Biointerphases*, 2007, (2), MR17–MR71.



- 12 S. Wu, *et al.*, Antibacterial Au nanostructured surfaces, *Nanoscale*, 2016, (8), 26202625.
- 13 J. T. Seil and T. J. Webster, Antimicrobial applications of nanotechnology: methods and literature, *Int. J. Nanomed.*, 2012, (7), 2767.
- 14 G. Mohammadi, *et al.*, Development of azithromycin-PLGA nanoparticles: Physicochemical characterization and antibacterial effect against *Salmonella typhi*, *Colloids Surf. B Biointerfaces*, 2010, (80), 34–39.
- 15 Z. Fohlerova and A. Mozalev, Anodic formation and biomedical properties of hafnium-oxide nanofilms, *J. Mater. Chem. B*, 2019, (7), 2300–2310.
- 16 A. Tian, *et al.*, Nanoscale TiO₂ nanotubes govern the biological behavior of human glioma and osteosarcoma cells, *Int. J. Nanomed.*, 2015, (10), 2423.
- 17 K. M. Kummer, *et al.*, Biological applications of anodized TiO₂ nanostructures: a review from orthopedic to stent applications, *Nanosci. Nanotechnol. Lett.*, 2012, (4), 483–493.
- 18 X. Zhang, *et al.*, A functionalized Sm/Sr doped TiO₂ nanotube array on titanium implant enables exceptional bone-implant integration and also self-antibacterial activity, *Ceram. Int.*, 2020, (46), 14796–14807.
- 19 Y. Cheng, *et al.*, Progress in TiO₂ nanotube coatings for biomedical applications: a review, *J. Mater. Chem. B*, 2018, (6), 1862–1886.
- 20 C. Mohan, *et al.*, In vitro hemocompatibility and vascular endothelial cell functionality on titania nanostructures under static and dynamic conditions for improved coronary stenting applications, *Acta Biomater.*, 2013, (9), 9568–9577.
- 21 Z. Fohlerova and A. Mozalev, Tuning the response of osteoblast-like cells to the porous alumina-assisted mixed-oxide nano-mound arrays, *J. Biomed. Mater. Res. B Appl. Biomater.*, 2018, (106), 1645–1654.
- 22 Q. Wang, *et al.*, TiO₂ nanotube platforms for smart drug delivery: a review, *Int. J. Nanomed.*, 2016, (11), 4819.
- 23 H. Zhang, *et al.*, Improved antibacterial activity and biocompatibility on vancomycin-loaded TiO₂ nanotubes: in vivo and in vitro studies, *Int. J. Nanomed.*, 2013, (8), 4379.
- 24 K. C. Popat, *et al.*, Decreased *Staphylococcus epidermidis* adhesion and increased osteoblast functionality on antibiotic-loaded titania nanotubes, *Biomaterials*, 2007, (28), 4880–4888.
- 25 X. Zhang, *et al.*, Synergistic effects of lanthanum and strontium to enhance the osteogenic activity of TiO₂ nanotube biological interface, *Ceram. Int.*, 2020, (46), 13969–13979.
- 26 J. Li, *et al.*, Plasmonic gold nanoparticles modified titania nanotubes for antibacterial application, *Appl. Phys. Lett.*, 2014, (104), 261110.
- 27 T. Yang, *et al.*, Cytocompatibility and antibacterial activity of titania nanotubes incorporated with gold nanoparticles, *Colloids Surf. B Biointerfaces*, 2016, (145), 597–606.
- 28 W. Liu, *et al.*, Synthesis of TiO₂ nanotubes with ZnO nanoparticles to achieve antibacterial properties and stem cell compatibility, *Nanoscale*, 2014, (6), 9050–9062.
- 29 O. Bilek, *et al.*, Enhanced antibacterial and anticancer properties of Se-NPs decorated TiO₂ nanotube film, *PLoS One*, 2019, (14), e0214066.
- 30 W. Liu, *et al.*, Selenium nanoparticles incorporated into titania nanotubes inhibit bacterial growth and macrophage proliferation, *Nanoscale*, 2016, (8), 15783–15794.
- 31 M.-Y. Lan, *et al.*, Both enhanced biocompatibility and antibacterial activity in Ag-decorated TiO₂ nanotubes, *PLoS One*, 2013, (8), e75364.
- 32 S. Mei, *et al.*, Antibacterial effects and biocompatibility of titanium surfaces with graded silver incorporation in titania nanotubes, *Biomaterials*, 2014, (35), 4255–4265.
- 33 Z. Guo, *et al.*, Fabrication of silver-incorporated TiO₂ nanotubes and evaluation on its antibacterial activity, *Mater. Lett.*, 2014, (137), 464–467.
- 34 H. Li, *et al.*, Antibacterial activity of TiO₂ nanotubes: influence of crystal phase, morphology and Ag deposition, *Appl. Surf. Sci.*, 2013, (284), 179–183.
- 35 U. F. Gunpath, *et al.*, Anodised TiO₂ nanotubes as a scaffold for antibacterial silver nanoparticles on titanium implants, *Mater. Sci. Eng. C*, 2018, (91), 638644.
- 36 A. Roguska, *et al.*, Evaluation of the Antibacterial Activity of Ag-Loaded TiO₂ Nanotubes, *Eur. J. Inorg. Chem.*, 2012, 5199–5206.
- 37 S. Yenyol, *et al.*, Antibacterial activity of As-annealed TiO₂ nanotubes doped with Ag nanoparticles against periodontal pathogens, *Bioinorgan. Chem. Appl.*, 2014, (2014), 829496.
- 38 N. Esfandiari, *et al.*, Size tuning of Ag-decorated TiO₂ nanotube arrays for improved bactericidal capacity of orthopedic implants, *J. Biomed. Mater. Res.*, 2014, (102), 2625–2635.
- 39 A. Burkowska-but, *et al.*, Influence of stabilizers on the antimicrobial properties of silver nanoparticles introduced into natural water, *J. Environ. Sci.*, 2014, (26), 542–549.
- 40 D. van Phu, *et al.*, Study on antibacterial activity of silver nanoparticles synthesized by gamma irradiation method using different stabilizers, *Nanoscale Res. Lett.*, 2014, (9), 162.
- 41 L. O. Cinteza, *et al.*, Chitosan-stabilized Ag nanoparticles with superior biocompatibility and their synergistic antibacterial effect in mixtures with essential oils, *Nanomaterials*, 2018, (8), 826.
- 42 O. Bilek, *et al.*, Enhanced antibacterial and anticancer properties of Se-NPs decorated TiO₂ nanotube film, *PLoS One*, 2019, (14), e0214066.
- 43 R. Vazquez-muñoz, *et al.*, Enhancement of antibiotics antimicrobial activity due to the silver nanoparticles impact on the cell membrane, *PLoS One*, 2019, (14), e0224904.
- 44 I. X. Yin, *et al.*, The Antibacterial Mechanism of Silver Nanoparticles and Its Application in Dentistry, *Int. J. Nanomed.*, 2020, (15), 2555–2562.
- 45 S. Prabhu and E. K. Poulouse, Silver nanoparticles: mechanism of antimicrobial action, synthesis, medical applications, and toxicity effects, *Int. Nano Lett.*, 2012, (2), 32.



- 46 A. Borowik, *et al.*, The Impact of Surface Functionalization on the Biophysical Properties of Silver Nanoparticles, *Nanomaterials*, 2019, (9), 973.
- 47 T. Juhna, *et al.*, Detection of Escherichia coli in biofilms from pipe samples and coupons in drinking water distribution networks, *Appl. Environ. Microbiol.*, 2007, (73), 7456–7464.
- 48 Z. Khatoun, *et al.*, Bacterial biofilm formation on implantable devices and approaches to its treatment and prevention, *Heliyon*, 2018, (4), e01067.
- 49 S. M. Stocks, Mechanism and use of the commercially available viability stain, *BacLight*, 2004, (61A), 189–195.
- 50 M. Rosenberg, *et al.*, Propidium iodide staining underestimates viability of adherent bacterial cells, *Sci. Rep.*, 2019, (9), 6483.
- 51 B. Ercan, *et al.*, Diameter of titanium nanotubes influences anti-bacterial efficacy, *Nanotechnology*, 2011, (22), 295102.
- 52 A. Mazare, *et al.*, Corrosion, antibacterial activity and haemocompatibility of TiO₂ nanotubes as a function of their annealing temperature, *Corros. Sci.*, 2016, (103), 215–222.
- 53 K. A. Huynh and K. L. Chen, Aggregation kinetics of citrate and polyvinylpyrrolidone coated silver nanoparticles in monovalent and divalent electrolyte solutions, *Environ. Sci. Technol.*, 2011, (45), 5564–5571.
- 54 Z. Qiao, *et al.*, Silver nanoparticles with pH induced surface charge switchable properties for antibacterial and antibiofilm applications, *J. Mater. Chem. B*, 2019, (7), 830–840.
- 55 K. Niska, *et al.*, Capping Agent-Dependent Toxicity and Antimicrobial Activity of Silver Nanoparticles: An In Vitro Study. Concerns about Potential Application in Dental Practice, *Int. J. Med. Sci.*, 2016, (13), 772–782.
- 56 X. van Doorslaer, *et al.*, UV-A and UV-C induced photolytic and photocatalytic degradation of aqueous ciprofloxacin and moxifloxacin: Reaction kinetics and role of adsorption, *Appl. Catal. B Environ.*, 2011, (101), 540–547.
- 57 L. Crémet, *et al.*, Orthopaedic-implant infections by Escherichia coli: Molecular and phenotypic analysis of the causative strains, *J. Infect.*, 2012, (64), 169–175.
- 58 N. M. Maurice, *et al.*, Pseudomonas aeruginosa Biofilms: Host Response and Clinical Implications in Lung Infections, *Am. J. Respir. Cell Mol. Biol.*, 2018, (58), 428–439.
- 59 P. R. Hunt, *et al.*, Bioactivity of nanosilver in Caenorhabditis elegans: Effects of size, coat, and shape, *Toxicol. Rep.*, 2014, (1), 923–944.
- 60 K. Vasilev, Nanoengineered antibacterial coatings and materials: A perspective, *Coatings*, 2019, 9, 654.
- 61 J. L. Lister and A. R. Horswill, Staphylococcus aureus biofilms: recent developments in biofilm dispersal, *Front. Cell. Infect. Microbiol.*, 2014, (4), 178.



Článek 3

Tuning the response of osteoblast-like cells to the porous alumina-assisted mixed oxide nanomound arrays

Tuning the response of osteoblast-like cells to the porous-alumina-assisted mixed-oxide nano-mound arrays

Zdenka Fohlerova, Alexander Mozalev

CEITEC-Central European Institute of Technology, Brno University of Technology, Brno, Czech Republic

Received 24 May 2017; revised 27 July 2017; accepted 4 August 2017

Published online 24 August 2017 in Wiley Online Library (wileyonlinelibrary.com). DOI: 10.1002/jbm.b.33971

Abstract: Nanostructuring of biomaterials is used to create an appropriate interfacial layer that promotes stable cellular adhesion, proliferation, and differentiation on orthopedic and dental implants. Here, we synthesize self-organized arrays of composite-oxide nano-mounds through anodizing Al/Ta bilayers sputtered on substrates to cover the “missing” smallest size range of 10–40 nm for structuring an advanced inorganic biomaterial—Al₂O₃-doped Ta₂O₅ films. The osteoblast-like cells appear to be able to recognize the finest differences in the film nano-morphologies. In the absence of serum proteins, the adhesion and cell growth are substantially enhanced on the 20 and 40 nm nanoarrays while in complete medium the cells show better initial adhesion on the 10 nm nanoarrays. The proliferation assay reveals a significant rise in cell number on the 20 and 40 nm nanoarrays

during the first 7 days. A remarkable increase in the alkaline phosphatase activity is noticed on the 40 nm nanoarray. Immunostaining of cells adhered to the nano-mound surfaces shows that the cells are well spread over all the nanostructured films with organized actin fibers. The larger surface areas and improved focal contacts are again associated with the 20 and 40 nm nanoarrays. The findings help improve compatibility of living cells with the metal-oxide nanostructured surfaces developed for tissue engineering. © 2017 Wiley Periodicals, Inc. *J Biomed Mater Res Part B: Appl Biomater*, 106B: 1645–1654, 2018.

Key Words: tantalum oxide, anodizing, porous anodic alumina, nanostructure, biomaterial, cell culture

How to cite this article: Fohlerova Z, Mozalev A. 2018. Tuning the response of osteoblast-like cells to the porous-alumina-assisted mixed-oxide nano-mound arrays. *J Biomed Mater Res Part B* 2018;106B:1645–1654.

INTRODUCTION

Recent progress in research and development for advanced functional materials has given rise to a number of surface finishing techniques for precisely controlling and modifying materials chemistry and morphology. Advances in surface structuring at the micro- and especially nano-scale have accelerated preparation and application of metallic biomaterials with the improved surface properties. Nowadays, commercially available biomaterials used as implants, such as titanium and its alloys, stainless steel, or chromium-cobalt alloy, are routinely applied due to their biocompatibility, favorable mechanical properties, and chemical stability.¹ However, an undesirable tissue reaction caused by released metal ions may shorten the lifespan of metallic implants owing to deteriorating the cell adhesion and osteointegration. Therefore, further optimization of chemical and physical properties of the well-known biomaterials for improving their cellular responses is worth doing in tissue engineering.

The bioinertness, biocompatibility, and bioactivity of metals may be modified by altering their surface properties. In this way various cellular responses can be induced and controlled.² Porous structures,¹ nanoleaf, and nanoneedles,³ nanotubes,⁴ nanodots,⁵ or random structures have been fabricated via various methods. In addition, a number of

extra modifications have been carried out to enhance osteointegration.^{6–10} It is now commonly accepted that the topography and chemistry at the micro- and nano-scale are the driving forces for protein adsorption and cellular adhesion, proliferation, and differentiation;¹¹ therefore, the surface properties of a biomaterial should be adjusted to achieve an optimal balance between the biocompatibility and bioactivity of the material.

Titanium dioxide nanostructures have been introduced in the field in many works. The most extensively studied TiO₂ nanotubes have proved their positive impact on cell responses compared with an unstructured titanium.^{12–16} Most recently, *tantalum* has been proposed as an alternative implant material or coating due to its excellent anticorrosive properties and good biocompatibility. To date, several biological characterizations have been carried out on the porous tantalum material structured at the micro- and nanoscale.^{17,18} Nanostructured tantalum-oxide domes and huts were reported to reveal good adsorption of fibronectin and directed cell surface interactions.¹⁹ Since it has been proved that nanotubes may be anodically grown on a variety of metals including zirconium, niobium and tantalum,^{20,21} the *tantalum-oxide* nanotube films have been examined on their anticorrosive and biocompatible properties promoting protein adsorption and improving

Correspondence to: Z. Fohlerova; e-mail: zdenka.fohlerova@ceitec.vutbr.cz

cellular function.⁴ Despite the reported improvements in the biomaterial surface properties in relation with cellular responses, some contradictory results have also been obtained.^{19,22,23} Obviously, the results reported so far need to be reproduced, compared, and sorted out before making final decisions on their importance for further *in vivo* research.

The tantalum biocompatibility studies have been extended to *tantalum-oxide nanodots* grown electrochemically on substrates,^{24,25} some covered with platinum,⁵ with sizes of 10, 50, 100, and 200 nm, tested on various cell lines.²⁶ The originality, reproducibility, and size diversity of this environmentally friendly approach (called in the modern literature the porous-anodic-alumina [PAA]-assisted anodizing), first reported by Sarganov and Mozalev²⁷ and elaborated in later publications,^{28–30} complemented by the promising biocompatibility results, deserves a special attention. From the recent reports,^{24–26} the behavior of various cells seems to be influenced by the dot sizes and spacing between the dots. However, in the mentioned publications a number of important details of the film morphology and chemical composition have been beyond the authors' consideration, which makes yet impossible to understand well and describe conceptually the functioning of the film/cell interface. As a matter of fact, the films are not “nanodots” but rather three-dimensional (3D) nano-hillocks or mounds, with the shape being tuned by the electrical conditions and the nature of anodizing solution.^{28,29} Second, the “dots” grown in oxalic acid electrolytes are not tantalum oxide but rather tantalum-nitrogen oxide, separated by a network of non-oxidized TaN metal, both being likely in contact with the cells when the dot size exceeds some 50 nm.^{24–26} Another important but unaddressed feature is that the dots might be doped with electrolyte-derived species and especially residues of the alumina barrier layer,²⁸ which may additionally modify their chemical and physical properties and hence impact the response of living cells. Additionally and importantly, the size range of 10–50 nm, which was reported to be most promising for improving the cell response,^{20,23} has not been addressed in the related works. Covering the tantalum-oxide nanostructures with platinum makes the reported results even more confusing since in such case the cells interact with platinum, not with tantalum or tantalum oxide.⁵ Therefore, in the above-mentioned research, an important consideration is missing of the actual chemical composition, shape differences, mutual arrangement, and size effects, especially within the 10–50 nm range, which is needed for understanding and improving the adhesion, morphology, proliferation, and enzymatic activity of living cells.

In this work, arrays of metal-oxide nano-mounds self-aligned on substrates have been fabricated via PAA-assisted anodization of a layer of tantalum in aqueous solutions of sulfuric acid (H₂SO₄), providing the possibility for a well-controlled fabrication and precise manipulation by their physical sizes within the range of 10–40 nm. Detailed consideration of the film morphology and surface chemistry has made it possible to distinguish between the nano-mounds themselves (mixed Al₂O₃-Ta₂O₅ oxides with sulfur species) and the spacing around the mounds (pure Ta₂O₅). This helped systematically consider the chemical composition, physical shape, population density, and size

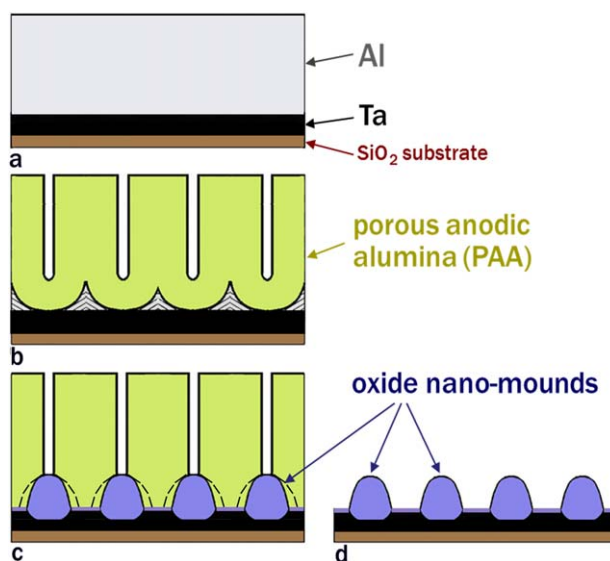


FIGURE 1. Main steps for forming an array of PAA-assisted mixed-oxide nano-mounds: (a) sputter-deposition of an Al/Ta bilayer onto a substrate, (b) formation of a porous anodic alumina (PAA) film via anodic oxidation (anodizing) of the Al layer, (c) anodizing the Ta underlayer through the alumina nanopores, and (d) selective chemical dissolution of the PAA layer.

diversity on the sensitive osteoblast-like cell response. Furthermore, serum proteins mediated interactions between the mixed-oxide nanofilms and living cells were studied in detail.

MATERIALS AND METHODS

Film preparation and characterization

Initial samples were prepared via sequential sputter-deposition of a layer of tantalum (99.99% purity, 100 nm thick) followed by a layer of aluminum (99.999% purity, 500 nm thick) onto SiO₂-coated silicon wafers. The wafers were then cut into 2 × 2 cm² pieces, which were anodically oxidized (anodized) individually in a specially designed polytetrafluoroethylene (PTFE) three-electrode cylindrical cell, with a protecting ring defining a working area within a circle of 1.5 cm². A platinum spiral was used as counter electrode while the reference electrode was an Ag/AgCl connected to the anodizing solution by a capillary containing agar-agar and KCl, as described elsewhere.²⁹

The key steps to form an array of tantalum-oxide-based nano-mounds from sputter-deposited Al/Ta metal layers are outlined in Figure 1. First, the Al layer is anodized in an H₂SO₄ aqueous solution³¹ at room temperature to form a PAA film having self-organized porous structure extended down to the Ta underlayer²⁸ [Figure 1(a)]. After the Al layer is fully converted to PAA, anodizing is sequentially continued at the same anode potential until the measured current goes to zero. During the current-decay period, oxidation of the underlying tantalum occurs locally beneath the alumina pores, and an array of nanosized tantalum-oxide protrusions forms at the Al₂O₃/Ta interface due to penetration in the alumina barrier layer by growing tantalum anodic oxide. Following anodizing, the specimens are re-anodized by sweeping anode potential at a constant rate of 50 mV s⁻¹ to a higher value, so as to force

the tantalum-oxide protrusions to overcome the thickness of the alumina barrier layer, come out in the pores, and expand at their bottoms [Figure 1(c)]. The extent to which the bases of the mounds widen in the in-plane direction is determined by the formation electrolyte and the value of anodizing/re-anodizing potential.^{28,29} To remove the PAA overlayer, the samples are dipped in a hot mixture of chromium and phosphoric acids for 3 min,²⁸ then washed in distilled water, and dried in an oven at 120°C [Figure 1(d)].

Three types of PAA films and hence the PAA-assisted tantalum-oxide-based nano-mounds were prepared by growing the PAA films in sulfuric acid electrolytes of concentrations ranging 2.0–0.4 mol L⁻¹ at three distinguished values of anode potentials: 5, 10, and 20 V (vs. Ag/AgCl) to address three characteristic ranges of alumina pore sizes and the oxide nano-mound dimensions, which have not been considered previously in related research.^{24–28}

The surfaces and cross-sections of the nano-mound samples were imaged in a TESCAN MIRA II field emission microscope, operated at 30 kV. As the material of the nano-mounds is a good dielectric,³⁰ a thin layer of gold, <3 nm thick, was evaporated onto the specimens before scanning electron microscopy (SEM) observation to reduce charge effect and improve image resolution. The samples used for cell culture experiments received no extra coatings after the PAA had been dissolved away.

Contact angle measurement

Wettability of a flat Ta₂O₅ film used as a reference surface and that of the nano-mound arrays were estimated by measuring the contact angle for water droplets using a SEO Phoenix 300 Touch analyzer. The measurements were carried out at room temperature with a 4 μL water droplet contacting the sample surface; the measurement results were evaluated by a four-point analysis.

Cell culture

Human osteoblast-like MG-63 cells (ECACC, UK) were used as a model for *in vitro* characterization of the nanostructured coatings prepared in this work. The MG-63 cells were maintained in complete Dulbecco's modified Eagle's medium supplemented with 10% fetal bovine serum (FBS), 2 mmol L⁻¹ L-glutamine, and 5% penicillin/streptomycin (50 U mL⁻¹ and 50 μg mL⁻¹ at 37°C in a humidified 5% CO₂ incubator). Cells were harvested by trypsinization (0.25% trypsin-ethylenediaminetetraacetic acid) at 70% confluency and seeded with a defined density onto the sterile substrates placed in a polystyrene microplate. All chemicals were purchased from Sigma.

Adhesion and proliferation assay

The initial adhesion of MG-63 cells to the nanostructured surfaces and to the reference (flat) Ta₂O₅ film was examined by counting the cells from images taken by an optical microscope (Axio Imager M2m, Zeiss). The cells were seeded onto the substrates placed in a 24-well plate at a density of 1 × 10⁵ cells per well. The experiment was carried out 2 h after the seeding in complete medium (in the presence of serum

proteins) and in serum-free medium. Proliferation of MG-63 cells on the nanostructured surfaces and on the flat film was measured with MTT assay and evaluated on days 1, 3, and 7 after the seeding; the initial cell density was 1 × 10⁵ cells per well. Briefly, the cells were incubated for a defined time and then gently washed twice with pre-heated phosphate buffer saline (PBS). The mixture of 150 μL culture medium and 50 μL of tetrazolium (3-(4, 5-dimethylthiazolyl-2)-2, 5-diphenyltetrazolium bromide (MTT), 1 mg mL⁻¹ in PBS, pH 7.4) was added into each well containing the samples. After 4 h inside the 5% CO₂ incubator, the samples were removed and placed into a new well plate, this being followed by the addition of 10% sodium dodecyl sulfate, and left overnight to solubilize the crystals of formazan produced by the cells. Hundred microliter solution portions were transferred from each well into a new 96-well plate and the absorbance was measured at 570 nm wave length with a microplate spectrophotometer (Beckman Coulter Paradigm). The proliferation was expressed in number of cells according to the MTT tetrazolium dye calibration curve.

Alkaline phosphatase assay

The activity of enzyme was measured on the nanostructured surfaces and on the flat film on day 5. The cells adhered to the nanostructured surfaces were lysed and alkaline phosphatase (ALP) was measured according to the manufacturer (ALP assay, BioVision Inc.). Briefly, 80 μL cell lysate was incubated with 50 μL *p*-nitrophenol phosphate (5 mmol L⁻¹) for 60 min, and the absorbance at a wave length of 405 nm was measured to the control. The amount of *p*-nitrophenol produced by the enzyme was calculated from the calibration curve and the activity of ALP from each substrate was expressed in nmol h⁻¹ mL⁻¹ units. The ALP activity was normalized to the total protein content of cells (ALP activity/microgram protein) measured at 595 nm wave length with Bradford reagent (Sigma) and serum albumin as a standard.

Immunostaining of β-actin and vinculin

To visualize and evaluate the cytoskeleton arrangement of cells on the different nanostructured surfaces relative to the flat tantalum pentoxide film, the β-actin and vinculin were stained for 24 h after cell seeding. The cells on the sample surfaces were washed with PBS and fixed with a fresh 4% paraformaldehyde in PBS for 15 min at room temperature. Followed by several washing steps with PBS, the cell membrane was permeabilized in 0.1% Triton-X for 15 min. The cells were gently washed in PBS and incubated overnight in a blocking solution of 2% bovine serum albumin. Mouse human anti-vinculin antibody (1:100 dilution) and AlexaFluor 488 phalloidin (6 μmol L⁻¹) were added for 1 h, this being followed by three washing steps. Finally, the samples were incubated with Alexa Fluor 488 goat anti-mouse antibody (1:100 dilution) for 1 h. The cellular components were imaged using a fluorescence microscope (Zeiss Axio Imager M2m). Antibodies and fluorescence probe were purchased from Sigma.

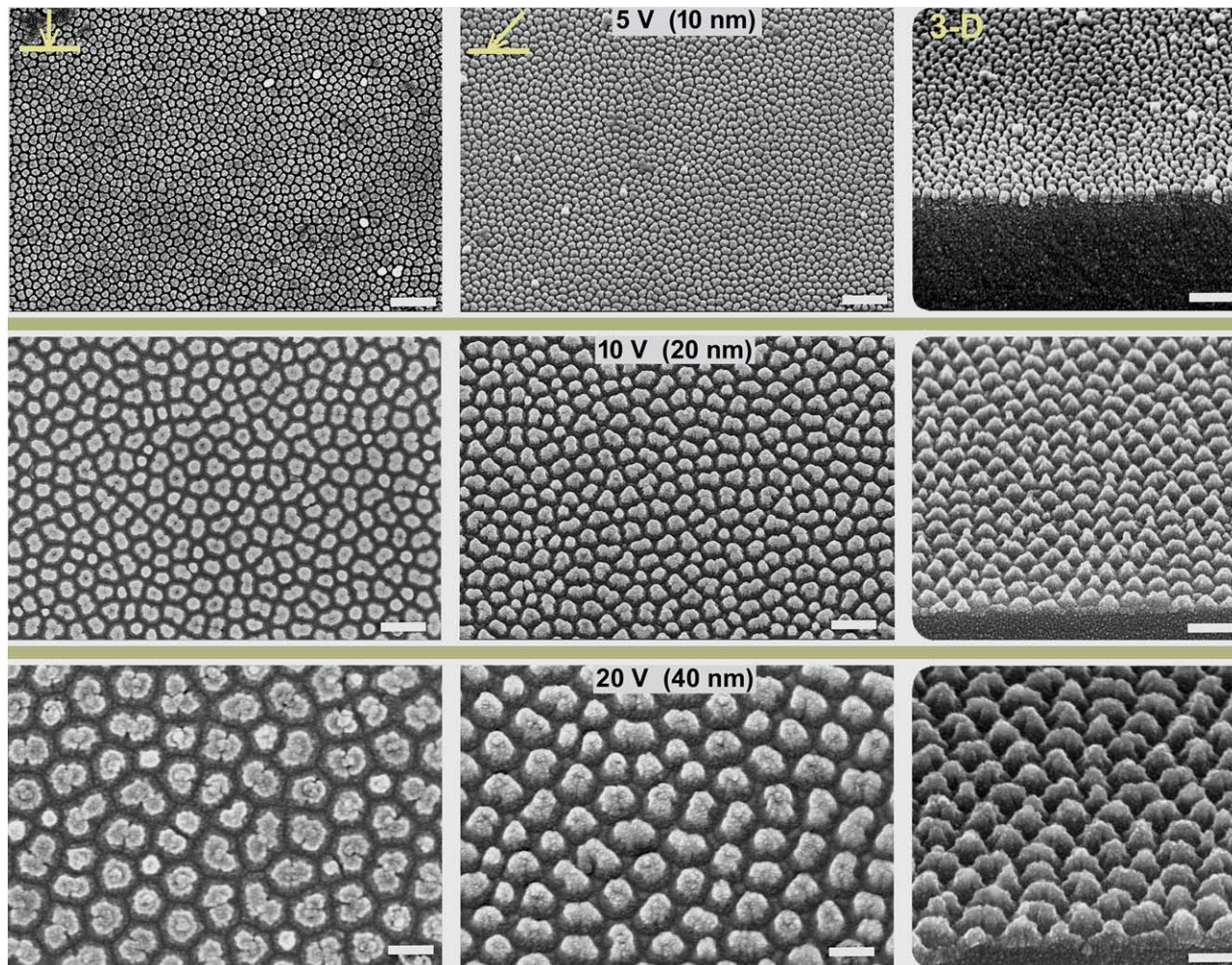


FIGURE 2. SEM images of the surfaces (vertical and tilted views) and cross-fractures (3D views) of the metal-oxide nano-mounds derived from the Al/Ta layers anodized at potentials of 5 V (upper panel), 10 V (middle panel), and 20 V (lower panel); the formation process is sketched in Figure 1. Scale bars are 50 nm for all images.

Statistical analysis

The mean values and standard deviations were calculated for the biological experimental data. Student's *t* test was used to determine significant differences between the groups. *p*-values of <0.05 and <0.01 were regarded as statistically significant.

RESULTS

Film morphology and composition

SEM images of the surfaces and cross-fractures of the nano-mounds derived from the Al/Ta coatings anodized at potentials of 5, 10, and 20 V and then re-anodized, respectively, to 8, 15, and 25 V (vs. Ag/AgCl) are shown in Figure 2. From the surface views, the mounds are shaped as distorted hexagons with wider bases and smooth edges. The cone-like tops of the mounds are composed of an Al₂O₃-doped Ta₂O₅ oxide, which will be explained in detail in the Discussion section. An example of the modeled film prepared via PAA-assisted anodization of tantalum is shown in Figure 3 while Table I summarizes the measured and calculated parameters of the three types of nano-

mound arrays prepared in this work. With increasing formation potential, the mean size of the nano-mounds systematically increases from 10 to 40 nm, the center-to-center distance changes from 12.5 to 50 nm, while the mean spacing between the mounds widens from 2 to 10 nm.

Figure 4 shows the contact angle for water droplets measured on the flat (reference) Ta₂O₅ surface and on the three types of nanostructured surfaces prepared in this study. As seen, the surface of the 10-nm nano-mounds has an improved hydrophilic behavior ($51.6 \pm 4.8^\circ$) relative to the flat film ($58.5 \pm 2.6^\circ$), while with increasing size of the mounds the films become relatively more hydrophobic, with the contact angle slightly exceeding 60° .

Cell adhesion in complete and serum-free media

The cells were seeded onto the samples under the two distinguished conditions, that is, in complete (10% FBS) and serum-free media, with the same population densities and left for 2 h, after which the number of attached cells and the cell morphology were evaluated from the microscopic images.

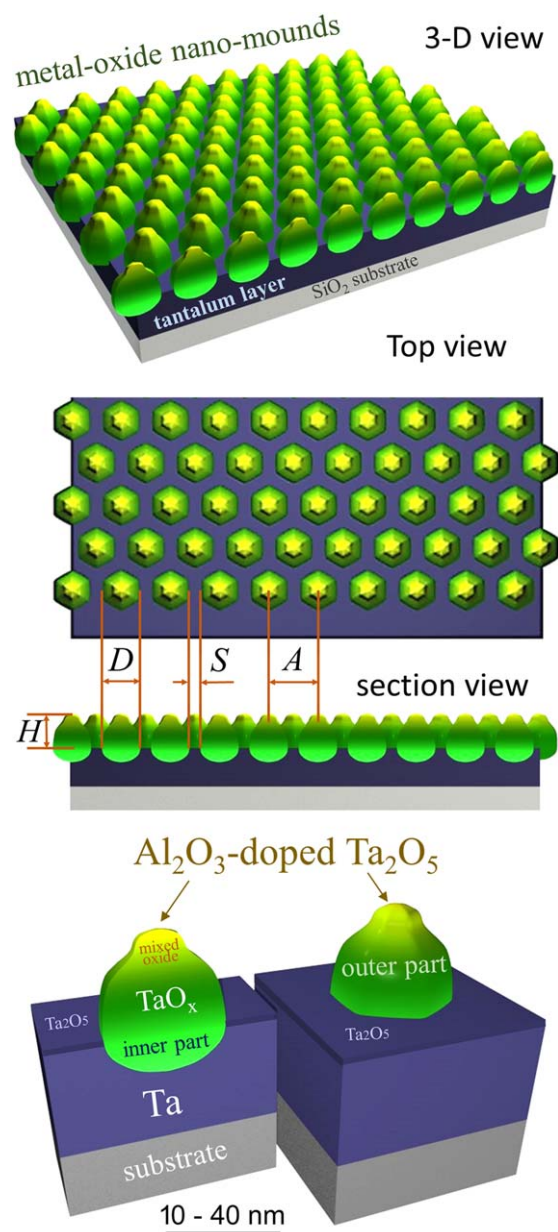


FIGURE 3. Examples of 3D computer-aided modeling of metal-oxide nano-mounds synthesized via PAA-assisted anodizing of tantalum on a substrate. Definition and the measured values of potential-dependent parameters A , D , S , and H are given in Table I.

TABLE I. Relationship between the anodizing/re-anodizing potentials and the geometrical parameters of the PAA-assisted mixed-oxide nano-mound arrays. Definition of the measured parameters is given in Figure 3.

Anodizing/re-anodizing potential/ V vs Ag/AgCl	5/8	10/15	20/30
Center-to-center distance (A)/nm	12	25	50
Diameter (D)/nm	10	20	40
Spacing (S)/nm	2	5	10
Height (H)/nm	10	20	50
Population density (P)/cm ² × 10 ¹⁰	25	12	4

Definition of the measured parameters is given in Figure 3.

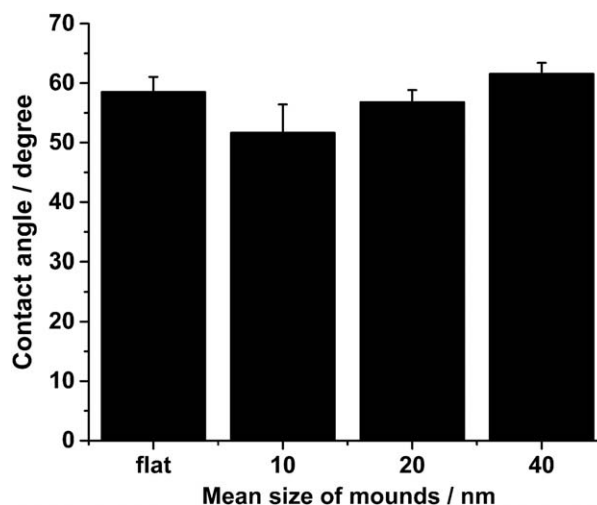


FIGURE 4. Measured values of static contact angles for water on the flat (reference) Ta₂O₅ film and 10, 20, and 40 nm nano-mound surfaces.

The results of this experiment are shown in the graphs and (c)-images of Figure 5. The following tendencies in the cell behavior are worth mentioning. The initial cell adhesion in the presence of serum proteins, being best on the flat and 10 nm nanofilm, then deteriorates with increasing size of the nano-mounds. The percentage of rounded cells remains nearly constant regardless of film structuring. Contrarily and surprisingly, in the serum-free experiment, the best cell adhesion is revealed on the 40 nm mounds, slightly deteriorating on the 20 nm mounds, dropping further on the 10 nm surface, and reaching a minimum on the flat Ta₂O₅ film. Moreover, in the serum-free medium, the population of cells weakly adhered and hence having the round shape appears to be minimal on the 20 nm mounds (18 ± 3%), increasing on the 40 and 10 nm mounds (25 ± 3% and 68 ± 2%, respectively), being maximal on the flat Ta₂O₅ film.

Cell proliferation

The reduction of tetrazolium salts is now widely accepted as a reliable way to examine cell proliferation or cell viability. The population of MG-63 cells cultured on the nanostructured surfaces was checked on days 1, 3, and 7 after cell seeding (Figure 6); the cell number was calculated from the MTT calibration curve. The results show that, while the initial cell adhesion rate is slightly unfavorable toward the bigger nano-mounds in the serum-containing medium [Figure 5(a)], cell growth is significantly promoted on the 20 and especially 40 nm nanoarrays on day 7 whereas no consistent differences are observed for the flat and 10 nm structured films.

Evaluation of ALP activity

The activity of ALP was measured on day 5 after cell seeding (Figure 7). The cells showed significantly higher biochemical activity on all the nano-structured surfaces relative to the flat Ta₂O₅ film, with best activity revealed on the 40 nm array. From the above consideration, one may see that the 40 nm structured surface is most preferred by osteoblast cells in

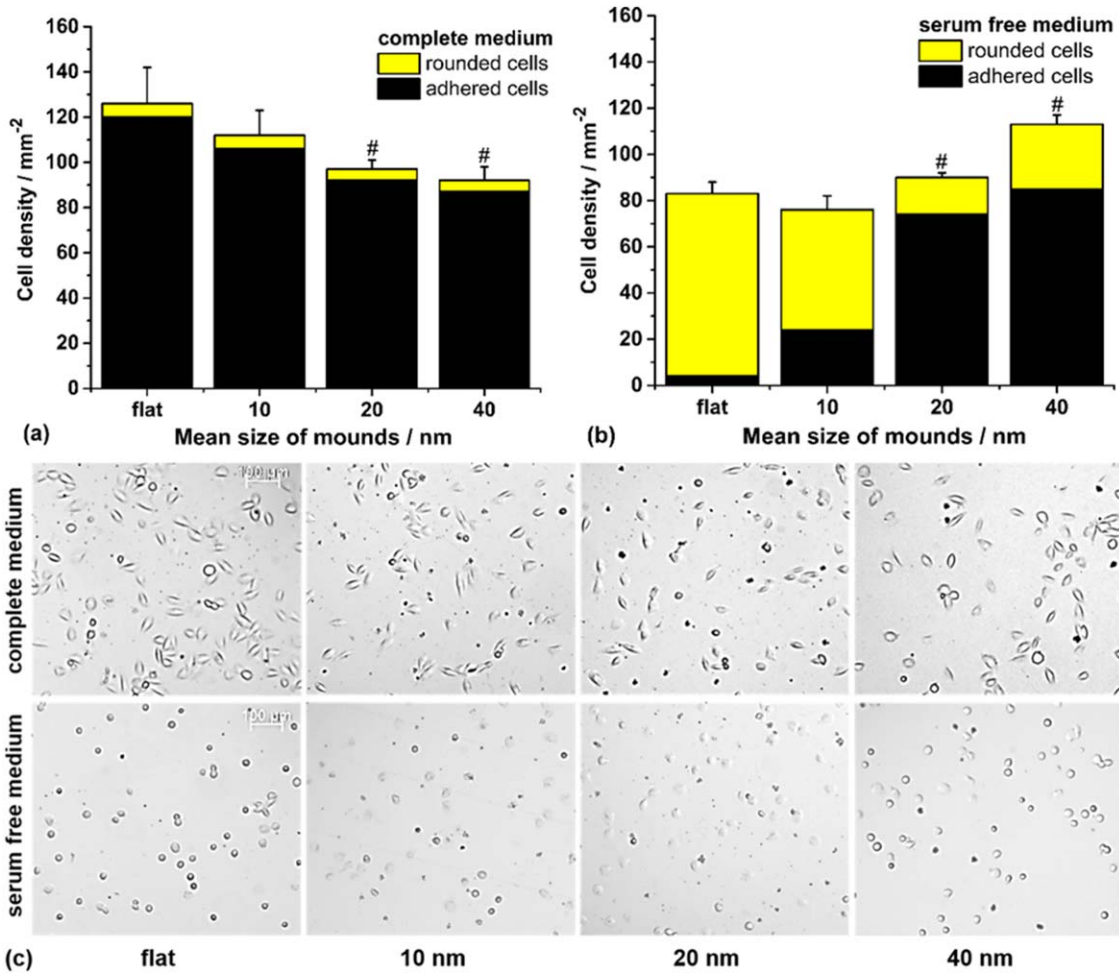


FIGURE 5. Cell adhesion and adaptation in (a) serum-containing and (b) serum-free media. MG-63 cells were seeded with the same population density on the flat Ta₂O₅ film and on the nano-mound arrays. The cell number along with cell shape were microscopically evaluated immediately after the seeding and in 2 h in both media, as shown in images of panel (c). *p* values reaching statistical significance (*p* < 0.05) between nanostructured and the flat Ta₂O₅ film are marked as # (*n* = 4).

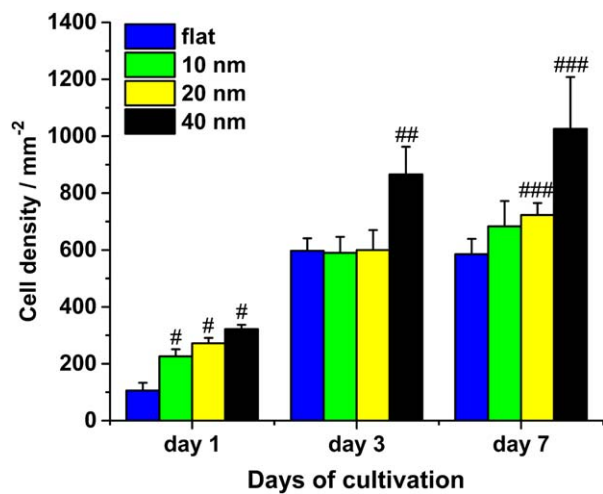


FIGURE 6. MTT proliferation test on MG-63 cells cultured on the flat Ta₂O₅ film and 10 to 40 nm nano-mounds evaluated on days 1, 3, and 7 after seeding the cells. # indicates *p* < 0.05 for day 1, ## indicates *p* < 0.05 for day 3, and ### indicates *p* < 0.05 for day 7, all relative to the flat surface (*n* = 8).

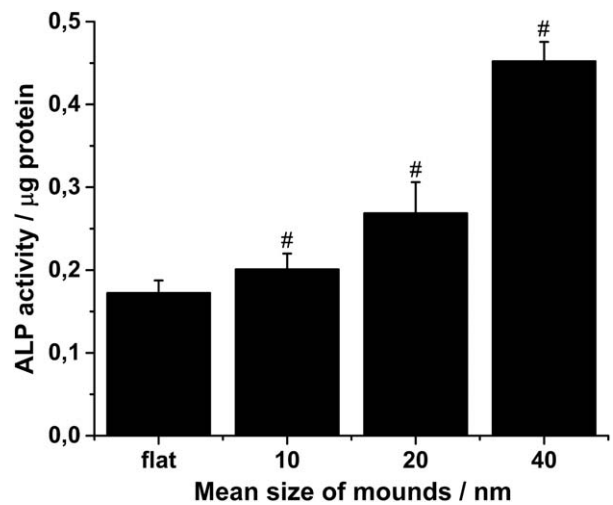


FIGURE 7. Activity of ALP of MG-63 cells on day 5 versus the size of the nano-mounds. The # indicates *p* < 0.01 relative to the flat Ta₂O₅ film (*n* = 8).

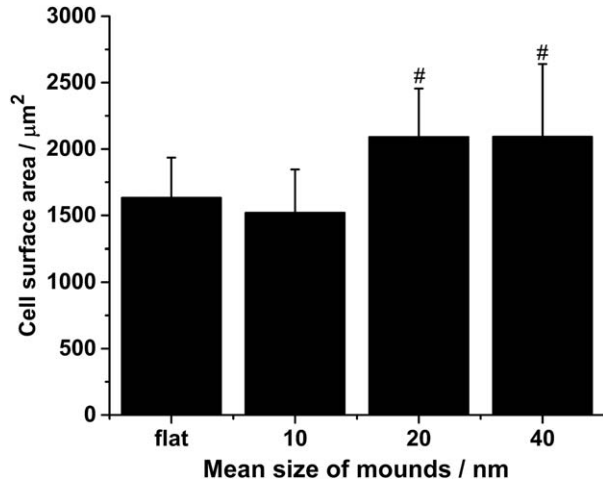


FIGURE 8. Evaluation of cell surface area on the flat Ta_2O_5 film and 10 to 40 nm mixed-oxide nano-mound arrays. # indicates $p < 0.01$ relative to the flat film ($n = 30$).

terms of adhesion, proliferation, and metabolic activity and can thus be first considered for tissue engineering.

Cell surface area and immunostaining

In this work, with help of a Java-based image processing program (ImageJ), the cell surface area was displayed and analyzed on day 1 after cell seeding. The results show that the

cells occupy larger areas on the 20 and 40 nm structured surfaces compared with the flat and 10 nm structured films, on which no significant differences are observed, as seen from the graph of Figure 8 and (a)-images in Figure 9. Furthermore, experiment on fluorescence staining of actin filaments show that the cells spread on the nanostructured surfaces have a more spherical shape with a well-organized cytoskeleton and well developed lamellipodia, as seen in (b)-images of Figure 9. The cells on the flat Ta_2O_5 film have more compact shapes, being also spread with organized actin stress fibers, while the lamellipodia seem to be more reduced. All surfaces tested here exhibited the huge filopodia projections, as showed in (c)-images of Figure 9. From the focal adhesion view-point, the cells spread on the 20 and 40 nm structured surfaces create more focal points compared with the flat film and the 10 nm structures, as seen in (d)-images of Figure 9. Thus, it is suggested that the larger surface area taken by the well-spread cells and more focal contacts created on the 20 and 40 nm arrays are due to the more favorable topography sensed by the cells.

DISCUSSION

Analysis of SEM images of the nano-mound arrays revealed that the population density of the mounds is equal to that of pores in the corresponding anodic alumina films, that is, each nanopore causes the growth of a mound. The shape and

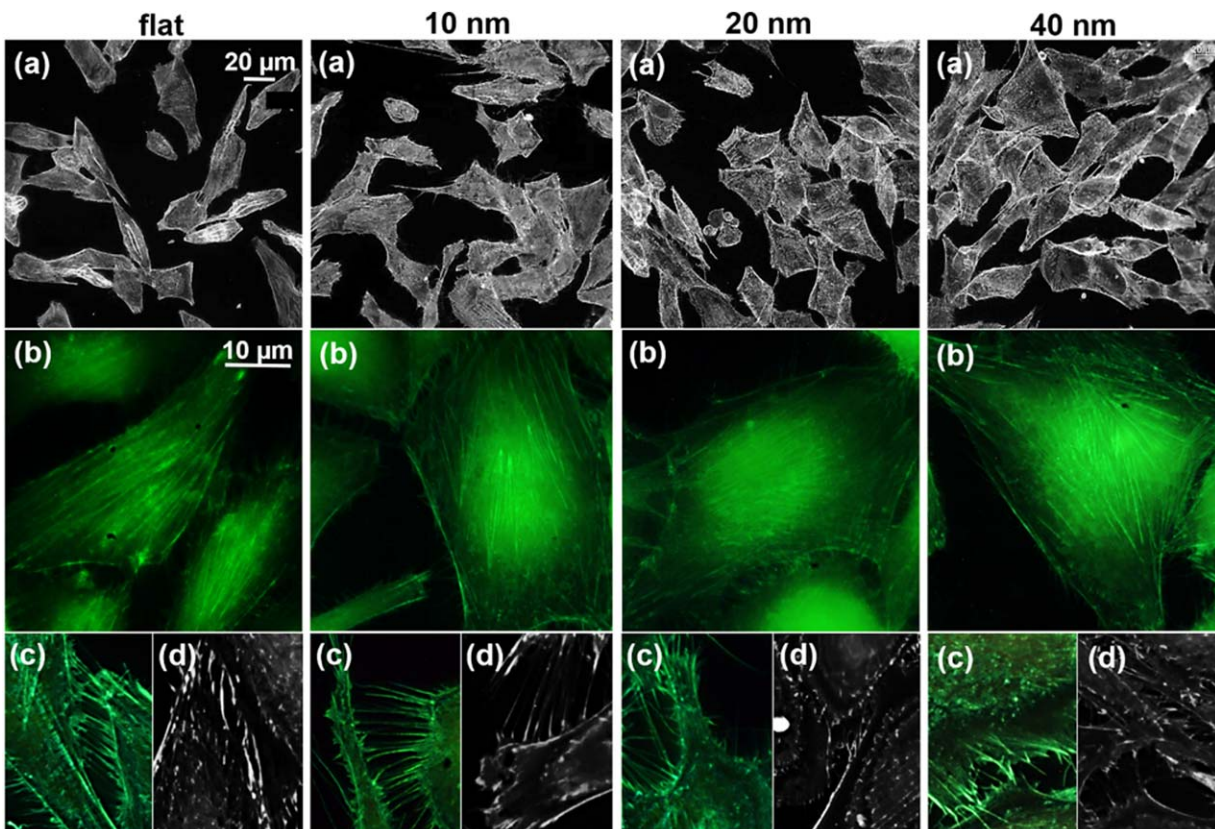


FIGURE 9. (a) Optical microscopy images showing the morphology of the cells on the nano-mound arrays. (b) Topographical fluorescence microscopy images of actin staining with (c) the details of filopodia projection of MG-63 cells cultured on the flat Ta_2O_5 film and the nano-mound arrays. (d) Images show the development of focal adhesion contacts by staining of vinculin.

dimension of the oxide nano-mounds are determined by the hexagonal configuration and size of the alumina cells, being further affected by the field-assisted solid-state reactions and stress generation at the alumina/tantalum interface.³² An important feature is that the spacing between the mounds (the darker areas in the micrographs of Figure 2) is self-organized in a network consisting of Ta₂O₅ nano-gaps having rather constant width despite the differences in size distribution inevitable among the mounds. The mound size distribution is due to the variation in pore diameters in a thin alumina film, unlike the case of much deeper anodizing of aluminum foils (approximately 20–200 μm).³³ No residual Al metal is observed over the spacing, which means that the aluminum was fully consumed during the anodic process. Based on the SEM examination and with reference to previous work on the formation and compositional analysis of tantalum-oxide nano-hillocks via PAA-assisted anodization in sulfuric acid electrolytes,²⁸ idealized 3D models are now developed with a computer-aided graphic software to elaborate the details of the surface morphology, oxide/substrate interface, and compositional profile within an array of the oxide nano-mounds (Figure 3).

As has been reported,²⁸ PAA-assisted anodizing of Ta underlayer in sulfuric acid solutions results in covering the tantalum metal network around the mounds with a layer of anodic oxide, obviously thicker than 5 nm, such that Ta metal is not x-ray photoelectron-spectroscopy-detected at the film surface even after an Ar-ion sputter-cleaning cycle. This is unlike the case of PAA-assisted anodization of Ta in *oxalic-acid* electrolytes,²⁹ where the oxide nanodots grow well separated by metallic tantalum having no anodic film over it. Thus, the technique used in the present work seems advantageous for biomedical application as it waves any uncertainty that may arise due to the contribution of metallic tantalum to the sensitive cell response. Moreover, the PAA-assisted anodization of tantalum metal results in a compositional depth profile within the nano-mounds owing to the specific co-operative ionic transport through the alumina barrier layer. This ends with the self-organized formation of an Al₂O₃-doped Ta₂O₅ oxide region located at the tops of the nano-mounds. As such mixing occurs under the high electric field, the mixed-oxide region forms as a ceramic-like outer layer over each nano-mound. Thus, the tops of the nano-mounds possess a unique combination of nano-mechanical properties and chemical stability, which makes the material extraordinary resistive in aggressive media, even in an SF₆ plasma commonly used in micro-fabrication for dissolution of Ta and Ta₂O₅. This implies that the material composing the mounds may not dissolve in the living cell environment and hence neither Ta⁵⁺ nor Al³⁺ ions may be injected in the surrounding media. A minor amount of sulfur-containing impurities originating from the electrolyte and incorporated in the nano-mounds is coordinated within the material and also may not dissolve away from the refractory-oxide nanocomposite.

All the films prepared here revealed the hydrophilic character, with the contact angles slightly increasing (approximately 51–61°) with increasing the size of the mounds, which generally fits the data reported elsewhere.²⁵ Although many

relevant studies point out that the cell attachment and spreading are favored on moderate hydrophilic biomaterial surfaces compared with hydrophobic surfaces,³⁴ the concept of cell-surface interaction is far too complex and unpredictable to approach the idea of strict correlation between the contact angle for water and cell behavior with a degree of caution.³⁵ Apparently, other factors, such as the film chemistry, topography, or protein adsorption may direct the behavior of living cells in a much more definite way than the surface wettability of a biomaterial.³⁶

One of the objectives was to evaluate the influence of adsorbed serum proteins, as a link between the surface topography and the cells, on the initial cell adhesion. Serum supplemented culture medium contains proteins, whose adsorption on biomaterials is primarily dependent on the chemistry and topography of the material surface and may significantly influence cell adhesion.³⁷ It is well known that cell adhesion is determined by the properties of substrates,¹⁰ being also time dependent. Although under the serum-free condition it is not possible to reliably evaluate the cell adhesion for longer times, the initial behavior of cells on the bare substrates gives the important characterization of cytocompatibility of the nanostructured coatings. Our findings showed clearly that, without serum proteins, the osteoblast-like cells are capable of effectively recognizing the differences in the film nano-morphologies and likely the chemical composition of the films. Obviously, the cells prefer most the 40 nm mounds and slightly less the 20 nm mounds, as confirmed by the higher number of cells flattened on these surfaces, especially in comparison with the flat Ta₂O₅ film, on which the cells are poorly adhered and keep their round shape [Figure 5(c)]. In the serum-containing medium, only ~5% of cells retain their round shape on all examined surfaces, which is obviously due to pre-adsorption of protein. Thus, in the serum-containing medium, the majority of cells exhibit good adhesion and get an elongated shape, slightly preferring the 10 nm mound array.

The proliferation of MG-63 cells was evaluated within 7 days using widely used MTT assay. It should be noted that the role of nanoscale features of various biomaterials in cell proliferation has been the subject of many studies, resulting however in contradictory reports,^{38,39} some noticing no impact of the nanoscale roughness on either proliferation of osteoblast cells or protein adsorption.⁴⁰ Our findings seem to complement well the previously reported results on biocompatibility of oxide nanodots synthesized from TaN layers, showing that the 50 nm morphology promoted best proliferation rate.^{24,25} To assess the influence of differently sized nano-mounds on the osteogenic cell contact, ALP activity was measured and normalized to total protein concentration. ALP enzyme is an efficient marker of osteoblast maturation, differentiation, and bone formation. Despite the published reports showing that the increased proliferation happens along with the increased ALP activity,^{41,42} a few contradictory conclusions are also found in the literature.^{39,43} Considering the diversity in cell lines, chemistry, and types of nano-morphologies of potential biomaterials for tissue engineering, it is obvious that the processes of cell-

material interaction should receive more studies and interpretations, followed by detailed comparisons of various authors' results, prior to making final conclusions and deciding the areas of application.

Cellular morphology is an important factor used in characterization of healthy cells, and it is influenced by the biomaterial properties. Cells adhering to, and spreading out on, a biomaterial could sensitively recognize the topography, chemistry, charge, and even more surface and interface phenomena.^{3,5,6} Generally speaking, although rather similar effects of the surface topography on cell morphology and activity have been described for various nanostructured biomaterials,⁴⁴ the reported results cannot yet be well summarized and described conceptually due to the complexity of experiments, the high number of important variables, and conflicting results obtained by different authors. For example, it has been shown that the progressive adhesion and shape elongation of cells onto the 70 and 100 nm TiO₂ nanotubes induced higher expression of ALP and other markers,⁴⁵ whereas rather contradictory conclusions on the preferable nanotube diameters smaller than 50 nm have been made in another related work.²³ Moreover, a great variety in the adhesion, proliferation, and differentiation behaviors have been obtained for the same or similar surface morphologies but in relation with different cell lines.^{22,46} It is evident that more multi-disciplinary studies are needed to fully define all aspects relative to the physico-chemical and biological characteristics of bioactive surfaces, including the search for new metal, metal-oxide, and composite biomaterials. More specifically, a concept of biomaterials with nanostructured surfaces should be established based on consideration of biocompatibility and bioactivity of cells in contact with such surfaces. The interaction of proteins and ions with bioactive materials, which may significantly impact the processes at the material/cell interface should also be studied with the focus on surface nanostructuring. Furthermore, exploring the relations between antibacterial properties and biocompatibility of nanomaterials and bioactivity of cells remains a great challenge due to the lack of relevant studies. However, our findings seem to agree with main results of applying proliferation assay and evaluating ALP activity of the cells in relation with the physical sizes and morphological features of the mixed-oxide nano-mounds developed in this work.

CONCLUSION

Arrays of composite-oxide nano-mounds self-aligned on substrates have been fabricated via PAA-assisted anodization of thin Ta layers in sulfuric acid electrolytes to address the specific topography and size range for the mounds of 10–40 nm, which has not been considered in previous studies. The films were examined in relation with the adhesion, proliferation, and ALP activity of osteoblast-like cells, with the following major conclusions emerging:

1. Detailed consideration of the film morphology and surface chemistry allows for precisely distinguishing between the nano-mounds themselves composed on Al₂O₃-doped Ta₂O₅

ceramic-like nanomaterial and a regular network of tantalum pentoxide separating the mounds. These details helped systematically consider the effect of composition, shape, population density, and physical sizes on the sensitive osteoblast-like cell response.

2. The adhesion of MG-63 cells to the nanostructured surfaces differs in the presence and absence of serum proteins. It is shown for the first time that the cells are able to sensitively recognize the features of surface structuring without pre-adsorbed proteins. The 20 nm and especially 40 nm nanoarrays in the absence of serum evoke best cell adhesion, probably due to the preferred relation between the composition, sizes, and spacing of the mixed-oxide nano-mounds. The cells show significantly higher proliferation and ALP activity on all the nanostructured surfaces relative to the flat Ta₂O₅ film, with best behavior revealed on the 40 nm array.
3. The well-organized actin fibers grow at all the nano-mound arrays, with the largest surface area and vinculin expression found on the 20 and 40 nm mounds. This is explained by the more favorable topographies of the bigger-size nanoarrays sensed by the cells as compared with that of the flat and 10 nm structured surfaces. Conceptually, the evolution of MG-63 cell morphology fits well the cell proliferation and ALP activity revealed in relation with increasing sizes of bioactive nano-mounds developed and examined in this work.

Apart from the practical importance of the concrete findings, the results and their interpretation may also contribute to conceptually understanding the interaction of living cells with the metal-oxide nanostructured biomaterials supporting the regeneration of damaged organs and tissues in human body.

ACKNOWLEDGMENT

This research was carried out under the project CEITEC 2020 (LQ1601) with financial support from the Ministry of Education, Youth, and Sports of the Czech Republic under the National Sustainability Program II.

REFERENCES

1. Levine BR, Sporer S, Poggie RA, Della Valle CJ, Jacobs J. Experimental and clinical performance of porous tantalum in orthopedic surgery. *Biomaterials* 2006;27:4671–4681.
2. Minagar S, Berndt ChC, Wang J, Ivanova E, Wen C. A review of the application of anodization for the fabrication of nanotubes on metal implant surfaces. *Acta Biomater* 2012;8:2875–2888.
3. Divya Rani VV, Vinoth-Kumar L, Anitha VC, Manzoor K, Deepthy M, Nair Shantikumar V. Osteointegration of titanium implant is sensitive to specific nanostructure morphology. *Acta Biomater* 2012;8:1976–1989.
4. Wang N, Li H, Wang J, Chen S, Ma Y, Zhang Z. Study on the anti-corrosion, biocompatibility, and osteoinductivity of tantalum decorated with tantalum oxide nanotube array films. *ACS Appl. Mater. Interfaces* 2012;4:4516–4523.
5. Pan H, Hung Y, Sui Y, Huang GS. Topographic control of the growth and function of cardiomyoblast H9c2 cells using nanodot arrays. *Biomaterials* 2012;33:20–28.
6. Rivera-Chacon DM, Alvarado-Velez M, Acevedo-Morantes YC. Fibronectin and vitronectin promote human fetal osteoblast cell attachment and proliferation on nanoporous titanium surfaces. *J Biomed Nanotechnol* 2013;9:1092–1097.



7. Neoh KG, Hu X, Zheng D, Kang ET. Balancing osteoblast functions and bacterial adhesion on functionalized titanium surfaces. *Biomaterials* 2012;33:2813–2822.
8. Tsuchiya H, Macak JM, Muller L, Kunze J, Muller F, Greil P, Virtanen S, Schmuki P. Hydroxyapatite growth on anodic TiO₂ nanotubes. *J Biomed Mater Res A* 2006;77:534–541.
9. Kokubo T, Kim HM, Kawashita M. Novel bioactive materials with different mechanical properties. *Biomaterials* 2003;24:2161–2175.
10. Lan G, Li M, Tan Y, Li L, Yang X, Ma L, Yin X, Xia H, Zhang Y, Tan G, Ning Ch. Promoting bone mesenchymal stem cells and inhibiting bacterial adhesion of acid-etched nanostructured titanium by ultraviolet functionalization. *J Mater Sci Technol* 2015;31:182–190.
11. Gittens RA, McLachlan T, Olivares-Navarrete R, Cai Y, Berner S, Tannenbaum R, Schwartz Z, Sandhage KH, Boyan BD. The effects of combined micron-/submicron-scale surface roughness and nanoscale features on cell proliferation and differentiation. *Biomaterials* 2011;32:3395–3403.
12. He M, Chen X, Cheng K, Weng W, Wang H. Enhanced osteogenic activity of TiO₂ nanorod films with microscaled distribution of Zn-CaP. *ACS Appl. Mater. Interfaces* 2016;8:6944–6952.
13. Sjöström T, Dalby MJ, Hart A, Tare R, Oreffo ROC, Su B. Fabrication of pillar-like titania nanostructures on titanium and their interactions with human skeletal stem cells. *Acta Biomater* 2009;5:1433–1441.
14. Majeed A, He J, Jiao L, Zhong X, Sheng Z. Surface properties and biocompatibility of nanostructured TiO₂ film deposited by RF magnetron sputtering. *Nanoscale Res Lett* 2015;10:56.
15. Miyauchi T, Yamada M, Yamamoto A, Iwasa F, Suzawa T, Kamijo R, Baba K, Ogawa T. The enhanced characteristics of osteoblast adhesion to photofunctionalized nanoscale TiO₂ layers on biomaterials surfaces. *Biomaterials* 2010;31:3827–3839.
16. Das K, Bose S, Bandyopadhyay A. TiO₂ nanotubes on Ti: Influence of nanoscale morphology on bone cell-materials interaction. *J Biomed Mater Res A* 2009;90:225–237.
17. Balla VK, Bodhak S, Bose S, Bandyopadhyay A. Porous tantalum structures for bone implants: Fabrication, mechanical and in vitro biological properties. *Acta Biomater* 2012;6:3349–3359.
18. Hacking SA, Bobyn JD, Toh K, Tanzer M, Krigyer JJ. Fibrous tissue ingrowth and attachment to porous tantalum. *J Biomed Mater Res* 2000;52:631–638.
19. Dolatshahi-Pirouz A, Jensen T, Kraft DCh, Foss M, Kingshott P, Hansen JL, Nylandsted Larsen A, Chevallier J, Besenbacher F. Fibronectin adsorption, cell adhesion, and proliferation on nanostructures tantalum surfaces. *ACS Nano* 2010;4:2874–2882.
20. Bauer S, Park J, Faltenbacher J, Berger S, von der Mark K, Schmuki P. Size selective behavior of mesenchymal stem cells on ZrO₂ and TiO₂ nanotube arrays. *Integr Biol* 2009;1:525–532.
21. de Arruda Rodrigues C, de Tacconi NR, Chanmanee W, Rajeshwar K. Cathodic electro-synthesis of niobium oxide one-dimensional nanostructures with tailored dimensions. *Electrochim Solid-State Lett* 2010;13:B69–B72.
22. Findlay DM, Welldon K, Atkins GJ, Howie DW, Zannettino AC, Bobyn D. The proliferation and phenotypic expression of human osteoblasts on tantalum metal. *Biomaterials* 2004;25:2215–2227.
23. Park J, Bauer S, von der Mark K, Schmuki P. Nanosize and vitality: TiO₂ nanotube diameter directs cell fate. *Nano Lett* 2007;7:1686–1691.
24. Dhawan U, Pan HA, Lee CH, Chu YH, Huang GS, Lin YR, Chen WL. Spatial control of cell-nanosurface interactions by tantalum oxide nanodots for improved implant geometry. *PLoS One* 2016;11:e0158425.
25. Pan H-S, Hung Y-C, Su C-W, Tai S-M, Chen C-H, Ko F-H, Huang GS. A nanodot array modulates cell adhesion and induced an apoptosis-like abnormality in NIH-3T3 cells. *Nanoscale Res Lett* 2009;4:903–912.
26. Hung Y-C, Pan H-A, Tai S-M, Huang GS. A nanodevice for rapid modulation of proliferation, apoptosis, invasive ability, and cytoskeletal reorganization in cultured cells. *Lab Chip* 2010;10:1189–1198.
27. Surganov V, Mozalev A. Kinetics of thin-film aluminum-tantalum anodization studied with electron microscopy. In: *Extended Abstracts: 40th ISE Meeting, Vol. 2, p. 81, Kyoto, Japan, September 17–22, 1989, published by The International Society of Electrochemistry*, pp 1364.
28. Mozalev A, Sakairi M, Saeki I, Takahashi H. Nucleation and growth of the nanostructured anodic oxides on tantalum and niobium under the porous alumina film. *Electrochim Acta* 2003;48:3155–3170.
29. Mozalev A, Gorokh G, Sakairi M, Takahashi H. The growth and electrical transport properties of self-organized metal/oxide nanostructures formed by anodizing Ta-Al thin-film bilayers. *J Mater Sci* 2005;40:6399–6407.
30. Mozalev A, Sakairi M, Takahashi H, Habazaki H, Hubálek J. Nanostructured anodic-alumina-based dielectrics for high-frequency integral capacitors. *Thin Solid Films* 2014;550:486–494.
31. Vrublevsky I, Parkoun V, Sokol V, Schreckenbach J, Marx G. The study of the volume expansion of aluminum during porous oxide formation at galvanostatic regime. *Appl Surf Sci* 2004;222:215–225.
32. Mozalev A, Vazquez RM, Bittencourt C, Cossement D, Gispert-Guirado F, Llobet E, Habazaki H. Formation-structure-properties of niobium-oxide nanocolumn arrays via self-organized anodization of sputter-deposited aluminum-on-niobium layers. *J Mater Chem C* 2014;2:4847–4860.
33. Mozalev A, Magaino S, Imai H. The formation of nanoporous membranes from anodically oxidized aluminum and their application to Li rechargeable batteries. *Electrochim Acta* 2001;46:2825–2834.
34. Eriksson C, Nygren H, Ohlson K. Implantation of hydrophilic and hydrophobic titanium discs in rat tibia: cellular reactions on the surfaces during the first 3 weeks in bone. *Biomaterials* 2004;25:4759–4766.
35. Gentleman MM, Gentleman E. The role of surface free energy in osteoblast-biomaterial interactions. *Int Mater Rev* 2014;59:417–429.
36. Kennedy SB, Washburn NR, Simon Jr CG, Amis EJ. Combinatorial screen of the effect of surface energy on fibronectin-mediated osteoblast adhesion, spreading and proliferation. *Biomaterials* 2006;27:3817–24.
37. Kulkarni M, Mazare A, Park J, Gongadze E, Killian MS, Kralj S, von der Mark K, Igljč A, Schmuki P. Protein interactions with layers of TiO₂ nanotube and nanopore arrays: Morphology and surface charge influence. *Acta Biomater* 2016;45:357–366.
38. Palin E, Liu HN, Webster TJ. Mimicking the nanofeatures of bone increases bone-forming cell adhesion and proliferation. *Nanotechnology* 2005;16:1828–35.
39. Biggs MJP, Richards RG, Gadegaard N, McMurray RJ, Affrossman S, Wilkinson CDW, Oreffo RO, Dalby MJ. Interactions with nanoscale topography: Adhesion quantification and signal transduction in cells of osteogenic and multipotent lineage. *J Biomed Mater Res Part A* 2009;91:195–208.
40. Cai KY, Bossert J, Jandt KD. Does the nanometre scale topography of titanium influence protein adsorption and cell proliferation? *Colloids Surf B* 2006;49:136–44.
41. Xia L, Feng B, Wang P, Ding S, Liu Z, Zhou J, Yu R. In vitro and in vivo studies of surface-structured implants for bone formation. *Int J Nanomed* 2012;7:4873–4881.
42. Popat KC, Daniels RH, Dubrow RS, Hardev V, Desai TA. Nanostructure surfaces for bone biotemplating applications. *J Orthop Res* 2006;24:619–627.
43. Zhao L, Mei S, Chu PK, Zhang Y, Wu Z. The influence of hierarchical hybrid micro/nano-textured titanium surface with titania nanotubes on osteoblast functions. *Biomaterials* 2010;31:5072–82.
44. Ball M, Grant DM, Lo W-J, Scotchford CA. The effect of different surface morphology and roughness on osteoblast-like cells. *J Biomed Mater Res A* 2008;86:637–647.
45. Oh S, Brammer KS, Li YSJ, Teng D, Engler AJ, Chien S, Jin S. Stem cell fate dictated solely by altered nanotube dimension. *PNAS* 2009;106:2130–2135.
46. Lee J, Kang BS, Hicks B, Chancellor TF Jr, Chu BH, Wang HT, Keselowsky BG, Ren F, Lele TP. The control of cell adhesion and viability by zinc oxide nanorods. *Biomaterials* 2008;29:3743–3749.

Článek 4

**Anodic formation and biomedical properties of hafnium-oxide
nanofilms**

Cite this: *J. Mater. Chem. B*, 2019,
7, 2300

Anodic formation and biomedical properties of hafnium-oxide nanofilms

Zdenka Fohlerova ^{*ab} and Alexander Mozalev ^a

Hafnium dioxide (HfO₂) is attracting attention for bio-related applications due to its good cyto-compatibility, high density, and resistance to corrosion and mechanical damage. Here we synthesize two types of hafnium-oxide thin films on substrates *via* self-organized electrochemical anodization: (1) an array of hierarchically structured nanorods anchored to a thin oxide layer and (2) a microscopically flat oxide film. The nanostructured film is composed of a unique mixture of HfO₂, suboxide Hf₂O₃, and oxide-hydroxide compound HfO₂·*n*H₂O whereas the flat film is mainly HfO₂. *In vitro* interaction of the two films with MG-63 osteoblast-like cells and Gram-negative *E. coli* bacteria is studied for the first time to assess the potential of the films for biomedical application. Both films reveal good cytocompatibility and affinity for proteins, represented by fibronectin and especially albumin, which is absorbed in a nine times larger amount. The morphology and specific surface chemistry of the nanostructured film cause a two-fold enhanced antibacterial effect, better cell attachment, significantly improved proliferation of cells, five-fold rise in the cellular Young's modulus, slightly stronger production of reactive oxygen species, and formation of cell clusters. Compared with the flat film, the nanostructured one features the weakening of AFM-measured adhesion force at the cell/surface interface, probably caused by partially lifting the nanorods from the substrate due to the strong contact with cells. The present findings deepen the understanding of biological processes at the living cell/metal-oxide interface, underlying the role of surface chemistry and the impact of nanostructuring at the nanoscale.

Received 3rd December 2018,
Accepted 25th February 2019

DOI: 10.1039/c8tb03180k

rsc.li/materials-b

1. Introduction

A biomaterial is an engineered substance specifically shaped to direct any of therapeutic or diagnostic procedures. Biomaterials differ widely in mechanical, physical, chemical, and biological properties, determining a specific biomedical application such as hard tissue replacement, fixation, making valves and heart pacemakers, or surgical instruments. Metal biomaterials such as stainless steels, cobalt-based alloys, and titanium and its alloys have been used for production of orthopedic and surgical implants for decades.¹ Various surface modifications of the metal biomaterials introducing for instance porosity, extra roughness, or diversity in surface chemistry have been the well-proved factors enhancing osteoconductive and osteoinductive responses to the implant surroundings.²

Several refractory metals including tantalum, niobium, titanium, zirconium, and hafnium have recently been explored

as alternatives for potential biomedical application due to their excellent hardness, malleability, tensile strength, high density, and melting point, complemented by natural passivity and, therefore, resistance to corrosion, and good electrical and heat conductance.³ As nowadays the raw materials are facing a shortage of supply while the production and processing costs of the bulk metals continue to increase, the mentioned metals have also been explored as alloying elements or coatings.^{4,5}

Hafnium (Hf) is a group IV transition metal, sharing the position in the periodic table with Ti and Zr. Hafnium is very dense, thermostable, malleable, and ductile. It is almost completely immune to chemical attack and it has a good resistance to mechanical damage due to its hardness. These properties have made it indispensable for many applications³ and also attractive for biomedicine.^{6,7} To date, the research reports on pure hafnium metal as a biomaterial have been limited by the implementation of hafnium wires or a thin plate *in vivo*^{3,8} and investigation of corrosion properties of pure hafnium in a biological environment.⁷ Hafnium has been more explored as a component of biomedical alloys, in combination with Ti, Ta, or Nb. For instance, the apatite-forming ability of Ti-Hf alloys has been utilized for bone bonding.⁹ Bulk hafnium alloys have been investigated for their mechanical properties,^{10,11} cytocompatibility, and hemocompatibility,¹² cell-surface interaction,

^a CEITEC – Central European Institute of Technology, Brno University of Technology, Purkynova 123, 612 00 Brno, Czech Republic.
E-mail: zdenka.fohlerova@ceitec.vutbr.cz

^b Brno University of Technology, Faculty of Electrical Engineering and Communication, Department of Microelectronics, Technicka 10, 616 00 Brno, Czech Republic

and protein adsorption.¹³ The results have shown that the Hf-based alloys have a potential for application as biomaterials, especially for regenerative medicine and tissue engineering.

To avoid undesirable tissue reactions that may be caused by released metal ions, the focus of biomaterials research has moved from the metals and metal alloys to metal oxides (ceramics) and composites (metals with metal-oxide or ceramic coatings).¹⁴ In this regard, hafnium dioxide (HfO₂) is attracting attention for potential application, for example, as implants due to its high resistance to corrosion and compression and low electrical and thermal conductivities. Moreover, recent advances in surface structuring at the nanoscale have accelerated preparation and application of metal-oxide biomaterials substantially improving in some sense cells/surface interaction, bioactivity, and resistance to corrosion. Modern fabrication and analysis approaches have made it possible to precisely investigate the complex effects of surface nanostructuring^{15,16} and further modifications¹⁷ on the cell/surface interface, protein adsorption, metabolic activity, bacterial adhesion, or biofilm formation in relation to nano-mechanical, chemical, and biological properties of nanostructured surfaces.

Hafnia-based nanostructures and nanostructured coatings have been developed as nanoporous hafnia *via* anodic oxidation/dissolution of hafnium foil,^{18,19} nanotubes within the anodic alumina templates *via* atomic layer deposition,²⁰ nanorods, nanosprings, and nanohelix by electron-beam evaporation,²¹ or hafnia nanoparticles through chemical synthesis.^{22–24} The most recent report describes the hafnium-oxide coatings with the unique self-organized nanostructured 3-dimensional architectures and tunable sizes, ranging 10 to 400 nm, synthesized *via* the anodizing of aluminum-on-hafnium (Al/Hf) metal layers.²⁵ The films consist of arrays of upright-standing hafnium-oxide nanorods anchored to a continuous hafnium-oxide bottom layer. The method is superfast, easy to implement, highly reproducible, cost-effective, and environmentally friendly. Although some cytotoxicity and antibacterial tests have been performed to hafnia nanoparticles and nanopowders,^{26,27} there have been no reports on interaction of any nanostructured HfO₂ films or coatings with living cells in an *in vitro* environment. Neither antibacterial properties of any known hafnium-oxide nanostructured coatings have been explored.

In our work to date, a hafnium-oxide nanorod array has been synthesized *via* electrochemical anodization of Al/Hf metal layers generally following the approach described in the previous work²⁵ and involving certain modifications to advance the morphology and chemical composition and optimize the film nanostructure through the adjustment of forming conditions to better meet the requirements for biomedical application. A combinatorial study has been performed to reveal the behavior of MG-63 osteoblast-like cells and viability of Gram-negative *E. coli* bacteria spread over the hafnium-oxide nanostructured film. For comparison, a thin anodic hafnium-oxide film with a microscopically flat morphology has also been prepared and made the subject of investigation. The vertical scratching technique available with an atomic force microscope (AFM) has been tried for the first time to measure and compare the stiffness and

adhesion force of cells on the structured and non-structured hafnium-oxide nanofilms. The surface and cell/film interface have been examined by high-resolution scanning electron microscopy (SEM) and X-ray photoelectron spectroscopy (XPS). Proliferation of model tissue cells and bacteria, protein adsorption, and oxidative stress have been revealed by optical spectroscopy and microscopy methods. The applied combination of advanced electrochemical fabrication, surface analysis, and biological characterization techniques was expected to explore the potential of the PAA-assisted hafnium-oxide nanofilm for biomedical applications and, more generally, improve the understanding of interaction of living cells and bacteria with metal-oxide nanostructured coating and films.

2. Experimental

2.1 Film preparation and characterization

A 100 mm thermally oxidized silicon wafer was used as a substrate for coating formation. A layer of hafnium, 100 nm thick, followed by a layer of aluminum, 400 nm thick, were successively deposited on the substrate *via* the ion-beam sputtering from respectively Hf (99.95%) and Al (99.999%) targets. The wafer with the deposited films was cut into pieces of 2 cm × 2 cm, which were then electrochemically processed in a cylindrical top-open two-electrode PTFE electrolytic bath. In the bath, the sample was placed horizontally onto a flat dielectric base, and a circle of 1.5 cm in diameter (1.8 cm²) was secured by a PTFE protecting ring attached to the upper electrolyte-containing part of the bath. The bath was filled with 300 cm³ electrolyte, the working temperature was maintained at 23 °C for all anodizing experiments. An Agilent 5752A programmable power supply, controlled by a homemade software written in LabVIEW was used as the anodizing unit. Further technical details of the anodizing setup may be found elsewhere.²⁸ Fig. 1 outlines the main stages of process for forming the hafnium-oxide (HO) nanostructured coating from the initial Al/Hf bilayer (Fig. 1a). The Al layer was first converted into a porous anodic alumina (PAA) film by anodizing in 0.2 M H₃PO₄ aqueous solution at 150 V (Fig. 1b). Then, an array of hafnium-oxide nanosized protrusions was formed on the Hf layer due to re-anodization to 300 V through the alumina nanopores (Fig. 1c). Eventually, the PAA layer was chemically dissolved away in a solution prepared as reported elsewhere²⁹ (Fig. 1c'). The specimens were rinsed in several deionized waters and dried in an oven at 120 °C for 30 min to fully desorb water from the specimen surface. For comparative experiments, the Al layer was dissolved away from the initial Al/Hf sample, and the remaining Hf metal was anodized in 0.2 M H₃PO₄ by sweeping potential from 0 to 50 V, with a rate of 0.1 V s⁻¹, followed by a 30 min current decay. This was expected to give a uniform compact anodic HfO₂ film, about 100 nm thick, with a featureless surface morphology (Fig. 1a'). The surfaces and cross fractures of the on-substrate HO nanofilms were examined in a field emission scanning electron microscope (TESCAN MIRA II), equipped with InBeam detector for secondary electrons,

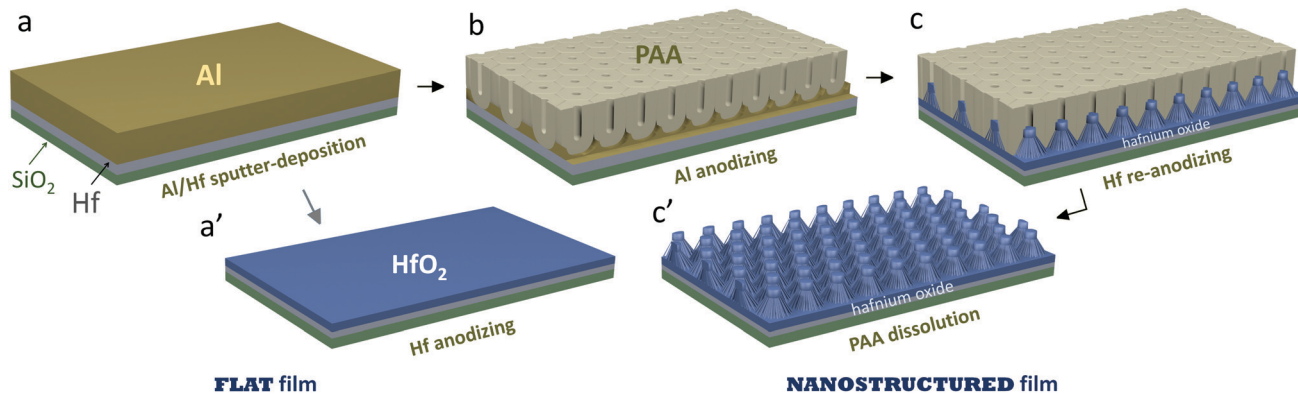


Fig. 1 Schematics for forming anodic hafnium-oxide nanofilms: (a) sputter-deposition of an Al/Hf bilayer onto a SiO₂-coated Si substrate, (b) formation of a porous anodic alumina (PAA) layer, (c) formation of hafnium-oxide nanorods via the PAA-assisted re-anodizing of the Hf underlayer, (c') dissolution of the PAA layer to finalize the nanostructured hafnium-oxide film. The flat hafnium-oxide film shown in panel (a') is prepared by chemical dissolution of the initial Al layer and subsequent compact anodization of the Hf layer.

which helps improve image resolution and allows for directly observing metal-oxide surfaces without any charge-reducing coating over the specimens. For SEM observation of cells on the nanostructured HO sample, the living cells were first fixed on the sample surface and completely dried. The fixation of cultured cells was performed by removing the culture media and rapidly dipping the samples into the 2% glutaraldehyde solution for 15 min, followed by rinsing with phosphate buffer three times over 5 minutes. Then the cells were dehydrated in 50, 70, 90, 95, and 100% ethanol series as reported elsewhere.³⁰ A thin layer of gold was magnetron sputtered over the cell-covered surfaces and cross-fractures of samples to reduce charge-accumulating effect during SEM observation. Chemical composition of the HO nanofilms was examined by XPS surface analysis carried out with a Kratos Axis Ultra DLD spectrometer using a monochromatic Al K α source. The X-ray emission energy was 150 W with a 15 kV accelerating voltage. Typical operating pressures were less than 10⁻⁹ Torr. The emitted electrons were detected at fixed pass energies of 160 eV for the survey spectra and 20 eV for the high-resolution spectra. The Kratos charge neutralizer system was used for all specimens. Experimental spectra were analyzed with CasaXPS software version 2.3.18 PR. A standard Shirley background was used in all fitted spectra. Spectra were charge-corrected to give the adventitious C 1s spectral component (C-C, C-H) a binding energy of 285.0 eV.

2.2 Cell culture

Human osteoblast-like MG-63 cells (ECACC, UK) were used for *in vitro* characterization of HO films prepared in this work. The MG-63 cells were maintained in complete Dulbecco's Modified Eagle's medium (DMEM) supplemented with 10% fetal bovine serum (FBS), 2 mM L-glutamine, and 5% penicillin/streptomycin (50 U mL⁻¹ and 50 μ g mL⁻¹ at 37 °C in a humidified 5% CO₂ incubator). The cells were harvested by trypsinization with 0.25% trypsin-EDTA at 75% confluency and seeded with a defined density onto the sterile samples placed in a polystyrene microplate.

2.3 Bacterial test of viability

Antibacterial activity against *Escherichia coli* (*E. coli*) was evaluated on the flat and nanostructured films. 45 μ L of suspension containing the bacteria was introduced on the sterilized film surfaces and incubated at 37 °C for 4 hours. Subsequently the samples were rinsed with sterile water and shortly sonicated to release the bacteria from the surfaces. The bacteria solution was diluted 100, 1000, and 10000 times before being plated on the solid agar. The agar plates with 200 μ L bacteria dilutions were incubated at 37 °C for 16 hours. Then the agar plates were photographed, and the bacteria colonies were counted. The number of colony-forming units per milliliter (CFU per mL) was calculated as the number of colonies divided by the amount plated (mL) and multiplied by the dilution.

2.4 Adsorption of proteins

Protein adsorption on the HO surfaces was analyzed using a Coomassie Brilliant Blue G. Bovine serum albumin (BSA; 1 mg mL⁻¹) and fibronectin (FN; 50 μ g mL⁻¹) stock solutions were prepared in phosphate buffer saline (PBS) and used as model proteins in this work. 50 μ L of a known concentration of the protein solution (0.5 mg mL⁻¹ BSA and 50 μ g mL⁻¹ FN) was pipetted onto the sample surface and kept in a 12-well cell culture plate for one hour inside the CO₂ incubator. The unattached proteins were collected, and their concentrations were then optically quantified. Coomassie Brilliant Blue assay was carried out by adding 250 μ L reagent to 5 μ L protein solution in a 96-well plate. The amount of unattached proteins was deduced from calibration curves and the initial amount of protein adsorbed on the surface. The calibration curves for BSA and FN proteins and the measurement of the sample solutions were performed by monitoring the absorbance at 595 nm in the 96-well plate (Beckman Coulter Paradigm).

2.5 Adhesion and proliferation assays

The initial adhesion of MG-63 cells to the HO surfaces was examined by counting the cells from images taken by an optical microscope (Axio Imager M2m, Zeiss). The cells were seeded

onto each sample surface placed in a 24-well plate at a density of 1×10^5 cells per well. The experiment was carried out 4 hours after the seeding in complete medium. Proliferation of MG-63 cells on the samples was measured with (3-(4,5-dimethylthiazol-2-yl)-2,5-diphenyltetrazolium bromide) tetrazolium assay (MTT) and evaluated on days 1, 3, and 7 after the seeding; the initial cell density was 1×10^4 cells per well. Briefly, the cells were incubated for a defined period and then gently washed twice with pre-heated PBS. The mixture of 150 μL culture medium and 50 μL tetrazolium dye (MTT, 1 mg mL⁻¹ in PBS, pH 7.4) was added into each well containing the samples. After 3-hour incubation, the samples were removed and placed into a new well-plate, this being followed by the addition of 10% sodium dodecyl sulphate (SDS). Then the samples were left overnight to solubilize the crystals of formazan produced by the cells. A 100 μL solution was transferred from each well into a new 96-well plate, and the absorbance was measured at 570 nm wavelength with a microplate spectrophotometer (Beckman Coulter Paradigm).

2.6 AFM utilization

A Bruker Dimension FastScan AFM (Bruker Nano Surfaces, Santa Barbara, CA, USA) equipped with FastScan-A probe (Bruker) was used to image surface topography in tapping mode (0.5 Hz scanning speed, image resolution 1000 \times 1000 points). Mapping of Young's modulus of the living cells was performed with a calibrated silicon nitride AFM cantilever equipped with a pyramidal silicon tip.³¹ The cantilever stiffness was calibrated by measuring its thermal noise. The force mapping procedure was performed as step by step recording of 16 \times 16 maps of force distance (FD) curves; set point 1 nN, Z length 15 μm , time per curve 0.5 s. The recorded FD curves were fitted with Bilodeau modification of Hertzian model. Gwyddion software was used to obtain numerical values of average stiffness. The vertical scratching of cells from the surface was studied with the AFM tip (Bruker SNL 10B) moving perpendicularly over the sample surface. A scanning direction of 90 degrees was used to monitor the cantilever deflection, calibrated in a standard way. A standard contact mode was used to perform the scratching study; the scanning speed was 0.25 Hz and the set point value was gradually increased in the range 0.5, 1.0, 2.0, 5.0, 7.5, 10.0 nN, until the point when the cell was scratched away from the surface.

2.7 Oxidative stress measurement

Qualitative detection of oxidative stress was performed microscopically with the cell permeant reagent 2',7'-dichlorofluorescein diacetate (DCFDA). The oxidative stress in cells cultured on the HO surfaces was examined in 24 hours after seeding the cells. The same experiment was performed with a piece of plastic used as a control (reference). Before the experiment the cells were seeded on the HO and plastic surfaces and washed in PBS. 25 μM DCFDA in PBS was added to stain cells for 15 min at 37 $^\circ\text{C}$. The samples were then rinsed in PBS and imaged in differential interference contrast (DIC) and fluorescence modes in an optical microscope at excitation/emission wavelength of 470/520 nm (Axiotron II Zeiss).

2.8 Morphology and immunostaining of actin and vinculin

To evaluate the morphology of cells and the distribution of actin filaments and vinculin on the HO surfaces, the cells were stained for β -actin and vinculin for 24 hours after seeding the cells. Briefly, the cells were washed with PBS and fixed with a fresh 4% paraformaldehyde in PBS for 15 min at room temperature. After several washing steps with PBS, the cell membrane was permeabilized in 0.1% Triton-X for 20 min. Subsequently, the cells were gently washed in PBS and incubated overnight in a blocking solution of 2% BSA. Mouse human anti-vinculin antibody (1:100 dilution) and ActinRed™ 555 (Invitrogen™) were added for 60 and 30 min, respectively. Finally, the samples were incubated with Alexa Fluor 488 goat anti-mouse antibody (1:100 dilution) for 1 hour. The cellular components were imaged and evaluated using a fluorescence microscope (Zeiss Axio Imager M2m).

2.9 Statistical analysis

The mean values and standard deviations were calculated for the biological experimental data. Student's *t*-test was used to determine significant differences between the groups. *P*-Values of <0.05 were considered as statistically significant.

3. Results and discussion

3.1 Film morphology and chemical composition

Among the three acid solutions tested so far for PAA-assisted anodizing of hafnium layers,²⁵ the phosphoric acid electrolyte was chosen since it allows for the highest formation potential of 150 V, which was estimated to give oxide nanorods aligned in an array with a pitch of about 500 nm and 7×10^8 cm⁻² population density. To optimize the height of the rods, the sample was re-anodized to a potential of 300 V, which was substantially lower than the previously reported value.²⁵ This was expected to make the hafnium-oxide nanoprotusions shorter, less than 300 nm in height, and therefore mechanically more stable, with wider tops directly connected to hafnium-oxide nanoneedles composing the bottom part of the rods. On the other hand, the potential was expected to be high enough to cause the formation of a continuous oxide layer beneath the rods, so that the remaining hafnium metal would become fully isolated from the surrounding environment by such oxide layer, as shown in the schematic of Fig. 1. This would guarantee that the anodic hafnium oxide, not the metal, will be in contact with a biological substance. Such structuring and dimension of the HO nanofilm were considered optimal for the present study, due to the reported success with PAA-assisted nanostructured oxide surfaces made on other metals, like TaN or Ti.^{32–34}

A row of SEM images in panel (a) of Fig. 2 shows the nanostructured anodic film synthesized *via* the PAA-assisted anodizing/re-anodizing at 150/300 V of an Al/Hf bilayer on a SiO₂/Si substrate and treated in the selective etchant to fully dissolve the PAA layer. SEM images in Fig. 2b demonstrate the compact HO film on the hafnium layer obtained by anodizing of the Hf layer to 50 V. As the view fields are the same in

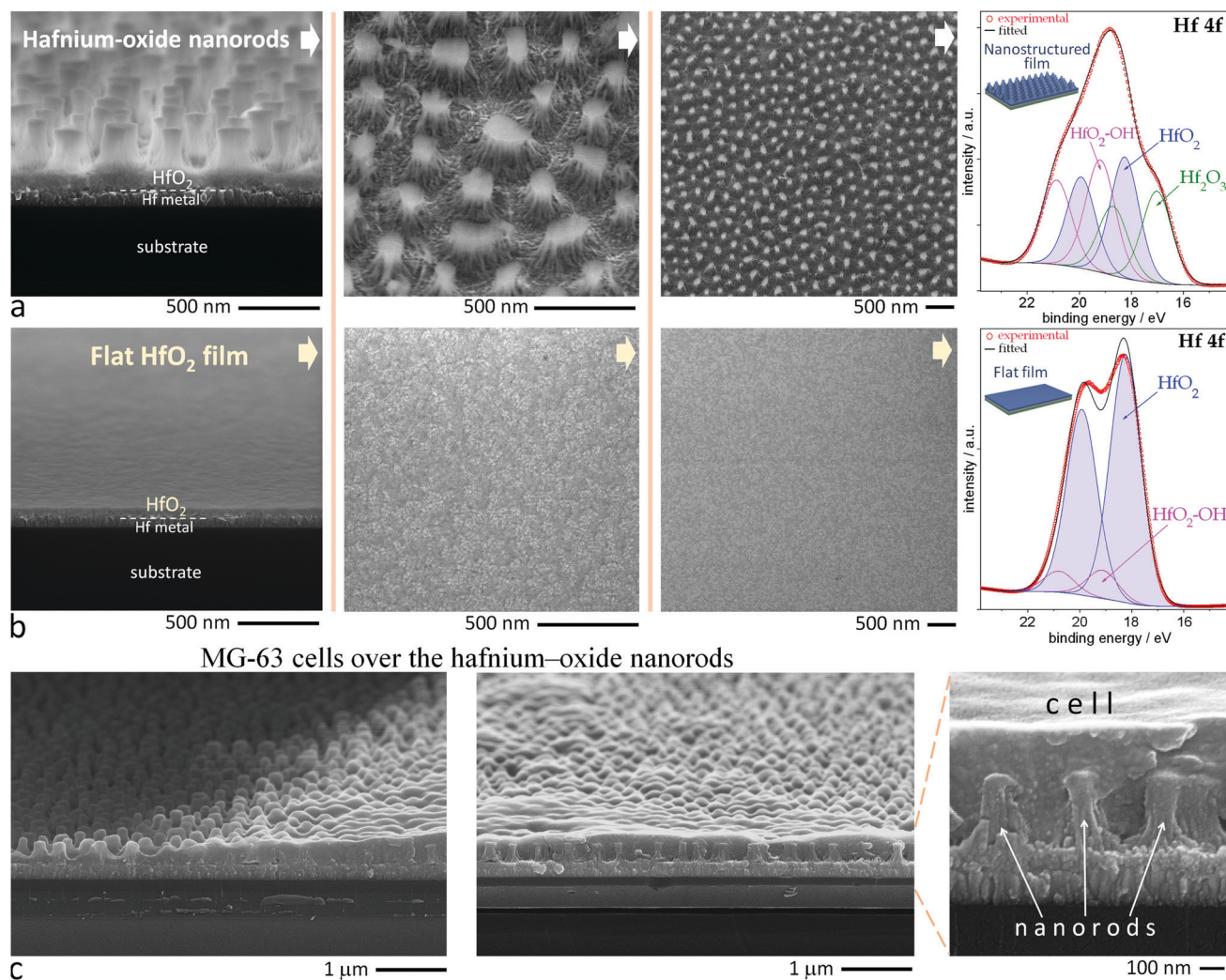


Fig. 2 Comparative SEM views of hafnium-oxide nanofilms synthesized *via* (a) anodization of the Al/Hf bilayer in 0.2 M H₃PO₄ solution at 150 V, re-anodization to 300 V, and PAA dissolution ('nanostructured' film), (b) anodization of the Hf layer in 0.2 M H₃PO₄ by increasing polarization from 0 to 50 V ('flat' film). The plots on the right show experimental and curve-fitted XP Hf 4f spectra of the corresponding film surfaces. SEM images in panel (c) show fragments of fractures of the nanostructured hafnium-oxide films with the fixed MG-63 cells.

columns of panels (a) and (b), the images may be visually directly compared, and one may see that the compact anodic HO film has a microscopically flat surface (hereafter the 'flat' film). Contrarily, the anodic film prepared *via* the PAA-assisted anodization (hereafter the 'nanostructured' film) fully meets the above-mentioned expectations and is composed of oxide nanorods having a cone-like shape, 280 nm high, ~200 and ~350 nm wide at the tops and bottoms respectively, of $7 \times 10^8 \text{ cm}^{-2}$ population density, being separated from the remaining hafnium metal by a continuous oxide layer, about 80 nm thick.

The group of images in panel (c) shows fragments of fractures of the nanostructured HO films with the adhered MG-63 cells. One may see that the cells cover not only tops of the rods but also the gaps between the rods thus interacting with the whole surface of the hafnium-oxide nanofilm. This is clearly unlike the case of previously reported PAA-assisted tantalum-oxide nanostructured film, having comparable dimension but not letting the cells spread around the rods.³⁵

The plots in Fig. 2a and b show the narrow scan Hf 4f spectra of respectively the nanostructured and flat HO films. For the nanostructured surface, the Hf 4f region can be fitted with three spin-orbit doublets all having symmetric lineshapes and nearly equal width, with the corresponding 4f_{7/2} binding energies at 17.0, 18.25, and 19.25 eV. With reference to XPS evaluation of the hafnium oxide nanofilms in the recent work,²⁵ the Hf 4f_{5/2} peak for each species was constrained to be at a fixed energy increment of 1.68 eV above the Hf 4f_{7/2} peak, and the peak intensity ratio was fixed to 4:3. In the spectrum, the dominating doublet may be assigned to the fully oxidized Hf⁴⁺ in stoichiometric HfO₂ (~37 at%). The lower-energy doublet, shifted to -1.23 eV, is associated with photoelectrons emitted from Hf³⁺ oxidation states created by Hf₂O₃ suboxide (~28 at%). The highest-energy doublet, shifted to +1.0 eV from the Hf⁴⁺ level, is associated with hydroxyl groups bonded with hafnium in an oxide-hydroxide compound HfO₂·*n*H₂O, which was formed due to incorporation of OH⁻ ions into the oxide structure during

the anodic processes (~ 35 at%). This interpretation may be further supported by the case of PAA-assisted WO_x nanorods, also giving a peak above the W^{3+} level associated with the oxide-hydroxide component – so called ‘tungstic’ acid.³⁶ The Hf 4f region of the flat film (Fig. 2b) is fitted by two spin-orbit doublets with symmetric lineshapes with the $4f_{7/2}$ binding energies at 18.2 and 19.1, which can be assigned to HfO_2 (~ 90 at%) and $\text{HfO}_2\text{-OH}$ (~ 10 at%). Both films revealed no traces of metallic Al or Hf, which confirms that the surfaces are fully oxidized, as required for the purpose of this study.

Conclusively, the structured surface developed here is a sort of unique from the morphology and chemical composition view-point, being represented by the hierarchically nanostructured metal-oxide coating comprising a mixture of hafnium dioxide, suboxide, and hydroxide in comparable amounts, thus contributing to the diversity of hafnium-oxide nanofilms reported so far. Contrarily, the surface of the flat film is incomparably smoother and microscopically featureless, being mainly composed of stoichiometric hafnium dioxide.

3.2 The nanostructuring promotes antibacterial activity

Over the past few decades, the positive effect of surface nanostructuring on cytocompatibility and antibacterial activity has been established for conventional biomaterials. To prevent the adhesion and proliferation of pathogenic bacteria on biomedical surfaces, coatings with biocidal agents, silver nanoparticles, and antibiotics have been proposed.³⁷ As hafnia nanoparticles and coatings have reportedly been effective with Gram-negative and Gram-positive bacteria,³⁸ we have examined the antibacterial capacity of HO nanofilms developed in this work. The antibacterial efficiency of the nanostructured HO film was estimated with Gram-negative *E. coli* and compared with that of the flat HO film. The films were exposed to the bacteria solution for 4 hours, and the viability assay counting bacterial colonies on solid agar was carried out as depicted in Fig. 3a and b. The quantitative results shown in Fig. 3c reveal almost two-fold enhancement of antibacterial capacity of the nanostructured HO surface. This finding supports the belief that bacterial contamination of biomaterials may lessen due to structuring at the nanoscale. Although the

exact mechanisms regulating the bacterial response of the micro-/nano scale surfaces have not been established, the dying of bacteria due to the surface roughness and chemistry has been suggested for biomaterials based on titanium, zirconium or tantalum oxides.^{39,40} Therefore, we assume that the unique surface chemistry and morphology of the nanostructured HO film improves the antibacterial performance. Further, the size and shape of the surface features may reportedly affect substantially bacterial adhesion.⁴¹ With the HO nanofilms prepared here, the influence of nanostructure dimension, which may potentially be tuned in the range of 50–800 nm,^{25,42} on the bacterial response to a broader variety of Gram-positive and Gram-negative bacteria will be researched in a future work.

3.3 Protein adsorption

Interaction of living cells with biomaterials is driven by the adsorption of proteins coming from the surrounding plasma environment. How proteins adsorb on the surface is often decided by the morphology and chemistry of the material,⁴³ and it is generally expected that the proteins lose their native structure when being adsorbed.⁴⁴ This may significantly affect the final adhesion and the behavior of cells on the nanostructured surfaces, as reported, for instance, for titanium and its alloys.⁴⁵ The roughness and increased surface area of nanostructured coatings are reportedly the factors that promote biocompatibility of the materials.⁴⁶ In the present work, we compared the ability of the two types of HO films to adsorb model proteins such as albumin (BSA; main blood plasma protein) and fibronectin (FN; glycoprotein of the extracellular matrix). The sensitive Bradford method was used to quantify the rate at which the proteins adsorb on the nanostructured and non-structured hafnium-oxide films in one hour since the incubation began. As seen from Fig. 4, there is no big difference between the amounts of each protein adsorbed on both surfaces. Although being rather rare in practice, a similar indifference in adsorption of BSA and FN has been pointed out for titanium surfaces having various roughness at the nanoscale.⁴⁷ In this regard, the result of the present work supports the statement

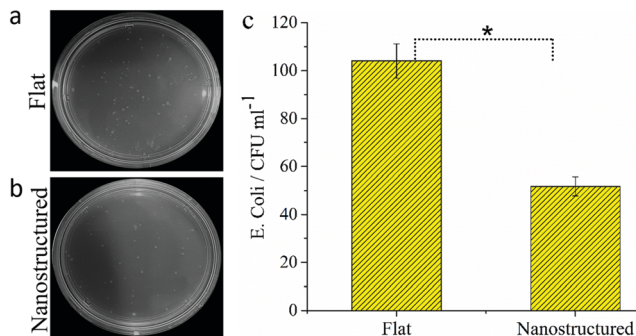


Fig. 3 Digital photographs of *E. coli* colonies as the results of 4 hour interaction between the bacteria and the (a) nanostructured and (b) flat hafnium-oxide films. (c) The bacterial colonies density measured on the flat and nanostructured hafnium-oxide surfaces. * indicates $p < 0.05$ for the flat surface in comparison with the nanostructured one ($n = 6$).

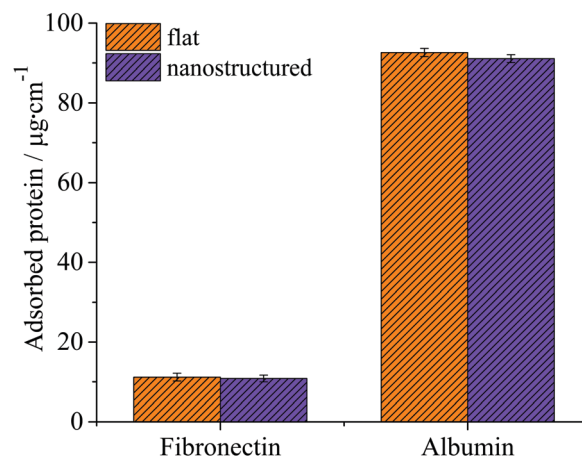


Fig. 4 Adsorption rate of fibronectin and serum albumin in one hour of incubation on the nanostructured and flat hafnium-oxide films.

previously made for titanium oxide that the nanoscale surface roughness has little effect on the amount of adsorbed proteins.⁴⁸ However, the amount of albumin adsorbed on both HO films appeared to be 9 times that of fibronectin. The faster adsorption rate for albumin can be explained by the Vroman effect of protein adsorption, which means that proteins having higher mobility arrive first to the surface.⁴⁹ For the case of titanium, a correlation has been suggested between the isoelectric points (Ip) of proteins and the features of the surface morphology.⁴⁷ However, we were unable to confirm such effect for the HO nanofilms (Ip ~ 7.0)⁵⁰ interacting with albumin (Ip ~ 4.8) or fibronectin (Ip ~ 5.5).⁵¹

3.4 Cell attachment, elasticity, and adhesion force

The initial cell attachment is one of the indicators of suitable biological properties of the material. It regulates the subsequent biological events of proliferation, differentiation, extracellular matrix production, and mineralization. To estimate the initial cell attachment and interaction with the HO films, the morphology of the attached cells was microscopically observed. The number of cells adhering to each film was counted in 4 hours after seeding the cells at the same density on the HO samples and a plastic control (Fig. 5a–c). All cells and those that gained a more spread morphology and kept the round shape were counted. Generally, the initial cell attachment allows for estimating the cell-sensing ability of different surface topographies through the faster adhesion on a more favorable surface. From Fig. 5d, although the plastic surface provides the highest number of spread cells, the nanostructured film promotes better cell spreading than the flat one. However, the number of round cells appeared to be slightly bigger on the HO surfaces compared with the plastic control. These results show that the hafnium oxide surfaces promote cell spreading, and the cells efficiently recognize the differences in the film surfaces at the initial phase of cell attachment, which agrees with previous studies on titanium.^{52,53}

Although the number, cellular markers, and morphology of cells are commonly considered as indicators of cell adhesion

and viability,⁵⁴ the importance of a quantitative understanding of cell adhesion on a surface by measuring the adhesion forces could provide additional valuable information about the interaction of cells with the biomaterial. Mechanical properties of cells are the factors that define the cellular processes important in developmental biology, pathology, tissue engineering, and regenerative medicine. Estimation of elastic modulus of cells and adhesion force and finding a correlation of these parameters with nanostructured metallic and metal-oxide biomaterials has not been the subject of any study. Here, we used, for the first time, the advanced AFM-based technologies⁵⁵ to evaluate the effect of morphology and chemistry of the HO anodic films on the cell elasticity and adhesion force. The results are summarized in Table 1. One may see that, on the nanostructured film, Young's modulus of the cell body is five-fold higher ('stiffer cell') while the adhesion force is weaker compared with the flat film ('softer cell'). The cell elasticity has been shown to be related to a number of cell functions corresponding to the response on many external chemical and physical cues including substrate properties.⁵⁶ An increased elasticity has been reported, for example, for cancer cells compared with normal cells.⁵⁷ A decrease in elasticity has been explained, for instance, by ageing or differentiation.⁵⁸ The effect of cell "stiffening" on nanostructured polystyrene-poly(bromostyrene) demixed polymer films compared to a flat film has been reported in previous study.⁵⁹ Even when the cellular mechanism involved in cell elasticity on different surfaces is unknown, the altered cytoskeletal structure and composition are considered as crucial elements.⁶⁰

In our work, the internal reorganization of actin stress fibers and/or the higher production of actin (cytoskeletal pre-stress) due to the cell adhesion on the nanostructured HO surface, as well as the differences in surface chemistry, might be the reasons for decreased cellular elasticity on the nanostructured HO film. The attachment of cells and adhesion force are the factors that ensure the structural integrity of tissues. The connection of the substrate to the cytoskeleton, which is often organized in the form of stress fibers, allows for transmitting the forces between the cells and substrate through focal contacts. The present experiments employing the AFM scratching technique show that the adhesion force decreases on the nanostructured HO surface. It is assumed that the differences in surface morphology, serum protein adsorption and conformation, and the final focal contact formation on the surfaces of the two films influenced the cell adhesion strength. Cell clustering and cell migration revealed on the nanostructured film, which will be described in detail

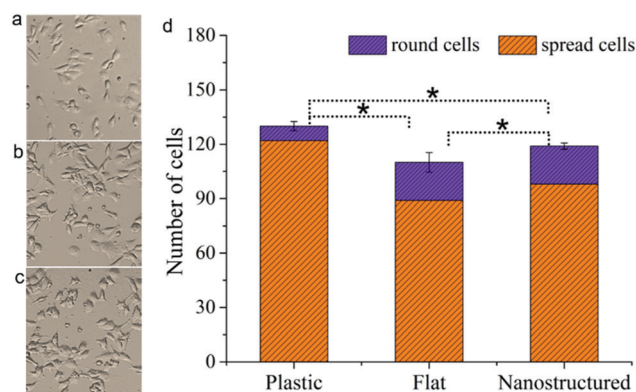


Fig. 5 Differential interference contrast (DIC) microscopy images of MG-63 cells attached to (a) a plastic control, (b) the flat hafnium-oxide surface, and (c) the nanostructured hafnium-oxide surface recorded in four hours after plating the cells. (d) The number of cells adhered to the same substrates, $n = 6$.

Table 1 The topography and AFM-measured mechanical properties of MG-63 cells on the flat and structured hafnium-oxide nanofilms. The roughness characterizes film structuring, the Young's modulus qualifies the cell elasticity, and the scratching force is attempted to estimate the cell/film adhesion force ($n = 4$) while the AFM is operated in a scratching mode

Hafnium-oxide film	Young's modulus, kPa	Scratching force, nN	Roughness R_a , nm
Flat	1.07 ± 0.32	8.75 ± 1.44	0.47
Nanostructured	5.72 ± 0.70	1.01 ± 0.02	96.30

in Fig. 8 and related text, may reportedly result from a higher internal pre-stress and stiffening the cells.⁶¹ From the above suggestions, the weaker adhesion force AFM-measured on the nanostructured HO surface may be due to a combination of factors involving the surface structuring, surface chemistry, focal contact formation and internal strength of cells to the substrate during the cell adhesion and migration. Additionally, the reason may be the very good contact between the cell body and the surface of nanorods, which may result in detaching the nanorods by the force generated by the cell and lifting a portion of cell along with the embedded rods up from the substrate. It is well seen from SEM's of Fig. 2c that the rods are tightly captured (fully covered) by the cell body, which should make the cell/rod interface rather stronger than weaker. Further, we observed by SEM the partial detaching of nanorods under the cell membrane (image not shown). The force generated by cells on the substrate differs with type of cells and surface properties and may range from pN to tens of nN,⁶² which correlates well with the values measured in our work. With the possibility of detachment of nanorods from the substrate by the cellular force, the measurements of the adhesion force on rod-like metal-oxide nanofilms by AFM may need more experimental justification in future works.

3.5 Oxidative stress

Physical and chemical characteristics of a biomaterial such as porosity, roughness, surface energy, chemical composition, or surface degradation may potentially induce oxidative stress in the cells.⁵⁴ Although several studies have suggested that the oxidative stress is related to cytotoxicity of nanoparticles, nanowires, or nanotubes,⁵³ there has been no experimental evidence of oxidative stress on nanostructured surfaces of metallic biomaterials. In the present work, the cells were stained with a fluorescence probe detecting intracellular reactive oxygen species (ROS) to estimate the influence of the surface topography and chemistry of the HO nanofilms on oxidative stress in the cells. Production of ROS in living cells is an indicator of the stressful environment, which may be detected in an early or late phase of cell attachment. Fig. 6 shows the fluorescence images of cells taken 24 hours after seeding the cells on the HO films. The qualitative analysis reveals a moderate generation of oxidative species, slightly increasing on the nanostructured film. ROS production may be a consequence of the normal cell function or pathological states causing the cellular damage including proteins, lipids, and DNA. Comparing the fluorescence images with the DIC ones in Fig. 6 left columns, one may see that the cells are firmly attached and spread on both surfaces except for a few apoptotic cells. The cells proliferated well on both HO films (Fig. 7), which excludes the possibility of gradual apoptosis of the cells. A slight rise of ROS production over the nanostructured film could be due to a small disturbance among the cells because of the changed mechanical properties of cells (Table 1). Anyway, it is obvious that both HO surfaces developed here do not produce pathological effect on living cells. Even if there would be a risk of stressful conditions on these substrates, the cells could effectively defend themselves by producing and activating cellular antioxidants.

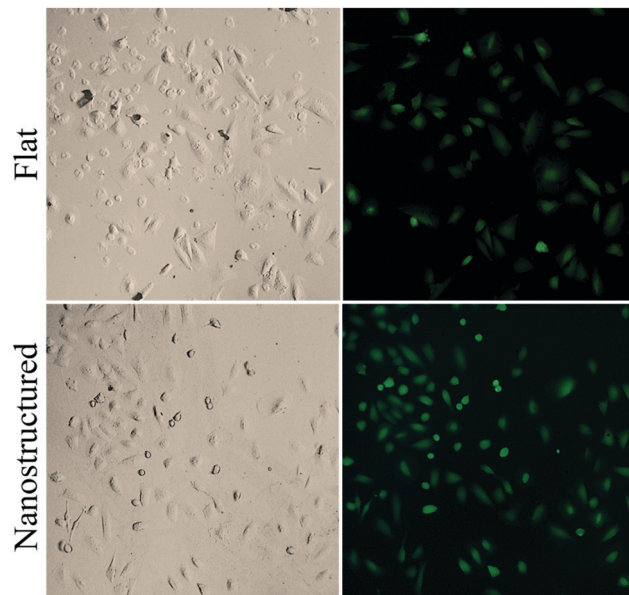


Fig. 6 Evaluation of oxidative stress in MG-63 cells after a 24 hour interaction with the flat and nanostructured anodic hafnium-oxide films.

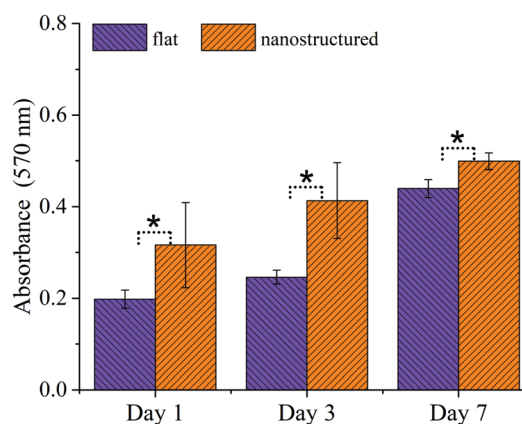


Fig. 7 The MTT viability test of MG-63 cells cultured on the nanostructured and flat hafnium-oxide surfaces on day 1, 3, and 7. * indicates $p < 0.05$ for the nanostructured surface in comparison with the flat one ($n = 6$).

3.6 Cell proliferation

To examine the viability and proliferation of cells on the HO surfaces, the MTT viability test was performed on days 1, 3, and 7. The cells were seeded at the same density on each sample surface and incubated over a period of time inside the CO₂ incubator. Correlating with the adhesion experiment, the proliferation of MG-63 cells appeared to be more significantly and systematically promoted on the nanostructured HO film (Fig. 7). The enhanced cell viability revealed for the nanostructured hafnium-oxide film agrees with the behavior of nano- and microstructured surfaces of titanium and tantalum oxides reported elsewhere.^{16,63} Therefore, proliferation results of the present study confirm the general trend of a significant promotion and activation of cell growth due to introducing nanoscale structuring to biomaterial surfaces. Nevertheless, variations in

the cell behavior may arise due to differences in the diameter, spacing, or population density of structural elements composing the films, which could significantly affect cell proliferation, adhesion, or differentiation.^{16,64}

3.7 Nanostructured hafnium oxide induces cell clustering

It has been proved that the surface topography at micro-/nanoscale guides the morphology and spatial patterning of cells.^{65–67} To find out whether the structuring of HO anodic film induces morphological changes in cell shape and distribution of focal complexes, the actin and vinculin were fluorescently stained and imaged. Fig. 8b–e shows the actin (red) and vinculin (green) staining of MG-63 cells on the two HO films. In the case of vinculin, there is no obvious difference in its distribution on both HO films. The cells on the flat HO surface mostly take shape of a well-spread polygon, stretched in one direction, with well-organized actin filaments, and the densely distributed vinculin homogenously disseminates throughout the cells (Fig. 8a–c).

On the other hand, the cells on the nanostructured surface show more condensed actin and generally have smaller surface area compared with the flat surface (Fig. 8c and f). The dense actin could be due to the cell stiffness (as measured by AFM, Table 1), as discussed above. Surprisingly, the nanostructured surface induces cell clustering and formation of cell multilayers, as seen in Fig. 8d displaying the islands of clumped cells. Clustering can be induced by extracellular ligands⁶⁸ or through

the force mediated between the attached cells.⁶⁹ Thus, the assembly of clusters may result from a random or directed migration, or mechanically-induced cell compaction, or continual division of well-attached daughter cells.⁷⁰ Alternatively, the clustering may arise from minimizing the unfavorable contacts of cells with the substrate, resulting in cell multilayers.⁷¹ From Fig. 8c and f, it is evident that MG-63 cells exhibit well-developed lamellipodia on both HO surfaces, while more migrating cells were found on the nanostructured film (insert in Fig. 8f). The cells on the nanostructured surface are denser in actin and form clustered multilayers. Notably, although overgrowth is a frequently observed phenomenon for osteoblast-like cells, no clustering has been revealed for MG-63 cells cultured on the tantalum-oxide nanodot arrays synthesized and examined in our previous work.¹⁶ We would refrain from making further speculations on the reason of cell clustering revealed in this work until a detailed investigation on the matter is carried out. Beyond any doubt, the nanoscale surface structuring of hafnium-oxide anodic film is the factor that increases cell migration and clustering and enhances viability of the cells.

4. Conclusions

A coating comprising an array of hierarchically structured hafnium-oxide nanorods on a thin hafnium-oxide layer (the nanostructured film) and a microscopically featureless hafnium-oxide nanofilm (the flat film) were synthesized *via* respectively

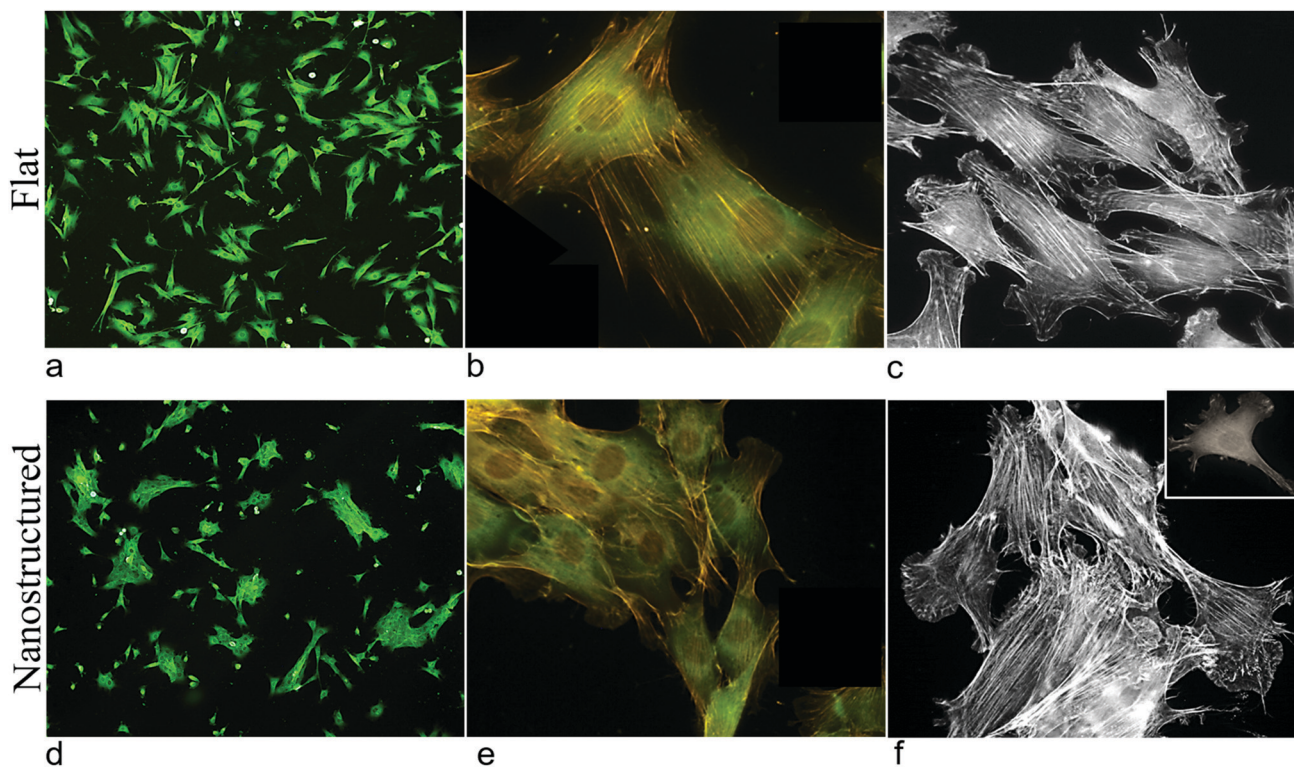


Fig. 8 Immunostaining of actin and vinculin. (a) Cells growing on the flat hafnium-oxide surface and (d) cell clusters (multilayers) on the nanostructured hafnium-oxide films. (b and e) Immunofluorescence from vinculin (green) and actin (red) distribution. Black and white images of panels (c) and (f) show respectively actin density and lamellipodia extensions, with the detail of a migrating cell in the inset.

the PAA-assisted anodizing and a conventional compact anodizing of a layer of hafnium metal sputtered on a Si substrate. The surface of the nanostructured film is composed of a mixture of hafnium dioxide (HfO_2), suboxide (Hf_2O_3), and oxide-hydroxide compound ($\text{HfO}_2 \cdot n\text{H}_2\text{O}$) in comparable amounts, whereas the flat film is mainly HfO_2 . The two surfaces disclosed good antibacterial behavior, the nanostructured one showing even a two-fold enhanced antibacterial effect with *E. coli*, which is also likely due to the specific surface chemistry of the nanostructured coating. Both surfaces absorb well fibronectin and albumin, the latter being absorbed in nine times larger amount. The nanostructured film provides relatively better initial attachment and significantly promotes the viability of the cells. Compared with the flat surface, the structuring results in a fivefold rise in Young's modulus of the cells whereas makes the adhesion force at the cell/surface interface weaker as determined by the AFM scratching technique. The effect, however, may be mostly due to the excellent contact between the cells and the oxide nanorods, which are detached from the substrate being embedded in the cell body during the scratching. Although a slightly stronger generation of reactive oxygen species and the affinity for cell cluster formation are among the features of the nanostructured film, both surfaces reveal good cytocompatibility and do not produce pathological effects on the living cells.

The new knowledge gained in the present work is believed to advance the understanding of chemical and biological processes during the interaction of living cells and bacteria with nanostructured and non-structured metal-oxide coatings in the pursuit of advanced materials and technologies for biomedical applications.

Conflicts of interest

There are no conflicts to declare.

Acknowledgements

Research leading to these results was supported by a grant from the Czech Science Foundation (GA ČR) no. 17-13732S. CIISB research infrastructure project LM2015043 funded by MEYS CR is gratefully acknowledged for the financial support of the measurements at the CF Nanobiotechnology. The authors wish to thank Zdenek Pytlíček of CEITEC BUT for the help with modeling film morphology.

References

- N. S. Manam, W. S. W. Harun, D. N. A. Shri, S. A. C. Ghani, T. Kurniawan, M. H. Ismail and M. H. I. Ibrahim, *J. Alloys Compd.*, 2017, **701**, 698–715.
- E. A. Lewallen, S. M. Riester, C. A. Bonin, H. M. Kremers, A. Dudakovic, S. Kakar, R. C. Cohen, J. J. Westendorf, D. G. Lewallen and A. J. van Wijnen, *Tissue Eng., Part B*, 2015, **21**, 218–230.
- H. Matsuno, A. Yokoyama, F. Watari, M. Uo and T. Kawasaki, *Biomaterials*, 2001, **22**, 1253–1262.
- S. Minagar, Ch. C. Berndt, T. Gengenbach and C. Wen, *J. Mater. Chem. B*, 2014, **2**, 71–83.
- E. Eisenbarth, D. Velten and J. Breme, *Biomol. Eng.*, 2007, **24**, 27–32.
- E. Cerreta, C. A. Yablinsky, G. T. Gray, S. C. Vogel and D. W. Brown, *Mater. Sci. Eng., A*, 2007, **456**, 243–251.
- J. R. Sin, A. Neville and N. Emami, *J. Biomed. Mater. Res., Part B*, 2014, **201**, 1157–1164.
- S. Mohammadi, M. Esposito, M. Cucu, L. E. Ericson and P. Thomsen, *J. Mater. Sci.: Mater. Med.*, 2001, **12**, 603–611.
- T. Miyazaki, M. Sueoka, Y. Shirosaki, N. Shinozaki and T. Shiraishi, *J. Biomed. Mater. Res., Part B*, 2018, **106**, 2519–2523.
- H. Sato, M. Kikuchi, M. Komatsu, O. Okuno and T. Okabe, *J. Biomed. Mater. Res., Part B*, 2004, **72**, 362–367.
- J. Lin, S. Ozan, Y. Li, D. Ping, X. Tong, G. Li and C. Wen, *Sci. Rep.*, 2016, **6**, 37901.
- B. L. Wang, L. Li and Y. F. Zheng, *Biomed. Mater.*, 2010, **5**, 044102.
- C. Herranz-Diez, C. Mas-Moruno, S. Neubauer, H. Kessler, F. J. Gil, M. Pegueroles, J. M. Manero and J. Guillem-Marti, *ACS Appl. Mater. Interfaces*, 2016, **8**, 2517–2525.
- A. Saenz, W. Brostow and E. Rivera-Muñoz, *J. Mater. Educ.*, 1999, **21**, 297–306.
- J. C. Bettinger, R. Langer and T. J. Borenstein, *Angew. Chem., Int. Ed.*, 2009, **48**, 5406–5415.
- Z. Fohlerova and A. Mozalev, *J. Biomed. Mater. Res., Part B*, 2018, **106**, 1645–1654.
- R. Huang, Y. Han and S. Lu, *J. Mater. Chem. B*, 2014, **2**, 4531–4543.
- S. Berger, F. Jakubka and P. Schmuki, *Electrochem. Solid-State Lett.*, 2009, **12**, K45–K48.
- H. Tsuchiya and P. Schmuki, *Electrochem. Commun.*, 2005, **7**, 49–52.
- D. Gu, H. Baumgart, G. Namkoong and T. Abdel-Fattah, *Electrochem. Solid-State Lett.*, 2009, **12**, K25–K28.
- N. Jie, Z. Yu, Q. Zhou and Z. Zhang, *J. Am. Ceram. Soc.*, 2008, **91**(10), 3458–3460.
- J. Tang, J. Fabbri, R. D. Robinson, Y. Zhu, I. P. Herman, M. L. Steigerwald and L. E. Brus, *Chem. Mater.*, 2004, **16**, 1336–1342.
- A. Benamira, J. P. Deloume and B. Durand, *J. Mater. Chem.*, 1999, **9**, 2659–2662.
- B. Matovic, J. Pantic, J. Lukovic, M. Cebela, S. Dmitrovic, M. Mirkovic and M. Prekajski, *Ceram. Interfaces*, 2016, **42**, 615–620.
- A. Mozalev, M. Bendova, F. Gispert-Guirado and E. Llobet, *Chem. Mater.*, 2018, **30**, 2694–2708.
- M. Jayavel, N. Ramalakshmi and S. Arul, *J. Nanosci. Technol.*, 2017, **3**, 245–248.
- N. Kumar, B. P. A. George, H. Abrahamse, V. Parashar, S. S. Ray and J. C. Ngila, *Sci. Rep.*, 2017, **7**, 9351.
- A. Mozalev, R. Calavia, R. M. Vázquez, I. Gràcia, C. Cané, X. Correig, X. Vilanova, F. Gispert-Guirado, J. Hubálek and E. Llobet, *Int. J. Hydrogen Energy*, 2013, **38**, 8011–8021.
- M. Bendova, J. Kolar, M. Marik, T. Lednický and A. Mozalev, *Electrochim. Acta*, 2018, **281**, 796–809.

- 30 E. B. Montufar, M. Casas-Luna, M. Horynová, S. Tkachenko, Z. Fohlerová, S. Diaz-de-la-Torre, K. Dvořák, L. Čelko and J. Kaiser, *Acta Biomater.*, 2018, **70**, 293–303.
- 31 G. Nardone, J. Oliver-De La Cruz, J. Vrbsky, C. Martini, J. Pribyl, P. Skládal, M. Pešl, G. Caluori, S. Pagliari, F. Martino, Z. Maceckova, M. Hajduch, A. Sanz-Garcia, N. M. Pugno, G. B. Stokin and G. Forte, *Nat. Commun.*, 2017, **8**, 15321.
- 32 H. A. Pan, Y. C. Hung, Y. P. Sui and G. S. Huang, *Biomaterials*, 2012, **33**, 20–28.
- 33 U. Dhawan, S. M. Wang, Y. H. Chu, G. S. Huang, Y. R. Lin, Y. C. Hung and W. L. Chen, *Sci. Rep.*, 2016, **6**, 31998.
- 34 M. Kulkarni, A. Mazare, J. Park, E. Gongadze, M. S. Killian, S. Kralj, K. von der Mark, A. Iglíč and P. Schmuki, *Acta Biomater.*, 2016, **45**, 357–366.
- 35 U. Dhawan, H. A. Pan, C. H. Lee, Y. H. Chu, G. S. Huang, Y. R. Lin and W. L. Chen, *PLoS One*, 2016, **11**, e0158425.
- 36 A. Mozalev, M. Bendova, F. Gispert-Guirado, Z. Pytlíček and E. Llobet, *J. Mater. Chem. A*, 2016, **4**, 8219–8232.
- 37 P. Huang, J. Wang, S. Lai, F. Liu, N. Ni, Q. Cao, W. Liu, D. Y. B. Deng and W. Zhou, *J. Mater. Chem. B*, 2014, **2**, 8616–8625.
- 38 A. W. Hayes, *Principles and Methods of Toxicology*, 5th edn, 2008.
- 39 S. Pogodin, J. Hasan, V. A. Baulin, H. K. Webb, V. K. Truong, H. Phong Nguyen, V. Boshkovikj, Ch. J. Fluke, G. S. Watson, J. A. Watson, R. J. Crawford and E. P. Ivanova, *Biophys. J.*, 2013, **104**, 835–840.
- 40 J. Rosenbaum, D. L. Versace, S. A. Andalousi, R. Pires, Ch. Azevedo, P. Cenedes and P. Dubot, *Biomater. Sci.*, 2017, **5**, 455.
- 41 C. Faille, J. M. Membre, J. P. Ussier, M. N. Bellon-Fontaine, B. Carpentier, M. A. Laroche and T. Benezech, *Biofouling*, 2000, **15**, 261–274.
- 42 A. Mozalev, H. Habazaki and J. Hubalek, *Electrochim. Acta*, 2012, **82**, 90–97.
- 43 M. Rahmati and M. Mozafari, Biocompatibility of alumina-based biomaterials – A review, *J. Cell. Physiol.*, 2019, **234**, 3321–3335.
- 44 W. Yang, X. Xi, Q. Ran, P. Liu, Y. Hu and K. Cai, *Mater. Sci. Eng., C*, 2014, **34**, 410–416.
- 45 M. A. Kulkarni, P. Schmuki and A. Iglíč, *Nanomedicine*, 2014.
- 46 M. Kulkarni, A. Flašker, M. Lokar, K. Mrak-Poljšak, A. Mazare, A. Artenjak, S. Čučnik, S. Kralj, A. Velikonja, P. Schmuki, V. Kralj-Iglíč, S. Sodin-Semrl and A. Iglíč, *Int. J. Nanomed.*, 2015, **10**, 1359–1373.
- 47 K. Cai, J. Bossert and K. D. Jandt, *Colloids Surf., B*, 2006, **49**, 136–144.
- 48 P. Cacciatista, A. D. L. Humphris, K. D. Jandt and M. J. Miles, *Langmuir*, 2000, **16**, 8167–8175.
- 49 S. L. Hirsh, D. R. McKenzie, N. J. Nosworthy, J. A. Denman, O. U. Sezerman and M. M. M. Bilek, *Colloids Surf., B*, 2013, **103**, 395–404.
- 50 J. Shim, J. Rivera and R. Bashir, *Nanoscale*, 2013, **5**, 10887.
- 51 G. B. Sigal, M. Mrksich and G. M. Whitesides, *J. Am. Chem. Soc.*, 1998, **120**, 3464–3473.
- 52 T. Raimondo, S. Puckett and T. J. Webster, *Int. J. Nanomed.*, 2010, **5**, 647–652.
- 53 P. A. Mouthuy, S. J. B. Snelling, S. G. Dakin, L. Milkovic, A. C. Gasparovic, A. J. Carr and N. Zarkovic, *Biomaterials*, 2016, **109**, 55–68.
- 54 J. Lu, M. P. Rao, N. C. MacDonald, D. Khang and T. J. Webster, *Acta Biomater.*, 2008, **4**, 192–201.
- 55 J. Zemła, J. Danilkiewicz, B. Orzechowska, J. Pabijan, S. Seweryn and M. Lekka, *Semin. Cell Dev. Biol.*, 2018, **73**, 115–124.
- 56 M. Y. M. Chiang, Y. Yangben, N. J. Lin, J. L. Zhong and L. Yang, *Biomaterials*, 2013, **34**, 9754–9762.
- 57 K. Hayashi and M. Iwata, *J. Mech. Behav. Biomed. Mater.*, 2015, **49**, 105–111.
- 58 H. Jin, X. Xing, H. Zhao, Y. Chen, X. Huang, S. Ma, H. Ye and J. Cai, *Biochem. Biophys. Res. Commun.*, 2010, **391**, 1698–1702.
- 59 J. C. Hansen, J. Y. Lim, L. C. Xu, C. A. Siedlecki, D. T. Mauger and H. J. Donahue, *J. Biomech.*, 2007, **40**, 2865–2871.
- 60 E. Takai, K. D. Costa, A. Shaheen, C. T. Hung and X. E. Guo, *Ann. Biomed. Eng.*, 2005, **33**, 963–971.
- 61 J. R. Lange and B. Fabry, *Exp. Cell Res.*, 2013, **319**, 2418–2423.
- 62 W. J. Polacheck and C. S. Chen, *Nat. Methods*, 2016, **13**, 415–423.
- 63 G. Wang, Y. Wan, B. Ren and Z. Liu, *Mater. Lett.*, 2018, **212**, 247–250.
- 64 J. Park, S. Bauer, K. von der Mark and P. Schmuki, *Nano Lett.*, 2007, **7**, 1686–1691.
- 65 G. Abagnale, A. Sechi, M. Steger, Q. Zhou, C. C. Kuo, G. Aydin, C. Schalla, G. Müller-Newen, M. Zenke, I. G. Costa, P. van Rijn, A. Gillner and W. Wagner, *Stem Cell Rep.*, 2017, **9**, 654–666.
- 66 S. Oh, K. S. Brammer, Y. S. J. Li, D. Teng, A. J. Engler, S. Chien and S. Jin, *Proc. Natl. Acad. Sci. U. S. A.*, 2009, **106**, 2130.
- 67 V. V. Divya Rani, L. Vinoth-Kumar, V. C. Anitha, K. Manzoor, M. Deepthy and V. N. Shantikumar, *Acta Biomater.*, 2012, **8**, 1976–1989.
- 68 M. A. Guvakova and E. Surmacz, *Exp. Cell Res.*, 1997, **231**, 149–162.
- 69 M. R. Ng, A. Besser, G. Danuser and J. S. Brugge, *J. Cell Biol.*, 2012, **199**, 545–563.
- 70 H. Yue, R. Laura Lara, W. Juan and C. S. Ian, *Phys. Biol.*, 2014, **11**, 056007.
- 71 A. Ranella, M. Barberoglou, S. Bakogianni, C. Fotakis and E. Stratakis, *Acta Biomater.*, 2010, **6**, 2711–2720.

Článek 5

Nanostructured ZrO₂ bioceramic coatings derived from the anodically oxidized Al/Zr metal layers

ARTICLE

Nanostructured ZrO₂ bioceramic coatings derived from the anodized Al/Zr metal layers

Zdenka Fohlerova,^{a,b,c} Kirill Kamnev,^a Marcela Sepulveda,^a Jan Prasek,^a and Alexander Mozalev^{*a,b}

Received 00th January 20xx,
Accepted 00th January 20xx

DOI: 10.1039/x0xx00000x

ZrO₂-based bioceramics are actively introduced into commercial use due to their superior durability, corrosion resistance, and in-vitro compatibility with the body's own materials. The nanostructuring of ZrO₂ ceramics may further enhance their useful properties. Here we synthesized ZrO₂ ceramic coatings comprising arrays of several highly distinctive types of 3-dimensional nanostructures that protrude above a thin oxide layer, ranging in shapes, sizes, spacings, and population densities, termed as the nanomounds (~80 nm), nanopillars (~250 nm), and nanostumps (~650 nm), *via* the porous-anodic-alumina-assisted anodizing of Zr layers. The nanostructured coatings, alongside a flat ZrO₂ anodic film, were explored as a potential biomaterial in experiments with the Saos-2 cell line. All coating types revealed no cytotoxicity to living cells. The population density and spreading area of the cells, being the largest on the flat film, slightly decreased with increasing nanostructure dimensions. The cells progressively proliferated on all the surfaces, the nanomounds and especially nanopillars promoting the best viabilities and the highest proliferation rates. The flat, nanomound, and nanopillar coatings revealed the well-defined organizations of actin filaments across the entire cell bodies with no disruption in the cytoskeletal network and the mature large dash-shaped focal adhesions. The largest amount of alkaline phosphatase and the biggest deposition of a mineralization-competent extracellular matrix were observed on the nanopillars, the other nanostructured coatings showing a better result than the flat one, though. The similarities, differences, and paradoxes in biological responses of Saos-2 cells to the coatings developed here are explained with the help of high-resolution electron-microscope observation of the cell surface morphologies and the cell/film interfaces.

Introduction

The fabrication of biomaterials with improved mechanical and appropriate chemical properties is crucial for achieving the long-term stability and functionality of medical implants. The selection of a biomaterial is based on its physicochemical properties and the surrounding biological environment. In modern medicine, biomaterials are commonly utilized as fixatives, replacements, and bases for the reconstruction of osseous and dental tissue.¹ Besides the well-known metallic materials such as titanium and its alloys, stainless steel, niobium, tantalum, gold, or cobalt-chromium alloys,² the metal-oxide ceramics such as titania or zirconia have become indispensable in dental and bone tissue reconstruction, including prostheses, osteogenic scaffolds, and medically implanted devices to deliver medication, monitor body functions, or provide support to organs and tissues.³ The

feasibility of biomaterials for in-vitro applications strongly depends on their chemical composition, surface wettability, roughness, hardness, and stability. The differences in the surface morphology may significantly affect the adhesion and viability of living cells and bacteria, protein adsorption, or differentiation of stem cells and osteoblasts.⁴ The precise control of surface topography and properties of a biomaterial is an essential factor for modulating its biological response.

To date, several techniques have been developed to create bio-viable surfaces with micro- and nanoscale topographies, striving to enhance the material biocompatibility.⁵ The mechanical roughening enables a random pattern of surface features with various amplitudes and spacings.⁶ It is also possible to achieve well-defined and controlled surface features *via* diverse micro- and nanofabrication techniques such as photolithography, laser machining, or 3-D printing.^{7,8,9} Additionally, biocompatible surfaces with precisely modeled and controlled topographies at the nanoscale may be synthesized *via* self-organized electrochemical anodizing of metals. This has proved to be the technically simple, cost-effective, eco-friendly, and versatile approach for creating essential bioceramic materials, such as Al₂O₃, TiO₂, and ZrO₂, with nanoporous surface morphologies.^{10,11,12,13}

As an alternative to the nanoporous ceramics, metal-oxide protrusions such as nanohillocks, nanopillars, or nanorods, upright-standing and highly aligned on substrates, with well-controlled dimensions, shapes, and population densities can be

^a CEITEC – Central European Institute of Technology, Brno University of Technology, Purkynova 123, 61200 Brno, Czech Republic, email: alexander.mozalev@ceitec.vutbr.cz

^b Brno University of Technology, Faculty of Electrical Engineering and Communication, Department of Microelectronics, Technicka 10, 616 00 Brno, Czech Republic

^c Department of Biochemistry, Faculty of Medicine, Masaryk University, Kamenice 753/5, 625 00 Brno, Czech Republic

† Electronic Supplementary Information (ESI) available: details and summary of XRD evaluation. See DOI: 10.1039/x0xx00000x

produced *via* the so-called porous-anodic-alumina (PAA)-assisted anodizing of metal of interest.¹⁴ In the approach, a metal to be structured is covered by a layer of aluminum prepared using one of the physical deposition techniques. First, the aluminum overlayer is converted into PAA layer *via* the anodizing in an aqueous acid electrolyte, then the underlying metal is further anodized through the alumina nanopores. The method has proved to be highly appropriate for growing arrays of Ta₂O₅, Nb₂O₅, TiO₂, HfO₂, and WO₃ nanostructures of diverse shapes and dimensions.^{15,16,17,18,19} The PAA-assisted anodizing of refractory metals aiming to produce potential bioceramics allows for a range of unique properties relating to surface chemistry, roughness, wettability, and cytocompatibility that are of fundamental importance for biomedical applications and not achievable in the nanoporous metal oxides.²⁰ Up to date, Ta₂O₅ and HfO₂ nanostructured coatings synthesized *via* the PAA-assisted anodizing have reportedly helped significantly improve the adhesion of living cells, proliferation, protein absorption, and alkaline phosphatase activity, alongside the pronounced antibacterial effect.^{21,22}

ZrO₂-based biomaterials possess superior mechanical properties, wear resistance, thermal stability, corrosion resistance, and excellent in-vitro compatibility with human body parts.²³ In in-vivo experiments, ZrO₂-based coatings have shown an enhancement of the osseointegration of implants.²⁴ The amassed reports underline good biocompatibility and reduced plaque formation for ZrO₂ ceramics due to the low bacterial adhesiveness.²⁵ Since ZrO₂-based biomaterials are designed to interact with the human body environment, it is of high interest to investigate how the structured surface topographies influence the behavior of osteoblast-like cells. The bioactivity of nanoporous anodic ZrO₂ ceramics^{26,27} has already been assessed in experiments with living cells^{28,29} and simulated body fluids,^{30,31} both showing promising results.

From the above consideration, it is highly anticipated that the fabrication of self-organized nanoarrays of ZrO₂ protrusions *via* the PAA-assisted anodizing³² and investigation into their biocompatibility may be a steppingstone toward advancing the properties and extending the niche of biomedical applications of ZrO₂-based materials.

In the present work, ZrO₂ coatings comprising arrays of 3-D nanostructures rising from continuous compact oxide layers, widely ranging in sizes, shapes, spacings, and population densities, were synthesized *via* the PAA-assisted anodizing of sputter-deposited zirconium layers. The morphology, adhesion, viability, population density, spreading area, proliferation, focal contacts, cytoskeletal organization, matrix maturation, and mineralization of Saos-2 cells onto the ZrO₂ nanostructured surfaces were studied in comparison with a flat unstructured ZrO₂ anodic film. More broadly, the findings expected from these experiments, linking the response of Saos-2 cells with the features of novel ZrO₂ nano-morphologies, were foreseen to improve the understanding of complex processes occurring during the interaction of osteoblast-like cells with ZrO₂ bioceramics and with nanostructured metal-oxide biomaterials in general.

Experimental

Sample fabrication

The starting substrate was a single-side polished 4" Si wafer covered with a thermally grown 400 nm thick SiO₂ layer. A layer of zirconium, 150 nm thick, followed by a layer of aluminum, 500 nm thick, were successively deposited on the substrate *via* the magnetron sputtering of Zr (99.95%) and Al (99.999%) targets. The wafer with the deposited films was cut into *ca.* 2 cm × 2 cm square pieces, which were electrochemically processed in a cylindrical top-open two-electrode electrolytic bath made of polytetrafluoroethylene. Further technical details of the anodizing setup are described elsewhere.³³ Generally, the anodizing approach involved processing the Al/Zr bilayer in aqueous acid solution to convert the aluminum layer into PAA film, which was followed without interruption by the PAA-assisted re-anodizing of the Zr underlayer to a higher voltage to achieve the growth of hafnium oxide within the alumina nanopores. Oxalic (C₂H₂O₄), phosphoric (H₃PO₄), and etidronic (C₂H₈O₇P₂) acid solutions were used as anodizing electrolytes. Anodizing of aluminum was carried out at voltages covering a wide range of 40 to 300 V followed by re-anodizing of the Zr underlayer to voltages higher than the anodizing values, generally following the procedures reported in our previous works.^{15,34} After the completion of the re-anodizing process, the PAA overlayers were dissolved away in a chemical solution prepared and used as described elsewhere.³⁵ For comparative experiments, the Al layer was dissolved from the initial Al/Zr sample, and the remaining Zr metal was anodized in 0.1 M H₃PO₄ by sweeping the voltage from 0 to 50 V. This was expected to generate a uniform, compact anodic ZrO₂ film, about 150 nm thick, with featureless surface morphology.

Surface analysis

The surfaces of anodic films were examined *via* SEM in a TESCAN MIRA II field emission electron microscope operated at 30 keV. The cross-fractures of the substrates with anodic films were observed in an FEI Verios 460L high-resolution electron microscope operated at 15 keV. The geometrical and morphological parameters of anodic films were estimated *via* analysis of SEM images with help of ImageJ software.

Cell culture

Human osteosarcoma Saos-2 cells (ATCC® HTB-85™) were maintained in complete Dulbecco's Modified Eagle's medium (DMEM) supplemented with 10% fetal bovine serum and 5% penicillin/streptomycin (50 U mL⁻¹ and 50 µg mL⁻¹) at 37 °C in a humidified 5% CO₂ incubator. Cells were harvested by trypsinization with 0.25% trypsin-EDTA solution at 75% confluence and plated at a seeding density of 1 × 10⁴ viable cells per cm² onto the sterile samples placed in a polystyrene microplate. All chemicals were purchased from Sigma Aldrich.

Cytotoxicity and proliferation assay

The cell cytotoxicity was evaluated by the colorimetric measurement of lactate dehydrogenase enzyme (LDH) released

from dead cells in 24 hours at 490 nm using a plate-reading spectrophotometer. The procedure followed the manufacturer's protocol, and the obtained data were compared to a plastic control (Thermo Scientific™ Pierce™ LDH Cytotoxicity Assay Kit). The LDH activity was expressed as the viability in percent. To quantitate cell proliferation on days 1, 2, and 3, the colorimetric measurement of 5-bromo-2'-deoxyuridine (BrdU) incorporation during DNA synthesis in proliferating cells was determined at 370 nm, according to the manufacturer's protocol (Sigma, Cell Proliferation ELISA, BrdU).

Cell morphology and adhesion

For SEM observation of cells on the anodic films, the living cells were first fixed on the surfaces and completely dried. To this end, the cells on the films were washed three times with phosphate buffer saline (PBS) and stabilized with 4% paraformaldehyde in PBS for 20 min at room temperature. The cells were then dehydrated in a series of increasing concentrations of ethanol (50, 70, 80, 90, and 100%) for 5 min each. The interfaces between the cells and anodic films were evaluated *via* direct SEM observation of cross-fractures of the anodic films together with the adhered cells.

The immunocytochemistry was performed *via* detecting cytoskeletal actin fiber organization and vinculin as the protein in focal adhesions. The fixed cells were permeabilized with a solution of 0.5 % Triton-X 100 supplemented with 2 % bovine serum albumin for 1 hour and washed in deionized H₂O. Mouse human anti-vinculin antibody (1:100 dilution) and Alexa Fluor 488 goat anti-mouse antibody (1:100 dilution) were added for 1 hour each to stain vinculin. The actin fibers were stained with ActinRed™ 555 (Invitrogen™) for 30 min at room temperature. The stained actin and vinculin were imaged using a fluorescence microscope (Zeiss Axio Imager M2m).

The quantification of the mean spreading area per cell and the spreading area of cells per μm^2 adhered to anodic films was performed using the images of stained actin with the help of Image J software. A hundred living cells from different spots across the surface of each sample were analyzed.

Alkaline phosphatase assay

The enzyme activity was measured on the anodic films on day 9. The cells adhered to the surfaces were lysed, and alkaline phosphatase (ALP) was measured according to the manufacturer's protocol (ALP assay, BioVision Inc.). Briefly, 80 μL cell lysate was incubated with 50 μL *p*-nitrophenol phosphate (5 mmol L⁻¹) for 60 min, and the absorbance at a wavelength of 405 nm was measured using a plate-reading spectrophotometer. The amount of *p*-nitrophenol produced by the enzyme was calculated from the calibration curve and the activity of ALP from each substrate was expressed in nmol h⁻¹ mL⁻¹ units. The ALP activity was normalized to the total protein content of cells (ALP activity per microgram protein) measured at 595 nm wavelength with Bradford reagent (Sigma) and serum albumin as a standard.

Mineralization

Alizarin Red S was used to detect the extracellular deposition of calcium on day 9 and 21. The Saos-2 cells cultured in normal DMEM medium were washed once in DPBS (w/o Ca²⁺/Mg²⁺) and fixed with 4% paraformaldehyde for 20 min at room temperature. Then the cells were washed twice in deionized water, and 500 μL Alizarin Red S solution (20 mg mL⁻¹ in H₂O) was added and incubated at room temperature in the dark for 1 hour. The calcium deposition was identified microscopically as the bright red-orange color spots.

Statistical analysis

The data are presented as mean \pm standard error. The statistical analysis was performed using Student's t-test and one-way analysis of variance (ANOVA) with a confidence level of 95%.

Results and Discussion

Morphology of anodic ZrO₂ films

The PAA-assisted zirconium anodizing was expected to produce an anodic film consisting of a thin uniform ZrO₂ layer populated with the ordered arrays of self-aligned spatially separated ZrO₂ nanosized protrusions. By varying the current density, formation potential, polarization mode, and electrolyte composition we intended to achieve distinctively different nanoscale topographies in terms of dimensions, shapes, population densities, and spacings across the sample surfaces. A uniform microscopically flat ZrO₂ film was also prepared to complement the set of samples to estimate the impact of nanostructuring on the biocompatibility of the zirconium-oxide films. The surface morphologies of anodic films were examined *via* SEM. The observation results revealed the formation of four distinct types of anodic oxides, grouped in Fig. 1.

Type 1 sample is represented by an anodic oxide film that was grown *via* anodizing of a Zr layer in 0.1 M H₃PO₄ electrolyte at 50 V. The surface and sectional views of Fig. 1a show a lack of any specific nanoscale surface features. Therefore, this anodizing, as expected, resulted in a completely smooth and uniform in thickness ZrO₂ coating, hereafter termed in the text as 'flat' oxide film.

Type 2 sample is represented by an anodic oxide film that was prepared *via* anodizing an Al/Zr bilayer in 0.6 M oxalic acid electrolyte at a steady-state voltage of 50 V (Fig. 1b). An array of spatially separated ZrO₂ nanostructures is seen protruding from the general film surface. From the cross-fracture SEM image in Fig. 1b, each nanostructure in the array is shaped like a mound and is attached to the surface by the tiny roots sprawling over the compact anodic zirconium-oxide film. The mounds are separated from each other by a regular self-organized network of zirconium-oxide nano-gaps.

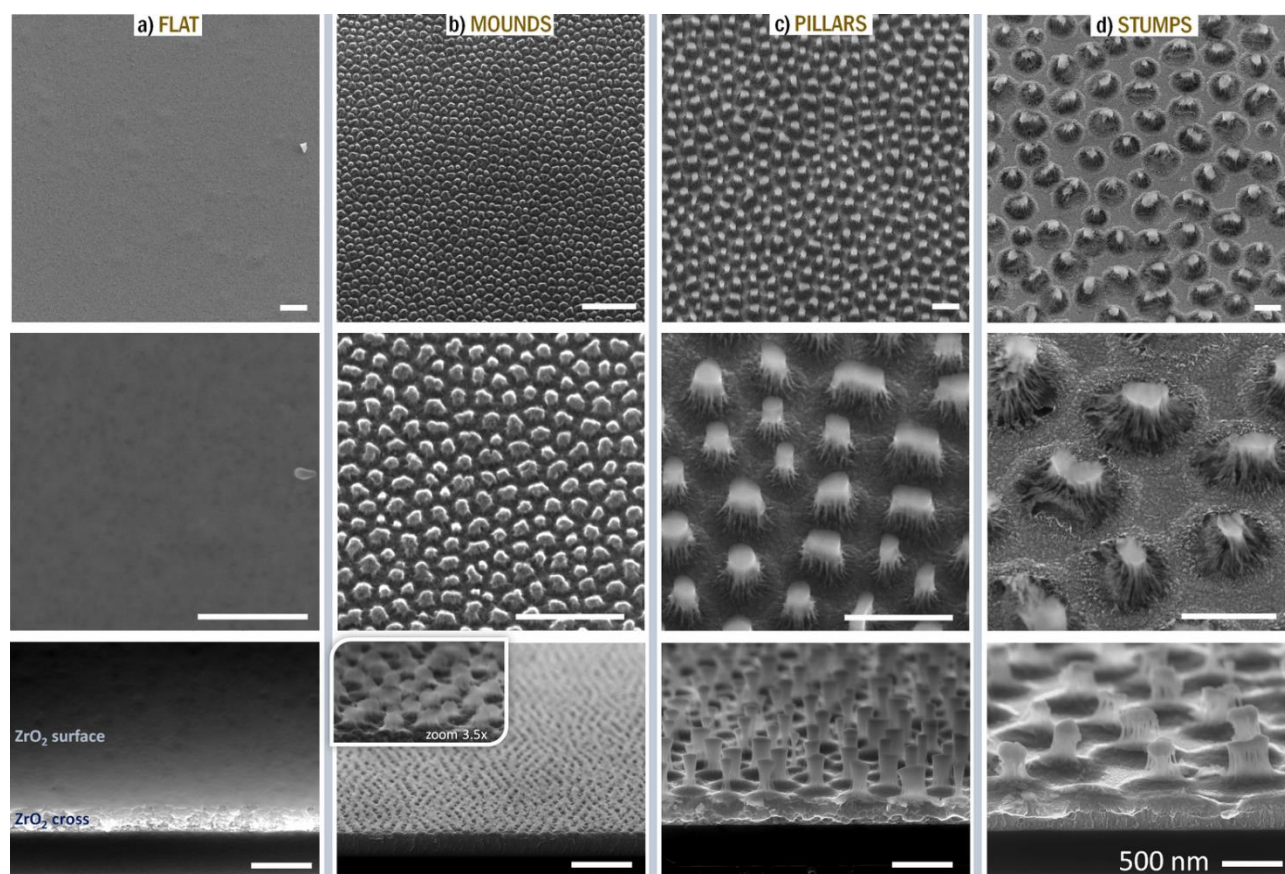


Fig. 1 SEM surface and cross-fracture views of ZrO_2 films derived from an Al/Zr bilayer on a SiO_2/Si substrate via anodizing in (b) 0.6 M oxalic acid ('nanomounds'), (c) 0.1 M phosphoric acid ('nanopillars'), and (d) 0.02 M etidronic acid ('nanostumps'). Column (a) shows a uniform compact ZrO_2 film fabricated via anodizing a layer of Zr in 0.1 M phosphoric acid ('flat' film). All unlabeled scale bars are 500 nm.

The mounds have the smallest size and spacing but the biggest population density among the films prepared in this study. Type 2 nanostructures are hereafter referred to in the text as 'nanomounds'.

Type 3 sample is represented by an anodic oxide film that was formed *via* anodizing an Al/Zr bilayer in 0.1 M phosphoric acid at a steady-state voltage of 150 V (Fig. 1c). Such process resulted in a significant increment in nanostructure dimensions and a decrease in their population density relative to the nanomounds. The protrusions are shaped like pillars with the plane tops, nearly vertical sides, broader bases attached to the film surface by the tiny roots. Type 3 nanostructures will be termed as 'nanopillars'.

Type 4 sample is represented by an anodic oxide film that was fabricated *via* anodizing an Al/Zr bilayer in 0.02 M etidronic acid at a steady-state voltage of 300 V (Fig. 1d). One may see that the oxide protrusions are noticeably wider and separated by the wider gaps. The population density of these protrusions is obviously smaller compared with the two other sample types. The structures are shaped as stumps, featuring the wide-spread bottoms and swollen tops. Type 4 nanostructures will be termed in the text as 'nanostumps'. The anodizing details and the SEM-measured dimensions of ZrO_2 anodic films are presented in Table 1.

Table 1 Types, formation conditions, and geometrical parameters of nanostructured ZrO_2 anodic films prepared (as shown in Fig. 1) for biomedical experiments.

Sample type	Anodizing electrolyte	PAA growth/ V	ZrO_2 growth / V	Diameter/ nm	Spacing/ nm	Length/ nm	Population density/ cm^{-2}
nanomounds	0.6 M $\text{C}_2\text{H}_2\text{O}_4$	40	50	65	95	55	1.3×10^{10}
nanopillars	0.1 M H_3PO_4	150	250	130	260	290	1.7×10^9
nanostumps	0.02 M $\text{C}_2\text{H}_8\text{O}_7\text{P}_2$	300	450	220	650	320	2.4×10^8

Cytocompatibility of anodic ZrO₂ coatings

The impact of nanostructuring of metal and metal-oxide surfaces on their cytocompatibility, estimated through altering and comparing the surface chemical and physical properties has been reported in several studies.^{36,37,38} The introduction of nanostructuring to bioceramics has been reported to modify their surface wettability and significantly influence important criteria of biocompatibility such as cellular adhesion, morphology, metabolic activity, proliferation, and differentiation.^{39,40} From our previous works, the nanostructuring of various common and emerging bioceramic materials such as TiO₂ (nanotubes), Ta₂O₅ (nanorods), and HfO₂ (nanodots) is a prominent route for enhancing their biomedical properties.^{11,21,22} Those findings confirmed the positive role of surface nanostructuring in improving the viability and metabolic activity of MG-63 cells. This motivated us to extend the range of electrochemically nanostructured metal-oxide nanoceramics that are feasible for biomedical applications. In the present work, we have synthesized nanostructured ZrO₂ coatings with several characteristic morphologies and explored their compatibility with Saos-2 osteosarcoma cells, looking for differences and similarities in the behavior of the cells on each film surface. Should Saos-2 cells be able to recognize the surface features of each sample type and make their preferences, this would be a key step toward modulating and tuning the cellular response.

The cytocompatibility of the ZrO₂ anodic films was quantitatively evaluated by determining viability, cell adhesion, and metabolic activity. The Saos-2 viability was estimated after day 1 through the measurements of LDH enzyme released from the dead cells, while the LDH of the intact healthy cells did not contribute to the positive results (Fig. 2a). This allowed the evaluation of the cytotoxic effect of the ZrO₂ anodic films on Saos-2 cells in terms of adhesion, proliferation, and survivability based on the specific surface topography at the nanoscale. The cytotoxic effect of the ZrO₂ nanofilms was compared with that of the plastic surface of the micro-well plate used as a standard. Neither of the anodic oxide films revealed an increase in cytotoxicity towards Saos-2 cells relative to the plastic control. The cells were well adhered to and spread over all the ZrO₂ surfaces, being viable throughout the experiment. No significant cell death was observed, which characterizes the anodic ZrO₂ surfaces as noncytotoxic to Saos-2 cells. The number of the adhered and spread Saos-2 cells were counted after a 4-hour incubation period (Fig. 2b). The result shows that the cells adhere to the plastic and flat ZrO₂ surface with no significant difference. However, the number of adhered cells slightly decreases on the nanostructured ZrO₂ surfaces in the following sequence of films: nanomounds > nanopillars > nanostumps. The increase in nanostructure dimensions is likely the factor worsening the initial cell adhesion and introducing certain adhesive incompatibility to the nanostructured ZrO₂ surfaces. Nevertheless, the adhered cells spread well on the surface and were viable through the adhesion experiment. The BrdU measurement was carried out on days 1, 2, and 3 (Fig. 2c) to assess the ability of Saos-2 cells to proliferate on the ZrO₂

nanofilms. This assay measures the incorporation of BrdU into the newly synthesized DNA. It expresses the proliferation level of cells more accurately than the metabolic activity assays based on the reduction of tetrazolium dyes, the latter being unable to distinguish between the dividing and non-dividing cells. On day 1 the cell proliferation on the nanostructured films is slightly poorer (nanomounds) or comparable (pillars and stumps) to that on the flat oxide surface. However, on day 2 the nanomound and nanopillar films surpass the flat film in cell proliferation. This tendency is preserved on day 3, the nanopillars becoming ~25% more efficient than the flat film. The nanostumps appear to be the worst surface in terms of proliferation and adhesion. The behaviors of the nanomounds and nanopillars imply that the certain structuring of anodic ZrO₂ surfaces at the nanoscale accelerates DNA synthesis. Moreover,

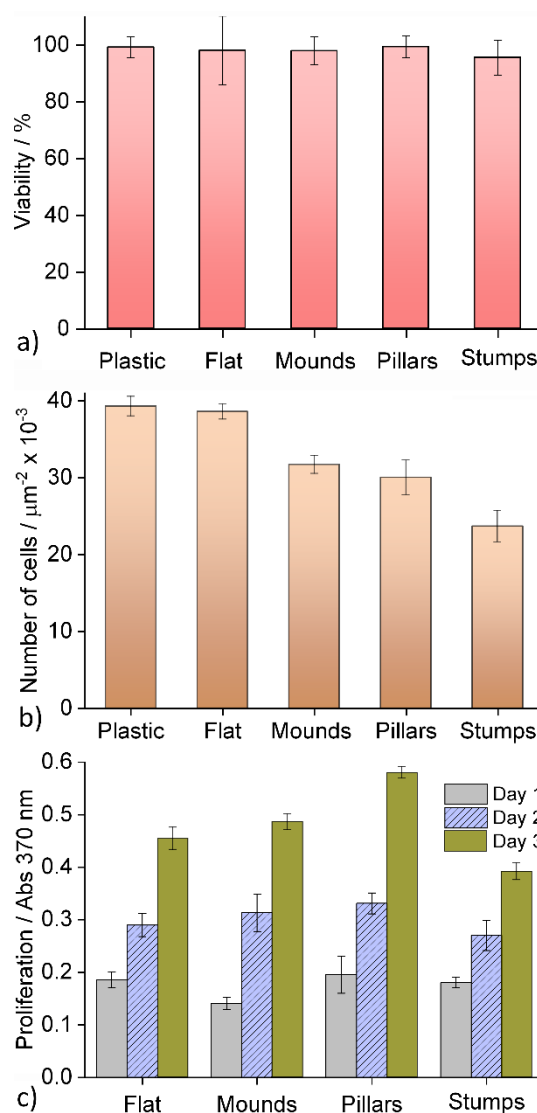


Fig. 2 Saos-2 cells cultured on ZrO₂ surfaces derived from the anodically oxidized Al/Zr bilayers on SiO₂/Si substrates (as shown in Fig. 1). (a) Lactate dehydrogenase-based cytotoxicity assay after a 24-hour culture of Saos-2 cells expressed as the viability relative to a plastic surface vs type of structuring. (b) The number of cells counted after a 4-hour culture of Saos-2 cells vs type of structuring. (c) Proliferation assay of Saos-2 cells vs type of structuring. The level of BrdU incorporation into the newly synthesized DNA was measured calorimetrically.

the cells recognize the features of structuring and chose the nanopillar surface as the most appropriate for their effective proliferation, despite the relatively weaker initial adhesion, as seen in Fig. 2b. The cell viability and proliferation behaviors disclosed in this study are generally in good agreement with the other literature reports stating that a specific nanoscale surface structuring may positively modulate the living cell response.^{41,42,43}

Cell spreading area and cell/surface interface.

It has been reported that the nanosized surface features may modulate the cell adhesion and cytoskeletal organization. For example, the silicon surfaces with a high roughness at the nanoscale have been prepared and optimized to improve the fibroblast cell adhesion.⁴⁴ In the present work, the spreading area of Saos-2 cells was evaluated using the image analysis of the spread cells after 24 hours (Fig. 3). The spreading area was found to decrease in the following sequence of films: flat > nanomounds > nanopillars > nanostumps. On the nanomounds, the cell spreading area decreases insignificantly, being within the experimental error relative to the flat film. A more obvious shrinking of the cell spreading area is observed on the nanopillars and nanostumps. This finding suggests that the spreading of cells on the nanostructured ZrO₂ anodic films worsens with an increase in the surface roughness. Therefore, the smaller the structuring, the better the spreading.

To gain a deeper insight into the cell/surface interactions, we performed direct SEM observation of the cells cultured and dried on the zirconium oxide anodic films (Fig. 4). From Fig. 4a, the cells fully cover the flat ZrO₂ film, evenly attaching to the microscopically featureless oxide surface. Similarly, the cells well cover the nanomounds (Fig. 4b), being in perfect contact with both the mounds and the gaps between them. Such good cell propagation and perfect contact over the nanomound array may be the reason for an almost similar number of viable cells and spreading area relative to the flat ZrO₂ film.

A conformal attachment of Saos-2 cells to the oxide surface is noted in the case of the nanostump array (Fig. 4d). The cell membrane completely covers the big and rough nanoprotusions and fully permeates the wide gaps between them. However, such surface nanoscale topography

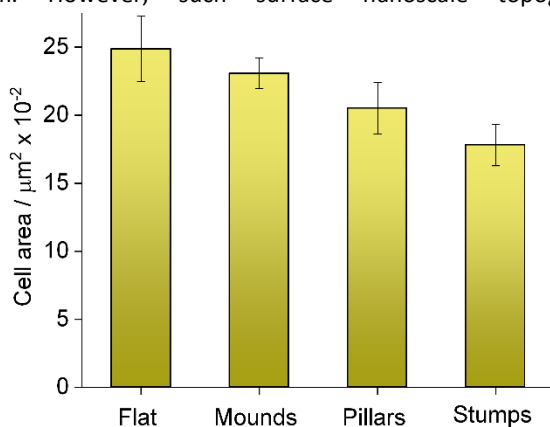


Fig. 2 Evaluation of spreading area of Saos-2 cells on ZrO₂ surfaces derived from the anodically oxidized Al/Zr bilayers on SiO₂/Si substrates.

configuration might negatively impact the cell adhesion since the cell membranes are sometimes seen not fully adhering to the sidewalls of the nanostumps (Fig. 4 d). This finding correlates with the cytocompatibility tests showing the cells exhibiting the lowest proliferation rate on the oxide nanostumps (Fig. 2). Obviously, the cells feel less comfortable and more stressed over the nanostumps due to the very curved cell/surface interface, comparable with the thickness of the cell membranes.

A unique cell/surface interface was observed in the case of the nanopillar array (Fig. 4c). The Saos-2 cells neither cover the sidewalls of the protrusions nor penetrate the gaps between them. Instead, the cells are seen residing merely on the pillar tops. The contact between the cell membrane and the pillar tops looks perfect and flawless across the entire cell spreading area. Such a cell/pillar-top interface is likely to result from the specific architecture of the protrusions ensuring the flat and reasonably wide tops separated by the gaps that are not yet too wide to force the cell membrane to distort and permeate the gaps. Feeling comfortable over such a morphology, the cells exhibit the highest proliferation rate (Fig. 2c).

The present results of measurements of the cell surface area and observation of the cell/surface interfaces are generally in good agreement with previous studies of nanostructured biomaterials.^{45,46,47} The features of nanoscale surface topographies of the anodic films impact the surface area of the seeded cells. The cell behavior is speculated to originate from the preferences of the cells to form focal adhesions over the nanostructures.⁴⁸ The observed cell/surface interfaces might result from the intracellular stress control, with the cells changing the focal adhesions positions, their sizes, and attachment strengths to meet the features of the surface morphology of the anodic films.⁴⁸ The intracellular self-organization might lead to a rare situation when the cells reside merely on tops of the pillars. Similar effects have been reported in several previous studies.^{46,47} Obviously, the sizes, shapes, spacings, and population densities of the oxide nanostructures impact the behavior of the cells on the ZrO₂ nanofilms. Despite the high population density of the nanomounds, the small sizes and narrow gaps along with the absence of sharp edges in contact with cells do not dramatically distort the cell membrane and, therefore, do not make the cells uncomfortable on such a surface. The nanomound morphology causes only a moderate increase in the proliferation rate relative to the flat anodic film. On the other hand, the relatively taller but densely spaced and extraordinary uniform in height nanopillars allow the cells to spread only on tops of the protrusions, and this further improves the proliferation. Different to the nanomounds and nanopillars, the nanostumps, lacking the above-mentioned features of surface morphology, do not provide good enough membrane support. This produces a negative impact on the cell adhesion and spreading, increases the stress, and lowers the cell survivability.

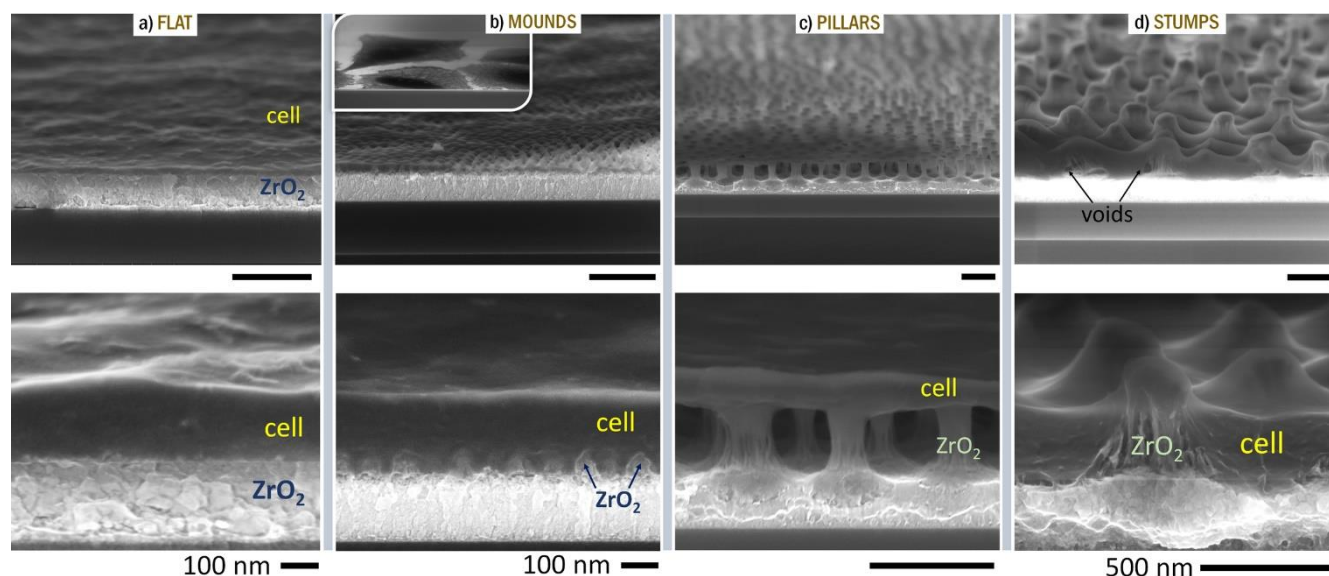


Fig. 3 SEM cross-fracture views of (a) a flat ZrO_2 anodic film, (b, c, and d) nanostructured ZrO_2 anodic films on SiO_2/Si substrates imaged after Saos-2 cells were cultured and dried for direct observation of the cell/surface interfaces. Unlabelled scale bars are 500 nm.

Focal contacts and cytoskeletal organization

To complement the viability, spreading, proliferation, and surface-cell interaction analysis results, the focal contacts and cytoskeletal organizations were fluorescently visualized and imaged in Fig. 5. The Saos-2 cells show mature dash-shaped focal adhesions on all the anodic ZrO_2 films. The biggest amount of large focal adhesions was found on the flat surface, well correlating with the observed cell surface area and surface/cell interfaces. Although the nanomound and nanopillar films both exhibit slightly fewer focal adhesions, the large contacts are well established. The staining of vinculin reveals substantially smaller adhesion sites and a smaller number of contacts on the nanostump film (Fig. 5, upper row), which correlates with the worsening of the adhesion and viability of the cells on these surfaces. The examination of cell morphology reveals the

polygonal shape of the well-spread Saos-2 cells, with a few elongated shapes observed on the nanostructured films. The population of elongated and rounded cells over the nanostump film increases whereas the cell spreading areas become apparently smaller. The effect might be due to oncoming apoptosis. The behavior observed correlates with the lowering of the cell survivability rate and the worsening of the cell/surface adhesion on the nanostump array relative to the other ZrO_2 nanofilms.

The focal adhesions connect the actin filaments *via* integrins to the surface. The process of making the filaments is crucial for the cells to maintain their morphology and osteogenic potential.⁴⁹ Both the flat and nanostructured films reveal a well-defined organization of actin filaments crossing the cell from end to end, with no disruption in the cytoskeletal organization (Fig. 5, bottom row). A slightly smaller number of actin filaments was observed on the

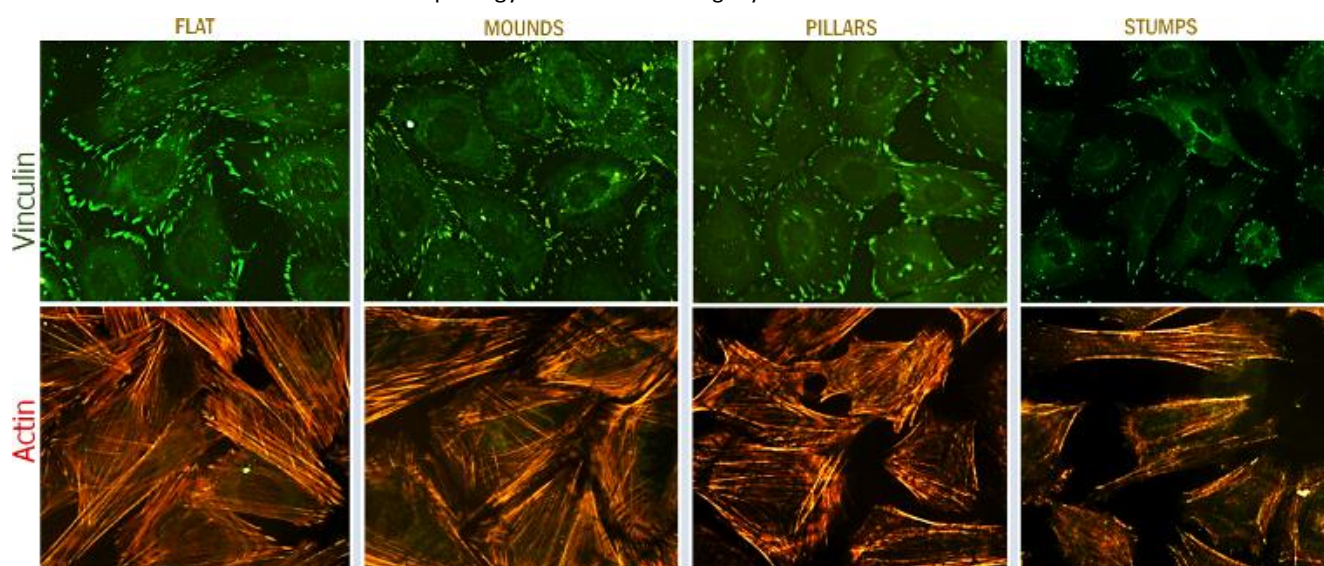


Fig. 5 Immunofluorescence staining of vinculin (top row) and actin filaments (bottom row) of Saos-2 cells after one day of culture on ZrO_2 surfaces derived from the anodically oxidized Al/Zr bilayers (as shown in Fig. 1 and 4). Focal adhesions positive for vinculin are indicated by green spots, and the organization of actin fibers is indicated by red color.

zirconium-oxide nanostumps, which may be explained by the above-described features of their surface morphology and the corresponding cell/film interface.

ALP activity and mineralization

In vitro differentiation of Saos-2 cells into osteoblasts can be evaluated by matrix maturation and mineralization, both events being enhanced by culturing the cells in a confluent layer. The progress is assessed by the expression of proteins, such as osteocalcin and osteopontin, and through monitoring the calcification, supported by the addition of the specific osteogenic supplements into the culture medium.⁵⁰ Nanostructured surfaces have previously been reported to enhance the production of these specific markers even in the absence of osteogenic factors.⁴⁴ The ALP is known as the mineralization promoter, which increases the local concentration of inorganic phosphate and can be used to characterize the progress in matrix maturation in-vitro.⁵¹ The impact of the surface topography on the differentiation of Saos-2 into osteoblasts was evaluated by the quantitative detection of ALP enzyme on day 9 (Fig. 6). The result shows distinguishable statistical differences addressing the specific surface morphologies of the anodic films. The flat and nanostump films promote comparable ALP activity, which is, however, higher than that on the plastic control. The nanomound array gives a two-fold rise in the amount of alkaline phosphatase than the plastic control on day 9. The nanopillar array promotes the highest ALP activity among all the films. Such a standing-out ALP activity on the nanopillar array most likely originates from the unique mechanism of surface-cell interaction, such as the wish of Saos-2 cells to contact merely the pillar tops.

The investigation of APL activity on the different ZrO₂ coatings was complemented by the mineralization experiment, which visualized calcium deposits on days 9 and 21 (Fig. 7). The microscopic images of the Alizarin-Red stained extracellular calcium demonstrate the abundance of large calcium nodules on the nanopillar array, especially on day 21. Although the mineralization capacity is relatively smaller on the other surfaces, it is substantially higher with respect to the plastic control. Obviously, the mineralization is clearly

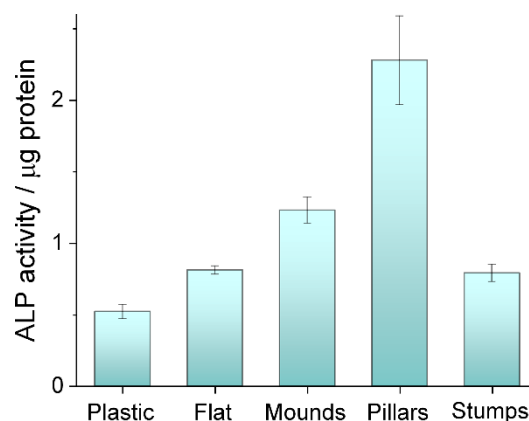


Fig. 4 Alkaline phosphatase produced by Saos-2 cells cultured on ZrO₂ surfaces derived from the anodically oxidized Al/Zr bilayers (as shown in Fig. 1 and 4) in comparison with a plastic control on day 9.

dependent upon the structuring, increasing in the following sequence of surfaces: plastic > flat > nanostumps > nanomounds > nanopillarsflat. Beyond doubts, all the nanostructured films promote mineralization in Saos-2 cells. In general, this finding does not contradict a previous study,⁵² where the specific surface topography was the key factor stimulating osteoblast maturation and mineralization.

Summary and perspectives

The qualitative comparison of the anodic ZrO₂ films showing the impact of the structuring on the major responses of Saos-2 cells is presented in a bar chart in Fig. 8. The lengths of the bars symbolizing the major characteristics obtained in this work are proportional to the values they represent, the best score being 5 for each characteristic.

From Fig. 8, the flat anodic film is obviously preferred by the cells in terms of cell adhesion and cell spreading area. The nanomound and nanopillar arrays greatly promote the osteoblast differentiation while the nanostump array hinders some of the vital bioproperties. For instance, the stump-like structuring results in slightly lower viability and obviously poorer cell adhesion, due to the specific cell-membrane/surface

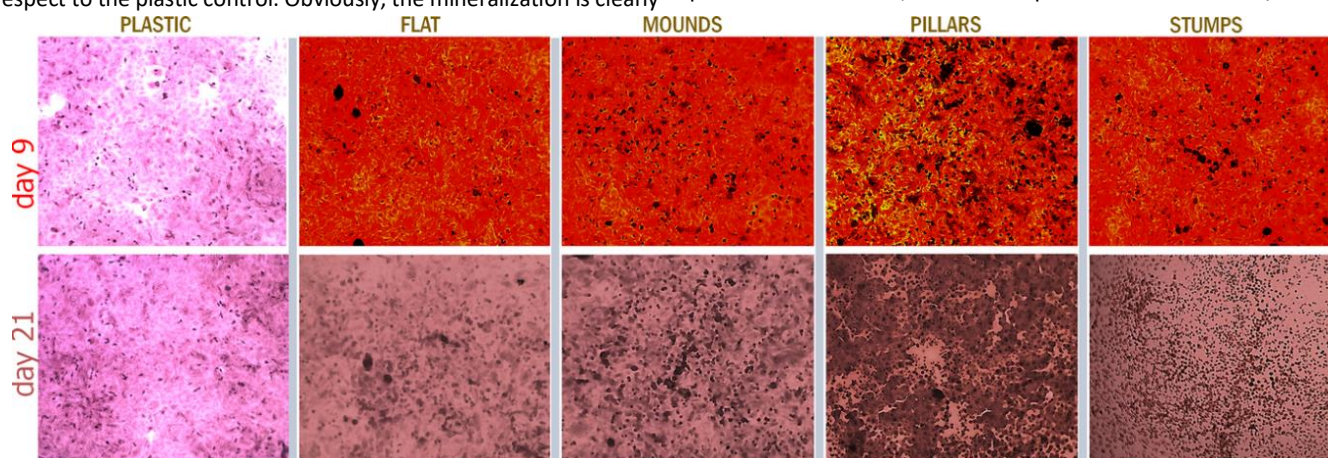


Fig. 5 Optical microscope images of Alizarin-Red stained extracellular calcium visualizing the effect of ZrO₂ nanostructuring on mineralization in the Saos-2 cells. The cells were cultured 9 and 21 days in complete DMEM medium without osteogenic supplements.

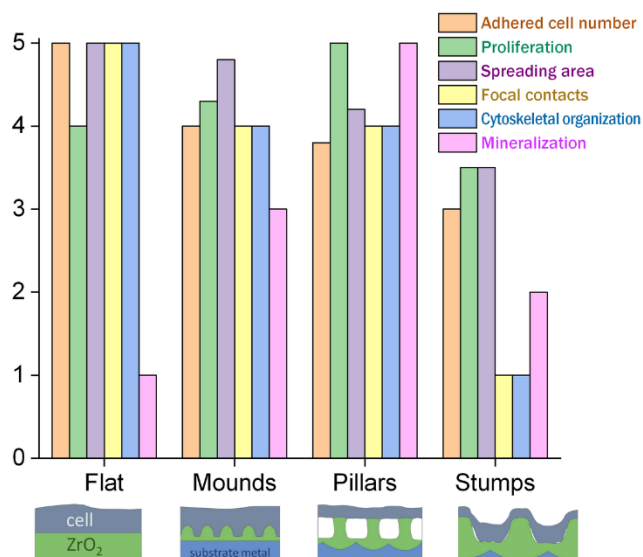


Fig. 6 Qualitative comparative biological responses of Seos-2 cells to ZrO_2 surfaces derived from the anodically oxidized Al/Zr bilayers (as shown in Fig. 1 and 4).

interaction. This also increases the number of stressed and dying cells and reduces the number of surface contacts. Contrarily, the mound-like structuring enables excellent cell survivability, adhesion, and spreading, which is revealed, for the first time, *via* direct SEM observation additionally to the commonly used actin and vinculin staining to expose the polygonal unstressed cells having mature focal adhesions and no disruption in the cytoskeletal organization. The benefits of the nanomound array are further expressed in a noticeably higher ALP activity and promotion of Saos-2 mineralization compared with the flat film.

While interacting with the nanopillar array, although facing practically no cytotoxicity, Saos-2 cells demonstrate a poorer spreading and adhesion compared with the nanomound array. However, the nanopillar array is vital for the promotion of proliferation and osteoblast differentiation of Saos-2 cells, demonstrating a substantially higher ALP activity and calcium deposition relative to the other nanostructured surfaces. Such auspicious conditions for the osteoblast differentiation and the enhanced surface adhesion are most likely to originate from the unique interaction with the nanopillar array, with no analogs among the other morphologies prepared in this study.

More generally, the findings of this work indicate that the specific surface structuring at the nanoscale achieved *via* the PAA-assisted anodization is a versatile tool for modulating the interaction of living cells with the anodic zirconium oxide films. The easy and precise control over the morphologies, dimensions, mutual arrangements, and population densities of the nanoscale surface features *via* the PAA-assisted anodization technique allows for facile production of nanostructured ZrO_2 bioceramic coatings with advanced biomedical properties. The anodizing technology is scalable for large surfaces and is also suitable for non-planar objects.⁵³ The PAA-assisted anodization can be used to cover the surfaces of many other metals and metal oxides with a thin nanostructured ZrO_2 bioceramic layer.

It is of high interest to continue the investigation of cell-surface interactions and their contribution to living cell activity

via the fabrication of surfaces with novel types of nanoscale topographies using the PAA-assisted anodization. The influence of such surfaces not only on living cells but also on various types of pernicious bacteria might also be assessed in future works. Furthermore, the nanostructured bioceramic coatings achieved *via* the PAA-assisted anodization may incorporate dopants from the anodizing solutions, which may enhance or modulate the biological response of various cell lines.¹⁵ In this course, the exploration of novel solutions for PAA-assisted anodization such as, for instance, selenic acid⁵⁴ may open unprecedented opportunities for tailoring the surface properties of zirconium oxide biomaterials to achieve antibacterial and anticancer effects.⁵⁵

Conclusions

All the anodic ZrO_2 coatings prepared in this study revealed the properties promising for biomedical applications. The findings emerging from this work suggest that the specific nanostructuring of the anodic ZrO_2 coatings (nanopillars and nanomounds) accelerates proliferation, stimulates APL production, and promotes matrix maturation and mineralization in Saos-2 cells relative to the flat anodic film. The cell spreading area, focal contacts, and cytoskeletal organization, although being the best on the flat ZrO_2 surface, only slightly worsen on the nanopillars and nanomounds. Paradoxically, the cells can sensitively recognize the features of surface structuring such as the shapes, sizes, spacings, and population densities of the zirconium-oxide nano-protrusions, giving their preferences to the nanopillars and nanomounds as compared with the nanostumps. The paradoxical appreciation by the cells of the nanopillar array, where the cell membrane only makes contacts with the flat pillar tops, extends the understanding of complex processes of cell/surface interaction. Living cells likely prefer either the small nanomounds without steep slopes or the tall nanopillars with the flat tops and optimal spacings, both surfaces preventing the cell membrane from undergoing a stressful distortion. The relatively better adhesion and the wider cell-spreading area on the flat ZrO_2 surface and the worse cytocompatibility of the big and rough ZrO_2 nanostumps reinforce this conclusion.

Conflicts of interest

There are no conflicts to declare.

Acknowledgements

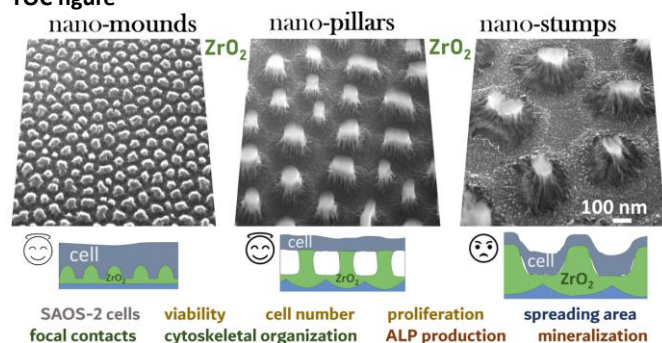
This research was supported by a grant of the Czech Science Foundation (GA ČR) no. 17-13732S. Part of this research was financially supported by the Ministry of Education, Youth and Sports of the Czech Republic under the project CEITEC 2020 (LQ1601). CzechNanoLab project LM2018110 funded by MEYS CR is acknowledged for the financial support of the sputter-deposition and SEM analysis at CEITEC Nano Research Infrastructure.

References

- N. Huebsch and D. J. Mooney, Inspiration and application in the evolution of biomaterials, *Nature*, 2009, **462**, 426–432.
- K. Prasad, O. Bazaka, M. Chua, M. Rochford, L. Fedrick, J. Spoor, R. Symes, M. Tieppo, C. Collins, A. Cao, D. Markwell, K. Ostrikov and K. Bazaka, Metallic biomaterials: Current challenges and opportunities, *Materials (Basel)*, 2017, **10**, 884.
- M. Saini, Y. Singh, P. Arora, V. Arora and K. Jain, Implant biomaterials: A comprehensive review, *World J. Clin. Cases WJCC*, 2015, **3**, 52.
- M. Rahmati, E. A. Silva, J. E. Reseland, C. A. Heyward and H. J. Haugen, Biological responses to physicochemical properties of biomaterial surface, *Chem. Soc. Rev.*, 2020, **49**, 5178–5224.
- S. Bose, S. F. Robertson and A. Bandyopadhyay, Surface modification of biomaterials and biomedical devices using additive manufacturing, *Acta Biomater.*, 2018, **66**, 6–22.
- M. Albakry, M. Guazzato and M. V. Swain, Effect of sandblasting, grinding, polishing and glazing on the flexural strength of two pressable all-ceramic dental materials, *J. Dent.*, 2004, **32**, 91–99.
- K. Balani, V. Verma, A. Agarwal and R. Narayan, *Biosurfaces A Mater. Sci. Eng. Perspect.*, 2015, 1–364.
- J. Qin, D. Yang, S. Maher, L. Lima-Marques, Y. Zhou, Y. Chen, G. J. Atkins and D. Losic, Micro- and nano-structured 3D printed titanium implants with a hydroxyapatite coating for improved osseointegration, *J. Mater. Chem. B*, 2018, **6**, 3136–3144.
- L. Yang, J. Wei, Z. Ma, P. Song, J. Ma, Y. Zhao, Z. Huang, M. Zhang, F. Yang and X. Wang, The fabrication of micro/nano structures by laser machining, *Nanomaterials*, 2019, **9**, 1789.
- J. P. St-Pierre, M. Gauthier, L. P. Lefebvre and M. Tabrizian, Three-dimensional growth of differentiating MC3T3-E1 pre-osteoblasts on porous titanium scaffolds, *Biomaterials*, 2005, **26**, 7319–7328.
- O. Bilek, Z. Fohlerova and J. Hubalek, Enhanced antibacterial and anticancer properties of Se-NPs decorated TiO₂ nanotube film, *PLoS One*, 2019, **14**, e0214066.
- S. Berger, F. Jakubka and P. Schmuki, Formation of hexagonally ordered nanoporous anodic zirconia, *Electrochem. Commun.*, 2008, **10**, 1916–1919.
- M. Karlsson, E. Pålsgård, P. R. Wilshaw and L. Di Silvio, Initial in vitro interaction of osteoblasts with nano-porous alumina, *Biomaterials*, 2003, **24**, 3039–3046.
- A. Mozalev, M. Sakairi, I. Saeki and H. Takahashi, Nucleation and growth of the nanostructured anodic oxides on tantalum and niobium under the porous alumina film, *Electrochim. Acta*, 2003, **48**, 3155–3170.
- A. Mozalev, M. Sakairi and H. Takahashi, Structure, Morphology, and Dielectric Properties of Nanocomposite Oxide Films Formed by Anodizing of Sputter-Deposited Ta–Al Bilayers, *J. Electrochem. Soc.*, 2004, **151**, F257.
- A. Mozalev, R. M. Vazquez, C. Bittencourt, D. Cossement, F. Gispert-Guirado, E. Llobet, H. Habazaki, Formation-structure-properties of niobium-oxide nanocolumn arrays via self-organized anodization of sputter-deposited aluminum-on-niobium layers, *J. Mater. Chem. C*, 2014, **2**, 4847–4860.
- A. Mozalev, M. Bendova, F. Gispert-Guirado and E. Llobet, Hafnium-Oxide 3-D Nanofilms via the Anodizing of Al/Hf Metal Layers, *Chem. Mater.*, 2018, **30**, 2694–2708.
- M. Sepúlveda, J. G. Castaño and F. Echeverría, Fabrication of highly-ordered TiO₂ nanocolumns by two-step anodizing of an Al/Ti layer in etidronic acid, *Mater. Chem. Phys.*, 2018, **216**, 51–57.
- A. Mozalev, M. Bendova, F. Gispert-Guirado, Z. Pytlíček and E. Llobet, Metal-substrate-supported tungsten-oxide nanoarrays via porous-alumina-assisted anodization: from nanocolumns to nanocapsules and nanotubes, *J. Mater. Chem. A*, 2016, **4**, 8219–8232.
- M. Sepúlveda, K. Kamnev, Z. Pytlíček, J. Prasek, A. Mozalev, Superhydrophobic-oleophobic visible-transparent antireflective nanostructured anodic HfO₂ multifunctional coatings for potential solar panel application, *ACS Appl. Nano Mater.*, published online, dx.doi.org/10.1021/acsnm.0c03202.
- Z. Fohlerova and A. Mozalev, Anodic formation and biomedical properties of hafnium-oxide nanofilms, *J. Mater. Chem. B*, 2019, **7**, 2300–2310.
- Z. Fohlerova and A. Mozalev, Tuning the response of osteoblast-like cells to the porous-alumina-assisted mixed-oxide nano-mound arrays, *J. Biomed. Mater. Res. - Part B Appl. Biomater.*, 2018, **106**, 1645–1654.
- A. Afzal, Implantable zirconia bioceramics for bone repair and replacement: A chronological review, *Mater. Express*, 2014, **4**, 1–12.
- V. Sollazzo, F. Pezzetti, A. Scarano, A. Piattelli, C. A. Bignozzi, L. Massari, G. Brunelli and F. Carinci, Zirconium oxide coating improves implant osseointegration in vivo, *Dent. Mater.*, 2008, **24**, 357–361.
- P. F. Manicone, P. Rossi Iommetti and L. Raffaelli, An overview of zirconia ceramics: Basic properties and clinical applications, *J. Dent.*, 2007, **35**, 819–826.
- Y. J. Park, J. W. Kim, G. Ali and S. O. Cho, Enhancement of oxidation resistance of zirconium alloy with anodic nanoporous oxide layer in high-temperature air/steam environments, *Corros. Sci.*, 2018, **140**, 217–222.
- L. Guo, J. Zhao, X. Wang, X. Xu, H. Liu and Y. Li, Structure and bioactivity of zirconia nanotube arrays fabricated by anodization, *Int. J. Appl. Ceram. Technol.*, 2009, **6**, 636–641.
- C. Hadjicharalambous, A. Buyakov, S. Buyakova, S. Kulkov and M. Chatzinikolaïdou, Porous alumina, zirconia and alumina/zirconia for bone repair: Fabrication, mechanical and in vitro biological response, *Biomed. Mater.*, 2015, **10**, 25012.
- C. Hadjicharalambous, O. Prymak, K. Loza, A. Buyakov, S. Kulkov and M. Chatzinikolaïdou, Effect of porosity of alumina and zirconia ceramics toward pre-osteoblast response, *Front. Bioeng. Biotechnol.*, 2015, **3**, 175.
- L. N. Wang and J. L. Luo, Electrochemical behaviour of anodic zirconium oxide nanotubes in simulated body fluid, *Appl. Surf. Sci.*, 2012, **258**, 4830–4833.
- M. Dehestani, L. Ilver and E. Adolfsson, Enhancing the bioactivity of zirconia and zirconia composites by surface modification, *J. Biomed. Mater. Res. Part B Appl. Biomater.*, 2012, **100**, 832–840.
- A. Mozalev, Z. Pytlíček, K. Kamnev, J. Prasek, F. Gispert-Guirado and E. Llobet, Zirconium oxide nanoarrays via the self-organized anodizing of Al/Zr bilayers on substrates, *Mater. Chem. Front.*, 2021, advance article, doi.org/10.1039/D0QM00862A.
- A. Mozalev and J. Hubalek, On-substrate porous-anodic-alumina-assisted gold nanostructure arrays: Meeting the challenges of various sizes and interfaces, *Electrochim. Acta*, 2019, **297**, 988–999.
- A. Mozalev, M. Bendova, R. M. Vazquez, Z. Pytlíček, E. Llobet and J. Hubalek, Formation and gas-sensing properties of a porous-alumina-assisted 3-D niobium-oxide nanofilm, *Sensors Actuators, B Chem.*, 2016, **229**, 587–598.
- M. Bendova, F. Gispert-Guirado, A. W. Hassel, E. Llobet and A. Mozalev, Solar water splitting on porous-alumina-assisted TiO₂-doped WO_x nanorod photoanodes: Paradoxes and challenges, *Nano Energy*, 2017, **33**, 72–87.
- K. Anselme, L. Ploux and A. Ponche, Cell/material interfaces: influence of surface chemistry and surface topography on cell adhesion, *J. Adhes. Sci. Technol.*, 2010, **24**, 831–852.

- 37 J. Chłopek, B. Czajkowska, B. Szaraniec, E. Frackowiak, K. Szostak and F. Béguin, In vitro studies of carbon nanotubes biocompatibility, *Carbon N. Y.*, 2006, **44**, 1106–1111.
- 38 Y. Wang, C. Wen, P. Hodgson and Y. Li, Biocompatibility of TiO₂ nanotubes with different topographies, *J. Biomed. Mater. Res. - Part A*, 2014, **102**, 743–751.
- 39 T. Kim, I. Sridharan, B. Zhu, J. Orgel and R. Wang, Effect of CNT on collagen fiber structure, stiffness assembly kinetics and stem cell differentiation, *Mater. Sci. Eng. C*, 2015, **49**, 281–289.
- 40 L. Lv, Y. Liu, P. Zhang, X. Zhang, J. Liu, T. Chen, P. Su, H. Li and Y. Zhou, The nanoscale geometry of TiO₂ nanotubes influences the osteogenic differentiation of human adipose-derived stem cells by modulating H3K4 trimethylation, *Biomaterials*, 2015, **39**, 193–205.
- 41 K. Metavarayuth, P. Sitasuwan, X. Zhao, Y. Lin and Q. Wang, Influence of surface topographical cues on the differentiation of mesenchymal stem cells in vitro, *ACS Biomater. Sci. Eng.*, 2016, **2**, 142–151.
- 42 C. J. Bettinger, R. Langer and J. T. Borenstein, Engineering substrate topography at the micro- and nanoscale to control cell function, *Angew. Chemie Int. Ed.*, 2009, **48**, 5406–5415.
- 43 S. Oh, K. S. Brammer, Y. S. J. Li, D. Teng, A. J. Engler, S. Chien and S. Jin, Stem cell fate dictated solely by altered nanotube dimension, *Proc. Natl. Acad. Sci.*, 2009, **106**, 2130–2135.
- 44 A. Ranella, M. Barberoglou, S. Bakogianni, C. Fotakis and E. Stratakis, Tuning cell adhesion by controlling the roughness and wettability of 3D micro/nano silicon structures, *Acta Biomater.*, 2010, **6**, 2711–2720.
- 45 N. Buch-Månson, D.-H. Kang, D. Kim, K. E. Lee, M.-H. Yoon and K. L. Martinez, Mapping cell behavior across a wide range of vertical silicon nanocolumn densities, *Nanoscale*, 2017, **9**, 5517–5527.
- 46 X. Xie, A. Aalipour, S. V. Gupta and N. A. Melosh, Determining the time window for dynamic nanowire cell penetration processes, *ACS Nano*, 2015, **9**, 11667–11677.
- 47 J. Vinje, N. A. Guadagno, C. Progidia and P. Sikorski, Actin cytoskeletal and focal adhesion organisation in U2OS cells on polymer nanostructures, *bioRxiv*, 2020, 2020.09.14.289330.
- 48 M. A. Stolarska and A. R. Rammohan, Center or periphery? Modeling the effects of focal adhesion placement during cell spreading, *PLoS One*, 2017, **12**, e0171430.
- 49 S. Pellegrin and H. Mellor, Actin stress fibres, *J. Cell Sci.*, 2007, **120**, 3491–3499.
- 50 C. A. Gregory, W. G. Gunn, A. Peister and D. J. Prockop, An Alizarin red-based assay of mineralization by adherent cells in culture: comparison with cetylpyridinium chloride extraction, *Anal. Biochem.*, 2004, **329**, 77–84.
- 51 M. G. Necula, A. Mazare, R. N. Ion, S. Ozkan, J. Park, P. Schmuki and A. Cimpean, Lateral spacing of TiO₂ nanotubes modulates osteoblast behavior, *Materials (Basel)*, 2019, **12**, 2956.
- 52 X. Shen, P. Ma, Y. Hu, G. Xu, J. Zhou and K. Cai, Mesenchymal stem cell growth behavior on micro/nano hierarchical surfaces of titanium substrates, *Colloids Surfaces B Biointerfaces*, 2015, **127**, 221–232.
- 53 C. Yao and T. J. Webster, Anodization: a promising nano-modification technique of titanium implants for orthopedic applications, *J. Nanosci. Nanotechnol.*, 2006, **6**, 2682–2692.
- 54 Y. Nazarkina, K. Kamnev, A. Dronov, A. Dudin, A. Pavlov and S. Gavrilov, Features of porous anodic alumina growth in galvanostatic regime in selenic acid based electrolyte, *Electrochim. Acta*, 2017, **231**, 327–335.
- 55 T. Li and H. Xu, Selenium-Containing Nanomaterials for Cancer Treatment, *Cell Reports Phys. Sci.*, 2020, 100111.

TOC figure



Článek 6

SiO₂-decorated Parylene C micropillars designed to probe cellular force

SiO₂-Decorated Parylene C Micropillars Designed to Probe Cellular Force

Zdenka Fohlerova,* Imrich Gablech, Alexandr Otahal, and Peter Fecko

Living cells sense and respond to mechanical signals through specific mechanisms generating traction force. The quantification of cell forces using micropillars can be limited by micropillar stiffness, technological aspects of fabrications, and microcontact printing of proteins. This paper develops the new design of SiO₂/Parylene C micropillars with an aspect ratio of 6 and 3.5 and spring constant of 4.7 and 28 μN μm⁻¹, respectively. The upper part of micropillars is coated with a 250 nm layer of SiO₂, and results confirm protein deposition on individual micropillars via SiO₂ interface and non-adhesiveness on the micropillars' sidewalls. Results show an absence of cytotoxicity for micropillar-based substrates and a dependence on its stiffness. Stiffer micropillars enhance cell adhesion and proliferation rate, and a stronger cellular force of ≈25 μN is obtained. The main contribution of SiO₂/parylene C micropillars is the elimination of the step involving the fabrication of polydimethylsiloxane stamp because the array enables covalent binding of proteins via SiO₂ chemistry. These micropillars stand on Si wafer and thus, any warping of underlying polymer membrane does not have to be considered. Additionally, SiO₂/parylene C micropillars can broaden the range of stiffer substrates to be probed by cells.

1. Introduction

The mechanical and adhesion properties of living cells are guided by chemical signals and external physical stimuli; cells have been exposed to different external forces such as the magnetic force,^[1] shear stress,^[2] or the mechanical properties of the substrate.^[3,4] The importance of the interplay between chemical and physical stimuli and the sensitivity of cells' response to

these stimuli through the generation of traction force is fundamental for physiological and pathological pathways.^[5]

The investigation of cellular forces depends on in-vitro platforms that can mimic processes and the stiffness of cellular environments or these platforms serve as sensors detecting the force upon the exposure cells to the, for example, drugs. Recently developed tools to quantify the traction force generated by cells range from microscopy to molecular force sensors.^[6–11] All these techniques possess some advantages and disadvantages^[12] and offer a variety of mechanisms through which cells can move, divide, remodel, differentiate, communicate, and sense their microenvironment.^[13]

One of the approaches to measuring forces transmitted at the focal adhesion is the culturing of cells on patterned micropillars. Microfabrication techniques allow for the production of an array of thousands of elastic pillars of 0.5–5 μm in

diameter, fabricated by photolithography and replica molding with conventional polydimethylsiloxane (PDMS).^[14] The top of the pillar surface is coated with proteins of extracellular matrix via microcontact printing to render them cell-adhesive.^[15] The cylindrical pillars with a defined L/D aspect ratio (length *L*, diameter *D*) and Young's modulus of the material (*E*) allow for the calculation of the cellular force based on the pillar bending and the known spring constant *k*, which is in the range of 1 to 200 nN μm⁻¹ for typical PDMS pillars.^[16] For the small deformation Δ*x*, the lateral force *F* can be calculated using Hooke's law, as described in Equation (1):^[16]

$$F = k \cdot \Delta x = \frac{3\pi E D^4}{64 L^3} \cdot \Delta x \quad (1)$$

Most authors have published the micropillars with lower spring constant and thus the stiffness or high aspect ratio pillars from stiffer polymers for increasing the spatial resolution. The molding technique frequently used for polymers such as PDMS with Young's modulus 1 to 4 MPa^[17] permits the precise fabrication of a low aspect ratio micropillars. The molding high-aspect-ratio micropillars is more challenging because it is difficult to successfully de-mold the structure. Therefore, this technique requires good mold releasability during the de-molding. Additionally, high aspect ratio pillars may have tendency of cracking and clustering.

Prof. Z. Fohlerova, Dr. I. Gablech, P. Fecko
Central European Institute of Technology
Brno University of Technology
Purkynova 123, Brno 61200, Czech Republic
E-mail: zdenka.fohlerova@ceitec.vutbr.cz
Prof. Z. Fohlerova, Dr. I. Gablech, Dr. A. Otahal
Department of Microelectronics
Faculty of Electrical Engineering and Communication
Brno University of Technology
Technicka 3058/10, Brno 61600, Czech Republic
Prof. Z. Fohlerova
Department of Biochemistry
Faculty of Medicine
Masaryk University
Kamenice 753/5, Brno 625 00, Czech Republic

 The ORCID identification number(s) for the author(s) of this article can be found under <https://doi.org/10.1002/admi.202001897>.

DOI: 10.1002/admi.202001897

Nevertheless, molding allowed the production of PDMS micropillars of different stiffness by the modulation of pillar aspect ratio, geometry,^[18] UV-treatment,^[19] and the degree of the polymerization^[20] and this technique was also adopted for the fabrication of PDMS stamp required for microcontact printing of proteins. The variability in PDMS stiffness became an important progress in measurement of cellular forces because a broad range of substrate stiffness can mimic the various stiffness of physiological tissues, which can range from 10^2 to 10^7 Pa, from the softest brain to the stiffest bone, respectively.^[21] Moreover, the rigidity of tissue can be significantly changed due to diseases such as cancers, Alzheimer's disease, or spinal cord injury.^[22]

Besides PDMS, different polymers have been used to fabricate micropillars such as polyacrylamide,^[23] poly(methylmethacrylate),^[24] SU-8,^[25] and polycarbonate (PC).^[26] For instance, a high aspect ratio (≈ 11) of SU-8 micropillars with $E \approx 4$ GPa has been fabricated using lithography technique. Authors well-described the optimization of fabrication process,^[25] particularly when temporal stability and the high spatial resolution of the array should be required. In addition to the SU-8 polymer, a polycarbonate with Young's modulus of 2–3 GPa has been used to fabricate ultrahigh aspect ratio (up to 20) pillars with spring constant ≈ 5 nN μm^{-1} to enhance cell differentiation^[26] and similar aspect ratio has been used to measure cellular forces by other authors.^[4]

In this work, we show “top-down” fabrication of a highly ordered array of SiO₂/parylene C micropillars standing on the Si substrate that can be used as a probe to quantify the force generated from living cells. The array of micropillars with aspect ratio corresponding to 6 and 3.5 was characterized for its chemical and biological properties as a proof-of-principle for the functionality of array to be used as a force sensor. The technological significance of the cellular force transducer here is the elimination of the micro-contact printing of proteins, given that the SiO₂ thin film allows the covalent binding of proteins or peptides, or simply enables a charge or different wettability properties on top of micropillars via SiO₂ chemistry. This could help researchers to skip the fabrication of a PDMS stamp and to prevent the differences in printing quality.^[27,28] The second contribution of this work is to prove that the fabrication of pillars from parylene C as the highly rigid material with a Young's modulus of ≈ 4 GPa can, compared to other polymers used for pillar fabrication, broaden the range of material stiffness to be probed by cells. The third advantage of our micropillars is that our micropillars stand on Si wafer and thus any warping of underlying polymer membrane does not have to be considered as it has been reported for PDMS with lower aspect ratio.

2. Results and Discussion

2.1. Fabrication and Characterization of SiO₂/Parylene Pillars

The array of SiO₂/parylene micropillars was fabricated on a 0.5 mm \times 0.5 mm silicon substrate by “top-down” technology, as described in Figure S1, Supporting Information. The micro-fabrication process of micropillar development provided the array of the hexagonally ordered parylene pillars with a ≈ 1.6 μm

diameter, ≈ 3 μm center-to-center distance, and rod-like morphology, as confirmed by a scanning electron microscopy (Figure 1A). The deposition of a ≈ 250 nm SiO₂ layer on the top of the micropillars to mediate the selective covalent binding of protein was qualitatively analyzed via an scanning electron microscopy (SEM) equipped energy-dispersive X-ray (EDX) spectroscope. High-resolution elemental mapping enabled this study to discriminate between different elemental compositions, which allowed us to visualize the localization of the SiO₂ on top of the pillars. The EDX image in Figure 1B shows the highly localized EDX oxygen atoms on top of the pillars from the SiO₂ layer (colored red), while parylene C is shown as light blue. The elemental analysis confirmed the selective deposition of SiO₂ on top of the micropillars and therefore the efficacy of the proposed individual fabrication steps.

The stiffness of the micropillars was modulated by varying their height, giving the pillars a height of 9 and 5 μm and an aspect ratio corresponding to 6 and 3.5, respectively. The SiO₂ layer on top of the pillars did not change the bulk properties of parylene C, and the spring constant k of micropillar was approximately calculated according to Equation (1). Based on this Equation (1), the parylene micropillar with a length of 9 and 5 μm has a spring constant of $k = \approx 4.8$ $\mu\text{N} \mu\text{m}^{-1}$ and ≈ 28 $\mu\text{N} \mu\text{m}^{-1}$, respectively. The spring constants of the parylene micropillars are thus significantly higher, compared to the already published spring constant of 1–1500 nN μm^{-1} for widely used PDMS.^[18,19] Moreover, material with a higher Young's modulus of polycarbonate has been already investigated as platforms for the measurement of cellular force.^[4] The authors managed to produce an array of PC pillars with $k = \approx 3$ $\mu\text{N} \mu\text{m}^{-1}$ and $k = \approx 7$ $\mu\text{N} \mu\text{m}^{-1}$ by changing the aspect ratio. To our knowledge, micropillars with such high $k = \approx 28$ $\mu\text{N} \mu\text{m}^{-1}$ have not been used for the measurement of cellular force as we further confirmed that they can be sensed and bent by cells. Additionally, the fabrication process of our micropillars provides technological resolution of ≈ 0.8 μm , ensures good spatial stability of micropillars as well as temporal stability due to the chemical inertness of parylene.

2.2. Micropillars Patterning

Patterning the micropillars to enhance cell adhesion is the first step guaranteed by the use of nanotechnology to selectively deposit a thin layer of SiO₂ on top of pillars. Generally, the protein modification of micropillars in order to measure cellular force requires the selective deposition of a protein such as fibronectin on top of the pillars via microcontact printing^[28] and by the non-adhesive treatment of pillar sidewalls.^[29] Such pillar patterning avoids the undesired attachment of cells to the vertical side of the micropillar and improves cell adhesion. However, the micro-contact printing of proteins requires the additional fabrication of the stamp and is limited in terms of which proteins can be printed as well as the printing quality.^[28] Our design and patterning of SiO₂/parylene micropillars is able to covalently bind any proteins of interest to the upper surface of the micropillars via SiO₂ interface, as shown in Figure S2, Supporting Information. The SiO₂/parylene patterning was first investigated on bulk substrates because the chemistry on such pillars differs from PDMS ones and must be optimized. To ensure the binding of

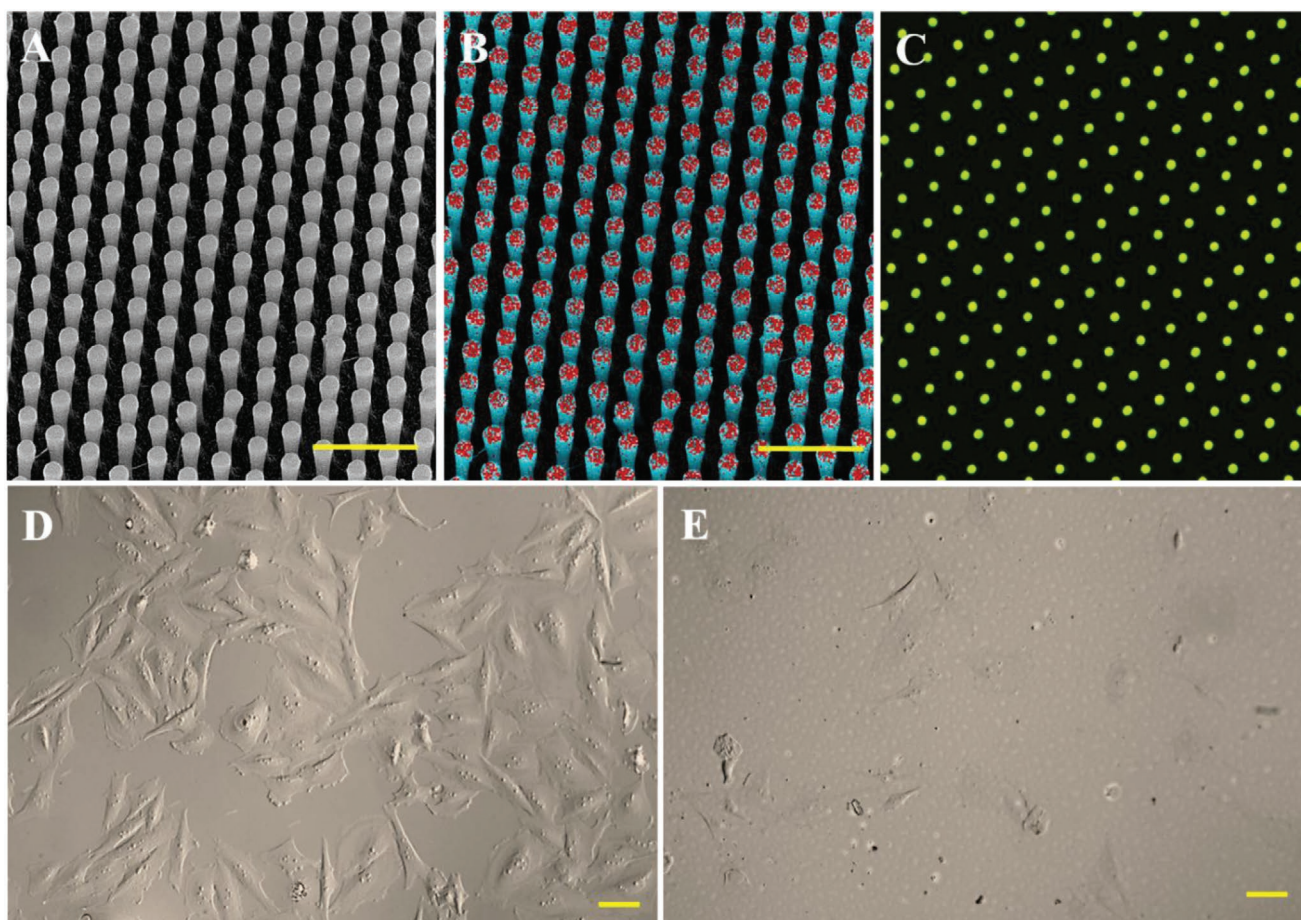


Figure 1. SEM image of an array of well-ordered SiO₂/parylene C micropillars (A). A qualitative EDX analysis of the micropillars. The red spots represent the targeted SiO₂ layer on top of the parylene C micropillars, while the blue represents the parylene C pillars (B). A fluorescent image of the micropillars with covalently bound FITC-collagen protein (C). A DIC image of 3T3-fibroblasts adhered on fibronectin-coated SiO₂ (D). A DIC image of 3T3-fibroblasts adhered on Pluronic F-127-treated parylene C (E). The scale bar of the SEM and DIC image corresponds to 10 μm and 50 μm, respectively.

the protein to the SiO₂ layer, selective SiO₂ oxidation was performed by treating it with a piranha solution at a 5:3 ratio (step 1 in Figure S2, Supporting Information). The procedure exposed hydroxyl groups on the silica surface, while the parylene C sidewalls remained unreacted,^[30] as confirmed by the measurement of contact angle (CA). The piranha-treated SiO₂ decreased the CA value from ≈67° to ≈23°, making the surface more hydrophilic while the parylene C surface remained unchanged ≈109° (Figure 2a,b and a', b'). The silanization of the hydroxyl reached the SiO₂ substrate with the (3-aminopropyl)triethoxysilane (APTES), which fed the amino-terminal groups on the surface that changed the CA from ≈23° to ≈49° and from ≈109° to ≈104° for SiO₂ and parylene C, respectively (Figure 2c,c'). This SiO₂ chemistry has strong support in the literature^[31] and significantly, the result showed that the parylene C remained intact following the piranha oxidation and silanization process.^[30] To ensure non-adhesive pillar sidewalls, the array was further incubated in a non-ionic surfactant Pluronic F-127. The deposition of the Pluronic via its hydrophobic moiety exposed the hydrophilic non-adhesive PEG groups to the parylene C that corresponds to the decreased CA value ≈76° (Figure 2d,d'). A similar CA value for Pluronic to treat polymers has been reported for

PDMS,^[32] suggesting the successful nature of parylene C coating. The amino-functionalized SiO₂ surface remained unmodified because the CA value did not change significantly. The patterned surface of the micropillars was finally modified by the covalent immobilization of the fibronectin on the amino-terminated SiO₂ surface by crosslinking it with glutaraldehyde. The CA value changed for both surfaces because the fibronectin was immobilized on the SiO₂ surface and a small amount of fibronectin was adsorbed on the Pluronic F-127-treated parylene C sidewalls (Figure 2e,e'), which is in strong agreement with the literature.^[33]

Moreover, even if the Pluronic adsorb some portion of the proteins^[34] and the exposition of polyethylene oxide moiety suppresses the cell adhesion,^[32] patterning with Pluronic F-127 is generally accepted for the reduction of protein adsorption and cell adhesion. Based on this phenomenon, fluorescently labeled collagen was covalently immobilized on the top of micropillars and the image was captured to confirm the selective deposition of protein (Figure 1C). Further, the adhesion of 3T3-fibroblasts to fibronectin (Figure 1D) and Pluronic-F127 (Figure 1E) coated surface confirmed the reduced cell viability on Pluronic treated micropillars. The cells adhered to and spread on fibronectin-coated SiO₂ at high

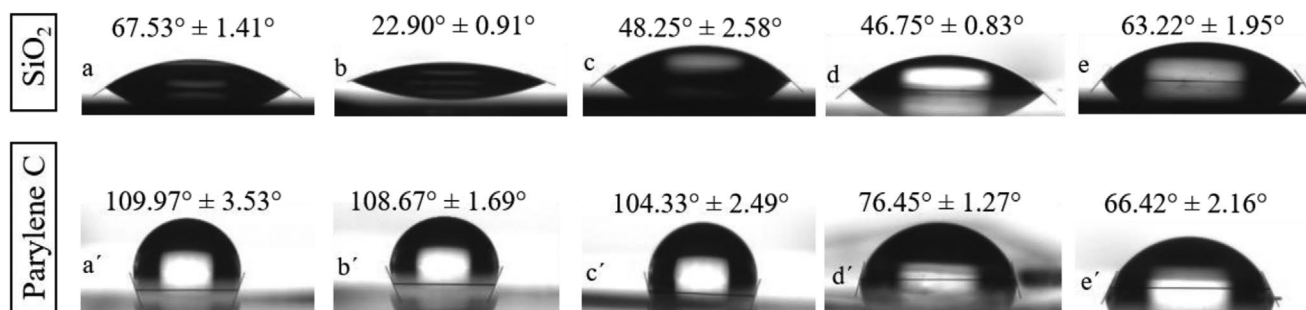


Figure 2. CA of the SiO₂ and parylene C modification. a,a') cleaned SiO₂ and parylene C substrates; b,b') substrates treated in 5:3 piranha solution for 10 min; c,c') substrates silanized with APTES at 120° for 30 min; d,d') surface treated with Pluronic F-127; e,e') covalently bonded fibronectin via glutaraldehyde on APTES-silanized surface.

density and had the characteristic elongated shape, while the cells on Pluronic F-127-treated parylene C adhered in a very small density and showed a smaller cell surface area.

The procedural steps of the surface oxidation and silanization were characterized by an X-ray photoelectron spectroscopy (XPS) analysis, as shown in Figure 3. The XPS spectra were analyzed by peak-fitting software (CasaXPS version 2.3.18PR1.0) provided by SPECS GmbH (Berlin, Germany). The raw data were processed by the subtraction of a Shirley background for secondary electrons and element peak fitting was used to estimate the relative elements' molar fraction. The integral of the peak was divided by a relative sensitivity factor that was characteristic of each element. Even if some elemental contaminants were to occur, a significant ≈20% increment of N 1s was observed, which could be attributed to the amino-functionalized SiO₂, while the increase in N 1s on parylene C was just 3.5% as shown in the table of Figure 3. A significant increase and unchanged percentage of C 1s was observed for APTES/SiO₂ and APTES/parylene C, respectively, confirming the successful selective silanization of the SiO₂ surface. Additionally, the high-resolution

spectra of nitrogen N 1s and silicon Si 2p for the APTES-treated SiO₂ surface are also shown in Figure 3.

2.3. Cell Adhesion and Cell Surface Area

The response of living cells to micro-/nanostructured surfaces is a well-known and widely investigated phenomenon.^[35] Living cells respond to chemical composition, wettability, topography, stiffness, and stress and these cues^[36] have been found to influence cellular adhesion, morphology, metabolic activity, proliferation, migration, and differentiation.^[37–42] The cellular characterization of SiO₂/parylene C micropillars was assessed by the morphology of 3T3-fibroblasts adhered to micropillar arrays to measure the cell spread area and the proliferation of cells on the micropillars, and qualitatively evaluate the organization of cellular cytoskeleton and the presence of focal contacts via fluorescently labeled actin fibers and vinculin. Since our micropillar arrays differed from the pillar height, we compared the cellular behavior of both arrays via the parameter of pillar

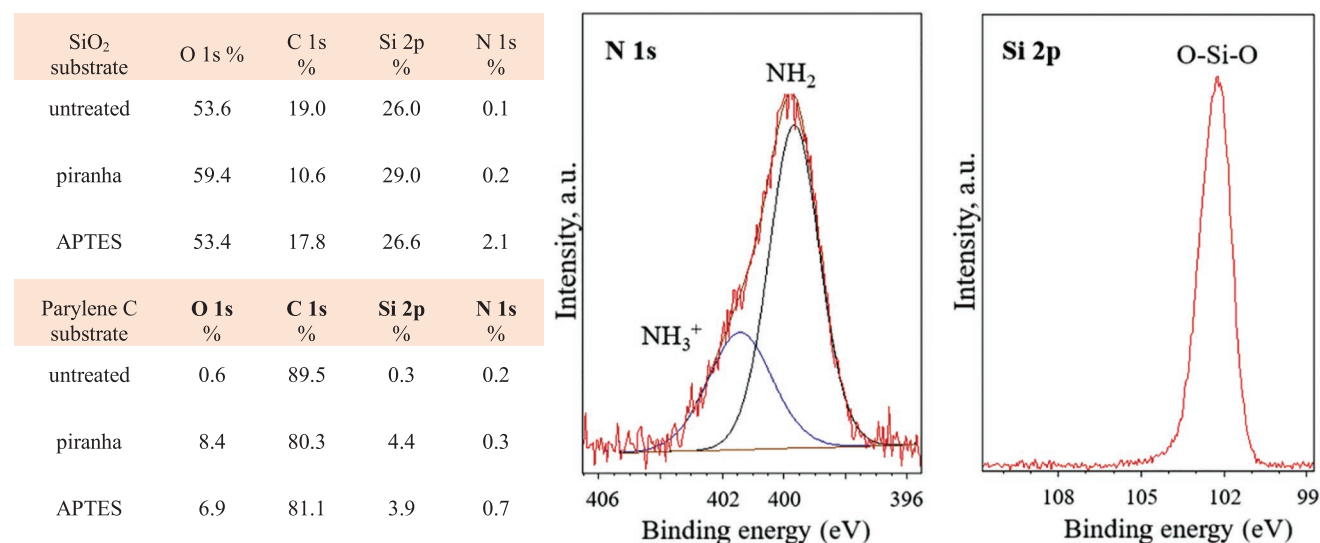


Figure 3. Table shows an elemental analysis of individual steps of SiO₂ and parylene C modification as extracted from the XPS spectrum in percentage; XPS analysis is performed for cleaned untreated SiO₂ and parylene C substrate, SiO₂ and parylene C treated in piranha solution and SiO₂ and parylene C silanized with APTES. The graphs show high-resolution spectra of nitrogen N 1s and silicon Si 2p for the APTES-treated SiO₂ surface.

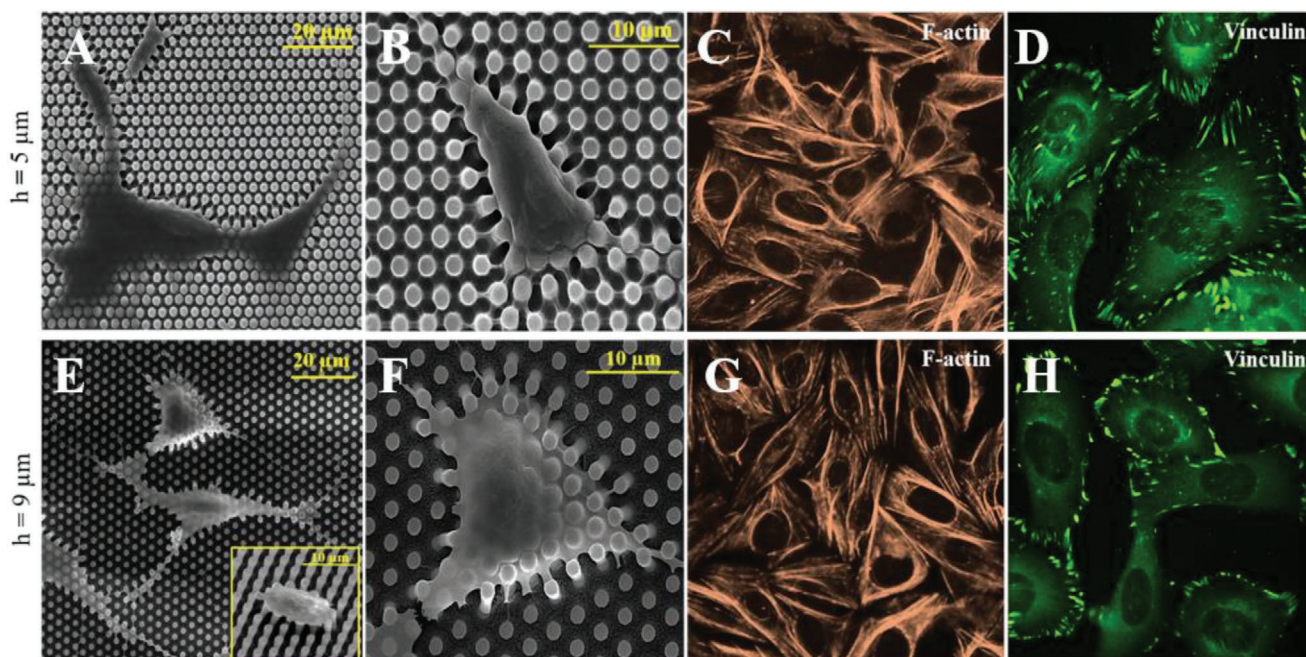


Figure 4. 3T3-fibroblasts on the micropillars with heights of 5 μm (stiffer; upper images) and 9 μm (softer; bottom images), respectively. Scans of the electron microscopy of cells showing the morphology and pillar's deflection (A,B,E,F). Fluorescently labeled actin fibers showing as a red (C, G) and a green staining of vinculin as the protein of the focal contacts (D,H).

stiffness. The morphology of the 3T3-fibroblasts attached to “softer” ($k \approx 4.7 \mu\text{N } \mu\text{m}^{-1}$) and “stiffer” ($k \approx 28 \mu\text{N } \mu\text{m}^{-1}$) pillars did not differ significantly since the shape of the cells ranged from polygonal to elongated (Figure 4A,B,E,F). The shape of 3T3-fibroblasts on both types of micropillars corresponds to the typical morphology in the stationary state of well-spread fibroblastic cells. The cells on both substrates had more extruding protrusions and larger lamellae. The staining of the actin filaments revealed prominent stress fibers that crossed the cell from end to end, and no disruption in the cytoskeletal organization was observed for either softer or stiffer micropillars (Figure 4C,G). A notable finding was observed for the vinculin staining, as shown in Figure 4D,H. The cells on “stiffer” micropillars (Figure 4D) showed a higher number of focal contacts, compared to the “softer” substrate (Figure 4H) and were larger in size and more distributed over the whole cells. The cell surface area was calculated from previously obtained fluorescence

images of cells using ImageJ software. We set the scale to know the number of pixels per area and the individual cells were dragged to measure their surface area. The statistical analysis was performed on hundred cells for each micropillar substrate. The evaluation of the cell spreading area revealed significantly larger areas for cells cultured on “stiffer” micropillars, compared to a “softer” surface (Figure 5A). These findings revealed better adhesion and cell contact with the underlying micropillars on the “stiffer” substrate since the larger surface area and extensive focal contacts were enhanced here, compared to the “softer” substrate.

2.4. Proliferation Assay

Our results from cell adhesion were further supported by the experiment of cell proliferation on both substrates. The

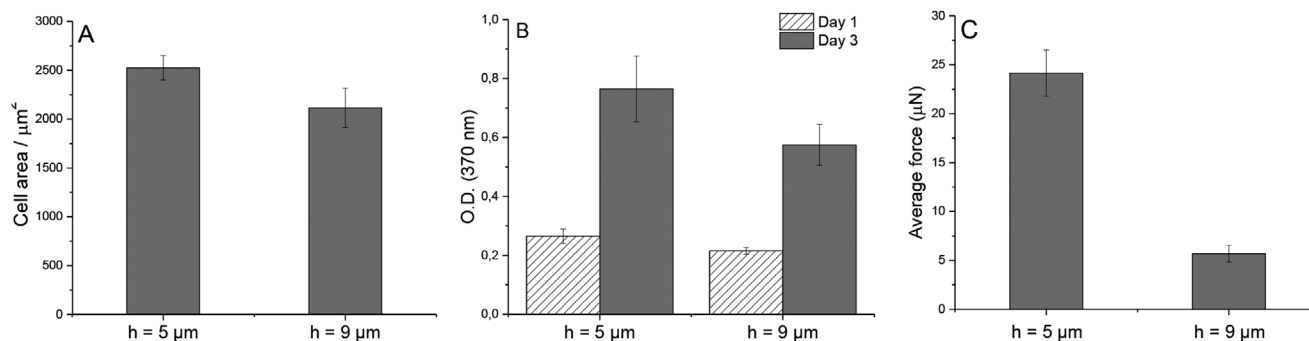


Figure 5. Evaluation of the spreading area of 3T3-fibroblasts per surface area (A). BrdU proliferation assay of fibroblasts on nanopillars (B). The average cellular force calculated from the periphery of stationary cells (C).

measurement of 5-bromo-2'-deoxyuridine (BrdU) was performed on days one and three (Figure 5B). This assay measured the incorporation of BrdU into the newly synthesized DNA and introduced the most reliable information about cell division. On day one, no significant differences in cell proliferation were observed between “stiffer” and “softer” micropillars, while on day three, a significantly higher proliferation rate could be seen for the “stiffer” micropillar array. The higher proliferation of cells could be a consequence of the enhanced cell adhesion on “stiffer” micropillars.

To conclude our preliminary observations of the cytocompatibility of SiO₂/parylene C micropillars, the 3T3-fibroblasts sensed the different stiffness of micropillars due to changes in cell adhesion and proliferation, which is in good agreement with the literature.^[43,44] From a more general perspective, neither micropillar arrays showed any cytotoxic effect in terms of cell viability and adhesive properties.

2.5. Estimation of Cellular Force

A preliminary examination was performed to substantiate the suitability of SiO₂/parylene C micropillars to probe cellular force. The assessment was performed on stationary polygonal-shaped fibroblasts selected from SEM images in order to obtain a symmetric cellular force profile. The deflection of the micropillars were measured from their original, undeflected position using Image J software. The extent of the deflection was then used to quantify the traction forces generated by the 3T3-fibroblasts by applying Equation (1). To compare the force exerted from the cells on the “stiffer” and “softer” micropillars, the average force was calculated from the pillar's deflection that occurred on the cell periphery (Figure 5C). Our finding showed that the cells on the “stiffer” micropillars exert almost five times more traction force than those cultured on the “softer” substrate. For 3T3-fibroblasts, the average traction force calculated at the cell periphery was $\approx 25 \mu\text{N}$ and $\approx 5 \mu\text{N}$ for “stiffer” and “softer” micropillars, respectively. This corresponds well with the findings obtained from our cell adhesion and viability assays. The stronger traction force could be a consequence of the cells' ability to achieve more stable adhesion on an appropriate substrate and to increase the cell surface area to maintain effective cellular homeostasis. Our findings also support the general trend of cellular force to be stronger on a stiffer than a softer substrate;^[45] the force is suggested to be strongest at the lamellipodia and to decrease toward the center of the cell, as has been reported previously.^[4]

The cellular force measured for different aspect ratios of commonly used micropillars made of PDMS as a very soft polymer has been reported around tens to hundreds of nN.^[13] High aspect ratio polycarbonate pillars as the stiffer polymer with Young's modulus, a little bit lower than parylene C, have been fabricated by nanoimprinting method.^[4] Considering the same dimension of parylene C and polycarbonate micropillars, the difference in spring constant is $\approx 2 \mu\text{N} \mu\text{m}^{-1}$ which does not have to be such a significant difference but it can be still successfully recognizable by sensitive cells. Further, we would like to show that cells can sense and bent pillars with very high spring constant of $\approx 28 \mu\text{N} \mu\text{m}^{-1}$ with cellular force calculated $\approx 25 \mu\text{N}$ which has not been published in the literature so far.

3. Conclusion

We introduced “top-down” fabrication of a highly ordered array of SiO₂/parylene C micropillars for use as a probe for the quantification of cellular traction force. Micropillars with different spring constants were fabricated from the parylene C and a thin layer of SiO₂ was introduced to the top of each pillar to enable the covalent binding of proteins via silanization. The experimental results confirmed the patterning of micropillars via the selective chemistry of the SiO₂ interface and the chemistry performed on the parylene C micropillars' sidewalls. Such patterned micropillars constitute a technological advance that eliminates the micro-contact printing of proteins on the top of micropillar array. The cytocompatibility of SiO₂/parylene C micropillars was assessed by the morphology of 3T3-fibroblasts adhered to micropillar arrays, measuring the cell spread area, proliferation of cells, qualitative evaluations of the cytoskeleton, and the development of focal contacts. Our results did not show a cytotoxic effect of the micropillar-based substrates but did indicate a dependence on stiffness. A stiffer micropillar array enhanced the cell adhesion and proliferation rate and consequently led to a stronger cell traction force.

Parylene C is a highly rigid material with a Young's modulus of ≈ 4 GPa; it is more rigid than other polymers used for pillar fabrication and thus broadens the range of material stiffness that can be probed by cells or used as the cellular sensor. We revealed that SiO₂/parylene C micropillars with a high stiffness corresponding to the spring constant $k = \approx 4.8 \mu\text{N} \mu\text{m}^{-1}$ and $\approx 28 \mu\text{N} \mu\text{m}^{-1}$ were sensed by the cells, and that the traction force can be determined even on such stiff micropillars which could give us the information about the magnitude of cellular forces. To conclude, SiO₂/parylene C micropillars demonstrate innovative concept of a flexible micropillar substrate for the quantification of the cell traction force that eliminates the micro-contact printing of proteins, and provides a substrate with higher stiffness.

4. Experimental Section

Fabrication of Micropillars: The array of parylene micropillars with the SiO₂ layer on top of the pillars was fabricated via a “top-down” technological process (Figure S1, Supporting Information). Briefly, a 10 μm thick layer of parylene C (Palmchem) was deposited on the Si wafer using the chemical vapour deposition (CVD) method. A 250 nm thin layer of SiO₂ was deposited via a plasma-enhanced CVD at 100 °C. The deposition of a 500 nm thin Ti layer using the electron beam evaporation technique was followed by standard UV photolithography using the photoresist (PR) AZ 5214E. Photolithography of PR created the pattern of hexagonally arranged features with diameter of 2 μm and center-to-center distance of 4 μm . The titanium and SiO₂ layer was then etched using reactive-ion etching (RIE) in Cl₂ plasma and Ar/CHF₃ plasma by means of chlorine and fluorine-based RIE. Finally, the wafer was placed into the ion beam etching (IBE) instrument employing pure O₂ plasma to etch the parylene C from the areas uncovered by Ti/SiO₂. The PR was completely removed during the IBE process and the Ti residue was additionally removed using chlorine-based RIE.

Micropillar Patterning and Characterization: The micropillar morphology was analyzed via a scanning electron microscopy (SEM, TESCAN MIRA II) and an EDX analysis. The chemical patterning of the micropillars was performed as described in detail in Figure S2,

Supporting Information. The array of the micropillars was treated with piranha solution at a ratio of 5:3 (30% H₂O₂ and 96% H₂SO₄) for 10 min. The SiO₂ layer was silanized with 3-aminopropyl-triethoxysilane (APTES, Sigma) via CVD technique in a vacuum chamber at 120 °C for 30 min. The process of silane deposition spanned 30 min. The micropillars were then incubated with 0.5% (v/v) Pluronic F-127 in phosphate buffer (PBS) (Sigma) to selectively coat the parylene C. The fibronectin (50 µg·mL⁻¹ in PBS, Sigma) was covalently attached via 0.5% (v/v) glutaraldehyde (Sigma) cross-linked to the amino-functionalized SiO₂ layer. The modified micropillar array was characterized by the measurement of the CA (Phoenix 300, SEO) by applying water drop on the surface. The CA was evaluated using Surfaceware 8 software and the statistical analysis was performed on 10 drops from each step of modified surface. The CA measurement was accompanied by X-ray photoelectron spectroscopy analysis (XPS; AXIS SupraTM Kratos Analytical) for the quantification of the elemental composition on the material surface via CasaXPS software. A fluorescence microscopy (Zeiss) of the collagen-FITC conjugate (0.1 mg mL⁻¹ in PBS, Sigma) has been performed to confirm the covalent immobilization of the protein.

Cell Culture and Immunostaining: 3T3 fibroblasts (ATCC) were cultured in a complete DMEM supplemented with 10% (v/v) of fetal bovine serum and antibiotics (streptomycin 100 µg mL⁻¹, penicillin 100 UI mL⁻¹). Fibroblasts were harvested every third day. For immunofluorescence staining, the cells were fixed in 4% (w/v) of paraformaldehyde in PBS for 20 min and permeabilized in 2% (w/v) bovine serum albumin in 0.5% (v/v) Triton X-100 in PBS for 2 h. All chemicals were purchased at Sigma Aldrich. A fluorescence microscope was used to visualize the actin fibers stained with Alexa Fluor 533 RED phalloidin (ready probes from Thermo Fisher Scientific) for 30 min. The vinculin, being the protein of the focal contacts, was detected by the mouse anti-vinculin antibody (10 mg mL⁻¹, 1:100 dilution in PBS, Sigma) for 1 h and an Alexa Fluor 488 goat anti-mouse antibody (2 mg mL⁻¹, 1:100 dilution in PBS, Thermo Fisher Scientific) for 60 min.

Proliferation Assay: The BrdU (5-bromo-2'-deoxyuridine) cell proliferation assay was performed by plating 1 × 10⁴ cells onto the micropillar surface and cultured inside the humidified incubator at 37 °C and 5% CO₂. The proliferation assay was performed on days one and three, following the manufacturer's protocol (Cell proliferation ELISA, BrdU; Roche). Briefly, 10 µl of BrdU solution was added to each sample and re-incubated for an additional 2 h. The labeling medium was then removed and the cells were fixed and denatured with 200 µl of FixDenat solution for 30 min. The FixDenat solution was replaced with 100 µl of a BrdU-peroxidase (POD) antibody solution and incubated at room temperature for 90 min. The samples were rinsed three times with a buffer solution and incubated with 100 µl of the substrate solution for 20 min. The absorbance was measured at 370 nm using the microplate spectrophotometer.

SEM Characterization of Traction Force: SEM imaging was performed after the critical drying of fixed cells on patterned micropillars at an ethanol gradient from 50% to 100% for 5 min for each dilution. The dried cells were evaporated with ≈10 nm layer of gold before imaging to avoid sample charging. The deflection of the micropillars due to the cell traction force was obtained directly from the SEM images. The pillar bending was analyzed with ImageJ software on non-migrating cells at the edge of the extended lamellipodia from the initial position. Scale included in acquired SEM images and straight line selection tool were used for direct distance measurement. Since the fabricated pattern was repetitive, and thus, the distance between each two closest micropillars remains constant, we measured the shift between unbent and bent micropillars as the center-to-center distance. The average cellular traction force (*F*) from 15 imaged cells was calculated with Hooke's law (Equation 1) for higher (*h* = 9 µm) and lower (*h* = 5 µm) micropillars, respectively.

Statistical Analysis: A proliferation assay was conducted in triplicate for each substrate and the average cellular force was calculated for ten cells from each substrate. A student's *t*-test was used to determine significant differences between the groups. *P*-values of <0.05 were considered to be statistically significant.

Supporting Information

Supporting Information is available from the Wiley Online Library or from the author.

Acknowledgements

The authors would like to acknowledge the financial support provided by GACR Project Number GA19-04270Y from the Czech Republic. Thanks also go to Tomas Lednický for the XSP measurements.

Conflict of Interest

The authors declare no conflict of interest.

Data Availability Statement

Research data are not shared.

Keywords

cellular force, mechanobiology, micropillars, parylene C, silanization, silicon dioxide

Received: November 10, 2020

Revised: January 5, 2021

Published online:

- [1] T. Kojima, A. Husari, M. P. Dieterle, S. Fontaine, O. Prucker, P. Tomakidi, J. Rühle, *Adv. Mater. Interfaces* **2020**, *17*, 1901806.
- [2] R. H. W. Lam, Y. Sun, W. Chen, J. Fu, *Lab Chip* **2012**, *12*, 1865.
- [3] M. Nikkhah, F. Edalat, S. Manoucheri, A. Khademhosseini, *Biomaterials* **2012**, *33*, 5230.
- [4] F. Vielä, D. Granados, A. Ayuso-Sacido, I. Rodríguez, *Adv. Funct. Mater.* **2016**, *26*, 5599.
- [5] G. Bao, S. Suresh, *Nat. Mater.* **2003**, *2*, 715.
- [6] T. Lendenmann, T. Schneider, J. Dumas, M. Tarini, C. Giampietro, A. Bajpai, W. Chen, J. Gerber, D. Poulidakos, A. Ferrari, D. Panozzo, *Nano Lett.* **2019**, *19*, 6742.
- [7] C. G. Galbraith, M. P. Sheetz, *Proc. Natl. Acad. Sci.* **1997**, *94*, 9114.
- [8] J. L. Tan, J. Tien, D. M. Pirone, D. S. Gray, K. Bhadriraju, C. S. Chen, *Proc. Natl. Acad. Sci.* **2003**, *100*, 1484.
- [9] B. D. Hoffman, C. Grashoff, M. A. Schwartz, *Nature* **2011**, *475*, 316.
- [10] R. Farhadifar, J.-C. Röper, B. Aigouy, S. Eaton, F. Jülicher, *Curr. Biol.* **2007**, *17*, 2095.
- [11] R. Serrano, A. Aung, Y.-T. Yeh, S. Varghese, J. C. Lasheras, J. C. del Álamo, *Biophys. J.* **2019**, *117*, 111.
- [12] P. Roca-Cusachs, V. Conte, X. Trepat, *Nat. Cell Biol.* **2017**, *19*, 742.
- [13] W. J. Polacheck, C. S. Chen, *Nat. Methods* **2016**, *13*, 415.
- [14] S. Ghassemi, G. Meacci, S. Liu, A. A. Gondarenko, A. Mathur, P. Roca-Cusachs, M. P. Sheetz, J. Hone, *Proc. Natl. Acad. Sci.* **2012**, *109*, 5328.
- [15] M. Gupta, L. Kocgozlu, B. R. Sarangi, F. Margadant, M. Ashraf, B. Ladoux, *Methods in Cell Biology*, Elsevier, New York **2015**, pp. 289–308.
- [16] I. Schoen, W. Hu, E. Klotzsch, V. Vogel, *Nano Lett.* **2010**, *10*, 1823.
- [17] M. Kim, B.-U. Moon, C. H. Hidrovo, *J. Micromech. Microeng.* **2013**, *23*, 095024.

- [18] J. Fu, Y.-K. Wang, M. T. Yang, R. A. Desai, X. Yu, Z. Liu, C. S. Chen, *Nat. Methods* **2010**, *7*, 733.
- [19] Y. Sun, L.-T. Jiang, R. Okada, J. Fu, *Langmuir* **2012**, *28*, 10789.
- [20] Y.-C. Yeh, E. A. Corbin, S. R. Caliri, L. Ouyang, S. L. Vega, R. Truitt, L. Han, K. B. Margulies, J. A. Burdick, *Biomaterials* **2017**, *145*, 23.
- [21] P. A. Janmey, R. T. Miller, *J. Cell Sci.* **2011**, *124*, 9.
- [22] Z. Li, H. Persson, K. Adolffsson, L. Abariute, M. T. Borgström, D. Hessman, K. Åström, S. Oredsson, C. N. Prinz, *Nanoscale* **2017**, *9*, 19039.
- [23] N. Biais, D. Higashi, M. So, B. Ladoux, *Methods Mol. Biol.* **2012**, *799*, 197.
- [24] E. I. Liang, E. J. Mah, A. F. Yee, M. A. Digman, *Integr. Biol.* **2017**, *9*, 145.
- [25] L. Amato, S. S. Keller, A. Heiskanen, M. Dimaki, J. Emnéus, A. Boisen, M. Tenje, *Microelectron. Eng.* **2012**, *98*, 483.
- [26] C. H. Rasmussen, P. M. Reynolds, D. R. Petersen, M. Hansson, R. M. McMeeking, M. Dufva, N. Gadegaard, *Adv. Funct. Mater.* **2016**, *26*, 815.
- [27] A. Perl, D. N. Reinhoudt, J. Huskens, *Adv. Mater.* **2009**, *21*, 2257.
- [28] A. Bernard, J. P. Renault, B. Michel, H. R. Bosshard, E. Delamarche, *Adv. Mater.* **2000**, *12*, 1067.
- [29] M. W. H. Kirkness, C. S. Korosec, N. R. Forde, *Langmuir* **2018**, *34*, 13550.
- [30] B. J. Raos, C. S. Doyle, M. C. Simpson, E. S. Graham, C. P. Unsworth, *Sci. Rep.* **2018**, *8*, 2754.
- [31] P. Saengdee, W. Chairiratanakul, W. Bunjongpru, W. Sripumkhai, A. Srisuwan, W. Jeamsaksiri, C. Hruanun, A. Poyai, C. Promptmas, *Biosens. Bioelectron.* **2015**, *67*, 134.
- [32] J.-C. Wang, W. Liu, Q. Tu, C. Ma, L. Zhao, Y. Wang, J. Ouyang, L. Pang, J. Wang, *Analyst* **2015**, *140*, 827.
- [33] J. Jin, F. Huang, Y. Hu, W. Jiang, X. Ji, H. Liang, J. Yin, *Colloids Surf., B* **2014**, *123*, 892.
- [34] S. Stolnik, B. Daudali, A. Arien, J. Whetstone, C. R. Heald, M. C. Garnett, S. S. Davis, L. Illum, *Biochim. Biophys. Acta* **2001**, *1514*, 261.
- [35] X. Li, L. Lu, J. Li, X. Zhang, H. Gao, *Nat. Rev. Mater.* **2020**, *5*, 706.
- [36] G. Zan, Q. Wu, *Adv. Mater.* **2016**, *28*, 2099.
- [37] Y. Lai, J. Huang, Z. Cui, M. Ge, K.-Q. Zhang, Z. Chen, L. Chi, *Small* **2016**, *12*, 2203.
- [38] B. S. Eftekhari, M. Eskandari, P. A. Janmey, A. Samadikuchaksaraei, M. Gholipourmalekabadi, *Adv. Funct. Mater.* **2020**, *30*, 1907792.
- [39] J. I. Kim, T. I. Hwang, J. C. Lee, C. H. Park, C. S. Kim, *Adv. Funct. Mater.* **2020**, *30*, 1907330.
- [40] Z. Fohlerova, A. Mozalev, *J. Mater. Chem. B* **2019**, *7*, 2300.
- [41] O. Bilek, Z. Fohlerova, J. Hubalek, *PLoS One* **2019**, *14*, e0214066.
- [42] J. Song, J. H. Shawky, Y. Kim, M. Hazar, P. R. LeDuc, M. Sitti, L. A. Davidson, *Biomaterials* **2015**, *58*, 1.
- [43] L. Trichet, J. Le Digabel, R. J. Hawkins, S. R. K. Vedula, M. Gupta, C. Ribault, P. Hersen, R. Voituriez, B. Ladoux, *Proc. Natl. Acad. Sci.* **2012**, *109*, 6933.
- [44] X. Liu, R. Liu, B. Cao, K. Ye, S. Li, Y. Gu, Z. Pan, J. Ding, *Biomaterials* **2016**, *111*, 27.
- [45] M. Sun, G. Chi, P. Li, S. Lv, J. Xu, Z. Xu, Y. Xia, Y. Tan, J. Xu, L. Li, Y. Li, *Int. J. Med. Sci.* **2018**, *15*, 257.

**ADVANCED
MATERIALS**
INTERFACES

Supporting Information

for *Adv. Mater. Interfaces*, DOI: 10.1002/admi.202001897

SiO₂-Decorated Parylene C Micropillars Designed to Probe Cellular Force

Zdenka Fohlerova, Imrich Gablech, Alexandr Otahal, and Peter Fecko*

Supporting Information

SiO₂-decorated Parylene C micropillars designed to probe cellular force

Zdenka Fohlerova, Imrich Gablech, Alexandr Otahal, Peter Fecko*

The fabrication of SiO₂/Parylene C micropillars

Micropillars were fabricated with a Si (100) wafer of ~100 mm and ~535 μm diameter and thickness, respectively. The fabrication steps are shown in S1. The 10 μm of parylene-C was deposited on silicon using the CVD method, without substrate temperature elevation during the deposition. A ~250 nm SiO₂ thin film was deposited on the Parylene C via a plasma-enhanced chemical vapor deposition (PECVD) technique at 100 °C (**Figure S1, step 1**). The SiO₂ film was covered with a ~500 nm Ti layer using the e-beam evaporation technique, which increases the substrate temperature only in order of units of °C (**Figure S1, step 2**). After that, the deposition of the photoresist (PR) AZ 5214E spin-coated to a thickness of ~1.4 μm was performed (**Figure S1, step 3**). The PR substrate was subsequently baked at 110 °C for 50 seconds in an atmosphere of N₂. The resolution of the structures was 2 μm and due to this obstacle, it was not possible to use a thicker photoresist suitable for long-time dry-etching procedures, so a titanium hard mask was used. The substrate was then exposed to UV light (~ 90 mJ cm⁻²) using contact lithography (**Figure S1, step 4**). The processed wafer was developed in a TMAH-based developer for ~ 55 seconds, followed by a descum procedure in O₂ plasma for 45 seconds at ~300 W and a pressure of 100 Pa. The titanium layer was etched using reactive ion etching (RIE) in inductively coupled Cl₂ plasma with high-frequency source (600 W) and low-frequency source (50 W). The etching process took ~240 s and it was accompanied by optical spectrometer endpoint detection (**Figure S1, step**

5). The SiO_2 was etched by means of fluorin-based RIE in capacitively coupled Ar/CHF_3 plasma at 200 W and ~ 360 s (**Figure S1, step 6**), after which the wafer was placed into the ion-beam etching instrument to remove the Parylene-C (**Figure S1, step 7**). The Parylene was etched with O_2 plasma and the ion-mass spectrometric detection was performed. The photoresist was completely removed, while slight etching of the Ti was observed. The rest of the Ti layer on top of the pillars was completed via a Cl_2 plasma-based RIE process (**Figure S1, step 8**). Finally, the wafer was scratched with a diamond tip and broken into a number of pieces.

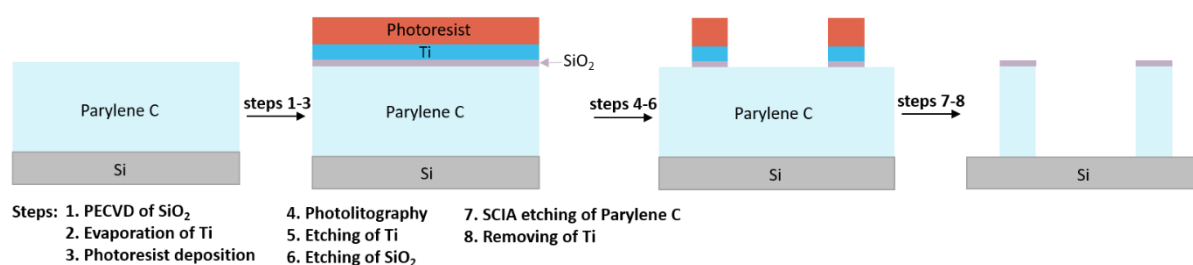


Figure S1. Scheme of the individual steps of the fabrication process of SiO_2 /Parylene C micropillars.

SiO_2 /Parylene C micropillars surface patterning

The array of micropillars was washed in deionized water, dried, and treated with piranha solution at a ratio of 5:3 (30 % H_2O_2 and 96 % H_2SO_4) for 10 minutes (**Figure S2, step 1**). The washing step was followed by a silanization process of SiO_2 with 3-aminopropyltriethoxysilane (APTES) using the chemical vapor deposition technique (CVD) in a vacuum chamber at 120°C for 30 minutes (**Figure S2, step 2**). The process of silane deposition spanned 30 minutes. The samples were purged three times by refilling the chamber with inert N_2 gas to remove residual and unreacted silane from the chamber and surface, respectively.

After that, the micropillars were incubated with 0.5% (v/v) Pluronic F-127 in PBS for 20 minutes to selectively coat the Parylene C (**Figure S2, step 3**). Subsequently, fibronectin ($50 \mu\text{g ml}^{-1}$ in PBS) was covalently bonded via a 0.5% glutaraldehyde solution to the amino-functionalized SiO_2 layer for 30 minutes (**Figure S2, step 4**).

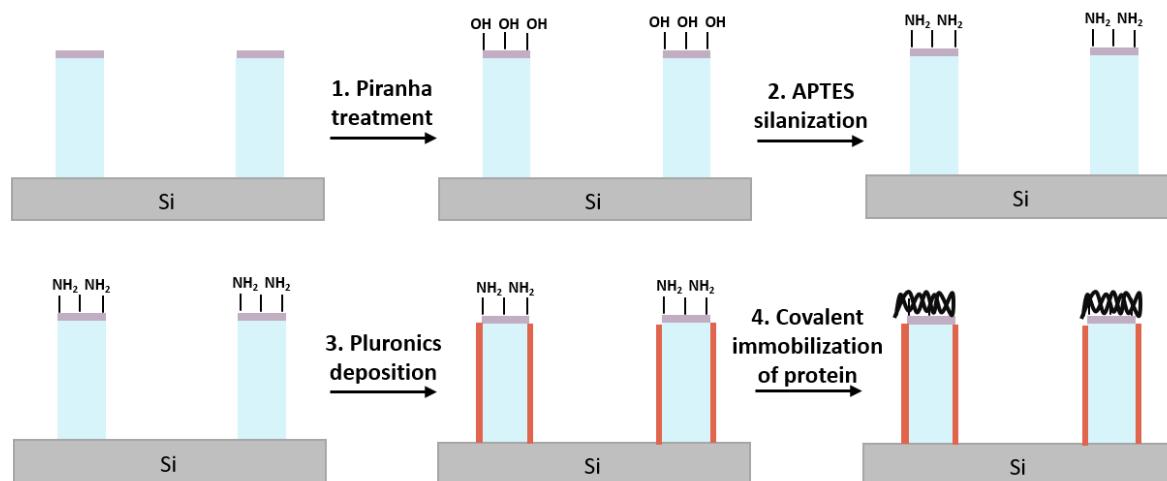


Figure S2. Scheme of micropillars surface modification.